Magnetic proximity effect and interfacial spin dependent transport in ferromagnet/heavy metal thin films

OTO-OBONG ANDREW INYANG

Magnetic proximity effect and interfacial spin dependent transport in ferromagnet/heavy metal thin films

Oto-obong Andrew Inyang

A Thesis Presented for the Degree of
Doctor of Philosophy

Magnetism and Spintronics Group
Department of Physics
University of Durham
England

April 2018

Dedicated to

God Almighty for the strength and grace throughout the period of studies. I also dedicate this work to my family, my loving husband Andrew Inyang and children, Samuel Inyang and Salem Inyang.

Whatever your hand finds to do, do it with all your might....

- Ecclesiastes 9:10 (NIV)

Magnetic proximity effect and interfacial spin dependent transport in ferromagnet/heavy metal thin films

Oto-obong Andrew Inyang

Submitted for the degree of Doctor of Philosophy
April 2018

Abstract

Platinum (Pt) has widely been used for interface driven spintronics applications due to its strong spin-orbit interaction. Pt has been reported to experience spin polarisation when placed in close proximity to a ferromagnetic (FM) material thereby influencing many spintronic phenomena. Consequently, the effect of proximity induced magnetization (PIM) in Pt is studied in this thesis with a detailed investigation of the mechanism and the implications of PIM on magnetoresistance measurements. In this work, CoFeTaB (CFTB) is the FM material investigated.

Structural and magnetic characterisation of CFTB/Pt, Pt/CFTB and Pt/CFTB/Pt samples were made in order to investigate PIM at the interface. X-ray reflectivity (XRR) and x-ray diffraction (XRD) were performed on these samples, where asymmetry in the Pt density and the crystalline texture were observed at the top and bottom interfaces. XRD measurements show the Pt crystalline texture depends on the CFTB thickness for the CFTB/Pt interface, but no significant thickness dependence was observed for the Pt/CFTB interface. The magnetic depth profile of the CFTB layer was obtained with polarised neutron reflectivity (PNR), which shows magnetisation grading. An asymmetry in Pt magnetisation was found between the two interfaces using x-ray resonant magnetic reflectivity (XRMR) with a higher moment at the top interface and lower at the buffer interface, giving a similar CFTB thickness dependence as the XRD results. This indicated that the Pt magnetisation depends slightly on Pt texture at the interface. No PIM was found in a YIG/Pt bilayer and the Pt XRD texture was poor, supporting a possible link of Pt polarisation to crystalline the morphology at the interface.

Magnetoresistance investigations in three geometries performed on Pt/CFTB and CFTB/Pt bilayers were used to decouple the magnetoresistance contributions as a result of the anisotropy of the sample, spin Hall effect and other processes. The spin Hall MR ratio obtained was ~ 0.2 %, with an additional contribution with a $\cos\theta$ dependence of ~ 0.1 %, which is a result of the impact of PIM generated spin current. No evidence of the Rashba effect was found in the symmetric CFTB/Pt/CFTB sample. Also, residual plots indicated the presence of higher harmonics that are dependent on the magnetisation direction.

Temperature dependent proximity induced magnetism in Pt in contact with CFTB was presented, with PNR providing the magnetic sensitivity to the FM layer while the XRMR provide sensitivity to Pt magnetisation. PIM scales linearly with CFTB magnetisation which is inconsistent with the Pauli susceptibility. Significantly, a threshold CFTB magnetisation is required for PIM to occur. Therefore the asymmetry in PIM at Pt/CFTB and CFTB/Pt interface is attributed to different magnetic susceptibilities at these interfaces.

Declaration

The work in this thesis is based on research carried out in the Nanomagnetism and Spintronics group, in the Centre for Material Physics, Department of Physics, Durham University, England. No part of this thesis has been submitted elsewhere for any other degree or qualification and it is solely that of the author unless referenced to the contrary in the text.

The magnetic thin films presented in this work were prepared by author. The structural characterisation with XRD presented in chapter 5 and 7 were performed by author with assistance from Dr Christy Kinane at the Rutherford Appleton laboratory, R53 material characterisation lab. SQUID measurements presented in chapter 7 were also conducted at the R53 material characterisation lab with the assistance of Dr Christy Kinane. Analyses were performed by the author.

The MR measurements in chapter 6 were made by Kathryn Moran in Prof Bryan Hickey's group at the University of Leeds. The transverse MOKE experiment in chapter 7 was performed by Mr Ben Nicholson at the Wolfson Nanotechnology Lab, Department of Physics, Durham University.

Polarised neutron reflectivity experiments were conducted at the Polref beamline at ISIS neutron facility, Didcot, England along with Dr Christy Kinane, Dr Aidan Hindmarch, Dr Mustafa Tokaç and Mr Sinan Azzawi. Analysis of experimental data was performed by author.

Synchotron radiation was employed in x-ray resonant magnetic reflectivity experiments conducted at the XMaS beamline, ESRF, France. These were coordinated by the author with a team which includes Prof Del Atkinson, Dr Aidan T Hindmarch, Mr Sinan Azzawi, Dr Laurence Bouchenoire, Dr Mustafa Tokaç, Mr Ben Nicholson and Mr Ariam Mora-Hernandez. Analysis was performed by the author with assistance from Dr Richard Rowan-Robinson and Dr Thomas Hase.

Acknowledgements

It is my genuine pleasure to express my deep appreciation to the people and institutions that have made this research work possible. My sincere thanks to TeTfund, Nigeria for providing the financial support that made this research work possible.

Immense thanks and gratitude to my supervisors Dr Aidan T. Hindmarch and Prof Del Atkinson for providing me with academic and pastoral support through out the course of this research. Their constructive advice, guidance, constant motivation, meticulous scrutiny and scientific approach have help me to a very great extent to a successful completion of each phase of the tasks on this thesis. Also, many thanks to the staff and student of Physics department for creating a conducive and engaging work and learning environment.

I am very grateful to Dr Christy Kinane along with the many support staff at ISIS neutron facility, Didcot for all the scientific support during experiment and analysis of PNR experiments. Also, my deep gratitude to Dr. Laurence Bouchenoire and the team in XMaS beamline, ESRF, France for their technical assistance during XRMR experiments. Many thanks to Prof Bryan Hickey and Kathryn Moran at the University of Leeds for providing me the assistance and opportunity to use their facility as well as the friendly collaboration. I gratefully acknowledge Dr Thomas Hase for insightful suggestion in the simulations of XRMR data.

I would like to appreciate all the people in room 142 (former room 12) which include Dr Sarah Dempsey, Dr Richard Rowan-Robinson, Dr Mustafa Tokac, Dr Jenny King, Liam Stubbington, Dr Jeovani Brandao, Sinan Azzawi, Ala Bahaaldin, Ben Nicholson, Charles Swindells, Ariam Mora-Hernandez and Joseph Troughton. Thank you for the great discussions and moment shared.

Finally, I wish to celebrate my family. My Mum, Mrs Christiana Inyang for encouraging us to achieve our dreams. My siblings Mkpouto Ekong, Godwin Inyang, Anietie Inyang, Ifiok Inyang amd Edidiong Inyang for your encouraging and funny calls and chats. To my wonderful husband Andrew Inyang for all the support, words cannot express my deep gratitude. I am so grateful to my children Samuel and Salem Inyang for your maturity and understanding which provides me with the motivation to finish well. Thank you and God bless you.

List of publications

- *Threshold interface magnetization required to induce magnetic proximity effect*

  O. Inyang, L. Bouchenoire, B. Nicholson, M. Tokaç, R.M. Rowan-Robinson, C.J. Kinane, A.T. Hindmarch

  In preparation

- *Effect of crystallite grain size on proximity induced magnetization in Pt*

  O. Inyang, L. Bouchenoire, M. Tokaç, R.M. Rowan-Robinson, C.J. Kinane, A.T. Hindmarch

  In preparation

- *Thickness dependence of the Dzyaloshinskii-Moriya interaction in Co_2FeAl ultrathin films: effects of the annealing temperature and the heavy-metal material*

  M. Belmeguenai, Y. Roussign, H. Bouloussa, S. M. Chrif, A. Stashkevich, M. Nasui, M.Gabor, A. Mora-Hernndez, B. Nicholson, **O.-O. Inyang**, A.T. Hindmarch, L. Bouchenoire

  Physical Review Applied, **9**, 044044 (2018)

Contents

List of Figures

List of Tables

Chapter 1

Introduction

Spin dependent transport has been at the centre of advances in spintronic applications with major interest in the development of high density, non-volatile magnetic recording and sensor devices. The discovery of giant magnetoresistance (GMR) by Albert Fert and Peter Grünberg [1, 2] and tunneling magnetoresistance (TMR) [3–6] has led to higher data densities magnetic random access memory (MRAM) and very sensitive magnetic sensors. In recent years, there has been significant advancement in the field of spin-based memory devices, which are non-volatile and offer low energy consumption. Improvements in device functionality in relation to these technologies has been achievable by way of reduced dimensionality. At reduced dimensions, the electronic and magnetic properties of these materials are modified and the interfacial phenomenon can be the dominant contribution to the observed electrical and magnetic functionalities. This is as a result of increased electrical scattering at the interface as the film thickness is smaller in comparison to the mean free path [7], changes in the interfacial crystalline morphology [8] and spin-dependent scattering. Phenomena such as the spin Hall effect (SHE), spin pumping, magnetic dead layer formation, and proximity induced magnetisation can improve or reduce the magnetic response necessary to support these applications. These phenomena are sometimes instigated by the spin-orbit interaction.

The spin-orbit interaction has been reported to play a major role in spin current generation in a ferromagnetic insulator (FMI)/nonmagnetic (NM) system by spin Hall effect (SHE), which was first predicted by D'yakanov and Perel in 1971 [9, 10]. Here, spins of opposite polarity

accumulates at the edge of a non-magnetic material when a charge current is passed through the sample generating a spin current transverse to the charge current direction. The generated spin current is experienced by the FMI layer as a spin torque crossing the interface modulating the electrical resistivity of the sample relative to magnetisation direction. This change in resistivity is defined by the spin conductance and spin-mixing conductance. The spin mixing conductance describes the mechanism of spin transport across the interface. It is understood as an interfacial effect and is defined by the scattering at the interface. The spin Hall angle obtained is relatively small, therefore, the spin current and the recovered charge current by inverse spin Hall effect are quite small. A report by Kim *et al.* in a ferromagnetic FM/NM system has shown a sizable spin current generated by the SHE, illustrating the role of the FM layer on spin transmission across the interface [11]. It is believed that MRAM built on a bilayer may be more efficient due to low current density required for writing and more reliable due to the physical separation between the read and write current [12], which makes this work very important.

Spin current generation and spin transport across the interface in a FMI/NM structure has been reported to be influenced by proximity induced magnetisation (PIM) of the adjacent NM, contaminating the pure spin current generated [13, 14]. PIM has also been implicated in many other spintronic phenomena such as the spin Seebeck effect [15], anomalous Hall effect [16], anomalous Nerst effect [17], interfacial spin-transparency [18], spin pumping [19], interfacial Dzyaloshinskii-Moriya interaction (iDMI) [20], spin relaxation [21], magnetic reversal by electric field [22] and by spin-orbit torque [23], and as such requires detailed investigation. PIM has been reported to be due to interfacial hybridisation between the Pt 5d band and 3d band of the FM [24–26] but little research has been done on the temperature dependence of PIM where the investigation in this thesis broadly applies.

1.1 Aims of thesis

The overall aim of this work is to ascertain the underlying mechanism of PIM and the impact of PIM on spin-dependence transport. Trilayer and bilayer thin film samples were designed to study the magnetic properties at the interface with a combinational approach, highlighting the

implications of PIM on spin transport. A detail understanding of the influence of PIM on spintronic phenomenon such as spin Hall magnetoresistance (SMR), anisotropic magnetoresistance (AMR), and Rashba effect may lead to a design of a more efficient non-volatile memory and sensor devices. Furthermore, presentation of the residual plots from the MR profile signals to the scientific world other possible MR contributions, which are dependent of magnetisation for deeper studies of its origin and influence on magnetisation processes.

1.2 Thesis Outline

The background theories of the Physics relevant to this work are discussed in chapter 2. Discussion of the classical and quantum theories of magnetism, the corresponding free energy contributions and their interactions are highlighted for a better understanding of the characteristic of ferromagnetic and paramagnetic materials needed to understand the results presented later. Furthermore, some theories of spin transport and magneto-transport phenomena are introduced, providing the foundational information required for a better description of the analysis and results in later chapters.

In chapter 3, the techniques used for sample preparation and structural and magnetic characterisation of the samples are described.

A detailed description of the GenX simulation setup and models employed in the simulation of the reflectivity data in this thesis is provided in chapter 4.

As most of the effect of PIM has been reported in materials at room temperature, chapter 5 presents the investigation of PIM in Pt in proximity with CoFeTaB (CFTB) at room temperature. The PIM effect is investigated at different thicknesses of CFTB in order to probe the interfacial contribution to the sample stack. Results were compared to the structural characterisation by XRD to consider the possible dependence on crystalline structure at the interface.

Chapter 6 presents the magnetoresistance (MR) investigation of Pt in proximity with CFTB with different sample structures, changing both the Pt and CFTB thicknesses. In order to distinguish the different contributions to magnetoresistance signal, measurements in three measurement geometries were considered.

In Chapter 7, the temperature dependence of PIM in Pt was investigated in order to understand the mechanism of PIM as a function of temperature and variation of the FM moment.

In chapter 8, the conclusions of this thesis are presented along with a brief summary of the major findings obtained in the investigations and suggestions for further work.

References

[1] M. N. Baibich, J. M. Broto, A. Fert, F. N. Van Dau, F. Petroff, P. Etienne, G. Creuzet, A. Friederich, and J. Chazelas, "Giant magnetoresistance of (001) Fe/(001) Cr magnetic superlattices," *Physical Review Letters*, vol. 61, no. 21, p. 2472, 1988.

[2] G. Binasch, P. Grünberg, F. Saurenbach, and W. Zinn, "Enhanced magnetoresistance in layered magnetic structures with antiferromagnetic interlayer exchange," *Physical Review B*, vol. 39, no. 7, p. 4828, 1989.

[3] W. Butler, X.-G. Zhang, T. Schulthess, and J. MacLaren, "Spin-dependent tunneling conductance of Fe— MgO— Fe sandwiches," *Physical Review B*, vol. 63, no. 5, p. 054416, 2001.

[4] J. Mathon and A. Umerski, "Theory of tunneling magnetoresistance of an epitaxial Fe/MgO/Fe (001) junction," *Physical Review B*, vol. 63, no. 22, p. 220403, 2001.

[5] S. Yuasa, T. Nagahama, A. Fukushima, Y. Suzuki, and K. Ando, "Giant room-temperature magnetoresistance in single-crystal Fe/MgO/Fe magnetic tunnel junctions," *Nature Materials*, vol. 3, no. 12, p. 868, 2004.

[6] S. S. Parkin, C. Kaiser, A. Panchula, P. M. Rice, B. Hughes, M. Samant, and S.-H. Yang, "Giant tunnelling magnetoresistance at room temperature with MgO (100) tunnel barriers," *Nature Materials*, vol. 3, no. 12, p. 862, 2004.

[7] Y. Namba, "Resistivity and temperature coefficient of thin metal films with rough surface," *Japanese Journal of Applied Physics*, vol. 9, no. 11, p. 1326, 1970.

[8] A. T. Hindmarch, "Interface magnetism in ferromagnetic metal–compound semiconductor hybrid structures," in *Spin*, vol. 1, pp. 45–69, World Scientific, 2011.

[9] M. D'yakonov and V. Perel, "Possibility of orienting electron spins with current," *Soviet Journal of Experimental and Theoretical Physics Letters*, vol. 13, p. 467, 1971.

[10] M. Dyakonov and V. Perel, "Current-induced spin orientation of electrons in semiconductors," *Physics Letters A*, vol. 35, no. 6, pp. 459–460, 1971.

[11] J. Kim, P. Sheng, S. Takahashi, S. Mitani, and M. Hayashi, "Spin Hall magnetoresistance in metallic bilayers," *Physical Review Letters*, vol. 116, no. 9, p. 097201, 2016.

[12] L. Liu, C.-F. Pai, Y. Li, H. Tseng, D. Ralph, and R. Buhrman, "Spin-torque switching with the giant spin Hall effect of tantalum," *Science*, vol. 336, no. 6081, pp. 555–558, 2012.

[13] Y. Lu, Y. Choi, C. Ortega, X. Cheng, J. Cai, S. Huang, L. Sun, and C. Chien, "Pt magnetic polarization on $Y_3Fe_5O_{12}$ and magnetotransport characteristics," *Physical Review Letters*, vol. 110, no. 14, p. 147207, 2013.

[14] C. O. Avci, K. Garello, A. Ghosh, M. Gabureac, S. F. Alvarado, and P. Gambardella, "Unidirectional spin Hall magnetoresistance in ferromagnet/normal metal bilayers," *Nature Physics*, vol. 11, no. 7, pp. 570–575, 2015.

[15] T. Kuschel, C. Klewe, J.-M. Schmalhorst, F. Bertram, O. Kuschel, T. Schemme, J. Wollschläger, S. Francoual, J. Strempfer, A. Gupta, *et al.*, "Static magnetic proximity effect in Pt/$NiFe_2O_4$ and Pt/Fe bilayers investigated by x-ray resonant magnetic reflectivity," *Physical Review Letters*, vol. 115, no. 9, p. 097401, 2015.

[16] S. Shimizu, K. S. Takahashi, T. Hatano, M. Kawasaki, Y. Tokura, and Y. Iwasa, "Electrically tunable anomalous Hall effect in Pt thin films," *Physical Review Letters*, vol. 111, no. 21, p. 216803, 2013.

[17] G. Guo, Q. Niu, and N. Nagaosa, "Anomalous Nernst and Hall effects in magnetized platinum and palladium," *Physical Review B*, vol. 89, no. 21, p. 214406, 2014.

[18] W. Zhang, W. Han, X. Jiang, S.-H. Yang, and S. S. Parkin, "Role of transparency of platinum–ferromagnet interfaces in determining the intrinsic magnitude of the spin Hall effect," *Nature Physics*, vol. 11, no. 6, p. 496, 2015.

[19] M. Caminale, A. Ghosh, S. Auffret, U. Ebels, K. Ollefs, F. Wilhelm, A. Rogalev, and W. Bailey, "Spin pumping damping and magnetic proximity effect in Pd and Pt spin-sink layers," *Physical Review B*, vol. 94, no. 1, p. 014414, 2016.

[20] R. M. Rowan-Robinson, A. Stashkevich, Y. Roussigné, M. Belmeguenai, S.-M. Chérif, A. Thiaville, T. Hase, A. Hindmarch, and D. Atkinson, "The interfacial nature of proximity-induced magnetism and the Dzyaloshinskii-Moriya interaction at the Pt/Co interface," *Scientific Reports*, vol. 7, no. 1, p. 16835, 2017.

[21] R. Freeman, A. Zholud, Z. Dun, H. Zhou, and S. Urazhdin, "Evidence for Dyakonov-Perel-like spin relaxation in Pt," *Physical Review Letters*, vol. 120, no. 6, p. 067204, 2018.

[22] S. Miwa, M. Suzuki, M. Tsujikawa, K. Matsuda, T. Nozaki, K. Tanaka, T. Tsukahara, K. Nawaoka, M. Goto, Y. Kotani, *et al.*, "Voltage controlled interfacial magnetism through platinum orbits," *Nature Communications*, vol. 8, p. 15848, 2017.

[23] T. Peterson, A. McFadden, C. Palmstrøm, and P. Crowell, "Influence of the magnetic proximity effect on spin-orbit torque efficiencies in ferromagnet/platinum bilayers," *Physical Review B*, vol. 97, no. 2, p. 020403, 2018.

[24] G. Schütz, R. Wienke, W. Wilhelm, W. Zeper, H. Ebert, and K. Spörl, "Spin-dependent x-ray absorption in Co/Pt multilayers and $Co_{50}Pt_{50}$ alloy," *Journal of Applied Physics*, vol. 67, no. 9, pp. 4456–4458, 1990.

[25] N. Nakajima, T. Koide, T. Shidara, H. Miyauchi, H. Fukutani, A. Fujimori, K. Iio, T. Katayama, M. Nỳvlt, and Y. Suzuki, "Perpendicular magnetic anisotropy caused by interfacial hybridization via enhanced orbital moment in Co/Pt multilayers: Magnetic circular x-ray dichroism study," *Physical Review Letters*, vol. 81, no. 23, p. 5229, 1998.

[26] X. Liang, Y. Zhu, B. Peng, L. Deng, J. Xie, H. Lu, M. Wu, and L. Bi, "Influence of interface structure on magnetic proximity effect in $Pt/Y_3Fe_5O_{12}$ Heterostructures," *ACS Applied Materials & Interfaces*, vol. 8, no. 12, pp. 8175–8183, 2016.

Chapter 2

Theory of Magnetism in relation to spin-transport mechanism

2.1 Introduction

This chapter provides the necessary physical basis on which to understand the experimental data and interpretation presented in the later part of this thesis. It covers the major concepts and theories of magnetic moments in ferromagnets and paramagnets including the response to an external applied field. Although the origin of magnetic phenomena can be best described by quantum mechanical theory, we will begin with a brief classical description. Details on magnetic interactions that lead to the observed magnetic phenomenon in ferromagnetic materials are also covered. Finally, related theories of magneto-transport and spin-transport are discussed.

2.2 Origin of magnetic moments and magnetism

Electrons are characterized by both spin and charge. Classically, magnetism originates from electron motion about the nucleus and about its axis. Electrons with mass, m_e and charge, e^- can be thought of as orbiting the nucleus at separation r with a velocity of v. This motion is characterized by the angular momentum, L, to magnetic moment, μ_{orbital}, ratio [1, 2] (shown in Figure 2.1a). The orbital angular momentum, L and orbital magnetic moment, μ_{orbital},

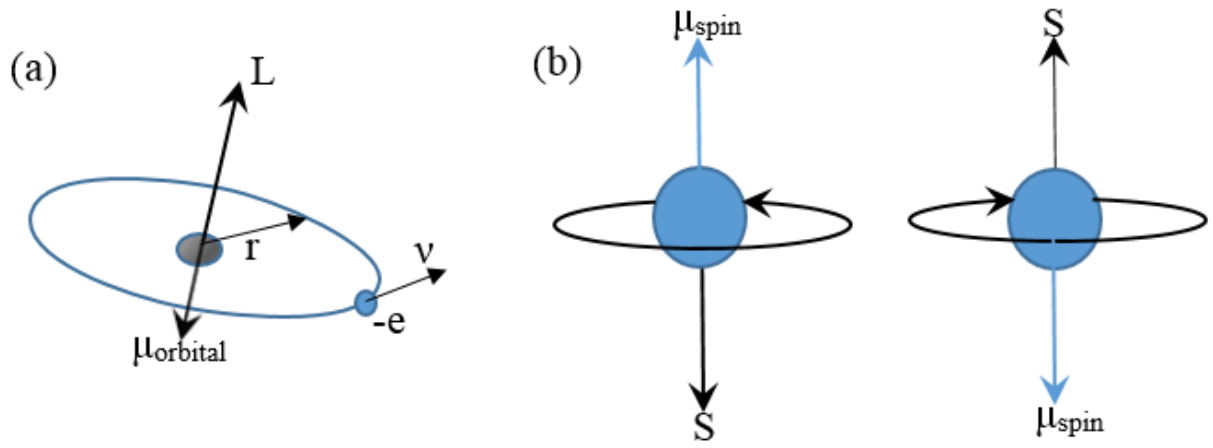

Figure 2.1: Schematic representation of (a) orbital magnetic moment due to orbital motion about the nucleus (b) Spin magnetic moment due to spin motion about the electron axis

lie perpendicular to the plane of the orbit in opposite directions [3, 4]. The orbital angular momentum is given as

$$\mathrm{L} = \mathrm{m_e} v \mathrm{r}. \tag{2.2.1}$$

Electron motion around the nucleus can be viewed as a circular electric current loop with zero resistance that gives rise to orbital magnetic moment defined as the product of the current and the area,

$$\mu_{\mathrm{orbital}} = \mathrm{I}\pi\mathrm{r}^2, \tag{2.2.2}$$

were $\mathrm{I} = -\mathrm{ev}/2\pi\mathrm{r}$. Equation 2.2.2 can be related to L by

$$\mu_{\mathrm{orbital}} = -\frac{\mathrm{e}}{2\mathrm{m_e}}\mathrm{L}. \tag{2.2.3}$$

An estimate of the atomic magnetic moment can be calculated classically using the Bohr model which describes the angular momentum as a quantized quantity. According to this model, the minimum allowed angular momentum is quantised in units of $\hbar$. Hence the magnetic moment

$$\mu_{\mathrm{orbital}} = -\frac{\mathrm{e}\hbar\mathrm{L}}{2\mathrm{m_e}} = -\mu_{\mathrm{B}} \tag{2.2.4}$$

where $\hbar = 1.0546\mathrm{x}10^{-34}$Js is the reduced Planck constant and μ_{B} is the Bohr magneton given in SI units [5].

As mentioned earlier, another contribution of magnetic moment is the electron's spin-like motion as shown in figure 2.1b. Electron spin can be viewed in two states: spin up(↑) and spin down (↓) and the associated magnetic moment can take only one of these spin directions. The spin-like motion of an electron about its axis produces a current loop which gives rise to spin magnetic moment, μ_{spin} oriented along the rotation axis (shown by Figure 2.1b). As a result there is an associated spin angular momentum, S, acting in a direction opposite to μ_{spin}. The magnetic moment to angular momentum ratio of electron spin is twice as large as its orbital motion contribution. This can be explained quantum mechanically as describe in [6]. As such, the spin magnetic moment is defined as

$$\mu_{\text{spin}} = -\frac{\text{e}}{\text{m}_\text{e}}\text{S}. \tag{2.2.5}$$

The combination of the contribution due to individual spin and orbital motion of each electron in an atom gives rise to the total angular momentum, J and total magnetic moment, μ_{total}. The total angular momentum is the vector sum of the orbital and spin angular momenta as

$$\text{J} = \text{L} + \text{S} \tag{2.2.6}$$

while the total magnetic moment between the magnetic moment and angular momentum can be written as

$$\mu_{\text{total}} = -\frac{\text{g}\mu_\text{B}}{\hbar}\text{J}. \tag{2.2.7}$$

where $\hbar$ is the reduced Planck constant, μ_B is the Bohr magnetron and g is the Landé g-factor: a dimensionless constant which account for the different contribution between the orbital and spin moment and is given by

$$\text{g} = 1 + \frac{\text{J}(\text{J}+1) + \text{S}(\text{S}+1) - \text{L}(\text{L}+1)}{2\text{J}(\text{J}+1)}. \tag{2.2.8}$$

This factor is only define where the spin-orbit coupling scheme such as Russel-Saunders coupling is well defined and takes a value of 1 for pure orbital moment and 2.0023193 for pure spin

moment [3]. In some complicated systems, its value varies between 1 and 2 indicating that both effects are involved and in feromagnetic (FM) metals it is usually more than 2. The g-factor can be determined from the frequency of electrons orbital motion known as the gyromagnetic ratio, γ, extracted from magnetic resonance experiment, which is determine from the ratio of angular momentum to magnetic moment,

$$\gamma = -\frac{\mathrm{eg}}{2\mathrm{m_e}} = -\frac{\mathrm{g}\mu_\mathrm{B}}{\hbar}. \tag{2.2.9}$$

The gyromagnetic ratio confirms that the largest contribution to the intrinsic magnetic moment in ferromagnetic materials is due to electron spin rather than the orbital momentum [7].

2.2.1 Quenching of orbital moment and the g-factor

The theoretical estimated magnetisation of 3d transition metals deviates from the experimental values because of the strong crystal field relative to spin orbit coupling in these materials when Hund's rules are followed. This is as a result of the breakdown in Hund's third rule which considers the spin-orbit coupling to be the most significant energy term after the Coulombic effect leading to wrong estimation of the magnetisation. In a partially filled 3d transition metal, the orbital angular momentum component, L, is greatly influence by the crystalline environment. The partially filled electrons are acted upon by an electric field that is not spherically symmetric but symmetric to the crystalline site relative to each ion's location. This field is known as the crystal field and is much stronger than the spin-orbit coupling (SOC), therefore overriding Hund's third rule. This crystal field is introduced as a perturbation, which acts as an addition to SOC in Hund's third rule which is modified to explain this effect [8]. The crystal field lifts the spin degeneracy, unlike the case of SOC which lifts only the orbital degeneracy if the SOC is sufficiently asymmetric. The lift in the spin degeneracy by the crystal field leads to a case where each component of L vanishes even though the average L ($\mathrm{L}^2 = \mathrm{L}(\mathrm{L}+1)$) still has a mean value. Experimental data tend to suggest that the system prefer a choice of ground state such as $\mathrm{L} = 0$ (i.e $\mathrm{J} = \mathrm{S}, \mathrm{g_J} = 2$) which produces a much better agreement between theoretical predictions and experimental moments [9]. This implies that the presence of a strong crystal field effectively

quenches the orbital angular momentum to zero, which means that we can neglect the value of L anticipated based on Hund's rules in the calculation of Landé g-factor [2]. This effect can be classically interpreted to be associated to the precession of the orbital angular momentum in the crystal field such that the magnitude of the L component does not change but the average component is zero.

Orbital angular momentum quenching is more complex in partially filled 4d and 5d transition metals because the SOC is much stronger. The splitting due to SOC is comparable to and in some cases greater than crystal field splitting. Cases like this which varies from the conventional cases explained by Hund's rule are described by a subtle application of group theory [10]

Partial orbital quenching is observed experimentally in 3d ions because the spin orbit coupling cannot be completely ignored. Spin orbit coupling can be consider as a perturbation and in some cases may lead to a mixed state with non-zero angular momentum. Variations of g-factor from 2 imply the presence of an orbital magnetic moment, which depends on the strength of the spin orbit coupling. The spin and orbital moments are parallel when $g > 2$ and anti-parallel when $g < 2$. In a 3d transition metal, the g-factor is slightly anisotropic [11], while in other cases it may be dependent on the direction of applied magnetic field with respect to the crystal axes [12].

2.2.2 Atomic magnet precession

A magnetic moment, μ, placed in a magnetic field B experiences a torque which tends to align it to the magnetic field. The magnetic moment will not simply align in the direction of the field because the magnetic moment is proportional to angular momentum. If the magnetic moment is seen as a current loop and the influence towards alignment is described as a torque τ on the current loop directed at an angle θ to the field direction. The torque is defined as [9]

$$\tau = \mu \times \mathrm{B} \tag{2.2.10}$$

and produces a change in angular momentum L perpendicular to the angular momentum as shown in Figure 2.2. This forces the magnetic moment to precess around the direction of applied

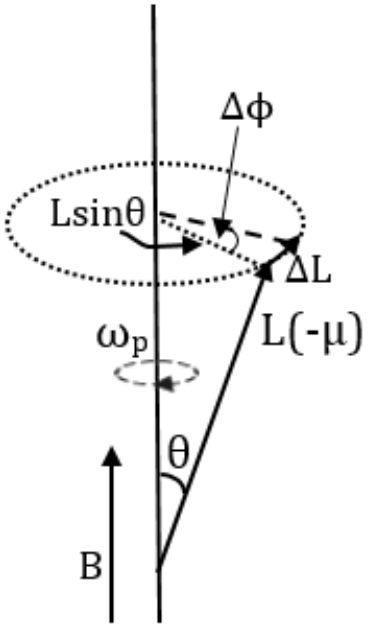

Figure 2.2: Magnetic moment procession in a magnetic field due to associated angular momentum L.

field rather than aligning to the field direction. The torque can be described as the rate of change of angular momentum. Hence, equation 2.2.10 becomes

$$\tau = \frac{\Delta L}{\Delta t} = \frac{L \sin\theta \Delta\phi}{\Delta t} = \frac{e}{2m_e} LB \sin\theta. \tag{2.2.11}$$

The energy of the magnetic moment is given by $-\mu \cdot \mathrm{B}$ and the minimum energy is achieved when the magnetic moment aligns with the field direction [8]. When electron spin precession is considered, the angular frequency, ω, is given as γB were γ is the gyromagnetic ratio [13]. A magnetic field does not only align the magnetic moment but is responsible for a variety of dynamic effects which will be discussed later in this section.

2.2.3 Exchange interaction

The exchange interaction has an electrostatic origin. It is a quantum mechanical interaction between neighbouring electrons that involves the Coulomb interaction between the charges when there is an overlap of electronic wavefunction and the Pauli exclusion principle (no two electrons can occupy the same energy and have the same quantum number). Electrons are

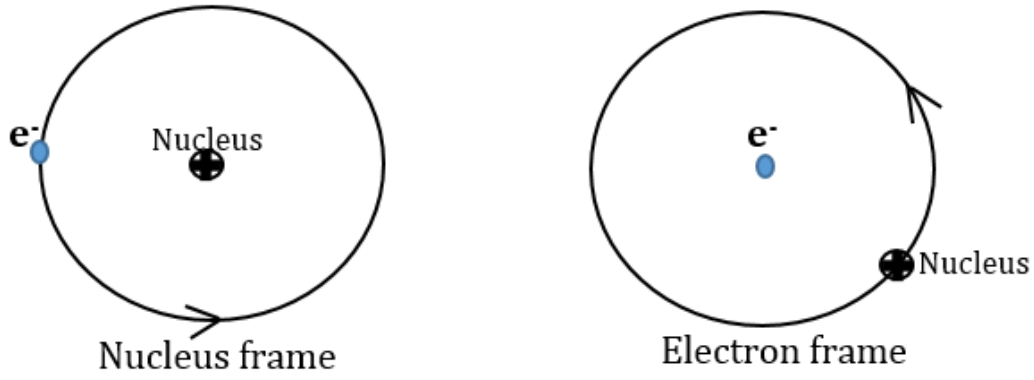

Figure 2.3: Schematic illustration of spin-orbit coupling, in the nucleus frame of reference with electron orbiting around the nucleus and the electron frame of reference showing the nucleus orbiting around the electron creating a current loop.

indistinguishable, therefore the total wave function would take an antisymmetric form in order to satisfy the Pauli exclusion principle: meaning the signs of the total wave function reverse upon exchange of the two electrons [9]. The two possible waveforms are

$$\Psi_{\mathrm{S}} = \frac{1}{\sqrt{2}}[\Psi_i(\mathrm{r}_1)\Psi_j(\mathrm{r}_2) + \Psi_i(\mathrm{r}_2)\Psi_j(\mathrm{r}_1)]\chi_{\mathrm{S}} \tag{2.2.12}$$

$$\Psi_{\mathrm{T}} = \frac{1}{\sqrt{2}}[\Psi_i(\mathrm{r}_1)\Psi_j(\mathrm{r}_2) - \Psi_i(\mathrm{r}_2)\Psi_j(\mathrm{r}_1)]\chi_{\mathrm{T}} \tag{2.2.13}$$

where Ψ_{S} is the singlet waveform comprising a symmetric spatial and antisymmetric spin singlet component χ_{S} and Ψ_{T} is the triplet waveform, consisting of antisymmetric spatial and symmetric spin triplet component χ_{T}. The neighbouring electron spin would align antiparallel (singlet state with S=0) or parallel (triplet state with S=1) due to attractive or repulsive Coulomb force. When Ψ_{S} is of a lower energy in the two waveform we have antiferromagnetic alignment but when Ψ_{T} is of a lower energy we have ferromagnetism. The associated energy due to the exchange interaction will be discussed in detail later in section 2.4.

2.2.4 Spin-orbit coupling

In the previous sections, spin and orbital angular momenta were treated independently but they weakly interact via spin-orbit coupling. Considering a nuclear frame of reference with electron orbiting the nucleus, as shown in figure 2.3. In the electron inertial frame, the nucleus orbits

around the electron generating a current loop that gives rise to a magnetic field B

$$\mathrm{B} = -\frac{E \times v}{\mathrm{c}^2} \tag{2.2.14}$$

where the electric field at the electron due to nucleus, $E = -\nabla \mathrm{V(r)} = -\frac{r\delta \mathrm{V(r)}}{\mathrm{r}\delta \mathrm{r}}$. V(r) is the Coulombic potential experienced by the electron, r is the electron distance from the nucleus and v is the velocity of electron orbit. $\mathrm{r} \times v$ is proportional to the classical angular momentum of the electron. This magnetic field couples with the spin moment yielding an energy

$$\varepsilon_{\mathrm{SO}} = \frac{\mathrm{e}\hbar^2}{2\mathrm{m_e c^2 r}} \frac{\mathrm{dV(r)}}{\mathrm{dr}} \mathrm{S \cdot L} \tag{2.2.15}$$

where $\mathrm{m_e}$ is the electron mass. The orbital angular momentum is given by $\hbar \mathrm{L} = \mathrm{m_e r} \times v$, the magnetic moment $\mu = (\mathrm{ge}\hbar/2\mathrm{m_e})\mathrm{S}$ and the factor of $\frac{1}{2}$ is known as the relativistic Thomas factor. Considering the Coulomb field in an hydrogen like atom,

$$\frac{1}{\mathrm{r}} \frac{\mathrm{dV(r)}}{\mathrm{dr}} = \frac{\mathrm{Ze}}{4\pi\epsilon_0 \mathrm{r}^3} \tag{2.2.16}$$

where Z is the atomic number of the nuclei and the expectation value $\langle \mathrm{r}^{-3} \rangle$ is proportional to Z^3. Substituting equation 2.2.16 into equation 2.2.15 shows that spin orbit coupling depends on atomic number (SOI $\propto \mathrm{Z}^4$)[9]. This explains why heavier element such as Pt, Ta, Pd and Ir have stronger spin orbit coupling. SOC acts as a perturbation to the state which is proportional to $\mathrm{L \cdot S}$, hence energy conservation is involved. Here, the total angular momentum $\mathrm{J = L + S}$ is conserved. This interaction is the root cause of several energy contributions in ferromagnets and will be discussed in detail in section 2.4.

2.2.5 Theories of paramagnetism

Paramagnetic materials have atoms and molecules with electrons in unfilled shells. Unpaired electrons give rise to permanent magnetic moments that align in the direction of the applied external field, B [9]. Classically, at zero field the atomic moments are dynamically randomly

oriented with no net magnetisation, but in the presence of an applied field takes a preferential orientation in the direction of applied field with the interaction energy, E=$-\mu$Bcosθ [10, 14]. When an external field is applied, the field energy tends to align the moments parallel to the field, but this is opposed by thermal activation. The net magnetisation can be calculated using Boltzmann statistics with $\mu\cos\theta$ the net moment along field direction B. The average moment along B is

$$< \mu_z >= \frac{\int_0^\pi \mu\cos\theta \exp(\mu \mathrm{B}\cos\theta/\mathrm{k_B T})\frac{1}{2}\sin\theta \mathrm{d}\theta}{\int_0^\pi \exp(\mu \mathrm{B}\cos\theta/\mathrm{k_B T})\frac{1}{2}\sin\theta \mathrm{d}\theta} \tag{2.2.17}$$

where $\mathrm{k_B}$ is the Boltzmann constant and T is the temperature. The total moment of a paramagnet can be described by the Langevin function, L(α)[15]

$$\frac{< \mu_z >}{\mu} = \coth\left(\frac{\mu \mathrm{B}}{\mathrm{k_B T}}\right) - \frac{\mathrm{k_B T}}{\mu \mathrm{B}} \equiv \mathrm{L}(\mu \mathrm{B}/\mathrm{k_B T}) \tag{2.2.18}$$

If μB/$\mathrm{k_B}$T is very small, the Langevin function can be approximated as μB/3$\mathrm{k_B}$T and the magnetisation defined as

$$\mathrm{M} = \frac{\mathrm{n}\mu^2 \mathrm{B}}{3\mathrm{k_B T}} \tag{2.2.19}$$

where n is the number of magnetic moments per unit volume [4, 10]. The magnetic susceptibility $\chi = \mathrm{M/H} \approx \mu_0 \mathrm{M/B}$ can be expressed as

$$\chi = \frac{\mathrm{n}\mu_0\mu^2}{3\mathrm{k_B T}} = \frac{\mathrm{C}}{\mathrm{T}}. \tag{2.2.20}$$

Equation 2.2.20 is called the Curie law where C is the Curie constant,which shows that the paramagnetic susceptibility varies inversely with temperature [14].

Quantum mechanically, the magnetic moment is now replaced by quantum spins $\mathrm{S} = \frac{1}{2}$ by considering a spin only system and ignoring the orbital contribution. The amount of magnet moment is quantized within the limit of J(J+1) where J is the total angular momentum with only two possible values as the spin $\mathrm{J} = \pm\frac{1}{2}$. The z component of moment, $\mathrm{m_J} = \pm\frac{1}{2}$ corresponding to alignment parallel and anti-parallel to applied field. Therefore the magnetic moment is $\pm\mu$

and the associated energy $\pm\mu$B [1]. The number of atoms per unit volume with spin-up is

$$\mathrm{n}_{\uparrow} = \mathrm{A}\exp(-\mu\mathrm{B}/\mathrm{k_B T}) \tag{2.2.21}$$

and that of spin down is

$$\mathrm{n}_{\downarrow} = \mathrm{A}\exp(+\mu\mathrm{B}/\mathrm{k_B T}). \tag{2.2.22}$$

The constant A is determined from the total number of atoms per unit volume n=$\mathrm{n}_{\uparrow}$+$\mathrm{n}_{\downarrow}$ and is expressed as

$$\mathrm{A} = \frac{\mathrm{n}}{\exp(+\mu\mathrm{B}/\mathrm{k_B T}) + \exp(-\mu\mathrm{B}/\mathrm{k_B T})} \tag{2.2.23}$$

and the average magnetic moment per atom is

$$\langle\mu\rangle_{\mathrm{av}} = \frac{\mu\mathrm{n}_{\downarrow} - \mu\mathrm{n}_{\uparrow}}{\mathrm{n}}. \tag{2.2.24}$$

The magnetisation, M, is expressed as

$$\mathrm{M} = \mathrm{M_s B_J(y)} \tag{2.2.25}$$

where $\mathrm{y} = \mathrm{g}\mu_{\mathrm{B}}\mathrm{JB}/\mathrm{k_B T}$, $\mathrm{M_s}$ is the saturation magnetisation and $\mathrm{B_J(y)}$ is the Brillouin function [16] given by

$$\mathrm{B_J(y)} = \frac{2\mathrm{J}+1}{2\mathrm{J}}\coth\Big(\frac{2\mathrm{J}+1}{2\mathrm{J}}\mathrm{y}\Big) - \frac{1}{2\mathrm{J}}\coth\frac{\mathrm{y}}{2\mathrm{J}}. \tag{2.2.26}$$

When $\mathrm{J} = \infty$, the Brillouin function reduced to the Langevin function [9]

$$\mathrm{B}_{\infty}(\mathrm{y}) = \mathrm{L(y)} \tag{2.2.27}$$

and when $\mathrm{J} = 1/2$, it reduces to

$$\mathrm{B}_{1/2}(\mathrm{y}) = \tanh(\mathrm{y}). \tag{2.2.28}$$

At high field tanh(y) approaches 1 predicting the state of saturation and all spins align in one direction. At low field or high temperature the magnetisation is approximated by equation

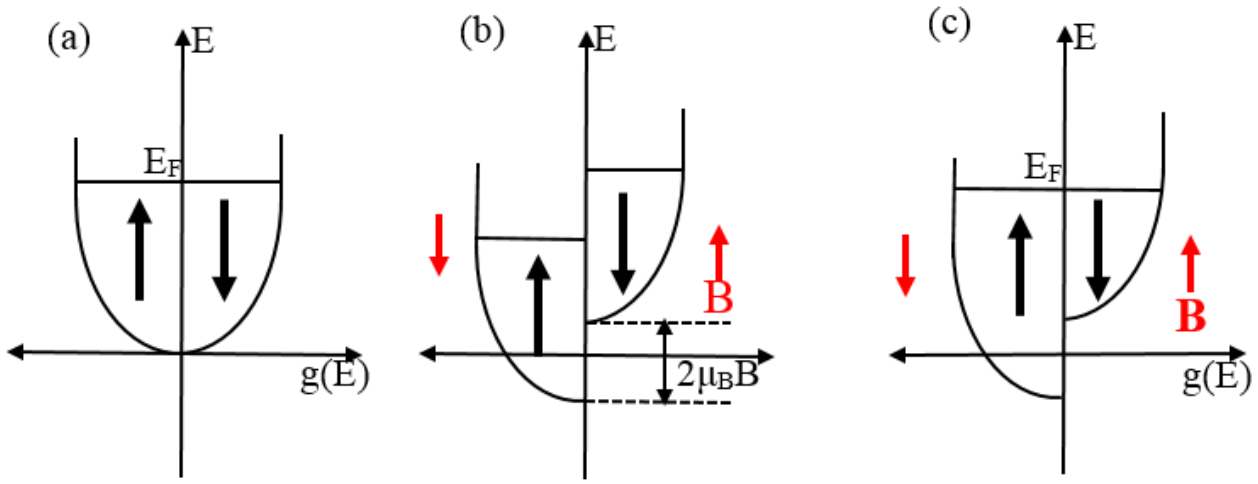

Figure 2.4: Schematic illustrations of Pauli paramagnetism for free electrons in a magnetic field B (a) At zero field (b) In a magnetic field B showing the energy different due to spin splitting (c) In a magnetic field after spin migration

2.2.19. The magnetic susceptibility is given as

$$\chi = \frac{\mathrm{n}\mu_0\mu_{\mathrm{eff}}^2}{3\mathrm{k_B T}}. \tag{2.2.29}$$

where $\mu_{\mathrm{eff}} = \mathrm{g}\mu_{\mathrm{B}}\sqrt{J(J+1)}$ is the effective moment, which results in the same form as the classical Curie law.

2.2.6 Pauli paramagnetism of free electrons

As earlier stated, free electrons in metals have spins which can align in the direction of an applied field. The Boltzmann statistics used previously are inappropriate for electrons in a degenerate Fermi gas because due to the Pauli exclusion principle, electron bands needed for spin flip are already occupy by other electrons. The electrons distribution within a metal have different energies, E, and wave vectors k_x, k_y, k_z. The energy of the most energetic electron in the system is defined as the Fermi energy which for a free electron gas is

$$\mathrm{E_F} = \frac{\hbar^2}{2\mathrm{m_e}}\mathrm{k_F^2} \tag{2.2.30}$$

where the Fermi wave vector, k_F, depends on the electron density and can be expressed as

$$k_F = \left(\frac{3\pi^2 N}{V}\right)^{\frac{1}{3}} \tag{2.2.31}$$

where $N/V = n$ is the number density of electrons. Putting equation 2.2.31 into 2.2.30, the number of electronic states, N is

$$N = \frac{V}{3\pi^2}\left(\frac{3m_e E}{\hbar^2}\right)^{\frac{3}{2}} \tag{2.2.32}$$

and the density of state per unit energy, g(E) is

$$g(E) = \frac{dn}{dE} = \frac{V}{2\pi^2}\left(\frac{2m_e}{\hbar^2}\right)^{\frac{3}{2}} E^{\frac{1}{2}} \tag{2.2.33}$$

if the Fermi surface smearing due to finite temperature and orbital contribution (i.e g=2, L=0, S=$\frac{1}{2}$ J=S) are neglected [9]. By neglecting the orbital contribution we consider an electron with only spin magnetic moment and no charge. In a magnetic field the electron band is spin split into sub-bands separated by $2\mu_B B$ as shown in figure 2.4b. Each electron contributes a magnetic moment to the magnetisation depending on the direction of its spin to the applied field causing a shift in the energy level by $\pm\mu_B B$.

Assuming the spin split energy is small, the number of electrons transfered from spin down (spin parallel and magnetic moment antiparallel to the magnetic field) to spin-up state (spin antiparallel and magnetic moment parallel to the magnetic field) is

$$n_\uparrow = \frac{1}{2} g(E_F)\mu_B B \tag{2.2.34}$$

and the corresponding deficit of spin-down electrons is

$$n_\downarrow = -\frac{1}{2} g(E_F)\mu_B B. \tag{2.2.35}$$

It is important to note that these definitions of 'spin up' and 'spin down' are applicable to all discussions in this thesis. This produces a magnetisation [14]

$$M = \mu_B(n_\uparrow - n_\downarrow) = g(E_F)\mu_B^2 B = \frac{3n\mu_B^2 B}{2k_B T_F} \tag{2.2.36}$$

where $E_F = k_B T_F$, T_F is the Fermi temperature and the magnetic susceptibility, known as the Pauli susceptibility is

$$\chi_p = \frac{M}{H} \approx \frac{\mu_0 M}{B} = \mu_0 \mu_B^2 g(E_F) = \frac{3n\mu_0\mu_B^2}{2E_F}. \tag{2.2.37}$$

By equation 2.2.37, the Pauli susceptibility is independent of temperature since T_F is a constant. The degenerate state holds well at all temperature below the melting temperature for most metals. In materials with low carrier concentration $E_F \propto n^{2/3}$ is much smaller, the non-degenerate limit may be reached and a Curie-like susceptibility obtained [9].

2.2.7 Theories of ferromagnetism

Ferromagnetic materials have spontaneous magnetisation. They are characterized by a large magnetic susceptibility that persists even in the absence of an applied field. Here, the magnetic moment is aligned due to an internal molecular field. At low temperatures the magnetic ordering is self sustained but as the temperature is raised the magnetisation, M, is destroyed at a critical temperature, T_C [9]. Weiss proposed a molecular magnetic field, B_{mf}, that is proportional to magnetisation,

$$M = \frac{C}{T}B. \tag{2.2.38}$$

This behavior can be presented as a paramagnetic system in a field $B_{app} + B_{mf}$ where $B_{mf} = \mu_0 \lambda M$ is the molecular field and λ is the molecular field constant. Therefore equation 2.2.38 becomes

$$M = \frac{C}{T}(B_{app} + B_{mf}) = \frac{C}{T}(B_{app} + \mu_0 \lambda M). \tag{2.2.39}$$

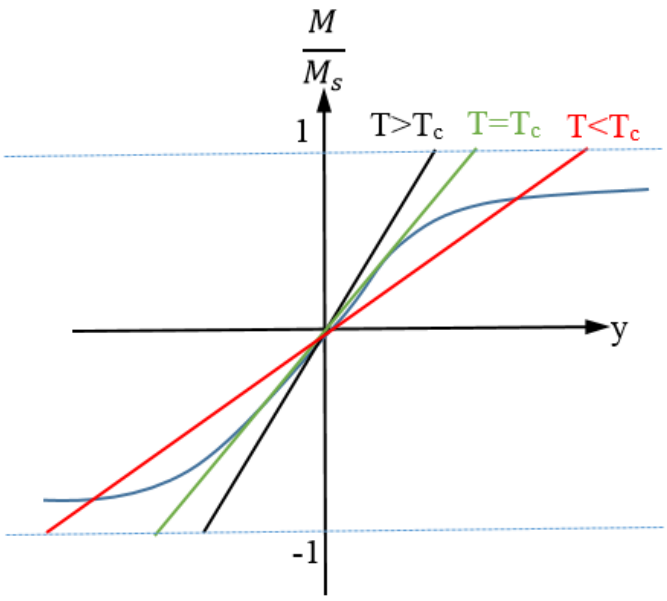

Figure 2.5: Graphical solution of equation 2.2.41 showing the temperature dependence of magnetisation above and below the critical temperature T_c with the horizontal axis, $y = g\mu_B B/k_B T$ [9].

From equation 2.2.39, the magnetic susceptibility can be written as

$$\chi = \frac{M\mu_0}{B_{app}} = \frac{C}{T(1 - \frac{\lambda C}{T})} = \frac{C}{T - T_c} \tag{2.2.40}$$

where the Curie temperature, $T_c = \lambda C$ and is known as the Curie-Weiss law. At $T < T_c$, the material has a spontaneous magnetisation which characterizes ferromagnet and when $T > T_c$ it behaves as a paramagnet (see figure 2.5). The magnetisation M of a most general case of ferromagnet can be expressed as

$$M = Ng\mu_B JB_J(y) \tag{2.2.41}$$

where B_J is the Brillouin function and $y = \frac{g\mu_B B}{k_B T} = \frac{g\mu_B \lambda M}{k_B T}$. The field B is substituted with a field with additional internal magnetic field when dealing with ferromagnetism. Solving the above equation graphically (shown in figure 2.5) reveals that at above the Curie temperature, T_c the spontaneous magnetisation M/M_s vanishes.

Ferromagnetic exchange materials can be considered quantum mechanically as paramagnetic materials with small perturbation by means of interactions [14], meaning the electrons on the neighboring atoms interact with each other. The magnetisation of multielectron atom can now

be expressed as

$$M = Ng\mu_B JB_J\left(\frac{gJ\mu_B\mu_0(H+\lambda M)}{k_B T}\right) \tag{2.2.42}$$

where H is the magnetic field strength. At high temperature M is uniform throughout the material, hence equation 2.2.42 becomes

$$M = \left(\frac{N\mu_0 g^2\mu_B^2 J(J+1)(H+\lambda M)}{3k_B T}\right) \tag{2.2.43}$$

and the susceptibility is

$$\chi = \frac{M}{H} = \frac{N\mu_0 g^2\mu_B^2 J(J+1)}{3k_B T - \lambda N\mu_0 g^2\mu_B^2 J(J+1)}. \tag{2.2.44}$$

This is similar to that in Curie-Weiss law (equation 2.2.40) with $C = N\mu_0 g^2\mu_B^2 J(J+1)/3k_B$ and $T_c = \lambda N\mu_0 g^2\mu_B^2 J(J+1)/3k_B$. By this the quantum mechanical picture is in agreement to the classical theory.

2.3 Band theory of ferromagnetism

Band theory of ferromagnetism is an extension of the theory of the Pauli paramagnet with an introduction of exchange coupling between the electrons as proposed by Stoner [17] and Slater [18]. Magnetisation arises due to unpaired electrons in a material, hence completely filled energy bands cannot contribute to the magnetic moment. The spin imbalance in partially filled bands leads to a net magnetic moment in a ferromagnetic material in the absence of external magnetic field and some of the spin down electrons at the Fermi level are considered to spin flip into the spin up band as shown in figure 2.6a. The number of electrons migrating due to spin flip increases the energy δE in the spin up channel which is considered as the energy required for a spin flip. The band splitting is equal to $2\mu_B$ and we have spin polarisation (i.e $n_\uparrow - n_\downarrow \neq 0$). The magnetization, M due to promoting electrons from spin-down to spin-up is given as

$$M = (n_\uparrow - n_\downarrow)\mu_B \approx \mu_B g(E_F)\delta E. \tag{2.3.1}$$

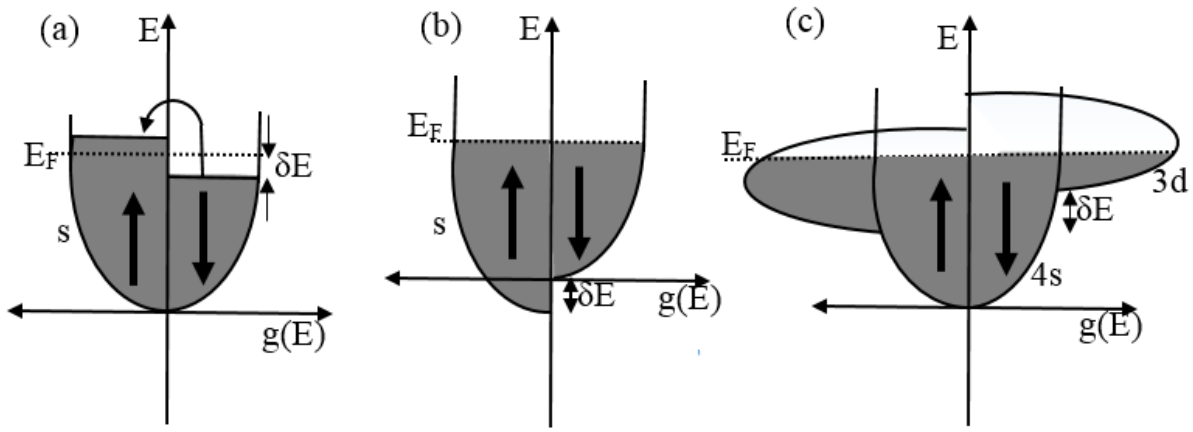

Figure 2.6: Schematic illustration of the electronic density of states showing spontaneous splitting of energy bands in the absence of an applied field (a) shows spin flip (b) resulting band splitting due to spin flip (c) spontaneous magnetisation in 3d transition metals

The total kinetic energy change due to a spin flip is

$$\Delta E_{K\cdot E} = \frac{1}{2} g(E_F) \delta E^2 \tag{2.3.2}$$

and the molecular field energy is

$$\Delta E_{P\cdot E} = -\frac{1}{2} U g(E_F)^2 \delta E^2 \tag{2.3.3}$$

where U is a measure of Coulomb energy and can be written as $U = \mu_0 \mu_B^2 \lambda$. The promotion of electrons from spin-down to spin-up sub-bands in the absence of an external field can be interpreted as an increase in the kinetic energy with a decrease in the molecular field energy which happens spontaneously. Hence the total energy change ΔE is given as

$$\Delta E = \Delta E_{K\cdot E} + \Delta E_{P\cdot E} = \frac{1}{2} g(E_F)(\delta E)^2 (1 - U g(E_F)) \tag{2.3.4}$$

Spontaneous magnetisation occurs only when $\Delta E < 0$. Therefore equation 2.3.4 can only be less than zero when $U g(E_F) \geq 1$: This is the Stoner criterion. To satisfy this, the Coulomb repulsion between electrons is large and the density of states at the Fermi-level for a particular channel is larger causing spin splitting by exchange interaction.

2.3.1 Magnetic properties of 3d elements

In 3d metals such as Fe, Co and Ni, the ferromagnetism is due to the dependence of exchange energy of these elements on particular arrangement of the electrons and their spin in the 3d band [19, 20]. Although these elements have 4s electrons, the magnetic properties arise from the high density of states in the 3d band which has a maximum occupancy of 10 electrons per atom and can be spin-split [21]. Possible electron excitations in this band with little kinetic energy increase can cause spin imbalance and a net magnetic moment per atom due to large density of states at the Fermi energy. The 4s electron band only contains up to two electron per atom and hence does not affect the magnetic properties [14]. This explains why Cu and Zn as 3d elements do not have a magnetic moment because of a completely filled 3d band which does not allow flexibility in electronic arrangement. Nevertheless, the Fe, Co, Ni counterparts exhibit ferromagnetism because the 3d sub-bands shift with respect to each other due to the presence of exchange interaction creating a spin imbalance as shown in figure 2.6c. Ferromagnetic ordering occurs when the gain in exchange energy is larger than the increase in the kinetic energy. Ferromagnetic metals exhibit finite magnetisation in thermodynamic equilibrium.

2.3.2 Stoner enhancement in paramagnet

Some materials that do not satisfy the Stoner ferromagnetic criterion can still have a susceptibility which is different from that of the Pauli paramagnet. In this case, when an external field is applied the total energy is expressed as

$$\Delta E = \Delta E_{K.E} + \Delta E_{P.E} = \frac{M^2}{2\mu_B^2 g(E_F)}\big(1 - Ug(E_F)\big) - MB \tag{2.3.5}$$

where MB characterized the effect of the applied magnetic field and U is the Coulomb energy. By finding the magnetisation that lowers the total energy ΔE which happens when,

$$\frac{M}{\mu_B^2 g(E_F)}(1 - Ug(E_F)) - B = 0; \tag{2.3.6}$$

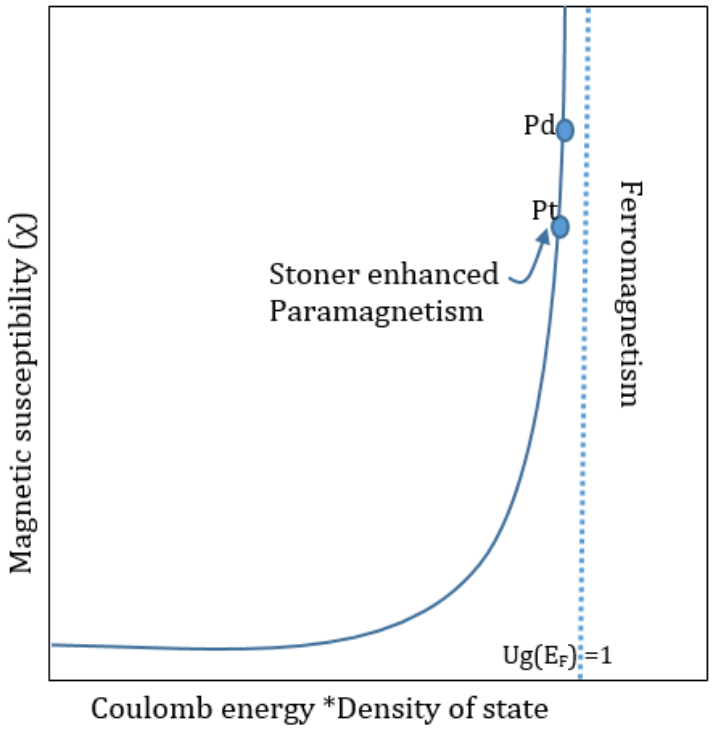

Figure 2.7: Magnetic susceptibility against the density of state $g(E_F)$ showing the enhanced magnetic susceptibility for Pt and Pd.(adapted from [22])

the magnetic susceptibility is reduced to

$$\chi = \frac{\mu_0 \mu_B^2 g(E_F)}{(1 - Ug(E_F))} = \frac{\chi_P}{(1 - Ug(E_F))} \tag{2.3.7}$$

where χ is larger than the expected χ_P in the absence of Coulomb interaction (i.e U = 0, $\chi = \chi_P$). According to equation 2.2.37, χ_P depends on the density of states $g(E_F)$.

Therefore paramagnetic materials with large densities of state are termed as Stoner enhanced paramagnets as shown in figure 2.7 because they have a large enough product of density of states and Coulomb energy to cause a significant enhancement of the magnetic susceptibility, but are unable to cause spontaneous ferromagnetism. This effect is known as Stoner enhancement which explains proximity magnetization in paramagnets such as Pt and Pd, which may assumes some ferromagnetic properties. This is as a result of induced transition into a ferromagnetic phase in paramagnet with large $g(E_F)$, which can be achieved by placing these paramagnetic material in proximity to a ferromagnet at the interface [23], alloying with a ferromagentic impurity [24–26] or by reducing dimensionality in materials [27]. This is an important concept in this work.

2.3.3 Diamagnetism

All materials exhibit diamagnetic properties, which is characterised by a weak negative magnetic susceptibility where the magnetic moment opposes the direction of the causing magnetic field. This is described classically as an action of a magnetic field on the orbital motion of the electron causing a back electro-motive force (EMF) that can be explained by Lenz's law as an opposing magnetic field. Here, the electron spin and orbitals are oriented to yield a zero net magnetic moment and only a change in the orbital moment leads to change in magnetic susceptibility. The magnitude of magnetic susceptibility is of the order of 10^{-5} or 10^{-6}. It can be described quantum mechanically by a scenario of an atom with no unfilled electron shell where the magnetic susceptibility is temperature independent. This effect can be easily ignored or requires a small correction in paramagnetic and ferromagnetic materials as it is very small in comparison to the dominant effect of paramagnetism or ferromagnetism.

Electrons are assumed to be localised spin in lattice space but conduction electrons are not spatially localised as they are free to move around. The paramagnetic effect explained earlier is due to the coupling of intrinsic spins with applied fields. There is also a diamagnetic response due to an induced orbital motion of the electrons in the presence of the applied magnetic field. This leads to the breaking of the electron distribution into series of Landau levels with a change in the total energy of the system equivalent to the magnetisation of the system. The difference in total energy between effect when $\mathrm{B} \neq 0$ and $\mathrm{B} = 0$ is given as

$$\Delta \mathrm{U} = \frac{\mathrm{V k_F e^2 B^2}}{24\pi^2 \mathrm{m_e}} \tag{2.3.8}$$

where V is the volume of the sample and $\mathrm{k_F}$ is the Fermi wave vector. The Landau diamagnetic susceptibility is expressed as

$$\chi_{\mathrm{L}} = -\frac{1}{3}\mu_0 \mu_{\mathrm{B}}^2 \mathrm{g}(\mathrm{E_F}) \tag{2.3.9}$$

and is related to the Pauli susceptibility by

$$\chi_{\mathrm{L}} = -\frac{\chi_{\mathrm{P}}}{3}. \tag{2.3.10}$$

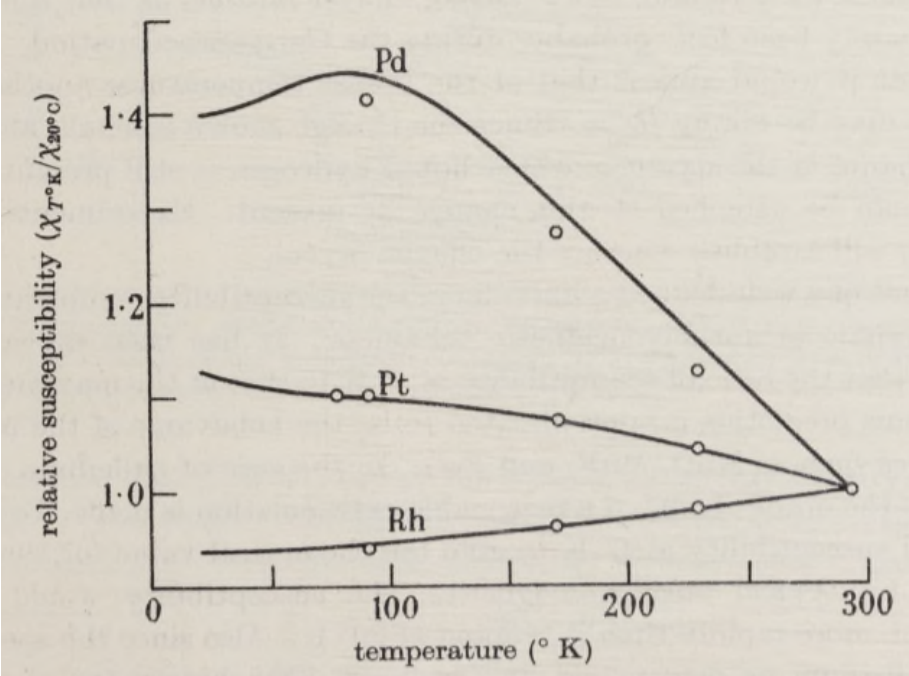

Figure 2.8: The temperature dependent of magnetic susceptibility of palladium, platinum and rhodium (adapted from [28]) .

Therefore equation 2.3.10 indicates that all metals will be paramagnetic as the Pauli paramagnetism (positive) is three times larger than the Landau diamagnetism (negative) [9, 10].

2.3.4 Magnetism of platinum

Platinum is a paramagnetic material and has been reported to interact with other ferromagnetic material forming alloys with enhanced magnetism. The earlier studies by Hoare *et al.* shows temperature dependent magnetisation profile of Pt with a peak at 90 K as shown in figure 2.8 [28]. The diamagnetic susceptibility obtained was -0.141×10^{-6}, which was similar to result reported by Kopp and Cabrera *et al.* and much smaller than the paramagnetic susceptibility on figure 2.8. [28–30]. A more recent theoretical investigation on Pt nanowires reports that Pt tends to exhibit a ferromagnetic ground state with spin moment of $0.6\mu_B$ at an equilibrium bond length 2.48 Å. The resultant paramagnetic state shows ballistic transport with magnetic field which is dependent on temperature [31]. In addition, an experimental report on Pt thin films exhibits a reversible electrical switching of the FM state by an introduction of a paramagnetic ionic liquid [32].

2.4 Energy contributions in ferromagnets

Ferromagnetic behaviour is a product of several physical processes for which the associated energies define the total magnetic energy of the material and is expressed as

$$\mathrm{E_{tot}} = \int_{\mathrm{V}} \varepsilon_{\mathrm{tot}} \mathrm{dV} \tag{2.4.1}$$

where V is the sample volume and $\varepsilon_{\mathrm{tot}}$ is the total free energy density, which is the sum of the individual energetic contributions from contributory effects defined as

$$\varepsilon_{\mathrm{tot}} = \varepsilon_{\mathrm{ex}} + \varepsilon_{\mathrm{Ze}} + \varepsilon_{\mathrm{mc}} + \varepsilon_{\mathrm{dem}} + \varepsilon_{\mathrm{ms}} + \varepsilon_{\mathrm{me}}. \tag{2.4.2}$$

Writing in terms of effective field $\mathrm{H_{eff}}$ in the system, equation 2.4.2 becomes [33]

$$\varepsilon_{\mathrm{tot}} = -\int \mu_0 \mathrm{H_{eff}} \cdot \mathrm{M} \mathrm{d}^3\mathbf{r} \tag{2.4.3}$$

where $\mathrm{d}^3\mathbf{r}$ represents the volume of the sample and $\mathrm{H_{eff}} = -\frac{1}{\mu_0} \bigtriangledown \mathrm{M}\varepsilon_{\mathrm{tot}}$. These energy contributions include exchange energy, Zeeman energy, magnetocrytalline anisotropy energy, demagnetisation energy, magnetostatic energy and magnetoelastic energy respectively. In the following sub-section, the physical origin and quantitative expressions for the various energy terms are discussed.

2.4.1 Exchange energy

This energy is responsible for magnetic ordering in materials. It is associated with the exchange interaction between neighboring spins and can be express as

$$\varepsilon_{\mathrm{ex}} = -2J_{ij}\mathrm{S}_i\mathrm{S}_j \tag{2.4.4}$$

where $\mathrm{S_i}$ and $\mathrm{S_j}$ are two neighboring spins. J_{ij} is the exchange integral that specifies the type and strength of exchange coupling. If J_{ij} is positive, the triplet state has a lower energy, spins

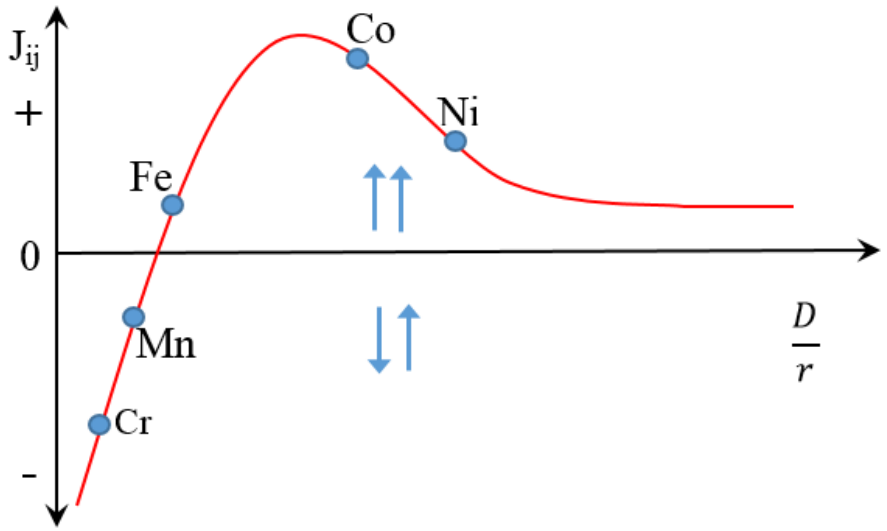

Figure 2.9: The Bethe-Slater curve showing the dependence of the exchange integral upon the interatomic separation and radius of a partially filled d-orbital.

are parallel and a ferromagnetic order result. But if J_{ij} is negative, the spin singlet state has a lower energy, spins are antiparallel and then an antiferromagnetic ordering results.

Investigation of the exchange integral by Slater and later by Bethe in 3d elements revealed that the ratio of interatomic distance D and radius of partially filled d-orbital correlate with the sign of exchange integral [34–36]. This is represented by the Bethe-Slater curve as shown in Figure 2.9 which correctly predicted the antiferromagnetic ordering. In a 3d ferromagnet, due to the large density of state of electrons close to the Fermi-level, the Coulomb repulsion is larger than the kinetic energy. Therefore, the triplet state as discussed earlier in section 2.2.3 is favored and the exchange integral is positive. The exchange integral depends on the interatomic and interelectronic spacings within the material. The ferromagnetic exchange interaction energy tries to keep the angle between the neighbouring spin small.

2.4.2 Zeeman energy

A magnetic material placed in an external magnetic field H_{ex} experiences an interaction between the saturation magnetisation and magnetic field. The interaction tends to align the magnetic moment into the field direction. The energy associated with this interaction is known as Zeeman

energy and the energy density is given as

$$\varepsilon_{\mathrm{Ze}} = -\mu_0 \mathrm{H}_{\mathrm{ex}} \cdot \mathrm{M}_{\mathrm{s}}. \tag{2.4.5}$$

The Zeeman energy is a minimum when the magnetic moment in the material (saturation magnetisation) is aligned parallel to the field direction and maximum when aligned antiparallel to the applied field.

2.4.3 Magnetocrystalline anisotropy

Electron orbitals in materials are coupled to the crystal lattice. By way of the spin-orbit interaction the spin magnetic moment interacts via the electron orbit thereby producing a magnetisation that is dependent on the orientation of the magnetisation with respect to the crystal lattice of the material. Materials tend to favour magnetisation alignment in certain crystallographic directions, known as easy axes, in contrast to certain directions known as the hard axes that requires a large field to saturate the magnetisation. This phenomenon is independent of grain size and shape of the material and is called the magnetocrystalline anisotropy. In a single crystal, this energy is required to switch the magnetisation from easy to hard axis thereby overcoming the spin orbit interaction. In most cases, the anisotropy energy is less than exchange energy.

Magnetocrystalline anisotropy energy is represented by a power series expansion in terms of angle between the direction of magnetisation and the easy axis. In materials with a single easy axis perpendicular to the hard axes such as Co, the energy associated with the magnetocrystalline anisotropy can be written as

$$\varepsilon_{\mathrm{mc}} = -\mathrm{K}_1 \sin^2\theta + \mathrm{K}_2 \sin^4\theta. \tag{2.4.6}$$

where θ is the angle between magnetisation and the easy axis and the coefficients K_1 and K_2 are the first and second order anisotropy constant with $\mathrm{K}_1 >> \mathrm{K}_2$. K_1 and K_2 may be positive or negative. They are found experimentally to be strongly temperature dependent, decreasing as temperature increases and becomes almost zero before the Curie temperature. This is due

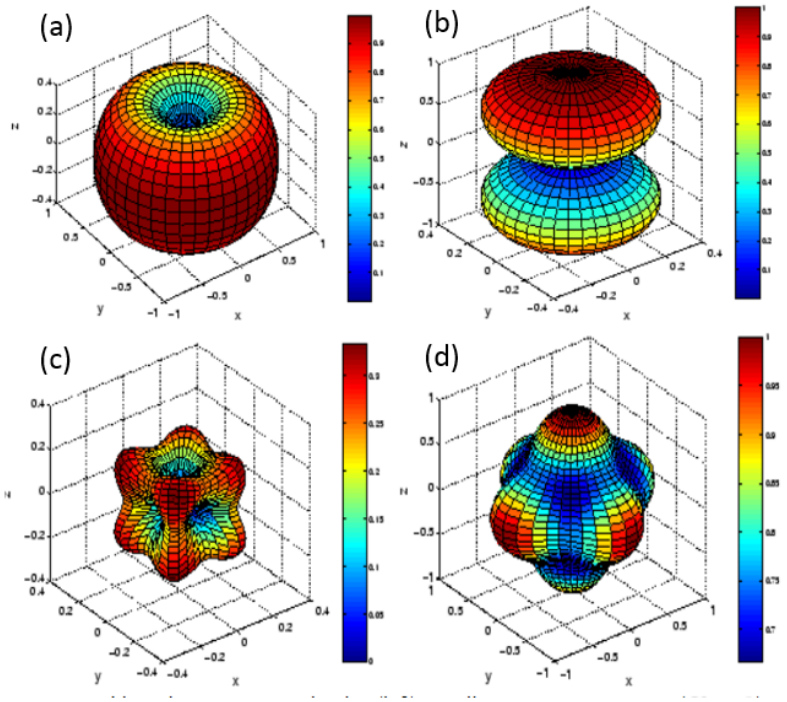

Figure 2.10: Magnetocrystalline anisotropy energy along the easy axis of (a) uniaxial crystal with $K_1 > 0$ (b) uniaxial crystal with $K_1 < 0$ (c) cubic crystal with $K_1 > 0$ (d) cubic crystal with $K_1 < 0$.[37]

to thermal expansion of the lattice parameter [38]. Also, the magnetocrystalline anisotropy constant can significantly vary with chemical composition in alloyed materials [39]. Equation 2.4.6 describes the magnetocrystalline anisotropy energy density of a uniaxial crystals while that of cubic crystals with three easy axes is given by

$$\varepsilon_{\mathrm{mc}} = -\mathrm{K}_1(\mathrm{S}_x^2\mathrm{S}_y^2 + \mathrm{S}_y^2\mathrm{S}_z^2\mathrm{S}_x^2) + \mathrm{K}_2(\mathrm{S}_x^2\mathrm{S}_y^2\mathrm{S}_z^2) \tag{2.4.7}$$

where $\mathrm{S}_{x,y,z} = \cos\theta_{x,y,z}$ are the directional cosines relative to the respective cube edges. θ is the angle between the magnetisation and the easy axes. In isotropic materials the magnetocrystalline anisotropy is zero. The anisotropy energy related to an elementary volume of a material and depends on the magnetisation of the sample.

2.4.4 Magnetoelastic anisotropy

Magnetoelastic anisotropy arises from an interaction between the magnetisation and mechanical strain where the magnetisation is coupled to the lattice of the sample. Here, the easy axis of magnetisation is changed because the distances between the magnetic atoms is altered and hence through spin-orbit coupling leads to a change in energy. This can occur as a result of magnetic ordering into domains when cooling through the Curie temperature (spontaneous magnetostriction) [14] or when magnetic field is applied to a ferromagnetic material (field induced magnetostriction) [14, 21]. Magnetostriction, λ, is the fractional change $\frac{\Delta \mathrm{l}}{\mathrm{l}}$ in a material length, l, as a result of saturating the magnetisation in the material. The value of magnetostriction can be positive (negative), indicating an expansion (contraction) due to a change in the material's dimensions from demagnetisation to saturation. The energy associated with this interaction is known as the magnetoelastic energy density, given as

$$\varepsilon_{\mathrm{me}} = \frac{3}{2}(\lambda_{\mathrm{s}}\sigma_{\mathrm{m}} \sin^2\theta) \tag{2.4.8}$$

where λ_{s} is the magnetostriction constant (saturation magnetostriction), σ_{m} is the magnetoelastic stress and θ is the angle between the magnetisation and stress direction. The physical origin stems from the spin-orbit interaction, where the applied stress will reorient the electron orbit which will then change the orientation of the spin moment of the material, changing the direction of magnetisation. In the case of 3d transition elements, the orbital momentum is almost quenched because the orbitals are fix to a crystal lattice. Thus, the reorientation is quite small. This explains the reason for small change in length to the order of 10^{-6} m by magnetostriction in 3d ferromagnetic elements. In the case of the unstrained crystal lattice the magnetoelastic energy is zero and the magnetisation energy behaviour is often dominated by magnetocrystalline and magnetostatic anisotropies

2.4.5 Magnetostatic energy and shape anisotropy

Magnetostatic energy is the energy associated with magnetic field generated from a magnetic body itself. This energy is due to interaction between the magnetic dipoles and the associated stray field. It is proportional to the integral over the the volume of the material as expressed:

$$\mathrm{E_{ms}} = \frac{\mu_0}{2} \int \mathrm{H_s^2 dV} \tag{2.4.9}$$

where $\mathrm{H_s}$ is the stray field and dV is a volume element of the material. Magnetic dipole-dipole interactions are typically smaller than the strong exchange interaction discussed earlier. The magnetostatic energy density can be written as

$$\varepsilon_{\mathrm{ms}} = \frac{\mu_0}{2} \mathrm{H_s} \cdot \mathrm{M_s}. \tag{2.4.10}$$

It is a minimum when the magnetic surface charge and the stray field are lowest. The stray field $\mathrm{H_s}$ tends to oppose the direction of saturation magnetisation $\mathrm{M_s}$. The magnitude of the stray field depends on the sample size and shape [40]. Considering the shape of a material, it is easier to magnetize a spherical shaped material along any direction in the absence of magnetocrystalline anisotropy, but in non-spherical shaped material the direction of easiest magnetisation is along their longest axis due to the magnetostatic energy. Looking at the non-shperical shape in two dimensions, where the longest axis is in the sample plane while the shorter axis is out of plane. The anisotropy of the material tends to favour in-plane magnetisation, making the in-plane direction the easy plane and out-of-plane the hard axis. This phenomenon is due to dipole-dipole interactions and is known as shape anisotropy.

2.5 3D Bloch-like magnon model

At zero temperature, a ferromagnet is ordered even though in reality the atoms are not static. As the temperature increases, the ordering is disrupted by thermal excitation (spin wave) in the form as shown in figure 2.11, which are quantized as magnons. The magnons can be produced

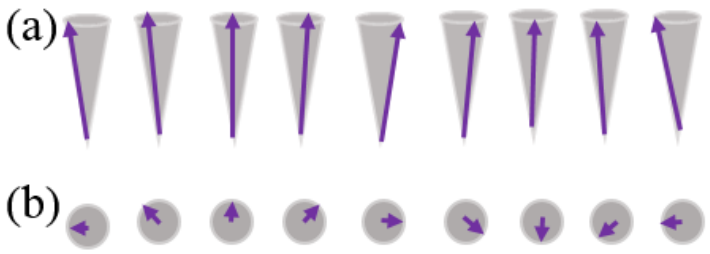

Figure 2.11: Schematic of spin wave on a line of spins. (a) Side view. (b) Top view.

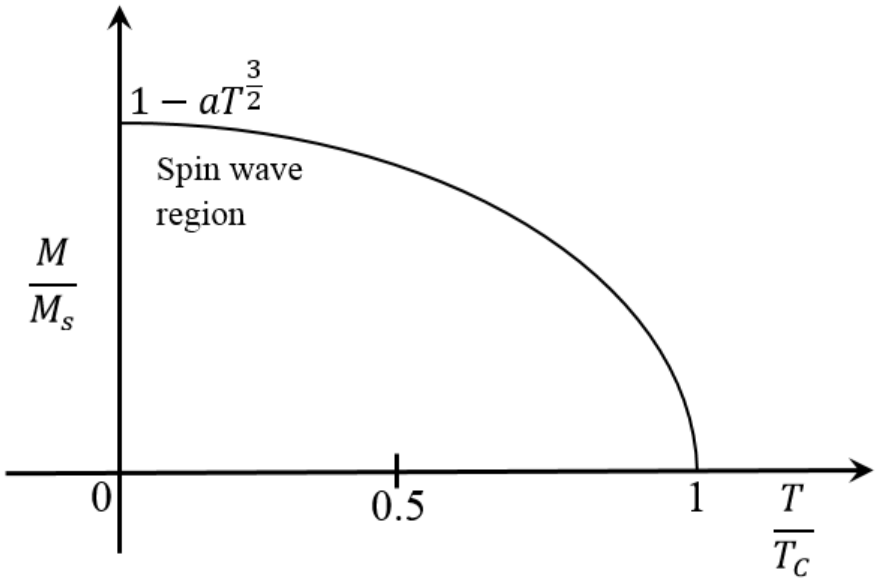

Figure 2.12: Spontaneous magnetisation profile showing the spin wave regime at low temperature, which is characterised by Bloch $T^{\frac{3}{2}}$ law

using a very small energy provided the wavelength is long enough. The behaviour of the magnon is characterized by a spin wave dispersion given as

$$\hbar\omega = 4\mathrm{JS}(1 - \cos \mathrm{q}a) \tag{2.5.1}$$

where J is the exchange integral, S is the spin, q the wave vector and a the lattice parameter. At small q, equation 2.5.1 is approximated as

$$\hbar\omega \approx 2\mathrm{JSq}^2a^2. \tag{2.5.2}$$

Therefore $\omega \propto \mathrm{q}^2$ where small ω and q characterizes low temperature features. The magnon density of states is express by

$$\mathrm{g(q)dq} \propto \mathrm{q}^2\mathrm{dq} \tag{2.5.3}$$

which leads to

$$\mathrm{g}(\omega)\mathrm{d}\omega \propto \omega^{\frac{1}{2}}\mathrm{d}\omega. \tag{2.5.4}$$

The number of excited magnon mode, $\mathrm{n_{magnon}}$ at temperature, T, is derived from equation 2.5.4 as

$$\mathrm{n_{magnon}} = \left(\frac{\mathrm{k_B T}}{\hbar}\right)^{\frac{3}{2}} \int_0^\infty \frac{\mathrm{x}^{\frac{1}{2}}\mathrm{dx}}{\mathrm{exp^x}} \propto \mathrm{T}^{\frac{3}{2}} \tag{2.5.5}$$

where $\mathrm{x} = \frac{\hbar\omega}{\mathrm{k_B T}}$. As each thermally excited magnon mode reduces the magnetisation by S=1, therefore at low temperature the reduction in spontaneous magnetisation is given by

$$\frac{\Delta \mathrm{M}}{\mathrm{M_s}} \propto \mathrm{T}^{\frac{3}{2}} \tag{2.5.6}$$

and is graphically expressed in figure .

2.6 Theory of spin transport

The spin of the electron is an additional degree of freedom for the manipulation of electrons for electronic applications. Considering electron spin transport within the Mott two current model

the orientation of the spin is up or down and is conserved in any scattering event. However, the probability of scattering for spin-up and spin-down electrons is different. As electrons obey the Pauli's exclusion principle, electron states below the Fermi level are occupied and scattered electron can only occupy empty state close to the Fermi level. For 3d feromagnets the available states at the Fermi level are spin-split. These scattering processes allow for various effects and phenomena which will be discussed in this section. The basic terms and effects associated with spin transport are covered along with its associated phenomenon.

2.6.1 Electronic transport in metals

The simplest explanation of electrical conductivity can be done with the Drude model [41]. Electrons are treated as freely moving point charges that move uniformly on a straight line only between collisions. On a collision, there is an abrupt change in velocity with a probability per unit time $\frac{1}{\tau}$. The time τ is the average time between two consecutive scattering events which is independent of the position and velocity of electron. τ is known as the relaxation time.

Also, the collision process allows the electrons to achieve thermal equilibrium because the electron emerges with a velocity different from its initial velocity before collision. In metals, electrons moves in different directions with different thermal energies. If the electrons in a unit volume moves at velocity v, the current density of these electrons would be parallel to v. If the average time elapsed since the last scattering event is τ, the net current density of these electron can be expressed as

$$\mathrm{J_c} = \frac{\mathrm{ne^2}\tau}{\mathrm{m_e}}\mathrm{E} \tag{2.6.1}$$

where $v_\mathrm{d} = -\frac{\mathrm{eE}\tau}{\mathrm{m_e}}$ is the drift velocity v_d, n is the number of electrons, e the charge of electron and m is the effective mass of charge carriers. From equation 2.6.1, the conductivity is given by

$$\sigma = \frac{\mathrm{ne^2}\tau}{\mathrm{m_e}}. \tag{2.6.2}$$

Equation 2.6.1 reveals three things which are:

- that high number of carriers lead to high current density

- the mass of charge carries determines the acceleration of electron in electric field
- large τ increases drift velocity

The above description of electron transport is a classical picture. Quantum mechanically, we can consider the current to be carried by a fraction of the electrons all moving with Fermi velocity. This leads to the fact that the relaxation time can only be from the electrons at the Fermi surface because only these electrons contribute to the conductivity of the material. Therefore the distance travelled before a scattered event occurs, known as the mean free path, λ, can be expressed as [2]

$$\lambda = \nu_{\mathrm{F}}\tau \tag{2.6.3}$$

where ν_{F} is the Fermi velocity of the charge carrier. As the resistivity, ρ, is define as the reciprocal of conductivity, we have

$$\rho = \frac{1}{\sigma} = \frac{\mathrm{m_e}}{\mathrm{ne}^2\tau}. \tag{2.6.4}$$

Resistivity increases in thin films as the film get thinner because the size effect comes into play as the mean free path, λ becomes comparable to film thickness, t. The film surface acts as an additional source of scattering; shortening mean free path and thereby lowering the conductivity. This was first proposed by Thomson [42] and later modified by Fuchs [43] and Sondheimer [44] using the Boltzmann transport equation under the following assumptions:

- The probability of scattering of an electron after collision with the film surface is independent of the initial and final direction of electron motion.
- The number of scattered electrons is independent of scattered directions.
- The mean free path in the bulk metal is constant λ.

As the resistivity is dependent on the mean free path, the measured resistivity ρ for thick films where thickness $\mathrm{t} \gg \lambda_0$ is

$$\rho = \rho_0\left(1 + \frac{3}{8}\frac{\lambda_0}{\mathrm{t}}(1-p)\right) \tag{2.6.5}$$

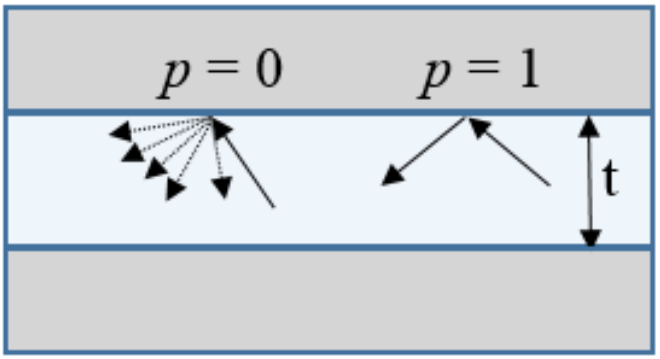

Figure 2.13: Schematic illustration of Fuchs-Sondheimer model of size effect, illustrating diffuse scattering represented with specularity parameter p=0 where all electron scattering is diffuse characterising electron scattering from a rough surface and p=1 which characterises specular scattering of electrons from a smooth layer surface. Adapted from [42].

and for very thin films, where t$\ll\lambda_0$

$$\rho = \rho_0 \frac{4}{3} \frac{(1-p)}{(1+p)} \frac{\lambda_0}{\mathrm{tln}(\frac{\lambda_0}{\mathrm{t}})}. \tag{2.6.6}$$

where ρ_0 is the bulk resistivity and p is the specularity parameter which describes the nature of the electron scattering. The boundary conditions imposed by external surfaces or interfaces are captured by the specularity parameter p which describes the fraction of electrons that are scattered elastically at the surface or interface [45]. If p=0, the electron scattering is diffused but if p=1 the scattering is specular. It is important to note that thicknesses above 50 nm are considered to have the resistivity value similar to bulk metal [46]. At room temperature, typical values of τ and λ are 10^{-14} - 10^{-15} sec and 10-100 Å respectively [10]. Also, this model does not provide a direct link to surface roughness of the film, but rather describes the scattering between two plane parallel smooth surfaces as shown in figure 2.13.

Several modifications have been made to the Fuchs-Sondheimer model to suit system investigation requirements such as systems with distinctively different interfaces, different scattering parameters [47–49], non-spherical Fermi surfaces [50], anisotropic mean free paths [51] or systems where the p is dependent upon the incident angle of the electron [52, 53]. One of these models, by Ziman [54] and Soffer [55] is based on optical arguments. In that model, the

scattering is attributed to the roughness and p varies with the angle between the surface and the incidence plane wave. More on this model is presented on the review paper [56, 57]

2.6.2 Spin-dependent conductivity and spin polarisation

In transition metal ferromagnets, the d and s band overlaps at the Fermi level. Hence, there are two contributory components to the spin polarisation in these materials which are from the narrow d band and broad s band. At the Fermi level the density of states (DOS) experiences a spin-splitting due to the exchange interaction which is characterised by differences in the chemical potential of the spin-up and spin-down bands. This consequently leads to a difference in conductivity, σ, for the spin-up and spin-down electrons. The 4s electrons contribute more to the conductivity of the material because they have lower effective mass compared to the 3d electrons. However, they are partly limited by spin dependent scattering into the empty 3d bands. The spin scattering affects the conductivity of the spin-up and spin-down electrons depending on the band splitting. Electrons from a nonmagnetic layer entering a ferromagnetic layer see a change in chemical potential as a potential barrier thereby reflecting the spin-up and spin-down electrons differently.

Spin polarisation, P, defines the degree to which a spin-type is aligned in a given direction based on the fact that spin-up and the spin-down electrons have different mobilities in a FM. Looking from the transport theory perspective, only electrons within k_BT around the Fermi energy are important. Spin-polarisation can be defined by the density of states of the spin-up and spin-down bands as

$$P = \frac{g_{\uparrow}(E_F) - g_{\downarrow}(E_F)}{g_{\uparrow}(E_F) + g_{\downarrow}(E_F)}. \tag{2.6.7}$$

where $g_{\uparrow(\downarrow)}(E_F)$ is the DOS for spin up(down) electrons at the Fermi level. It can also be defined in terms of the current associated with the spin-up, $I_{\uparrow}$ and spin-down, $I_{\downarrow}$ electrons as

$$P = \frac{I_{\uparrow} - I_{\downarrow}}{I_{\uparrow} + I_{\downarrow}} \tag{2.6.8}$$

where $I_{\uparrow} + I_{\downarrow}$ is the total charge current, I_c, and the corresponding spin current, I_s is $I_{\uparrow} - I_{\downarrow}$. The

difference in the electrochemical potential between the spin-up and spin -down electrons leads to the generation of spin current. In most transport experiments, the definition of polarisation is related to the current that can be different depending upon the relevant physical quantity for which the current is extracted [58].

A current applied in a ferromagnetic slab with different electron density for each state (spin-up and spin-down) causes the electrons to scatter generating charge current with an accompanying spin current. The electron movement is mediated by spin-orbit coupling acting on the electrons causing it to move in different direction depending on its spin type. However, it is possible for the spin current to be generated in the absence of charge transfer. This will be discussed in detail in section 2.7.5.

2.6.3 Mott two current model

Electrical properties of materials are due to the number of electrons at the Fermi energy. In metals, the rate of collisions of conduction electrons contributes to the bulk value of the electrical resistivity in a material and determines the electron motion at the Fermi energy. At low temperature, the resistivity of material is dominated by electron collisions with impurities, but at high temperature it is dominantly collisions with lattice vibrations.

In a ferromagnet the s and d bands overlap and hybridise at the Fermi energy where the s-electrons acquires the properties of the d electrons. This leads to a high probability of s-electrons scattering into unoccupied d states because of large density of states in the d band at the Fermi energy. This is know as s-d scattering. Mott [59] explains this phenomenon using a two channel model in terms of current contributions from the spin-up and spin-down charge carriers. The total resistance is modelled as the sum of the individual resistance contributions due to spin-up and spin-down electrons. The spin resistance corresponds to the two channels connected in parallel as shown in figure 2.14b. Each spin type is assumed to be characterised with a different distribution function and relaxation time τ. Also, in the presence of spin-flip scattering, another relaxation time is considered.

According to Campbell[60] and Fert [61], the total resistivity of the system is expressed as

$$\rho = \frac{\rho_{\uparrow}\rho_{\downarrow} + \rho_{\uparrow\downarrow}(\rho_{\uparrow} + \rho_{\downarrow})}{\rho_{\uparrow} + \rho_{\downarrow} + 4\rho_{\uparrow\downarrow}} \tag{2.6.9}$$

where $\rho_{\uparrow} = \frac{\mathrm{m}}{\mathrm{ne}^2\tau_{\uparrow}}$ is the resistivity of the spin-up band, $\rho_{\downarrow} = \frac{\mathrm{m}}{\mathrm{ne}^2\tau_{\downarrow}}$ is the resistivity of the spin-down band and $\rho_{\uparrow\downarrow} = \frac{\mathrm{m}}{\mathrm{ne}^2\tau_{\uparrow\downarrow}}$ is the resistivity that characterises the spin-flip scattering. Neglecting the spin-flip scattering effect, equation 2.6.9 becomes

$$\rho = \frac{\rho_{\uparrow}\rho_{\downarrow}}{\rho_{\uparrow} + \rho_{\downarrow}}. \tag{2.6.10}$$

The channel with a small resistivity is associated with a short mean free path λ. In the case of Co, the measured λ value is found out to be $\lambda_{\uparrow} = 5.5$ nm and $\lambda_{\downarrow} = 0.6$ nm [62].

In s-metals λ is small (about 10 nm) meaning that the electrons experiences more collisions and the momentum relaxation of the collisions determines the resistivity of the material. It is important to understand that this collision process does not lead to spin memory loss by electron because the spin-flip mechanism is governed only by exchange interaction or scattering by an impurity or defect with spin-orbit coupling.

In NM metals, the probability of spin-flip is only about $\frac{1}{100}$ or $\frac{1}{1000}$ of the scattering events because the spin diffusion length $\lambda_{\mathrm{s}} = \sqrt{2\mathrm{D}\tau}$ (as D is the diffusion coefficient) is several hundreds of times of λ. At room temperature, λ_s in Ag, Au and Cu is about 1-10 μm but at lower temperature (below 40K), λ_s for Al can reach 0.1mm [62]. This explains the usefulness of NM for the development of spintronic devices because of the long λ_s in NM materials.

Also at high temperature, there is strong excitation of magnons which causes the mixing of the spin-up and spin-down electrons by electro-magnon spin-flip scattering [63]. Therefore, the linear increase in electrical resistivity observed in non-feromagnetic materials above the Debye temperature is due to increased scattering from thermally excited lattice vibrations, but there is also a contribution due to spin-flip scattering in ferromagnetic metals that leads to an increase in electrical resistivity.

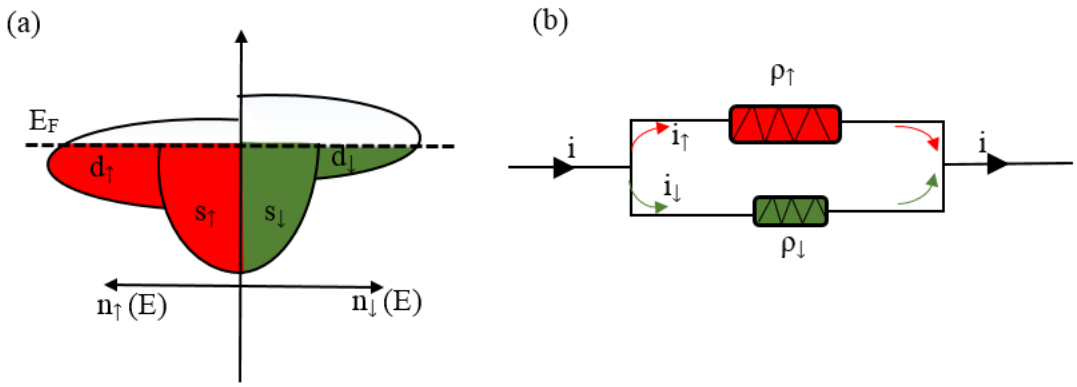

Figure 2.14: Schematic diagram of (a) density of state of a ferromagnet(b) Mott two current model.

2.7 Magneto-transport

Electrons in a ferromagnetic material deflect in different directions based on their spin in the presence of magnetic field. This can be thought of classically as a consequence of the Lorentz force acting on the charge carriers. The deflection of charge carriers leads to a change in resistance of the material relative to the local magnetisation of the material because of the coupling of the electron spins to the magnetisation. Electron motion in the presence of magnetic field can be detected electrically by the change in resistance and optically by a change of polarisation axis. Relative change in the resistance due to electron motion in the presence of an applied magnetic field is known as magneto-transport effect. Magneto-transport experiments are employed in the study of changes in magnetisation orientation and strength in materials relative to applied current. This section discusses some related magneto-transport effects investigated in this thesis, which includes anisotropic magnetoresistance (AMR), spin torque, spin Hall effect (SHE) and Rashba effect.

2.7.1 Ordinary magnetoresistance

All conductive material in the presence of a magnetic field experience a Lorentz force, F, given as

$$F = e(E + v \times B) \tag{2.7.1}$$

where E is the electric field, v is the velocity of charge carriers, e is the electronic charge and B is the magnitude of applied magnetic field. This force leads to the scattering of charge carriers in a curved trajectory which increases the total distance traveled and number of collision experienced by each electrons, leading to an increase in the resistance R_B of the material. The resistance is expressed by

$$R_B = R_0\rho_{MR}\left(1 + \mu_m^2 C_{MR} \cdot B^2\right) \tag{2.7.2}$$

where R_0 is the resistance of the material when B is zero, ρ_{MR} is the magnetoresistance coefficient, μ_m is the carrier mobility and C_{MR} is a coefficient depending on the geometry of the sample This effect follows a B^2 dependence and is larger when the field is perpendicular to current direction than in the parallel direction.

2.7.2 Anisotropic magnetoresistance

The resistivity of a ferromagnetic material can vary depending on the orientation of the magnetisation with respect to electric current direction. This phenomenon is known as anisotropic magnetoresistance (AMR). It is argued that this phenomenon is a consequence of anisotropic spin orbit mixing of spin up and spin down d band accompanied by a large probability of s-d scattering in the direction of magnetisation [46, 64]. Here, the symmetry of the atomic wave function is lower as the crystal axes determines the direction of orbital angular momentum **L** while the magnetisation determines the direction of spin angular momentum **S** thereby leading to the anisotropic spin-mixing leading to anisotropic scattering [9]. When a large external field is applied to a material, the magnetisation of the sample is in the field direction and the electron cloud around the nucleus is slightly deformed depending on the magnetisation direction. The deformation changes the scattering of the conduction electron when propagating through the lattice, which induces a dependent resistance change [65]. When the magnetisation is transverse (perpendicular) to the current direction, the electronic orbits in the plane of the current leads to small scattering due to smaller scattering cross section, giving rise to a lower resistivity, $\rho_\perp$. When the magnetisation is parallel to the current, the electron orbits perpendicular to the current leads to larger scattering due to large scattering cross section giving high resistivity, $\rho_\parallel$,

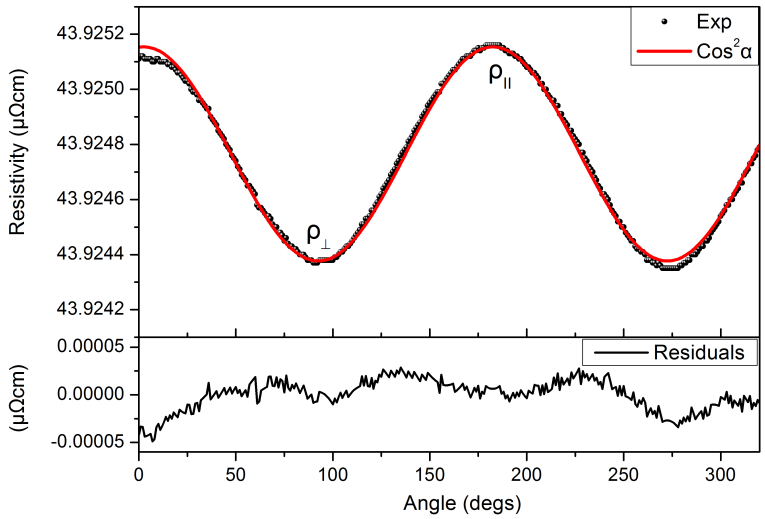

Figure 2.15: Angular anisotropic magnetoresistance of CoFeTaB(2nm)/Pt(2nm) where the longitudinal resistivity $\rho_{\parallel}$ is when the magnetisation is parallel to current direction and the transverse resistivity $\rho_{\perp}$ is when the magnetisation is perpendicular to current direction. The lower panel shows the residual plots.

as shown in figure 2.15.

The resistivity is maximum when the magnetisation is parallel to the current direction and minimum when the magnetisation is perpendicular to the current flow. The change in resistivity, $\Delta\rho = \rho_{\parallel}$-$\rho_{\perp}$ is proportional to square cosine of the angle α between the magnetisation and current direction:

$$\rho(\alpha) = \rho_{\perp} + \Delta\rho.\cos^2(\alpha) \tag{2.7.3}$$

as shown in figure 2.15. For a sample to be truly demagnetised at zero field, the resistivity can be approximated as $\rho_{\text{av}} \equiv \frac{1}{3}\rho_{\parallel} + \frac{2}{3}\rho_{\perp}$ where there is no consideration of the perpendicular component of the field. Therefore the AMR ratio defined as the relative change of resistivity when the sample is fully magnetised and its demagnetised state is estimated as

$$\frac{\Delta\rho}{\rho_{\text{av}}} = \frac{\rho_{\parallel} - \rho_{\perp}}{\frac{1}{3}\rho_{\parallel} + \frac{2}{3}\rho_{\perp}} \tag{2.7.4}$$

where the magnitude in thin films also depends on thickness, grain size, surface and/or interface condition. Smit [64], with an understanding of the Mott two current model [59], proposed that to get AMR where $\rho_{\parallel} > \rho_{\perp}$ there must be some spin-flip scattering in the spin band that is not

from magnons, because AMR tends to zero with increase temperature T. Smit attributed this to spin-flip scattering resulting from the presence of spin-orbit coupling [22].

2.7.3 Spin orbit torque

Spin dependent transport in a nonmagnetic (NM)|ferromagnetic (FM) bilayer with a current applied in the plane of the sample can generate a current induced spin torque as a result of SOC in the NM layer [66]. This is as a result of spin accumulation governed by energy dissipation due to spin flip scattering and precession of the spin within the length scale of the spin diffusion length. This effect is understood as the spin orbit torque (SOT) and the effective field due to the SOT is given as [67]

$$\mathrm{J_{ex}}\sigma_\mathrm{s} = \mathrm{a}(\sigma_\mathrm{s} \times \mathrm{M}) + \mathrm{b}\sigma_\mathrm{s} \tag{2.7.5}$$

where $\mathrm{J_{ex}}$ is the exchange coupling, σ_s is spin accumulation and M is the magnetisation. The parameters a and b depend on the spin-mixing conductance and the FM thickness.

To get a model for the SOT, we begin with the simple magnetisation dynamics model (LL model) proposed by Landau and Lifshitz in 1935, given as

$$\frac{\mathrm{dM}}{\mathrm{dt}} = \gamma \mathrm{M} \times \mathrm{H_{eff}} \tag{2.7.6}$$

where M is the magnetisation, the gyromagnetic ratio $\gamma = 2.8 \times \pi \times$ gMHz/Oe and $\mathrm{H_{eff}}$ is the effective field that determines the equilibrium orientation of magnetisation. $\mathrm{H_{eff}}$ consists of the applied magnetic field, $\mathrm{H_0}$, and effective internal fields such as anisotropic and demagnetisation fields as described in section 2.4. This model shows that M is associated with the total angular momentum that is subject to a torque resulting in precessional motion. However, the equation is for an undamped system which makes it inconsistent with experimental results. In 1955, Gilbert came up with a more robust model which includes a simpler representation of the damping in the system as the magnetisation returns to equilibrium orientation by loss of energy to the lattice [68]. Equation 2.7.6 was amended to includes a damping term which is a dimensionless

quantity. The equation is now known as the Landau-Lifshitz-Gilbert (LLG) equation given as

$$\frac{\mathrm{dM}}{\mathrm{dt}} = \gamma \mathrm{M} \times \mathrm{H_{eff}} - \frac{\alpha}{\mathrm{M_s}} \mathrm{M} \times (\mathrm{M} \times \mathrm{H_{eff}}) \tag{2.7.7}$$

where $\mathrm{M} \times \mathrm{H_{eff}}$ represents the torque field that generates the precession of M around the effective field, α is the Gilbert precessional damping constant, which determines the diminishing rotation of the M towards $\mathrm{H_{eff}}$ without reducing the torque field and $\mathrm{M} \times (\mathrm{M} \times \mathrm{H_{eff}})$ represent the relaxation of magnetisation due to damping [69, 70] without the magnetisation dynamics due to spin orbit torque. Therefore by putting equation 2.7.5 into equation 2.7.7 we have

$$\frac{\mathrm{dM}}{\mathrm{dt}} = \gamma \mathrm{M} \times \left(\mathrm{H_{eff}} + \mathrm{J_{ex}} \sigma_\mathrm{s} \right) - \frac{\alpha}{\mathrm{M_s}} \mathrm{M} \times (\mathrm{M} \times \mathrm{H_{eff}}) \tag{2.7.8}$$

which describes the magnetisation dynamics taking into account the spin orbit torque contribution as an effective field given by $\mathrm{J_{ex}} \sigma_\mathrm{s}$.

The details of the physics of these contributions are unclear and the topic is strongly debated. The two consequences of the SOT effect are a field-like torque and a damping-like torque. The field-like torque is associated to the Rashba-Edelstein effect and it corresponds to a finite imaginary component of the spin-mixing conductance, $\mathrm{G_i}$ [66, 71, 72]. The damping-like torque is associated with the spin Hall effect. It is proportional to the real component of the spin-mixing conductance, $\mathrm{G_r}$, with symmetry similar to the exchange mediated term [73]. From Equation 2.7.8 the field-like spin torque is $\tau_\mathrm{FL} = \mathrm{bM} \times \sigma_\mathrm{s}$ and the damping-like spin torque is $\tau_\mathrm{DL} = \mathrm{aM} \times \sigma_\mathrm{s} \times \mathrm{M}$. These contributions are due to the exchange interaction between the s and d electrons [74]. It is important to note that these torques are strong enough to switch magnetisation, which increases the possibility of application in magnetic storage. Both will be discussed in detail in the next section.

2.7.4 Spin Hall effect

When an electric current is passed through a material in the presence of an external applied magnetic field, there is a production of a voltage transverse to the current direction. This is the

ordinary Hall effect, which is due to Lorentz force acting on the charge carriers. The voltage generated is proportional to the applied field. Similarly, in a FM conductor, moving electrons acquire transverse voltage with spin dependent scattering. In these materials there is spin imbalance. Therefore, the different spin orientations scatter in different directions to generate a net transverse voltage when a charge current is applied. This is a consequence of the net spin polarisation of the current from the difference in the number of spin-up and spin-down electrons in the material. The net voltage generated is proportional to the sample magnetisation. This effect is known as the anomalous Hall effect and it is due to spin-orbit coupling. Conversely, when an unpolarised charge current J_c (voltage) flows in nonmagnetic (NM) material, the spin dependent transverse voltage in the absence of net polarisation is not measurable because the the number of spin up and spin down electrons are equal. Rather, spins of opposite polarity accumulate at opposite edges of the sample as shown in figure 2.16a forming a gradient in the chemical potential μ_s which generates a transverse spin current J_s. This effect is known as spin Hall effect (SHE) [75]. This was first predicted by Dyakonov and Perel [76]. The spin (charge) degree of freedom is converted to charge (spin) degree of freedom as a result of spin orbit scattering in the NM conductor. The spin current generated can be detected by the process of inverse spin Hall effect (ISHE). The SHE was first observed optically by Kato et al [77].

SHE can be categorised as intrinsic or extrinsic, which are distinguishable based on the spin relaxation if it occurs in between or during scattering [78]. Intrinsic SHE (int) originates from coherent band mixing effects induced by the applied magnetic field and disorder in the chemical potential. Therefore it is attributed to the intrinsic band structure of the crystal. The extrinsic SHE is due to scattering from material impurities. It is subdivided into skew scattering (SS) and side jump (SJ) scattering based on the scattering mechanism. Skew scattering comes from spin orbit coupling as the spin up and spin down electrons scatter with different final momentum within the disorder scattering potential (figure 2.16b) [79]. In this case, the spin orbit coupling results in an effective magnetic field which generates a net force acting towards or away from the scattering depending on spin direction. The scattering plane defines the spin-polarisation direction for the spin current generated. The magnitude of the skew scattering contribution depends on the difference in the spin-orbit coupling between the impurities and the host

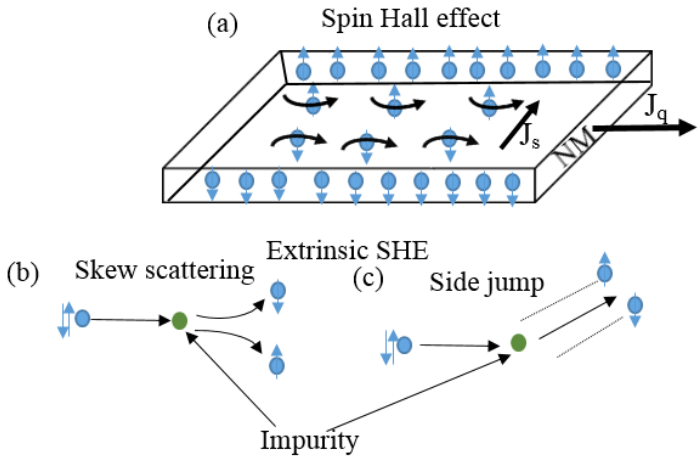

Figure 2.16: Schematic geometry of (a) the spin Hall effect with the charge current J_c in the plane scattering the spins in different direction which leads to spin accumulation in the sample edges.(b) Extrinsic skew scattering from an impurity (c) Extrinsic side jump scattering from an impurity

material. The spin-Hall angle which is the ratio of spin-Hall conductivity to longitudinal charge conductivity, is independent of the impurity concentration for the skew scattering mechanism. The side jump mechanism occurs as a result of the difference in the spin-dependent mobility during the scattering process that results in an effective transverse displacement of the electron upon repeated scattering. The side jump contribution to spin-Hall conductivity is smaller than the skew scattering contribution. Contrary to the skew scattering mechanism, the spin-Hall angle in the side jump mechanism is proportional to the impurity concentration [80]. The total spin Hall conductivity for the material is then given as

$$\sigma_{xy}^{\mathrm{H}} = \sigma_{xy}^{\mathrm{int}} + \sigma_{xy}^{\mathrm{SS}} + \sigma_{xy}^{\mathrm{SJ}} \tag{2.7.9}$$

which is the sum of intrinsic, skew scattering and the side jump contributions.

2.7.5 Spin Hall Magnetoresistance

Spin Hall magnetoresistance (SMR) is the process of change in electrical resistance of a material due to the spin Hall effect and was discovered in ferromagnetic insulator(FMI)/NM hybrid structures [81–85]. As describe earlier, charge current is converted to spin current due to SHE

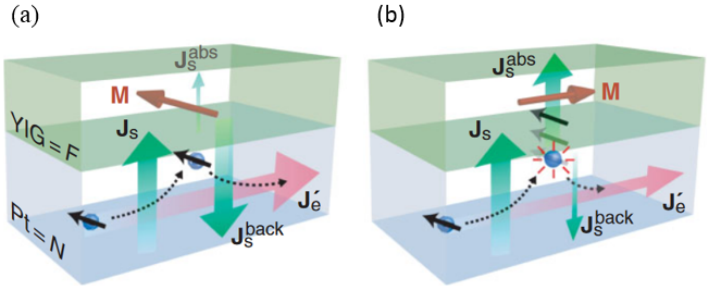

Figure 2.17: An illustration of spin Hall magnetoresistance (a) shows magnetisation is parallel to spin polarisation s (b) shows when the magnetisation is perpendicular to spin polarisation s. Sourced from [81]

and vice versa by the ISHE. This shows the coupling of the current induced spin accumulation to the electrical resistivity. When electric current J_c is passed through a NM layer spin current J_s is generated due to spin polarisation s of electrons flowing towards the interface which is absorbed or reflected as a spin transfer torque (STT) on the ferromagnetic layer. The effect of the STT at the interface can cause magnetisation damping [86] or switching [87]. This can be described by

$$J_s = \alpha_{SH}\left(-\frac{\hbar}{2e}\right)J_c \times s. \tag{2.7.10}$$

The spin current generated is transverse to the charge current J_c and the spin polarisation s. The spin Hall angle α_{SH} defines the strength of current conversion.

Ferromagnetic insulator (FMI)/NM structured materials are the common structure for SMR investigations where it is assumed that no charge current passes through the FMI. Most recently a similar effect had been observed in FM/NM hybrid structures [88, 89]. The induced spin-current perpendicular to the FMI/NM interface is transferred from the NM layer into the FMI creating a spin torque when the magnetisation M is perpendicular to the spin-polarisation s or vanishes when M is parallel to s because it is reflected at the interface back into the NM layer. The angular momentum via a spin torque is absorbed into the FMI leading to an increase in the electrical resistivity or is reflected from the FMI leading to decrease in electrical resistivity. This phenomenon is known as spin Hall magnetoresistance. At the interface, the gradient in the chemical potential as a result of the spin-dependent scattering leads to a change in the

resistance which is governed by the complex spin mixing conductance

$$G_{\uparrow\downarrow} = G_r + G_i. \tag{2.7.11}$$

The spin mixing conductance describes the spin rotation around the magnetisation axis of the FM [90]. In most SMR experiments the imaginary component of the spin mixing conductance G_i is assumed to be negligible, following the prediction that it is very small compared to the real component of the spin mixing conductance G_r [91]. The SMR ratio, with the assumption that $G_r >> G_i$, is defined as

$$\begin{aligned}\frac{\Delta\rho}{\rho} &= \alpha_{SH}^2 \frac{\lambda_s}{d_N} \mathrm{Re} \frac{2\lambda_s G_{\uparrow\downarrow} \tanh^2 \frac{d_N}{2\lambda_s}}{\sigma + 2\lambda_s G_{\uparrow\downarrow} \coth \frac{d_N}{\lambda_s}}, \\ &= \alpha_{SH}^2 \frac{\lambda_s}{d_N} \frac{2\lambda_s G_r \tanh^2 \frac{d_N}{2\lambda_s}}{\sigma + 2\lambda_s G_r \coth \frac{d_N}{\lambda_s}}.\end{aligned} \tag{2.7.12}$$

where $\rho = \sigma^{-1}$ is the intrinsic elastic resistivity of the bulk NM, $\lambda_s = \sqrt{D\tau_{sf}}$ is the spin diffusion length, which is the square root of the product of charge diffusion constant D and spin-flip relaxation time τ_{sf}, d_N is the thickness of the NM layer and G_r is the real component of the spin mixing conductance.

This is contrary to the Daniel Huertas-Hernando *et al* observation that G_i does not vanish, even when there is no conductance through the interface [92]. Generally, SMR increases with a large value of G_r but decreases with λ_s. The experimental measurement will be discussed in detail in chapter 6.

2.7.6 Rashba effect

Electrons confined in a thin layer by an asymmetric confinement potential experience a spin orbit interaction known as Rashba effect described by the Hamiltonian [93]

$$H_R = \frac{\alpha_R}{\hbar}(z \times p) \cdot \sigma \tag{2.7.13}$$

where p is the momentum vector, α_R is the Rashba coupling parameter which depends on the electric field strength, z is the symmetry-breaking axis and $\sigma = (\sigma_x, \sigma_y, \sigma_z)$ is a vector of Pauli spin matrix which describes the spin direction. The electrons experience an effective field with amplitude proportional to the electron's velocity, in the direction perpendicular to the k vector. The total Hamiltonian for the free electron is written as

$$H = \frac{p^2}{2m_e^*} + \frac{\alpha_R}{\hbar}(z \times p) \cdot \sigma \tag{2.7.14}$$

where m_e^* is the effective mass of electron and diagonalisation of equation 2.7.14 yields the dispersion spectra which is splited into two parabolas shifted in k direction with energy

$$E(k) = \frac{\hbar^2 k^2}{2m_e^*} \pm \alpha k \tag{2.7.15}$$

where $\pm$ represent the two possible spin directions with eigen states pointing perpendicular to k. Even in the absence of a magnetic field, the Rashba effect results in the lifting of spin degeneracy in the conduction band leading to a spin splitting. The spin degeneracy is a function of the time and spatial inversion symmetry which corresponds to the 2D representation of the energy dispersion spectra and Fermi contours for both the majority (blue) and minority (red) carriers shown in figure 2.18. In the nonmagnetic material, the Rashba effect causes the spins to align in the sample plane perpendicular to the electron momentum (see figure 2.18a) while in a ferromagnet it causes the spins to be canted away from the magnetisation because it is acting against the exchange interaction (see figure 2.18b) [22].

When a charge current is applied to a nonmagnetic material, the presence of Rashba effect leads to spin polarisation with a Berry phase as shown in figure 2.18c. This is represented with a shift in the Fermi contour (δk_x) in the x-direction along the electric field direction that result in an additional y-component for every spin direction. The y-component is responsible for the spin polarisation along the y-axis for minority carriers and -y-direction for majority carriers.

In a ferromagnet, the acquired Berry phase may lead to spin interference where the electron spin precesses around the local magnetisation because of the presence of exchange interaction.

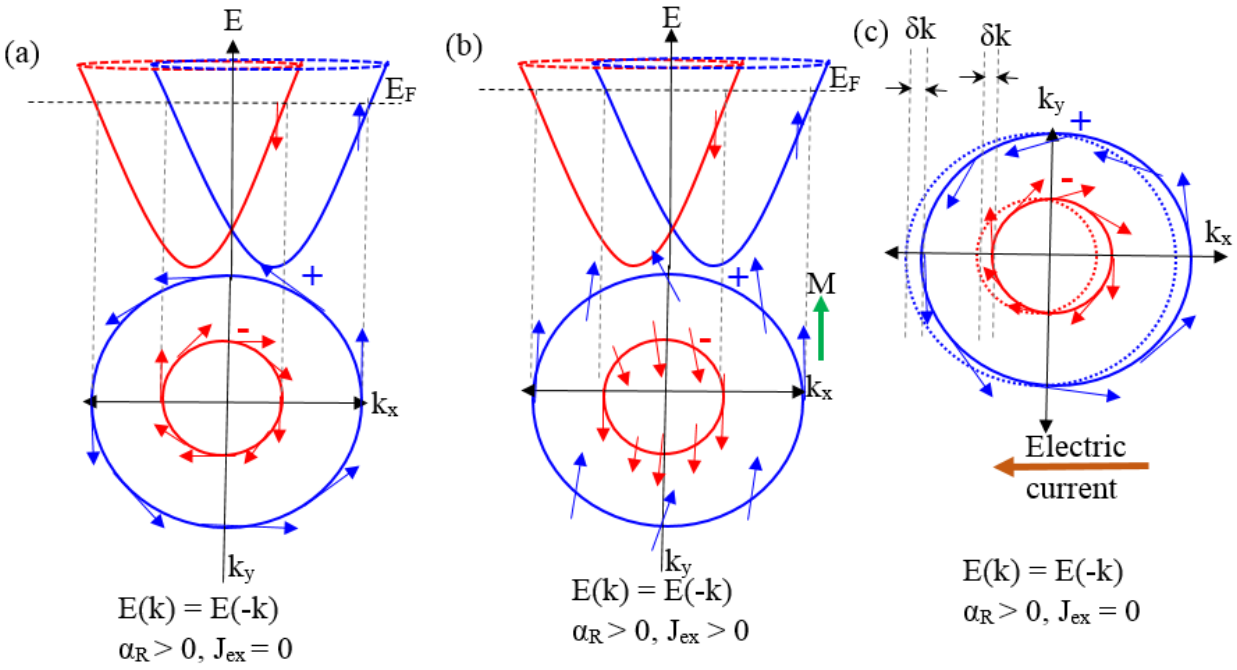

Figure 2.18: Illustration of two dimensional energy dispersion (top) and Fermi surface (bottom) with Rashba spin orbit coupling (α_R) of (a) a nonmagnetic material (b) a ferromagnetic material in applied field (c) the Fermi surface in applied current in $-$x direction.

Here, the spin precession is dependent on the electron path in the presence of the local magnetic field which is caused by the spin dependent scattering.

The Rashba effect is observed to be an interfacial effect [94, 95] where the spin polarisation at the interface in FM/NM structure exert a field-like torque on the magnetisation thereby transferring angular momentum to the FM. Similarly, the spin Hall effect introduces a damping-like torque on the magnetisation at the interface into the FM layer. If they have different symmetry it should be possible to distinguish them, but it is suggested that each have a little of the other's symmetry in part due to the imaginary mixing conductance.

2.8 Summary

This chapter is focused on the background theory of magnetism and spin transport. It begins with simple interactions in materials such as the exchange interaction and spin-orbit coupling, which have led to several effects that resulted in new discoveries for technological applications. Theories of ferromagnetism and paramagnetism were discussed following quantum mechanical

and classical approaches relating the two approaches to show that they are in agreement. Finally, spin transport theories with associated magneto-transport effects were introduced.

References

[1] R. P. Feynman, R. B. Leighton, and M. Sands, *The Feynman Lectures on Physics*, vol. 2. Addison-Wesley, 1979.

[2] C. Kittel, *Introduction to Solid State Physics*. John Wiley & Sons, 7th ed., 1996.

[3] B. Cullity and C. Graham, *Introduction to Magnetic Materials*. John Wiley & Sons, 2nd ed., 2009.

[4] M. Omar, *Elementary Solid State Physics: Principles and Applications*. Addison-Wesley, 1975.

[5] R. Turton, *The Physics of Solids*. Oxford University Press, 2000.

[6] M. Born, *Atomic Physics*. Blackie & Son Limited, London, 8th ed., 1969.

[7] R. Carey and E. D. Isaac, *Magnetic Domains and Techniques for their Observation*. Academic Press, 1966.

[8] A. H. Morrish, *The Physical Principles of Magnetism*. New York: Wiley, 1965.

[9] S. Blundell, *Magnetism in Condensed Matter*. New York: Oxford University Press, 2001.

[10] N. W. Ashcroft and N. D. Mermin, *Solid State Physics*. London: Saunders College Publishing, college ed., 1976.

[11] G. E. Uhlenbeck and S. Goudsmit, "Spinning electrons and the structure of spectra," *Nature*, vol. 117, no. 2938, p. 264, 1926.

[12] L. Shelford, *Ultrafast Nonlinear Optical Studies of Multilayered Thin Films and Interfaces*. PhD thesis, University of Exeter, 2009.

[13] B. Hillebrands and K. Ounadjela, *Spin Dynamics in Confined Magnetic Structure I*. New York: Spinger-Verlag Berlin Heidelberg, 2002.

[14] D. Jiles, *Introduction to Magnetism and Magnetic Materials*. CRC press, 2nd ed., 1998.

[15] P. Langevin, "Magnetism and theory of electrons," *Annales De Chimie Et De Physique*, vol. 5, pp. 70–127, 1905.

[16] Brillouin, L., "Les moments de rotation et le magntisme dans la mcanique ondulatoire," *J. Phys. Radium*, vol. 8, no. 2, pp. 74–84, 1927.

[17] E. C. Stoner, "Atomic moments in ferromagnetic metals and alloys with non-ferromagnetic elements," *The London, Edinburgh, and Dublin Philosophical Magazine and Journal of Science*, vol. 15, no. 101, pp. 1018–1034, 1933.

[18] J. C. Slater, "The ferromagnetism of nickel," *Physical Review*, vol. 49, no. 7, p. 537, 1936.

[19] S. Gasiorowicz, *Quantum Physics*. Massachusetts: John Wiley and sons, 3rd ed., 1974.

[20] M. Karplus and R. N. Porter, *Atoms and Molecules; an Introduction for Students of Physical Chemistry*. W. A. Benjamin, 1970.

[21] B. Cullity and C. Graham, *Magnetostriction and the Effects of Stress*. Wiley Online Library, 2nd ed., 2009.

[22] R. Rowan-Robinson, *Spin-orbit Phenomena and Interfacial Proximity Effects in Magnetic Multilayers*. PhD thesis, Durham University, 2016.

[23] J. Geissler, E. Goering, M. Justen, F. Weigand, G. Schütz, J. Langer, D. Schmitz, H. Maletta, and R. Mattheis, "Pt magnetization profile in a Pt/Co bilayer studied by resonant magnetic x-ray reflectometry," *Physical Review B*, vol. 65, no. 2, p. 020405, 2001.

[24] A. Clogston, B. Matthias, M. Peter, H. Williams, E. Corenzwit, and R. Sherwood, "Local magnetic moment associated with an iron atom dissolved in various transition metal alloys," *Physical Review*, vol. 125, no. 2, p. 541, 1962.

[25] J. Crangle, "Ferromagnetism in Pd-rich palladium-iron alloys," *Philosophical Magazine*, vol. 5, no. 52, pp. 335–342, 1960.

[26] R. Wienke, G. Schütz, and H. Ebert, "Determination of local magnetic moments of 5d impurities in Fe detected via spin-dependent absorption," *Journal of Applied Physics*, vol. 69, no. 8, pp. 6147–6149, 1991.

[27] Y. Sakamoto, Y. Oba, H. Maki, M. Suda, Y. Einaga, T. Sato, M. Mizumaki, N. Kawamura, and M. Suzuki, "Ferromagnetism of Pt nanoparticles induced by surface chemisorption," *Physical Review B*, vol. 83, no. 10, p. 104420, 2011.

[28] F. Hoare and J. Matthews, "The magnetic susceptibilities of platinum, rhodium and palladium from 20 to 290 K," *Proceeding of the Royal Society A*, vol. 212, no. 1108, pp. 137–148, 1952.

[29] W. Kopp, *Der thermische Verlauf des Paramagnetismus bei Magnetit, Platin und Palladium*. PhD thesis, ETH Zurich, 1919.

[30] B. Cabrera and A. Duperier, "Further results on the magnetism of chlorides of the palladium and platinum triads of elements," *Proceedings of the Physical Society*, vol. 51, no. 5, p. 845, 1939.

[31] A. Delin and E. Tosatti, "Emerging magnetism in platinum nanowires," *Surface Science*, vol. 566-568, pp. 262 – 267, 2004. Proceedings of the 22nd European Conference on Surface Science.

[32] L. Liang, Q. Chen, J. Lu, W. Talsma, J. Shan, G. R. Blake, T. T. M. Palstra, and J. Ye, "Inducing ferromagnetism and kondo effect in platinum by paramagnetic ionic gating," *Science Advances*, vol. 4, no. 4, 2018.

[33] W. F. Brown, *Micromagnetics*. New York: Interscience Publishers, 1963.

[34] J. C. Slater, "Cohesion in monovalent metals," *Physical Review*, vol. 35, no. 5, p. 509, 1930.

[35] J. C. Slater, "Atomic shielding constants," *Physical Review*, vol. 36, no. 1, p. 57, 1930.

[36] H. Bethe and R. Bozorth, "Ferromagnetism Handbook," *D. Physik*, vol. 24, p. 595, 1933.

[37] M. d'Aquino, *Nonlinear Magnetization Dynamics in Thin-Films and Nanoparticles*. PhD thesis, Università degli Studi di Napoli Federico II, 2005.

[38] R. Bozorth, "Directional ferromagnetic properties of metals," *Journal of Applied Physics*, vol. 8, no. 9, pp. 575–588, 1937.

[39] A. Aharoni, *Introduction to the Theory of Ferromagnetism*. Oxford University Press, New York, 2nd ed., 2000.

[40] L. Bogart, *An Investigation of the Structure, Pinning and Magnetoresistance of Domain Walls in $Ni_{81}Fe_{19}$ Planar Nanowires*. PhD thesis, Durham University, 2010.

[41] P. Drude, "Zur elektronentheorie der metalle," *Annalen der Physik*, vol. 306, no. 3, pp. 566–613, 1900.

[42] J. Thomson, "On the theory of electric conduction through thin metallic films," in *Proc. Cambridge Philos. Soc*, vol. 11, pp. 120–123, 1901.

[43] K. Fuchs, "The conductivity of thin metallic films according to the electron theory of metals," in *Mathematical Proceedings of the Cambridge Philosophical Society*, vol. 34, pp. 100–108, Cambridge Univ Press, 1938.

[44] E. H. Sondheimer, "The mean free path of electrons in metals," *Advances in Physics*, vol. 1, no. 1, pp. 1–42, 1952.

[45] M. Philipp, *Electrical Transport and Scattering Mechanisms in Thin Silver Films for Thermally insulating Glazing*. PhD thesis, Dresden: Leibniz Institut fr Festkrper-und Werkstofforschung (IFW) and Institut des NanoSciences de Paris, 2011.

[46] T. McGuire and R. Potter, "Anisotropic magnetoresistance in ferromagnetic 3d alloys," *IEEE Transactions on Magnetics*, vol. 11, no. 4, pp. 1018–1038, 1975.

[47] A. Cottey, "The electrical conductivity of thin metal films with very smooth surfaces," *Thin Solid Films*, vol. 1, no. 4, pp. 297–307, 1968.

[48] H. J. Juretschke, "Electrical Conductivity of Thin Metallic Films with Unlike Surfaces," *Journal of Applied Physics*, vol. 37, no. 1, pp. 435–435, 1966.

[49] M. Lucas, "Electrical conductivity of thin metallic films with unlike surfaces," *Journal of Applied Physics*, vol. 36, no. 5, pp. 1632–1635, 1965.

[50] R. Englman and E. Sondheimer, "The electrical conductivity of anisotropic thin films," *Proceedings of the Physical Society. Section B*, vol. 69, no. 4, p. 449, 1956.

[51] K. E. Saeger and R. Lück, "Evidence of anisotropic mean free path as furnished by galvanomagnetic measurements," *Physik der kondensierten Materie*, vol. 9, no. 1-2, pp. 91–97, 1969.

[52] J. Parrott, "A new theory of the size effect in electrical conduction," *Proceedings of the Physical Society*, vol. 85, no. 6, p. 1143, 1965.

[53] H. Müser, "The physical nature of a metal surface in conduction theory," *The London, Edinburgh, and Dublin Philosophical Magazine and Journal of Science*, vol. 45, no. 371, pp. 1237–1246, 1954.

[54] J. M. Ziman, *Electrons and Phonons: The Theory of Transport Phenomena in Solids*. Oxford University Press, 1960.

[55] S. B. Soffer, "Statistical model for the size effect in electrical conduction," *Journal of Applied Physics*, vol. 38, no. 4, pp. 1710–1715, 1967.

[56] M. Angadi, "Some transport properties of transition metal films," *Journal of Materials Science*, vol. 20, no. 3, pp. 761–796, 1985.

[57] J. Thompson, "The resistivity, temperature coefficient of resistivity and thermoelectric power of thin continuous metal films I: A survey and critical appraisal of the application of processing methods to experimental data," *Thin Solid Films*, vol. 150, no. 2-3, pp. 145–162, 1987.

[58] B. Nadgorny, R. Soulen Jr, M. Osofsky, I. Mazin, G. Laprade, R. Van de Veerdonk, A. Smits, S. Cheng, E. Skelton, and S. Qadri, "Transport spin polarization of Ni_xFe_{1-x}: Electronic kinematics and band structure," *Physical Review B*, vol. 61, no. 6, p. R3788, 2000.

[59] N. F. Mott, "Electrons in transition metals," *Advances in Physics*, vol. 13, no. 51, pp. 325–422, 1964.

[60] I. Campbell, A. Fert, and R. Pomeroy, "Evidence for two current conduction iron," *Philosophical Magazine*, vol. 15, no. 137, pp. 977–983, 1967.

[61] A. Fert and I. Campbell, "Two-current conduction in nickel," *Physical Review Letters*, vol. 21, no. 16, p. 1190, 1968.

[62] F. Duan and J. Guojun, *Introduction To Condensed Matter Physics: Volume 1*. Singapore: World Scientific Publishing Company, 2005.

[63] R. C. O'Handley, *Modern Magnetic Materials : Principles and Applications*. 2000.

[64] J. Smit, "Magnetoresistance of ferromagnetic metals and alloys at low temperatures," *Physica*, vol. 17, no. 6, pp. 612–627, 1951.

[65] J. Nickel, *Magnetoresistance overview*. Hewlett-Packard Laboratories, Technical Publications Department, 1995.

[66] P. Gambardella and I. M. Miron, "Current-induced spin–orbit torques," *Philosophical Transactions of the Royal Society of London A: Mathematical, Physical and Engineering Sciences*, vol. 369, no. 1948, pp. 3175–3197, 2011.

[67] C. O. Avci, *Current-induced Effects in Ferromagnetic Heterostructures due to Spin-orbit Coupling*. PhD thesis, ETH ZURICH, 2015.

[68] T. Gilbert, "A Lagrangian formulation of the gyromagnetic equation of the magnetization field," *Physical Review*, vol. 100, p. 1243, 1955.

[69] T. L. Gilbert, "A phenomenological theory of damping in ferromagnetic materials," *IEEE Transactions on Magnetics*, vol. 40, no. 6, pp. 3443–3449, 2004.

[70] D. Fang, *Current-induced Torque Driven Ferromagnetic Resonance in Magnetic Microstructures*. PhD thesis, University of Cambridge, 2011.

[71] V. M. Edelstein, "Spin polarization of conduction electrons induced by electric current in two-dimensional asymmetric electron systems," *Solid State Communications*, vol. 73, no. 3, pp. 233–235, 1990.

[72] A. Manchon and S. Zhang, "Theory of spin torque due to spin-orbit coupling," *Physical Review B*, vol. 79, no. 9, p. 094422, 2009.

[73] Y.-T. Chen, S. Takahashi, H. Nakayama, M. Althammer, S. T. Goennenwein, E. Saitoh, and G. E. Bauer, "Theory of spin Hall magnetoresistance (SMR) and related phenomena," *Journal of Physics: Condensed Matter*, vol. 28, no. 10, p. 103004, 2016.

[74] K. Garello, I. M. Miron, C. O. Avci, F. Freimuth, Y. Mokrousov, S. Blügel, S. Auffret, O. Boulle, G. Gaudin, and P. Gambardella, "Symmetry and magnitude of spin-orbit torques in ferromagnetic heterostructures," *Nature Nanotechnology*, vol. 8, no. 8, pp. 587–593, 2013.

[75] J. Hirsch, "Spin Hall Effect," *Physical Review Letters*, vol. 83, no. 9, p. 1834, 1999.

[76] M. D'yakonov and V. Perel, "Possibility of orienting electron spins with current," *Soviet Journal of Experimental and Theoretical Physics Letters*, vol. 13, p. 467, 1971.

[77] Y. Kato, R. Myers, A. Gossard, and D. Awschalom, "Observation of the spin Hall effect in semiconductors," *Science*, vol. 306, no. 5703, pp. 1910–1913, 2004.

[78] S. Takahashi and S. Maekawa, "Spin current, spin accumulation and spin Hall effect," *Science and Technology of Advanced Materials*, vol. 9, no. 1, p. 014105, 2008.

[79] J. Smit, "The spontaneous Hall effect in ferromagnetics II," *Physica*, vol. 24, no. 1-5, pp. 39–51, 1958.

[80] A. Fert and P. M. Levy, "Spin Hall effect induced by resonant scattering on impurities in metals," *Physical Review Letters*, vol. 106, no. 15, p. 157208, 2011.

[81] H. Nakayama, M. Althammer, Y.-T. Chen, K. Uchida, Y. Kajiwara, D. Kikuchi, T. Ohtani, S. Geprägs, M. Opel, S. Takahashi, *et al.*, "Spin Hall magnetoresistance induced by a nonequilibrium proximity effect," *Physical Review Letters*, vol. 110, no. 20, p. 206601, 2013.

[82] Y.-T. Chen, S. Takahashi, H. Nakayama, M. Althammer, S. T. Goennenwein, E. Saitoh, and G. E. Bauer, "Theory of spin Hall magnetoresistance," *Physical Review B*, vol. 87, no. 14, p. 144411, 2013.

[83] M. Althammer, S. Meyer, H. Nakayama, M. Schreier, S. Altmannshofer, M. Weiler, H. Huebl, S. Geprägs, M. Opel, R. Gross, *et al.*, "Quantitative study of the spin Hall magnetoresistance in ferromagnetic insulator/normal metal hybrids," *Physical Review B*, vol. 87, no. 22, p. 224401, 2013.

[84] C. Hahn, G. De Loubens, O. Klein, M. Viret, V. V. Naletov, and J. B. Youssef, "Comparative measurements of inverse spin Hall effects and magnetoresistance in YIG/Pt and YIG/Ta," *Physical Review B*, vol. 87, no. 17, p. 174417, 2013.

[85] N. Vlietstra, J. Shan, V. Castel, B. Van Wees, and J. B. Youssef, "Spin-Hall magnetoresistance in platinum on yttrium iron garnet: Dependence on platinum thickness and in-plane/out-of-plane magnetization," *Physical Review B*, vol. 87, no. 18, p. 184421, 2013.

[86] K. Ando, S. Takahashi, K. Harii, K. Sasage, J. Ieda, S. Maekawa, and E. Saitoh, "Electric manipulation of spin relaxation using the spin Hall effect," *Physical Review Letters*, vol. 101, no. 3, p. 036601, 2008.

[87] L. Liu, C.-F. Pai, Y. Li, H. Tseng, D. Ralph, and R. Buhrman, "Spin-torque switching with the giant spin Hall effect of tantalum," *Science*, vol. 336, no. 6081, pp. 555–558, 2012.

[88] Y. Lu, J. Cai, S. Huang, D. Qu, B. Miao, and C. Chien, "Hybrid magnetoresistance in the proximity of a ferromagnet," *Physical Review B*, vol. 87, no. 22, p. 220409, 2013.

[89] C. O. Avci, K. Garello, J. Mendil, A. Ghosh, N. Blasakis, M. Gabureac, M. Trassin, M. Fiebig, and P. Gambardella, "Magnetoresistance of heavy and light metal/ferromagnet bilayers," *Applied Physics Letters*, vol. 107, no. 19, p. 192405, 2015.

[90] A. Brataas, Y. V. Nazarov, and G. E. Bauer, "Finite-element theory of transport in ferromagnet–normal metal systems," *Physical Review Letters*, vol. 84, no. 11, p. 2481, 2000.

[91] X. Jia, K. Liu, K. Xia, and G. E. Bauer, "Spin transfer torque on magnetic insulators," *EPL (Europhysics Letters)*, vol. 96, no. 1, p. 17005, 2011.

[92] D. Huertas-Hernando, Y. V. Nazarov, and W. Belzig, "Absolute spin-valve effect with superconducting proximity structures," *Physical Review Letters*, vol. 88, no. 4, p. 047003, 2002.

[93] A. Manchon, H. C. Koo, J. Nitta, S. Frolov, and R. Duine, "New perspectives for Rashba spin–orbit coupling," *Nature Materials*, vol. 14, no. 9, p. 871, 2015.

[94] V. P. Amin and M. D. Stiles, "Spin transport at interfaces with spin-orbit coupling: formalism," *Physical Review B*, vol. 94, no. 10, p. 104419, 2016.

[95] P. M. Haney, H.-W. Lee, K.-J. Lee, A. Manchon, and M. D. Stiles, "Current induced torques and interfacial spin-orbit coupling: Semiclassical modeling," *Physical Review B*, vol. 87, no. 17, p. 174411, 2013.

Chapter 3

Sample preparation and experimental techniques

3.1 Introduction

This chapter covers the technical details used in sample preparation as well as electrical, structural and magnetic characterisation of the samples in the thesis. It begins with sample preparation which covers the deposition process and material deposition conditions, followed by structural characterisation that includes x-ray reflectivity and x-ray diffraction techniques. The magnetic characterisation techniques used were x-ray resonant magnetic reflectivity, magneto-optical Kerr effect, MOKE, polarised neutron reflectivity, PNR, as well as the superconducting quantum interference device, SQUID, magnetometer. Finally, descriptions of the measurement setup for magnetoresistance measurement using DC and lock-in detection techniques are discussed. These methods were used in chapters 5, 6 and 7.

3.2 Sample preparation

In this work, samples with thicknesses in the nanometre (nm) regime are prepared by the sputter deposition technique under ultra-high base vacuum conditions. This section describes the process of substrate preparation before deposition, the deposition process and the deposition

conditions.

3.2.1 Preparation of the Si substrate

The majority of this work was done with thermally oxidized Si/SiO_2 (100) substrates where the oxide layer acts as an electrical insulator to prevent electrical conduction through the silicon substrate during electrical measurements. The substrate was cut to a size appropriate to the investigative technique with the aid of a diamond scribe. Substrates of 10 mm×10 mm were cut for all x-rays measurements, 30 mm×30 mm for PNR measurement, 5 mm×5 mm for MOKE and SQUID magnetometer measurement. A stripe of 14 mm×3 mm was used for electrical measurements.

Each substrate was cleaned in acetone in order to get rid of grease, dust and debris from the substrate and later with iso-propanol (IPA) to remove the residue of acetone on the substrate. Substrate is left to dry on a clean sterile napkin with the polished surface, faced down on the napkin to prevent contamination during drying.

3.2.2 Sputter deposition process

In a basic sputtering process, a target (cathode) is bombarded by high energy ions derived from an electric discharge in a gas which generates a glow discharge plasma close to the surface of the target. These energetic ions impact on the target removing molecule(s)/atom(s) from the surface of the target, which then condense on another surface known as the substrate (anode). In most cases, the gas used in the generation of the energetic ion is argon gas because of its large mass, its inability to react with other materials and its available in a large affordable quantity [1]. It is referred as the working gas. Ar gas introduced into the deposition chamber is ionised and bombards the target. On arrival at the target this causes atomic collisions imparting momentum to atoms in the target. This momentum gives some atoms in the target enough energy to be ejected (shown in figure 3.1). Secondary electrons are also generated in this process, which help maintain the plasma.

The ejected atoms subsequently condense upon the substrate as adatoms by surrendering

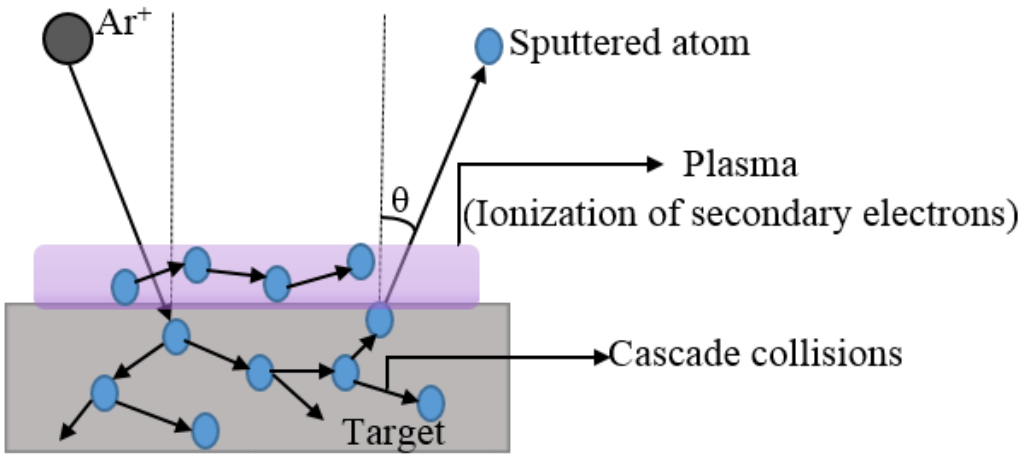

Figure 3.1: Schematic illustration of the sputtering process showing the initial collision of the Ar ion with the target and the momentum transfer that leads to the ejection of atoms/molecules from the surface of the target.

their energy to the substrate surface allowing them to remain on the substrate surface. This happens under the following conditions [2]:

- The working gas pressure in the vacuum chamber must be sufficiently low to about 10^{-3} Torr in order to allow about seven collisions between atoms and the working gas before condensation on the substrate.
- the ejected atoms must be able to move freely to the substrate with little impedance to their movement which is the reason why the process is conducted in a vacuum.
- the ejected atoms must arrive at the surface faster than their re-evaporation rate when deposited.

It is important to note that the deposition rate depends on the temperature, proximity of target to the substrate and the re-evaporation rate, which invariably depends on the chemical and physical properties of the substrate as well as temperature. When the adatoms arrive at the substrate, they have the ability to migrate. They also see a potential energy profile of the surface, which causes it to diffuse across the surface randomly with a jump rate Γ defined by the thermal jittering of the adatoms with an attempt frequency, ν, diffusion energy barrier, E_d,

and substrate temperature T. The jump rate is given as:

$$\Gamma = \nu \exp^{-\frac{E_d}{k_B T}} \tag{3.2.1}$$

where k_B is Boltzmann's constant. The diffusion energy barrier in the above equation is dependent on the atomic structure of the surface and varies between various materials, surface orientation and substrate surface directions [3]. The adatoms gives-up their energy according to the energy of the surface of the substrate becoming immobile at that site. As the number of deposited adatoms increases, they form islands that grow and coalesce into a continuous film if deposition continues. The properties of the continuous film tends to be different from that of the islands because the detail of the growth process affects the growth of the film. Several factors can influence the growth process which includes factors such as interface properties, temperature, deposition rate, working gas type, working gas pressure as well as ion and electron bombardment.

Although the sputtering process is an easy method of surface coating, in the earlier days of its use suffered several limitations such as low deposition rate, low ionisation efficiency in the plasma and high substrate heating, which reduced the number of collisions of the secondary electrons at the target. If the gas pressure is decreased, ions are produced far away from the target due to large mean free path. The overall ionisation efficiency is reduced due to less secondary electron ejection that enables more atoms to reach the substrate without producing gas ionisation. Therefore, in order to increase these collisions, a magnetically enhanced plasma discharge method known as magnetron sputtering process was introduced to help confine the electrons in orbits close to the target. The magnetron sputtering process is discussed in detail in the next section.

3.2.3 Magnetron sputtering

Magnetron sputtering applies the principle of a shaped magnetic field on a target and was invented by Penning in 1936 [4]. The target is placed on a ring of permanent magnets creating a magnetic field parallel to the target surface which constrains the secondary electron motion close

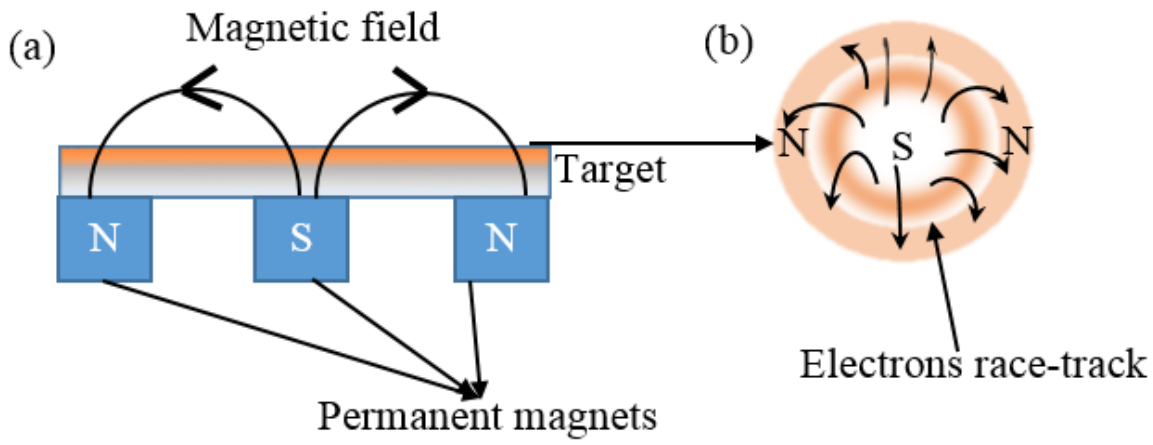

Figure 3.2: (a) Side view and (b) front view configuration of magnets for magnetron sputtering showing the magnetic field direction that enables the confinement of electrons for further ionisation of the working gas.

to the target surface. The magnets are arranged such that one pole (south) is positioned as the central axis while the second pole (north) is made as a ring of magnets around the outer edge of the target creating the parallel field as shown in figure 3.2b. At the same time, the electric field acts perpendicular to the magnetic field direction. This causes the electrons to be acted upon by a Lorentz force that confines the electrons in an orbit in the vicinity to the target. The confined electrons cause further ionisation through collisions increasing the ionisation efficiency which results in a dense plasma close to the target. It also allows the discharge to be maintained at lower pressure and voltage, leading to a reduction in the amount of Ar gas required for the process. Magnetron sputtering significantly increases the sputter rate of deposition [1, 2].

The above described sputtering process is the DC magnetron sputtering mode where the target is negatively biased and it is directly conducting electricity. This mode is used in the deposition of most metallic materials. However, if the material is insulating, positive charge builds up and eventually neutralises the electrical field applied to the target, preventing attraction of more ions. Therefore, the DC mode is not appropriate, but rather an alternating current mode known as RF magnetron sputtering is used. The RF sputtering mode can also be applied to metals. When RF power is applied to a target at low frequency (<50 kHz), the ions are mobile such that there is alternation of polarity between the target and substrate. However at higher frequency (typically 13.6 MHz) [4] the RF power applied to the target passes through

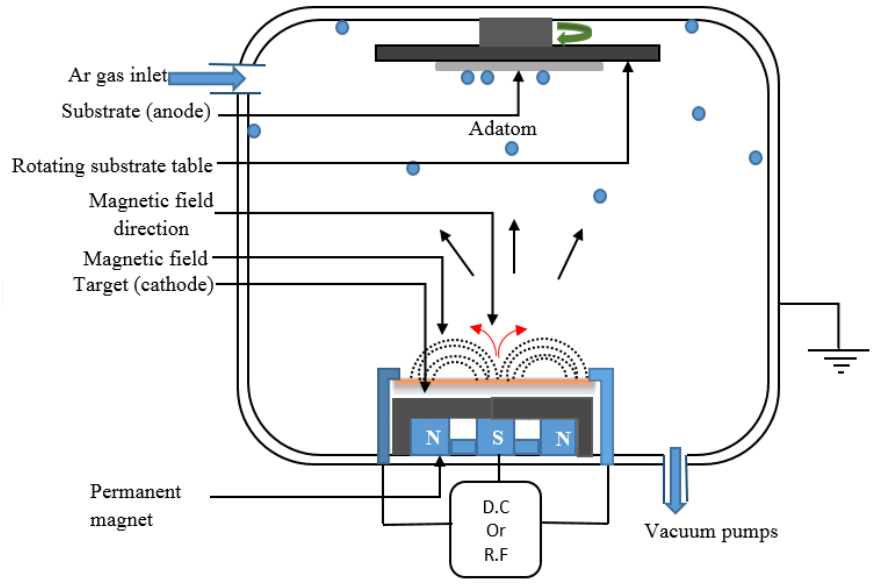

Figure 3.3: Schematic illustration of the sputtering process showing ejected atoms/molecules from the surface of the target that are deposited on the substrate mounted on a rotating table.

the target forming a DC potential by capacitive coupling and the electron and ion mobilities are different in the fluctuating field [2]. Since the system is capacitively coupled there is no net charge transfer, therefore the electrons are negatively biased. To compensate for this bias, a DC negative voltage is produced on the target surface and surface ion bombardment is ongoing as shown in figure 3.3 which helps the plasma to be sustained. Magnetron sputtering process can be used to deposit virtually any material, but the major limitation is the heating of the target surface which can be solved by water cooling the target.

3.2.4 Deposition system and procedure

The deposition system use to carry out most of the work in this thesis is the Mantis QPrep500 magnetron sputtering system shown in figure 3.4 [5]. This ultra-high vacuum, UHV, system is made up of two chambers: a load-lock and a main vacuum chamber separated by a gate-valve. This allows the load-lock vacuum to be vented for sample change without affecting the main chamber pressure. As part of the load-lock a carrier cell is used to store up to five different samples for transfer into the main chamber without breaking the vacuum pressure of the system.

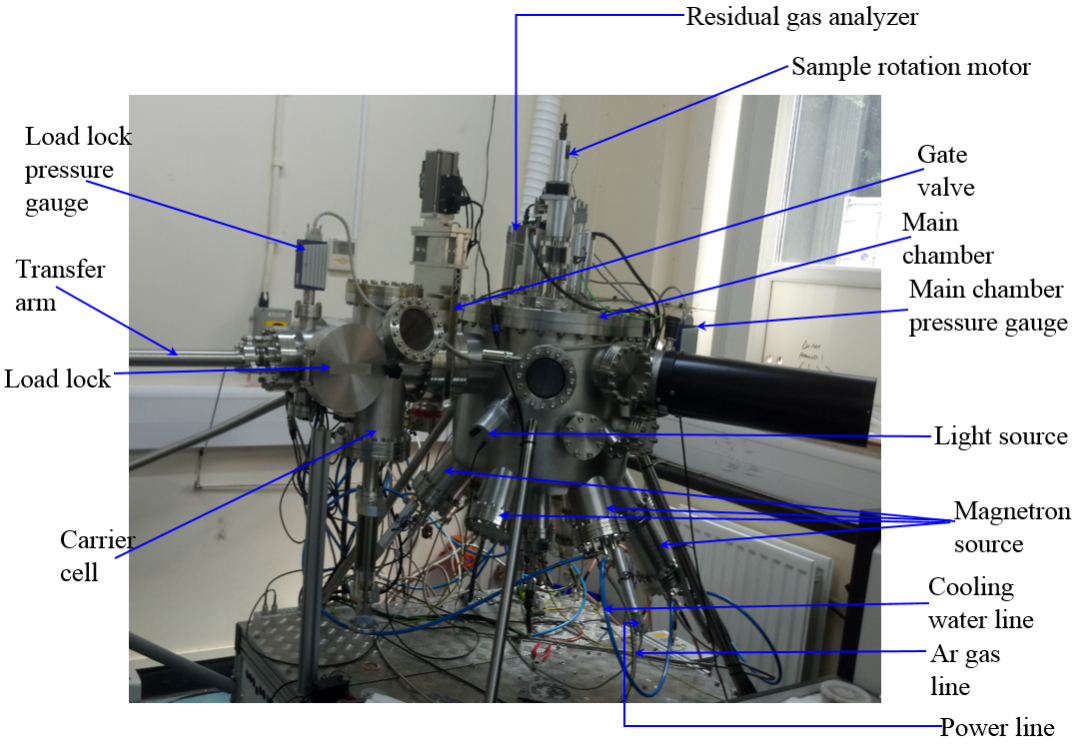

Figure 3.4: A photograph of the Mantis Qprep500 magnetron sputtering system in Durham University with labels identifying the main parts discussed.

The whole system can be vented to atmospheric pressure for target change by injecting nitrogen gas. This reduces the adsorption of water vapour onto the chamber. After a target change, the system is pumped down to 10^{-8} Torr using turbo pumps attached to each chamber. At 10^{-8} Torr, the residual gas analyser is turned on which gives information on the quantity of gases present in the chamber in a graphical form. For a good chamber pressure, the water (H_2O = 18 m/z) peak is expected to be the largest peak while carbon monoxide (CO=28 m/z) and nitrogen (N_2=28 m/z) peak to be four times larger than the oxygen (O_2=32 m/z) peak on the gas spectrum (see figure 3.5). This is a quick way of assessing the main chamber environment. It also informs on the flow characteristic of the remaining gas that switches to the molecular flow regime when the mean free path of the gas molecules is larger than the size of the vacuum chamber, meaning the molecules collide more with the walls of the chamber than between themselves.

The main vacuum chamber houses five magnetron sputtering guns where three are DC powered and two RF powered. Above each magnetron gun is a shutter mounted on a rotatory

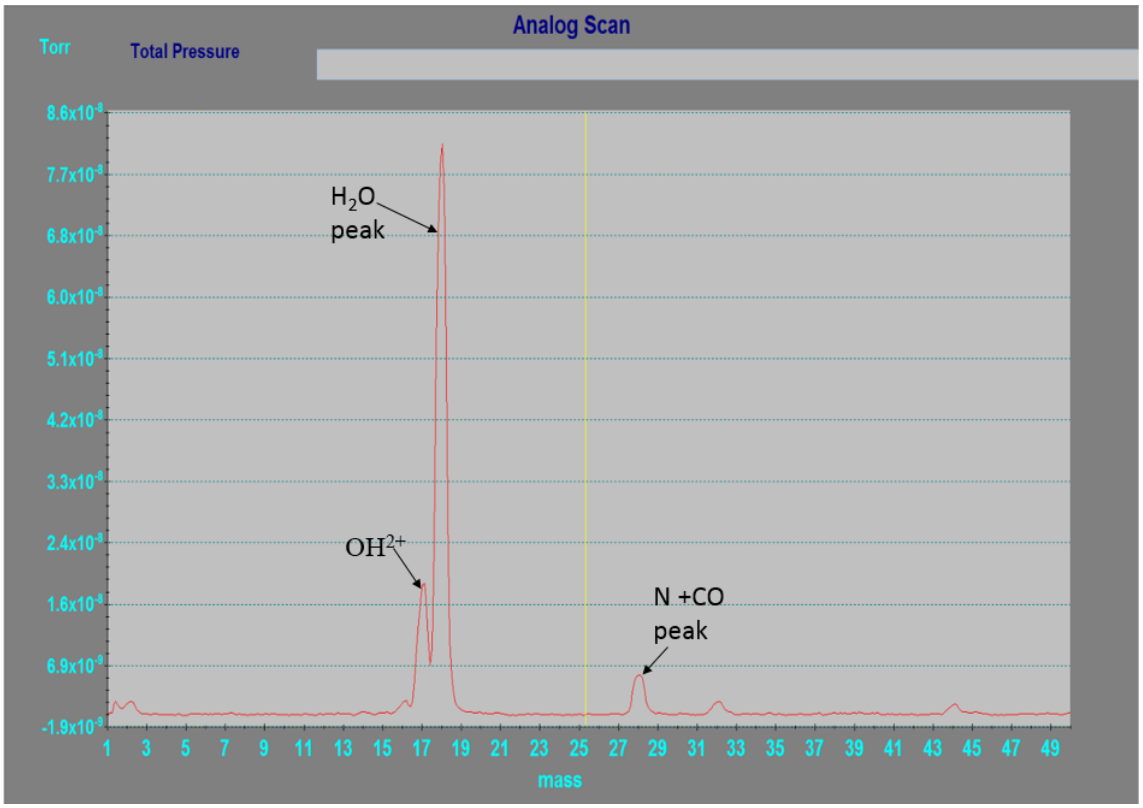

Figure 3.5: Graphical spectrum of the gases present in the main chamber of the Mantis QPrep 500 magnetron sputtering system made available by the mass spectrometer.

motion controller which prevents each target from being contaminated from other target materials during deposition. Due to heat dissipation during the sputtering process, each gun is water cooled and has its own individual argon gas line controlled by a mass-flow controller that provides the working gas. The substrate table is located above the magnetron guns attached to a rotatory controller which allows the sample to be rotated during deposition in order to ensure continuous film growth and prevent induced anisotropy from stray magnetic field from the magnetron source [6]. Between the substrate table and the magnetron guns is the substrate stage shutter that keeps the substrate covered during pre-sputtering processes. This feature allows proper control of deposition time in order to determine the actual thickness of material deposited. The deposition rate from each target is measured in-situ using a quartz crystal monitor and calibrated with x-ray reflectivity (XRR) that is discussed in the next section.

Prepared samples are firmly affixed on a mask using kapton tape. The mask gives the sample a fixed shape and size, which aides in determination of electrical parameters such as resistivity. The mask is then mounted on a sample holder placed on a transfer arm in the load lock, and

the load lock is then pumped down. When the load lock pressure is 10^{-7} Torr the sample is transfered into the main chamber for deposition as described above.

3.3 X-ray Scattering

X-rays were discovered as emitting from a cathode ray tube by W. Rontgen in 1896 [7]. They are electromagnetic radiation produced when a beam of high energy electrons accelerated with the aid of high voltage bombards a metal target (often Cu). On collision with the target, some of the high energy electrons decelerate generating Brehmsstrahlung radiation and in some cases, core electrons are ejected and electrons in the outer shell will drop to occupy the vacancy emitting x-ray photons with characteristic energies. X-rays interact with the electronic charges in a material giving vital information such as thickness, density, roughness and crystal structure of the interacting material. In some cases it may weakly interact with the magnetic moment of unpaired electrons giving information on the magnetic density profile of the probed material. As such it is a vital technique used in the investigation of structural, chemical and magnetic profiles of materials. In this section, the theory that supports the various x-ray techniques used in this thesis are discussed. These include grazing incidence x-ray reflectivity (GIXRR), which will be termed x-ray reflectivity (XRR) throughout this work and x-ray diffraction (XRD). Another x-ray technique used in this thesis is x-ray resonant magnetic reflectivity (XRMR) which is discussed in section 3.7. XRR measures the electron density change normal to the sample surface providing characteristic information on material thickness and interface width, while the XRD peak provides information on the out-of-plane crystallographic structure such as the crystallite grain size, lattice parameter, the crystallographic plane, and the degree of strain present in the grain. XRMR provides element specific information on magnetisation that enables the extraction of magnetic scattering length density profiles for the x-rays' interaction. The x-ray data fitting methodology, software and procedure are discussed in chapter 4.

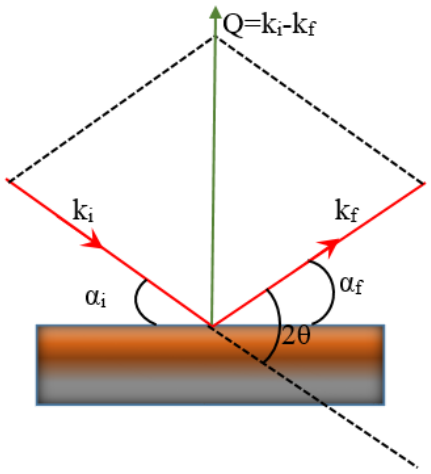

Figure 3.6: X-ray scattering geometry under specular reflectivity showing the scattering wave vector Q its relationship with the incident (k_i) and scattered wave vector (k_f).

3.3.1 X-ray scattering theory

X-rays are electromagnetic waves with electric and magnetic wave components. During interaction with a material, the electrons oscillate with the same wavelength and energy under the influence of the electric field from the incident x-ray beam [8]. The incident x-rays can be considered as a plane wave that interacts with electrons, which re-radiate as a spherical x-ray wave source with the same frequency in the plane of polarisation (π-polarisation) and an energy described by

$$E_{rad}(R) = -E_0 \frac{r_e}{R} \exp\left(ikR\right) \cos\Psi, \tag{3.3.1}$$

where E_0 is the amplitude of incident plane wave and Ψ is the angle within the plane of polarisation of the incident wave relative to the direction of propagation. The Thomson (elastic) scattering length $r_e = \frac{e^2}{4\pi\varepsilon_0 m_e c^2} = 2.8175 \times 10^{-15}$ m is the collection of all the constants in equation 3.3.1 and exp(ikR)/R describes the resultant spherical wave after scattering. The negative sign indicates that the scattered wave has a π phase shift from the incident wave. The cosΨ term becomes unity when the scattered direction of the incident wave is perpendicular to the direction of polarisation (σ-polarisation).

In the measurements presented in most of this thesis, the x-ray scattering plane is normal to the sample surface and is characterised by an incident wave vector k_i with an angle α_i to

the sample surface and a scattering wave vector k_f with angle $(2\theta - \alpha_i)$ as shown in figure 3.6. Where 2θ is the scattering angle which experimentally is the angle of the detector relative to the incident beam. In elastic (Thomson) scattering the wave vectors are equal:

$$|k_i| = |k_f| = |k| = \frac{2\pi}{\lambda}. \tag{3.3.2}$$

In this situation, x-ray scattering can be classically described within the Born approximation under the following assumptions that ignore the presence of multiple scattering processes [9]:

- The x-ray interaction with matter is weak, preventing rescattering after the initial interaction
- the point of observation of the scattered beam is made at a very large distance compared to the illuminated volume
- scattered wave fronts from each atoms are parallel.

The scattering vector Q is normal to the sample surface and in the case of x-ray diffraction correspond to a distance in reciprocal space lattice. The scattering vector (an inverse distance) is expressed as

$$Q_z = k_i - k_f = \frac{4\pi \sin\theta}{\lambda}. \tag{3.3.3}$$

This explains why structural information normal to thin film surface can be extracted at grazing incident angle. Here, the small angle at gazing incidence leads to a large real space distance.

3.3.2 Principle of grazing incidence specular x-ray scattering

The penetration depth of the incident wave at gazing incidence is defined by the incident angle and the attenuation coefficient μ_{att} of the material by

$$\tau_{1/e} = \frac{\sin\alpha_i}{\mu_{att}}, \tag{3.3.4}$$

which depends on the refractive index of the propagation medium. Above the critical angle, θ_c, the x-ray beam penetrates into the material with partial reflection from each interface, but

below θ_c the x-ray experiences total external reflection. Each reflection is a function of the refractive index above and below an interface. The refractive index, n, is directly related to the scattering factor of the material, which depends on the atomic number Z_A and the electron density ρ_a of the material. Generally, the refractive index is defined as the ratio of the speed of the x-ray in vacuum to the speed in the medium, but is slightly less than unity for x-rays. To correct for the deviation from unity, n is expressed in terms of a dispersion coefficient δ and an absorption coefficient β as

$$n = 1 - \delta + i\beta. \tag{3.3.5}$$

By substituting

$$\delta = \frac{r_e \rho_a \lambda^2}{2\pi}\{f_0 + f_c'(E)\} \tag{3.3.6}$$

and

$$\beta = -\frac{r_e \rho_a \lambda^2}{2\pi}\{f_c''(E)\} \tag{3.3.7}$$

equation 3.3.5 can also be expressed as

$$n = 1 - \frac{r_e \rho_a \lambda^2}{2\pi}\{f_0 + f_c'(E) + if_c''(E)\} \tag{3.3.8}$$

where λ is the x-ray wavelength [8, 10]. f_0, $f_c'(E)$ and $f_c''(E)$ are the scattering form factors which are the energy (E) dependent dispersion corrections that are most effective when the x-ray energy is tuned to an elemental absorption edge, as discussed in section 3.7.3. At gazing incidence, $f_0 \approx Z_A$ while $f_c'(E)$ and $f_c''(E)$ have only weak energy dependences [11, 12].

3.3.3 Specular x-ray reflectivity across interfaces

Within the Born approximation, the critical angle for total external reflection according to Snell's law is expressed as

$$\theta_c = \sqrt{2(1 - n_1)} \approx \sqrt{2\delta} \tag{3.3.9}$$

where it is assumed that there is no absorption (i.e $\beta = 0$). X-ray propagation across the interface between media of different refractive indices is described by Fresnel's law. The amplitude of

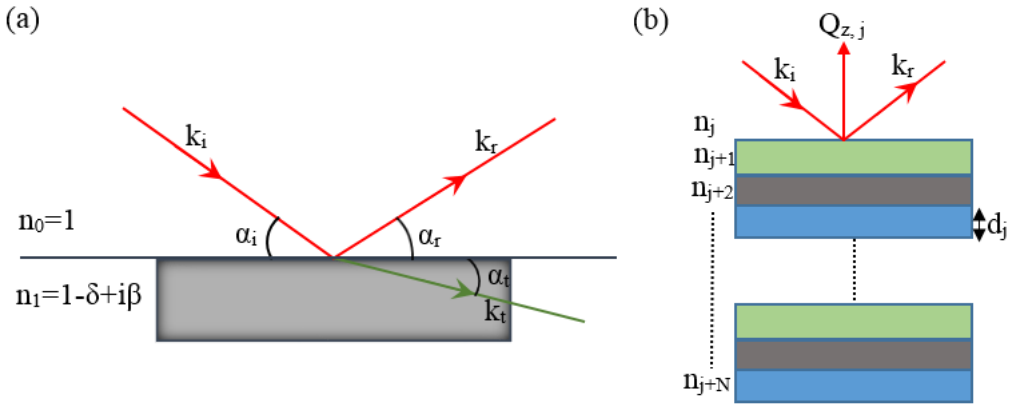

Figure 3.7: X-ray scattering model assumed for (a) Fresnel's algorithm for single layered films (b) Parratt's recursion algorithm for multilayer films

reflectivity, r, and transmission, t, is

$$r = \frac{n_0\alpha_{i,r} - n_1\alpha_t}{n_0\alpha_{i,r} + n_1\alpha_t}, t = \frac{2n_0\alpha_{i,r}}{n_0\alpha_{i,r} + n_1\alpha_t} \tag{3.3.10}$$

where the corresponding measured reflectivity is $R = |r|^2$ and transmission is $T = |t|^2$. n_0 and n_1 are the refractive indices of the different media of propagation (shown in figure 3.7a). X-ray reflectivity decreases rapidly with increasing angle of incidence α_i.

Multiple reflections and transmission arises in multilayer films which makes it inappropriate to describe with Fresnel's law because the model breaks down due to the presence of dynamic effects such as interference at low angles. Parratt's recursion formalism is used because it takes into account the contributions of transmission and reflection at the interfaces as well as the interference [13]. This model assumes the sample to be divided into layers with each layer having a scattering wave vector Q_z defined as

$$Q_{z,j} = 2k_0\sqrt{n_j^2 - \cos^2\alpha_i} \tag{3.3.11}$$

where k_0 is wave vector in vacuum and n_j is the refractive index of layer j (shown in figure 3.7b).

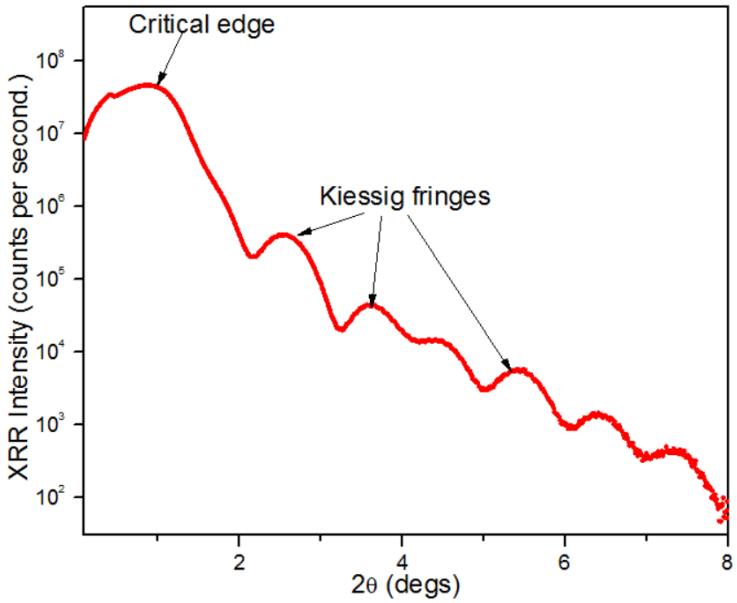

Figure 3.8: An example of a specular x-ray reflectivity curve for a CoFeTaB(4nm)/Pt(6nm) bilayer on a Si/SiO_2 substrate. The critical edge and Kiessig fringes are indicated. The vertical scale is logarithmic.

The total amplitude of reflectivity is given as

$$R_j = \frac{R_{j+1}e^{id_jQ_{z,j}} + r_{j,j+1}}{R_{j+1}r_{j,j+1}e^{id_jQ_{z,j}} + 1} \tag{3.3.12}$$

and

$$r_{j,j+1} = \frac{Q_{z,j} - Q_{z,j+1}}{Q_{z,j} + Q_{z,j+1}} \tag{3.3.13}$$

where d_j is the thickness of the j'th layer and r is the amplitude of the Fresnel reflectivity for an interface. The measured reflectivity intensity is $I = |R|^2 I_0$ for incident intensity I_0. Sample imperfections such as interface roughness and intermixing can be modeled as a roughness factor multiplied with Fresnel's reflection coefficient r. The roughness factor can be described by the Nevot-Croce factor $e^{-q_{z,j}q_{z,j+1}\sigma_j^2/2}$, Debye-Waller factor $e^{-q_{z,j}^2\sigma_j^2/2}$ or by making a concentration gradient (slicing the layer around the interface with variation in composition). Interface roughness is modeled as a continuous variation in electron density along the axis normal to the sample surface.

The reflectivity profile of a thin film is characterised by a clear appearance of the critical edge and periodic oscillations as shown in figure 3.8. The oscillations are known as Kiessig

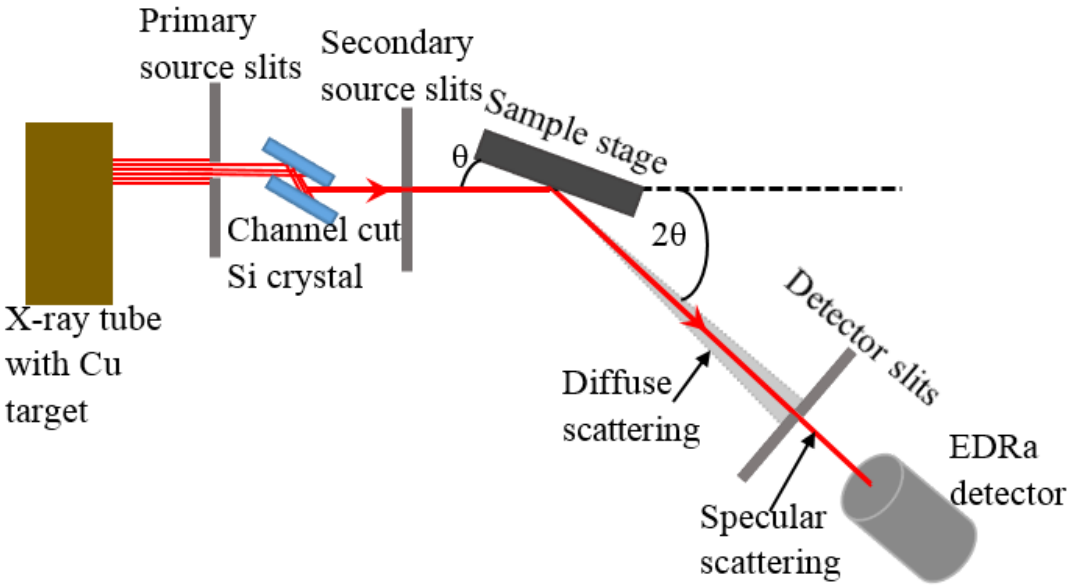

Figure 3.9: Experimental setup of the Bede D1 reflectometer at grazing incidence showing the component part.

fringes and were first observed by Kiessig in 1931 [14] when investigating glass coated with nickel. The critical edge and oscillation amplitude provide information on the density of the thin film. Information on interface roughness can also be extracted from the amplitude of oscillation. The period of oscillation is dependent on the film thickness. Therefore, thicker films have shorter period of oscillation. The decay in intensity of x-ray reflectivity depends on the surface roughness. Meaning, the intensity decreases rapidly when the surface roughness is large. The amplitude of oscillation also decreases with increasing interface roughness.

3.3.4 Experimental setup for grazing incident x-ray reflectivity

Specular XRR in this thesis used a Bede D1 x-ray reflectometer with a Cu-K_α x-ray source [15, 16]. The experimental setup is shown in figure 3.9. Electrons from a filament are accelerated towards a water cooled Cu target to generate Bremsstrahlung radiation and Cu-K_α and Cu-K_β emissions with a 1.6 kW (40 kV ; 40 mA) power supply. The beam passes through a primary slit which removes the Bremsstrahlung contribution. The Cu-K_α emission is selectively isolated from the Cu-K_β emission via a channel cut silicon crystal. The emerging Cu-K_α beam has a

lateral offset of 2.8mm which is trimmed to a spot size of 0.5 mm as it passes through the secondary slit as the incident beam. The reduction of the spot size enables a larger portion of the sample to be illuminated with a parallel incident beam. The incident beam hits the sample mounted on a six axis diffractometer and the reflected beam passes through the detector slit which removes the forward diffuse scatter beam before hitting the detector. The reflected intensity is measured on an EDRa detector at an angle of 2θ to the incident plane. The EDRa detector is a highly efficient scintillation crystal with a short decay rate that allows an overall count rate of up to 3×10^6 c.p.s with a low intrinsic background of 0.15 c.p.s [17]. In order to obtain the specular reflectivity profile, θ-2θ scans were made and the corresponding intensity at the detector measured. Similar scan for the off-specular (forward-diffuse) reflectivity were done by offsetting the θ rotation by 0.1° and the corresponding intensity at the detector was also measured. Finally, the true specular reflectivity profile was obtained by taking the difference between the intensity from specular and off-specular scans.

Each scan was done at grazing incidence by holding the x-ray beam fixed at a very shallow angle relative to the sample surface while scanning the sample and detector. Genx software using Parratt's recursion algorithm was used to fit the true specular XRR data [18]. Layer thickness, density and roughness were obtained from the fits. The GenX software is discussed in more detail in chapter 4

3.3.5 Principle of x-ray diffraction

X-ray diffraction is due to constructive interference of coherently scattered waves from a crystalline sample. When a beam of x-rays is incident on the sample surface, the scattered wave from the periodic array of atoms over the length scale of the illuminated surface interfere producing a diffraction pattern characteristic to the sample. Here, it is considered that the incident wave is a plane wave, which on interaction scatters to produce spherical wavefronts whose amplitude sum is equal to zero in certain directions (destructive interference), but produces a diffraction peak in other specific directions (constructive interference) relative to the lattice. The scattered waves are in phase and constructive interference is observed only when the path

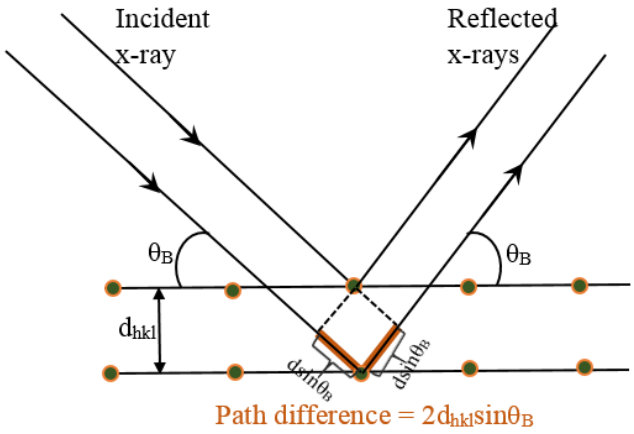

Figure 3.10: X-ray diffraction beam schematics for the derivation of Bragg's law showing the path difference highlighted in orange colour.

difference is equal to an integer number of wavelengths λ at Bragg's angle θ_B. This is shown in figure 3.10. The interference effect is mathematically described by Bragg's law [19]:

$$n\lambda = 2d_{h,k,l}\sin\theta_B \tag{3.3.14}$$

where n is a positive integer and $d_{h,k,l}$ is the interplanar spacing expressed as:

$$d_{h,k,l} = \frac{a_0}{\sqrt{h^2+k^2+l^2}}. \tag{3.3.15}$$

a_0 is the lattice parameter and h, k, l are the Miller indices that describes the reciprocal space lattice vector G according to:

$$G = hb_1 + kb_2 + lb_3. \tag{3.3.16}$$

In the same way, the real space lattice vectors R_n are given by

$$R_n = n_1a_1 = n_2a_2 + n_3a_3. \tag{3.3.17}$$

The b_i is the reciprocal space lattice basis and is related to the real space lattice basis a_i by

$$b_1 = \frac{a_2 \times a_3}{a_1 \cdot a_2 \times a_3}, b_2 = \frac{a_3 \times a_1}{a_1 \cdot a_2 \times a_3}, b_3 = \frac{a_1 \times a_2}{a_1 \cdot a_2 \times a_3}. \tag{3.3.18}$$

In a cubic coordinate system the reciprocal lattice axes are perpendicular to the [100], [010] and [001] plane of the real space lattice.

The position of the diffraction peak in reciprocal space is define by Laue's condition [20]. This happens when the scattering vector is equal to the reciprocal lattice vector

$$\mathrm{Q} = \mathrm{G}, \tag{3.3.19}$$

meaning that at Laue's conditions the phase of the scattered wave constructively interferes to produce a strong diffraction intensity which is a reinforcement of the individual weak scattering from each successive plane. Analysis of the diffraction peaks allows the location of the atoms in the material to be determined. In polycrystalline samples the coherent scattering path can be limited in length by the crystallite grain size which introduces additional peak broadening in the diffraction peaks.

3.3.6 Experimental setup for x-ray diffraction

X-ray diffraction (XRD) measurements were conducted using a Rigaku SmartLab diffractometer [21] in the ISIS R53 material characterisation laboratory. This system consists of a fully automated specially designed cross beam optics (CBO) with a 9 kW rotating anode source that generates Cu-K_α radiation of wavelength 1.54 Å and has a high resolution θ goniometer and a detector. The setup is similar to figure 3.9 but the combined functionalities of primary slits and the channel cut crystal in the XRR setup discussed in section 3.3.4 are replaced with the CBO, which is a patterned x-ray optical system that provides a selectable parallel and focused x-ray beam. The sample stage is a five axis high resolution gonoimeter.

Measurement begins with proper alignment from the scattered intensity at the detector. From the scattered intensity at the detector the x-ray focal spot with respect to the center of the gonoimeter is aligned by translating the x-ray tube and shielding vertically to focus the beam at the center of the goniometer. The beam is passed through an adjustable slit aperture that can be reduced and scanned vertically in order to optimise slit position and focus the incident x-ray beam. Finally, alignment is completed by scanning the detector slit vertically to

get the diffracted beam on the detector. The sample is mounted and aligned by automatically monitoring beam intensity of a known diffraction peak, usually Si(400) as the sample is tilted and adjusted. 2θ-θ scans are done and the corresponding diffraction peaks from the scattered intensity at the detector are measured automatically using the SmartLab guidance software.

3.4 Magneto-optical Kerr effect (MOKE)

Polarisation of light is a vectorial property of the electromagnetic wave where its electrical component interacts with the electron motion in the material. One of the means of light polarisation is with a polariser which transmits waves with electric field component aligned parallel to the polarisation axis (which is defined by the crystal formation on the materials used in making the polariser) of the polariser while blocking waves with electric component perpendicular to the polarisation axis. The interaction of polarised light with a magnetic material can give rise to a rotation of the plane of polarisation from that of the incident beam. In 1845, Faraday observed this rotation when polarised light was transmitted through a magnetic material [22]. An analogue of this rotation was also observed by Kerr in 1877 from the reflected beam of polarised light from a magnetic material [23]. This effect is known as the magneto-optical Kerr effect (MOKE).

The MOKE is understood to be proportional to the magnetisation of the material which makes it applicable as a non-destructive method of probing magnetic reversibility of materials within a skin depth of $10 - 20$nm [24]. In the following sections the theory, principles and experimental setup of the MOKE magnetometer are discussed.

3.4.1 Interaction of polarised light with magnetic material

Polarised light transmitted through a material generates two distinguishable geometries which are the Faraday geometry where the light wave travels along field direction and the Voigt geometry where the light travels perpendicular to the field direction. The polarised light beam in the Faraday geometry can be considered to be composed of left and right circularly polarised light (LCP and RCP) components while in the Voigt geometry it is comprised of linearly

polarised light with polarisation parallel and perpendicular to the direction of the magnetic field. The magnetic field in the material creates symmetry breaking that causes the two components of the incident beam to be propagated differently on transmission. In the case of the Faraday geometry, the polarisation modes of the incident beam are modified due to the difference in the velocity of the transmitted beam on interaction with the magnetic material. This effect is known as birefringence. Similarly, the difference in the Voigt geometry is due to difference in the absorption of the polarisation modes of the incident beam by the magnetic material. This effect is termed dichroism. The effect also occurs for other electromagnetic waves such as x-rays, which explains its application in the x-ray resonant magnetic reflectivity explained in section 3.7.3.

In the case of reflection of linearly polarised light from a magnetic material as in the case of MOKE, the compositional modes of polarisation are defined with respect to the plane of incidence. The modes are composed of linear s-polarised light (where the electric field vector is polarised perpendicular to the plane of incidence) and p-polarised mode (where the electric field vector is polarised parallel to the plane of incidence). When these modes are incident on a non-magnetic material it yields reflected s or p polarized light. But when passed through a magnetic material it yields rotation orthogonal to the plane of incidence with components of both s and p polarised light. For example if p polarised light is reflected from a magnetic medium, the reflected beam has a p-component of polarised beam and a small s-component beam. The additional s-component beam also has its electric field component out of phase with the reflected p-component [25]. Hence, the light beam becomes elliptically polarised.

The magneto-optical Kerr effect can be described macroscopically by dielectric tensor theory [26]. In this theory, the plane polarised light is considered as a superposition of LCP and RCP light, which on encountering a magnetic medium travel with different velocities and attenuation. This is due to the difference in the refractive index of these two modes of polarisation. The reflected beam is a recombination of the two polarised modes that produce the Kerr rotation (change in the polarisation of the in-phase component of the reflected beam) and ellipticity (change in the polarisation of the out-of-phase component of the reflected beam). The dielectric

tensor that defines the effect of the magnetic medium is given as:

$$\varepsilon = \varepsilon_0 \begin{bmatrix} 1 & -i\vartheta_z & i\vartheta_y \\ i\vartheta_z & 1 & -i\vartheta_x \\ -i\vartheta_y & i\vartheta_x & 1 \end{bmatrix} \tag{3.4.1}$$

where $\vartheta_{\mathrm{x,y,z}}$ are the Voigt magneto-optic constants that describe the MOKE and are proportional to the magnetisation of the material. The complex (off diagonal) terms are responsible for the modification of the polarisation giving the two modes of polarisation with refractive index:

$$\mathrm{n}_{\pm} = \frac{\pm \mathrm{c}k}{\omega} \tag{3.4.2}$$

where c is the speed of light, k is the wave vector and ω is the angular frequency. The notation of the Voigt magneto-optic constant is defined differently from that in the literature considering the pre-existing notations in this thesis.

The Kerr effect can also be described microscopically as a consequence of the spin orbit interaction [27]. An electron in a material with magnetic moment μ moving with motion v is influenced by the electric field component, E of the incident light. The electron experiences a magnetic field $\mathrm{B} \sim \mathrm{v} \times \mathrm{E}$ with associated spin orbit interaction $\mu \cdot (\mathrm{v} \times \mathrm{E})$ as a result of the interaction between the electric field of the light and magnetisation [28]. The relationship between the current density due to electron motion and the electric field from the incident light can be represented by Ohm's law in the form

$$\mathrm{J} = \sigma \cdot \mathrm{E} \tag{3.4.3}$$

where σ is the conductivity tensor and is related to dielectric tensor ε by the equation [29]

$$\varepsilon = 1 + \sigma \frac{4\pi i}{\omega}. \tag{3.4.4}$$

This interpretation links the microscopic point of view to the macroscopic consideration as

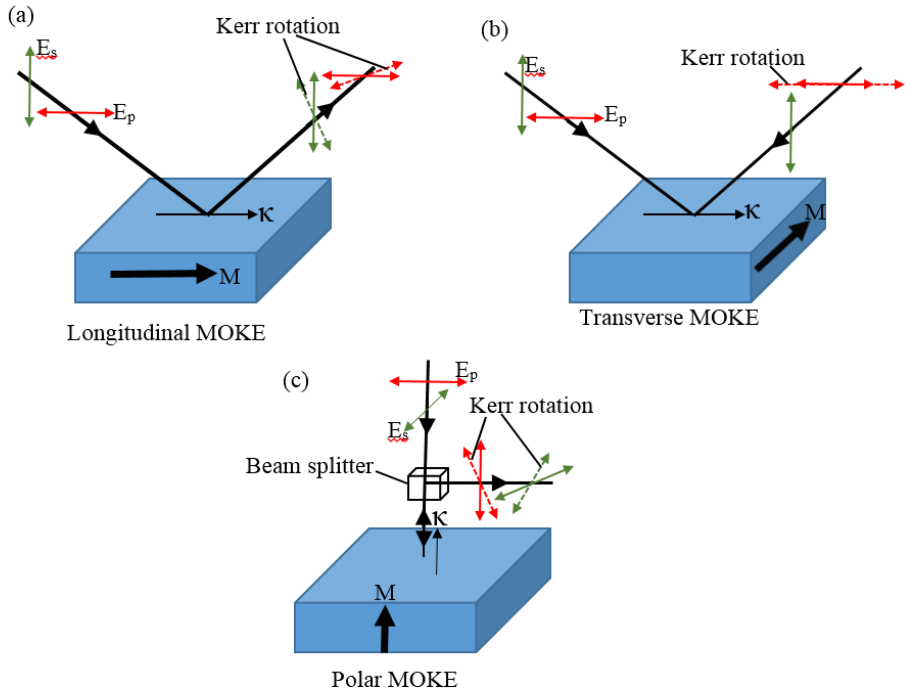

Figure 3.11: Schematic diagrams of the MOKE geometries showing the magnetisation M and wave propagation direction κ (a) Longitudinal geometry (b) Transverse geometry (c) Polar geometry.

explained earlier. The changes in the rotation and ellipticity are necessarily the same as in the macroscopic view point.

3.4.2 Geometries of magneto-optical Kerr effect

The magneto-optical Kerr effect is observed in three geometries defined based on the relative orientation of the scattering wave vector of the light wave Q(q) and the axis of magnetisation. They are longitudinal, polar and transverse geometries (shown in figure 3.11) and are sensitive to different components of magnetisation. It is important to note that Kerr rotation is obtained from the magnetisation component along the wave propagation direction. Thus, the longitudinal and transverse geometry are sensitive to the in-plane magnetisation of the material while the polar is sensitive to the out-of-plane magnetisation. All the MOKE measurements shown in this thesis were made with the longitudinal geometry, except where otherwise stated.

The longitudinal MOKE is configured to be sensitive to in-plane magnetisation by using

high angle incident beam with applied magnetic field parallel to the sample surface as shown in figure 3.11a. The major drawback in this geometry is that it is possible to have a polar component in the reflected beam depending on the magnetic anisotropy within the sample and angle of incidence [30]. As the angle of incidence approaches normal incidence the longitudinal Kerr rotation diminishes because the Lorentz force vanishes or points along the direction of propagation. The angle of incidence of the longitudinal MOKE setup in Durham University is set at 45°.

In the transverse geometry, the magnetic field is perpendicular to the plane of incidence as shown in figure 3.11b. This leads to a change in intensity and phase of the reflected p-polarised light from a magnetic medium. The projection of the k vector on the magnetisation direction is null, meaning there is no Kerr rotation because the magnetisation component does not lie along the scattering wave vector but rather gives a magnetisation dependent intensity variation. The advantage of this geometry is that it is insensitive to longitudinal and polar magnetisation components.

Finally, measurement in the polar geometry are usually performed at normal incident beam with magnetic field applied normal to the sample surface. In this case there is a Kerr rotation at normal incidence because the magnetisation points out-of-plane, leading to a Lorentz force at that angle. The polar effect is independent of incidence polarisation at normal incidence. Experimentally it has been shown that the polar effect is an order of magnitude larger than the longitudinal effect [30].

3.4.3 MOKE penetration depth

As mentioned earlier, the MOKE magnetometer is limited in sensitivity based on the penetration depth of the laser light used. Penetration depth is defined by

$$\lambda = \frac{1}{2\mathrm{k}\beta} \tag{3.4.5}$$

where k is the wave vector of incident light and β relates to the absorption component of the refractive index. Penetration depth is considered as the distance of penetration of the light

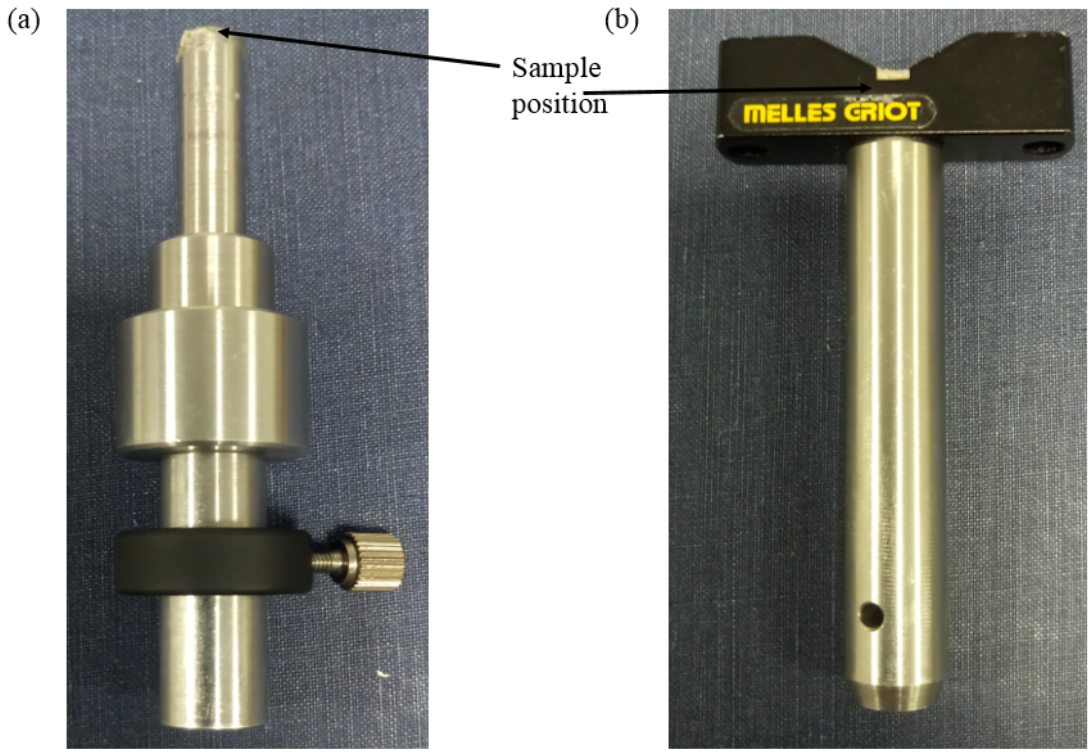

Figure 3.12: Magneto optical Kerr effect sample holders showing sample position (a) Longitudinal MOKE sample holder (b) Polar MOKE sample holder

into the sample where the attenuation of the beam intensity by 1/e of its initial intensity. This results in attenuation of approximately 37% of the incident beam intensity. At sample thickness less than the penetration depth, the Kerr rotation is proportional to the total magnetic moment in the sample but when sample thickness is greater than λ_{MOKE} the Kerr effect is only seen within the penetration depth due to absorption. Generally, MOKE magnetometry is sensitive to magnetisation within the penetration depth of 20 nm. The extraction of absolute magnetic moment with this technique is not trivial because the effect is highly influenced by reflections from interfaces in the sample. The MOKE experimental setup applicable in this thesis is discussed in the next section.

3.4.4 Experimental setup of polar and longitudinal MOKE

The experimental setup used was designed to perform both the longitudinal and polar MOKE measurements. This was achieved by adjusting the beam direction and changing the sample holder. The sample was mounted on an x-y translational stage between the poles of an electro-

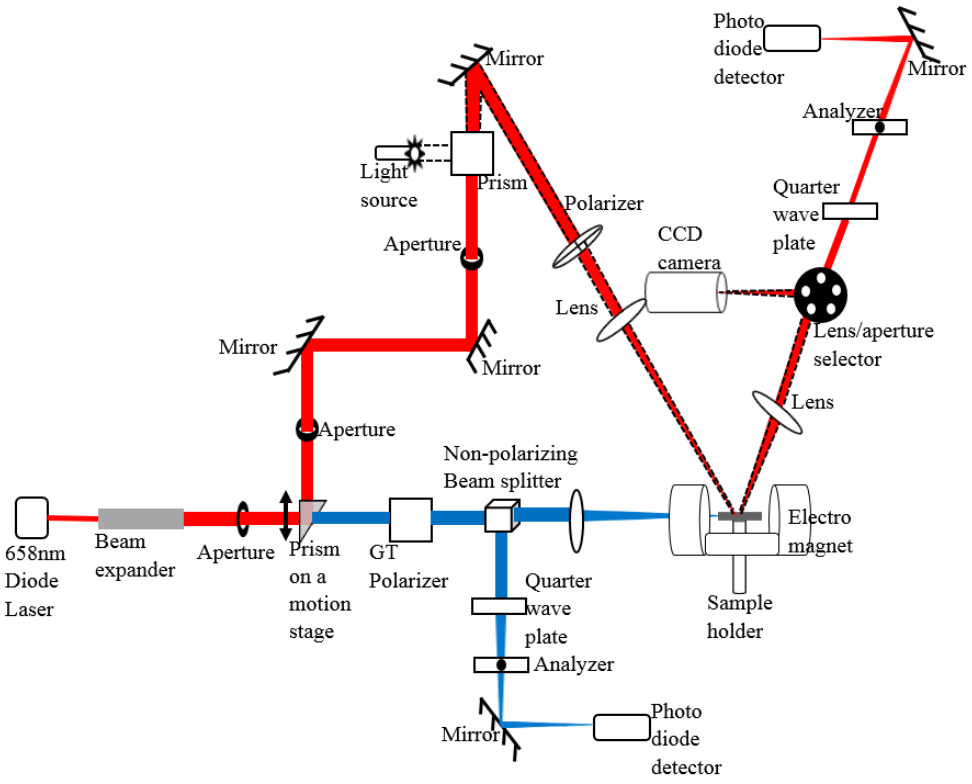

Figure 3.13: Schematic of the MOKE experimental setup where the red beam line shows the longitudinal MOKE trajectory and the orange beam line shows the polar MOKE trajectory.

magnet with a specifically designed sample holder (shown in Figure 3.12). The electromagnet was driven by a power supply connected to a signal generator that provides the magnetic field applied during measurements.

The incident beam from a diode laser with wavelength of 658 nm passes through a beam expander into a prism mounted on a motion stage which can be adjusted to direct the beam in longitudinal MOKE (colored red) or polar MOKE (colored orange) geometry. The beam is focused by some lenses, mirrors and a polariser (which helps to enhance the beam polarisation ratio) to a spot size of $\approx 7\mu$m on the sample at an angle of 45° for the longitudinal MOKE. Similarly in the polar MOKE geometry, the beam from the beam expander passes through a Glan-Taylor polarising prism with extinction ratio of 10^{-5} by adjusting the prism stage before hitting the sample at an angle of 90°. In both geometries, the reflected beam from the sample passes through a refocusing lens and then through the quarter wave ($\frac{\lambda}{4}$) plate to remove any induced ellipticity and finally through a Glan-Taylor polarising analyser before incident on the

photo-diode detector. The reflected beam in the polar geometry also passes through a beam splitter before going through the quarter-wave plate because it is reflected in the direction of incident beam. The signal on the photo-diode is transduced into a change in voltage and an hysteresis loop averaged over many field cycles is obtained.

Sample position alignment with the laser beam was accomplished with the use of white light placed on the beam path (see figure 3.13). During this process, a neutral density filter was used to attenuate the intensity of the laser beam onto the camera. A mirror was also placed before the quarter-wave plate in order to reflect the image of the sample surface on to the camera. The white light was only used to illuminate the sample surface for imaging and alignment, and was turned off before measurements were taken.

3.5 Superconducting Quantum Interference Device (SQUID) magnetometer

The superconducting quantum interference device (SQUID) magnetometer is a device designed to detect extremely small magnetic moments. It is a very sensitive and most effective technique for magnetic measurements in thin films because it allows the measurement of the total magnetic moment in the sample. It was developed following the theoretical prediction by Brian David Josephson in 1962 [31] of the properties of a supercurrent through a tunnel barrier. He predicted the detection of a current through two superconductors separated by a thin insulator. This phenomenon is known as the Josephson effect and was experimentally observed by Anderson and Rowell in 1964 [32]. This section we covers the Josephson effect in relation to the SQUID magnetometer as well as the experimental setup particular to the Quantum Design magnetic property measurement system (MPMS) XL-7 used in this thesis.

3.5.1 Josephson effect and SQUID magnetometer

The SQUID device consists of two superconducting materials forming a loop separated by insulating material as shown in figure 3.14b. The junction between the superconductor and the

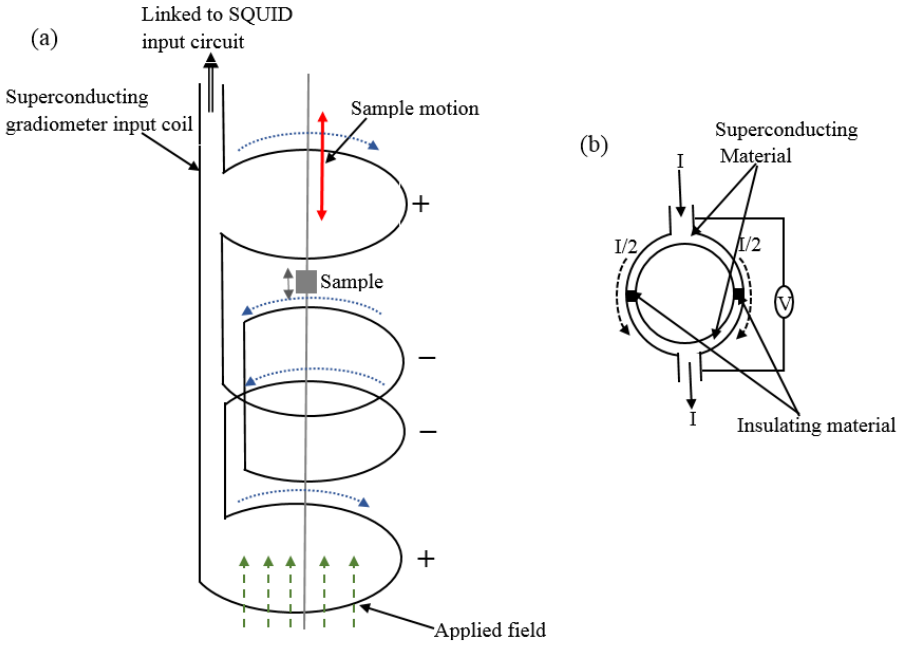

Figure 3.14: Schematic illustration of (a) the sample environment of the SQUID magnetometer (b) a DC SQUID with two Josephson junctions.

insulating material is the Josephson junction (JJ). It was realised that in the absence of an applied voltage that a tunneling current flows through this junction as Cooper pairs of electrons can pass from one superconductor to the other. The current density going through the JJ creates a flux which when measured are in integer multiple of the flux quantum. The amplitude of the tunneling current can be influenced by a magnetic field. If a magnetic field is applied to the loop, there is a phase evolution $\Delta\phi$ between the superconducting waveform on either side of the JJ which is quantised. The derivative of $\Delta\phi$ with respect to time relates to the voltage across the junction.

SQUID devices are categorised into two groups based on the number of JJs in the device. The first category is the RF SQUID device made of one JJ. The JJ is shorted by a second superconductor path and the voltage response is obtained by coupling the loop to an RF bias tank circuit. The second category is a double JJ SQUID termed DC SQUID. In this case the junctions are not shorted as the previous case. Instead a DC bias current that is slightly greater than the critical current is applied and the voltage drop across the device is monitored (shown in figure 3.14b) [33].

3.5.2 Experimental setup of SQUID magnetometer

The magnetization measurements were made at the ISIS R53 materials characterisation lab using a Quantum Design MPMS XL-7 [34, 35]. It consists of an RF SQUID, superconducting magnet, gradiometer coil, flux transformer, and superconducting shielding. Sputter deposited samples of 5mm×5mm placed inside a polycarbonate capsule were mounted inside a clear plastic tube made of weakly diamagnetic material in order to minimise background noise and induced flux. The tube was attached to a sample stick that was lowered into the sample environment of the SQUID magnetometer between the superconducting gradiometer input coil (as shown in figure 3.14) and then cooled to 5 K in a 500 Oe magnetic field. This procedure of field-cooling puts the sample in a saturated magnetic state. The sample was left for 5 minutes to thermalised before a temperature scan was taken with an applied field of 50 Oe, based on the sample coercive field from the MOKE measurement described earlier in section 3.4.4.

The data acquisition is achieved by scanning the sample vertically along the gradiometer coils. The change in magnetic flux from the sample induces an electric current in the coil following Faraday's law of electromagnetic induction. The induced current is sensed as a voltage variation which is measured by the signal coil as a voltage response providing a highly sensitive measurement of the magnetic moment of the sample [36]. The sample scan through the center of the superconducting gradiometer is configured to detect the gradient of magnetic field. The top and bottom counter-wound coils are the second-order field gradiometer coils which helps reject the pickup noise generated from the fluctuations in the magnets across the system (see figure 3.14a). When a bias current I_b is applied to the SQUID loop, an induced voltage, periodic in the magnetic field gradient sensed by the gradiometer coil, is measured across the JJ by the SQUID device. This is achieved via a flux transformer that couples the gradiometer with the SQUID [37]. The feedback voltage on the circuitry shown in figure 3.15 is for flux magnitude modulation. The output is amplified and sent to the integrator that produces a linear response from the SQUID. The voltage signal is analysed by computer and a corresponding magnetic moment profile relative to temperature change is obtained.

The sample environment is a temperature controlled variable temperature insert (VTI) cavity

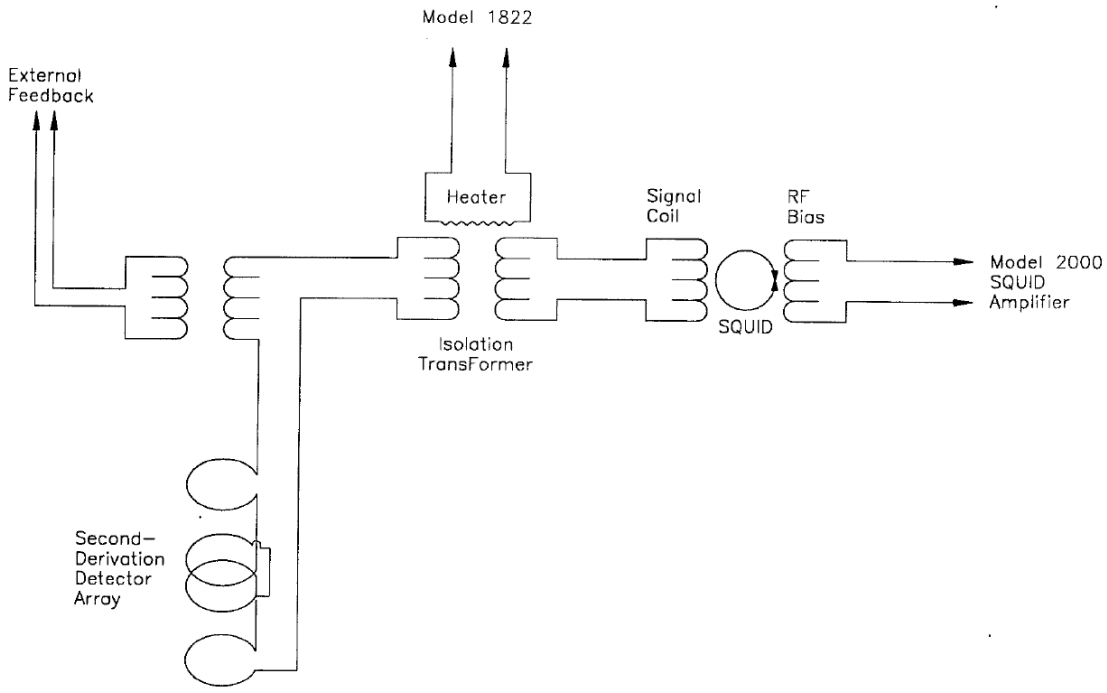

Figure 3.15: Circuit diagram of a RF SQUID magnetometer. Figure reproduced from Ref [35].

thermally isolated from the gradiometer and magnet by a vacuum. It is cooled by liquid helium drawn through a capillary tube attached to the bottom of the sample chamber. Cooled gas is pumped out from the top of the cryostat while the temperature control is achieved through a heater and thermometer attached on the sample holder and chamber. The lower section of the sample chamber is wrapped around with a slab of vertically oriented copper wire in order to ensure uniformity in temperature. The SQUID device also requires a liquid helium cryostat but this is embedded in a magnetic shield because the SQUID cannot tolerate a strong magnetic field. This allows the temperature to be varied between 2 K and 400 K with an applied field of up to 7 Tesla giving high sensitivity for small magnetic signal from the sample.

3.6 Neutron Reflectivity

Neutrons were first observed by Chadwick in 1932 following the bombardment of beryllium with alpha particles generated from polonium [38]. The development of neutron scattering as an investigative technique was attributed to Bertram Brockhouse and Clifford Shull who won a Nobel prize in 1994 for their pioneering work which was only possible because of the

significant characteristics of the neutron particle [39]. One of the earlier applications of the neutron technique was in the investigation of spin density distributions in ferromagnets [40]. Neutrons are neutrally charged which enable them to penetrate close to the nucleus as there is no Coulomb barrier to overcome. Neutron scattering is analogous to x-ray scattering but neutrons interact with the nucleons providing information on the structure, and the local magnetisation in the sample. These are possible because of the neutron's spin 1/2 property which leads to a coupling between the magnetic moment of the neutron and the magnetisation state of the material. As the neutron interaction is weak, they are a non-destructive probing technique with high penetration.

This section begins with methods of neutron generation followed by theoretical description and experimental setup for polarised neutron reflectivity (PNR).

3.6.1 Neutron sources

Atomic nuclei are usually the main source of neutron generation which may be by fission reaction or using an accelerator. The fission process involves a heavy nucleus splitting into lighter nuclei with the generation of a residual α-particle, neutrons and other subatomic particles on absorption of a neutron. In order to sustain the fission process, the emitted neutrons are made to undergo an elastic collision with nuclei in a moderator to bring them to a thermal equilibrium. The moderator slows down the neutron to produce a neutron beam suitable for the neutron investigative purpose. The neutron fluxes produced in reactor sources are usually constant with varying wavelength [41].

An alternate source of neutrons is via the accelerator technique which is similar to the synchrotron facilities. A fast stream of charged particles (in this case protons) at relativistic energies collide with a target of heavy metal such as tungsten, tantalum or uranium resulting in the ejection of neutrons and protons from the nuclei by a process known as spallation. The generated neutrons are hot and again require a moderator to bring them to thermal equilibrium. Moderators can be water at room temperature, liquid methane at 100 K or liquid hydrogen at 20 K depending on the required neutron scattering technique. Neutrons that have passed

through the moderator are known as thermal neutrons and are characterised by the wavelength from the de Broglie relation :

$$\lambda = \frac{\mathrm{h}}{\mathrm{m_n v}} \tag{3.6.1}$$

where $\mathrm{m_n}$ is the mass of the neutron, v is the velocity and the non-relativistic energy is

$$\mathrm{E} = \frac{\mathrm{m_n v^2}}{2}. \tag{3.6.2}$$

Therefore the relationship between λ, E and the temperature of a neutron is

$$\mathrm{E} = \mathrm{k_B T} = \frac{\mathrm{m_n v^2}}{2} = \frac{\mathrm{h^2}}{2\mathrm{m_n}\lambda^2} = \frac{\hbar^2 \mathrm{k^2}}{2\mathrm{m_n}} = \mathrm{hv}. \tag{3.6.3}$$

Spallation sources are less dangerous because the process can be stopped by power outage. Hence there is no danger of chain reaction as in the fission process.

3.6.2 Specular neutron interaction

Similar to other reflectivity techniques, neutron reflectivity provides cross-sectional information on the inhomogeneities normal to the sample surface or interface and the scattering vector is also defined by equation 3.3.3. The depth-dependent scattering potential, V, of the neutron particle is given as:

$$\mathrm{V} = \frac{2\pi\hbar^2}{\mathrm{m_n}} \mathrm{b_i}(\mathrm{r} - \mathrm{r_i}) \tag{3.6.4}$$

where $\mathrm{b_i}$ is the scattering length factor of the i-th nucleus at position $\mathrm{r_i}$. Based on the Born approximation, the reflectivity is represented as:

$$\mathrm{R(Q)} = \frac{16\pi}{\mathrm{Q^2}} |\rho(\mathrm{Q})|^2 \tag{3.6.5}$$

where ρ(Q) is the average scattering length density profile, which is a one dimensional Fourier transform of ρ(z)

$$\rho(\mathrm{Q}) = \int_{-\infty}^{\infty} \rho(\mathrm{z}) \exp(\mathrm{iQ_z}) \mathrm{dz}. \tag{3.6.6}$$

$\rho(z) = \sum N_i(z)b_i$ is the sum of all the products of the number density of atoms N_i and scattering length b_i. For thicker samples, the reflectivity is approximated as:

$$R \approx \frac{16\pi^2}{Q^4}(Nb)^2 \tag{3.6.7}$$

where N is the number density and b is the neutron scattering length. The function Nb describes the neutron scattering length density in unit of $Å^{-1}$. The neutrons refractive index, n(z), is given by: [41, 42]

$$n(z) = 1 - \sum_i N_i(z)b_i\lambda^2/2\pi \tag{3.6.8}$$

where λ is the neutron wavelength. For most materials, the refractive index is close to unity and the scattering length factor is positive and small. The critical wave vector given as $Q_c = \sqrt{16\pi Nb}$. Due to the presence of neutron spins, the interaction of the neutron with the magnetic moment of a material makes it an ideal probing technique for magnetic thin films, as explained in the next section.

3.6.3 Magnetic neutron reflectivity

The previous discussion on neutron scattering concentrated on nuclear scattering. Neutrons possess an intrinsic magnetic moment and spin that enables the scattering potential to be spin dependent. The neutron spin interacts with the local magnetisation as well as the nuclei of the probed material. Therefore, the total scattering factor of neutrons is the sum of the nuclear and magnetic scattering length:

$$b_{tot} = b_{nuc} + b_{mag}. \tag{3.6.9}$$

The full derivation of magnetic scattering for a single magnetic atom is provided by Squires [43]. In the same way, the neutrons incident on a magnetic material experience an additional potential V_{mag} additional to the nuclear potential, V_{nuc}, experienced in non-magnetic material given by

$$V_{mag} = -\mu \cdot B \tag{3.6.10}$$

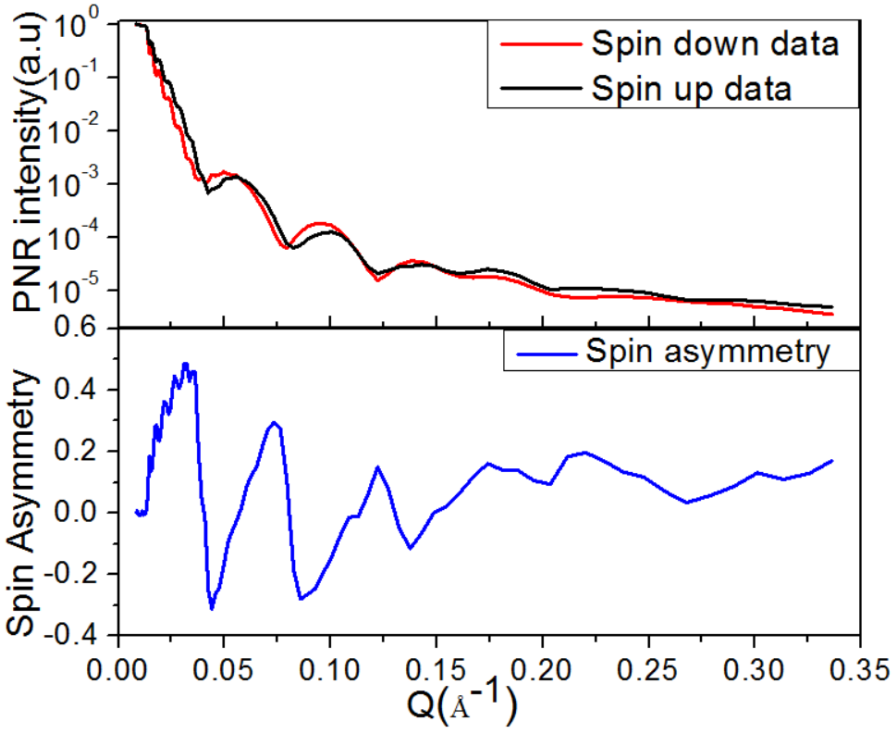

Figure 3.16: Experimental data of polarised neutron reflectivity (upper panel) with the corresponding spin asymmetry (lower panel) for Pt(3nm)/CoFeTaB(10nm)/Pt(3nm).

where μ is the magnetic moment of the neutrons. The total flux density is $B = B_0 + \mu_0 M$ given that B_0 is a externally applied magnetic flux density which does not contribute to the scattering and is present both inside and outside of the sample, μ_0 is the permitivity of free space and M is the magnetisation. In the case of polarised neutrons (where the polarisation axis is defined with respect to magnetisation), the total scattering potential is represented as:

$$V_{\mp} = V_{nuc} \pm V_{mag} = \frac{2\pi\hbar^2}{m_n} N(b_{nuc} \pm b_{mag}) \tag{3.6.11}$$

where the $+$ represents the spin-up polarised neutron state and $-$ represents the spin-down polarised state. The scattering potential reflects the difference in the total scattering length for spin-up and spin-down polarised neutrons. An example of the neutron reflectivity of both polarisation states are shown in the top panel of figure 3.16. The difference in the spin-up and spin-down polarisation is primarily the magnetic signal of the sample and is defined by the spin asymmetry factor given as [44]:

$$\text{S.A.} = \frac{R^+ - R^-}{R^+ + R^-}. \tag{3.6.12}$$

where $R^{+(-)}$ are the reflectivity of spin-up and spin-down polarised neutrons respectively (shown in lower panel of figure 3.16). The measured reflectivity corresponds to the amplitude of intensity at the detector, normalised to the incident intensity. The neutron reflectivity intensity decays as Q^{-4} and the signal-to-noise ratio at high angles are usually limited by background noise from incoherent scattering. Data was analysed here using simulations that were performed using the GenX software [18], which is discussed later.

3.6.4 Polarisation of neutron

Polarised neutron reflectivity (PNR) is a highly sensitive tool which is able to provide a cross-sectional magnetic profile of ultra-thin layers. In a PNR experiment, a magnetic field is applied to the sample to maintain the polarisation of the neutron beam and orientate the sample magnetisation parallel to the field. The neutron beam is polarised to two spin states by spin flippers which are positioned before and after the sample position to flip the neutron spin from one state to another. The spin flippers are OFF(ON) when the $+(-)$ polarisation is allowed through it. The scattered polarised states are separated before they get to the detector through an analyser as shown in figure 3.17. The neutron polarisation is maintained by a guide field of ~ 5 Oe. The polariser and the analyser only reject the spin-up neutrons. At the detector, measurement of four spin polarisation states are possible, that is $++$, $+-$, $-+$ and $--$ polarisation states, where the first sign represent the polarisation state of incident neutron and second the polarisation state of scattered neutron.

If the first flipper is OFF, the + polarisation state is incident on the sample and the analyser reflects only neutrons that had not experienced a spin flip, so the $++$ polarisation state is measured at the detector. The $-+$ state is measured when the first flipper is ON, meaning that only - polarised neutron are allowed through and the analyser allows only + polarised neutron state. Conversely, if the first flipper is OFF and the second flipper in ON. The $+-$ polarised state is measured. Finally, the $--$ polarisation state is measured by turning ON the two flippers. Generally, the $--$ and $++$ polarisation state are known as the Non Spin flip (NSF) state while the $-+$ and $+-$ polarisation state are known as the spin flip (SF) state [45].

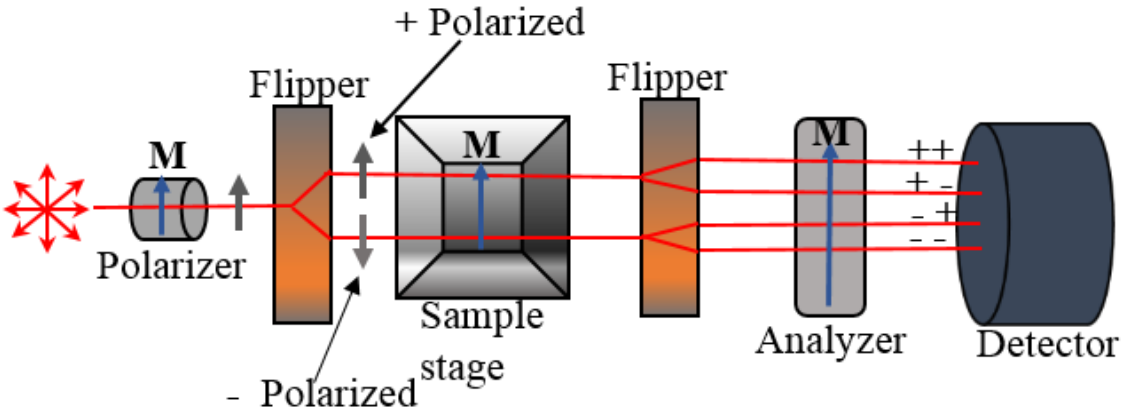

Figure 3.17: Schematic illustration of neutron polarisation to spin up (+) and spin down (−) states with the sample magnetisation in the sample plane.

These spin states can be measured simultaneously.

The scattering potential in equation 3.6.11 is rewritten as [46]

$$\mathrm{V} = \frac{2\pi\hbar^2}{\mathrm{m_n}} \begin{pmatrix} \rho_{++} & \rho_{+-} \\ \rho_{-+} & \rho_{--} \end{pmatrix} \tag{3.6.13}$$

where ρ is the scattering length density given as $\rho = \mathrm{Nb}$. The scattering length densities relative to the spin polarisation are expressed as

$$\begin{aligned} \rho_{++} &= \rho_{\mathrm{nuc}} + \rho_{\mathrm{zmag}}, \\ \rho_{--} &= \rho_{\mathrm{nuc}} - \rho_{\mathrm{zmag}}, \\ \rho_{+-} &= \rho_{\mathrm{xmag}} - \mathrm{i}\rho_{\mathrm{ymag}}, \\ \rho_{-+} &= \rho_{\mathrm{xmag}} + \mathrm{i}\rho_{\mathrm{ymag}}. \end{aligned} \tag{3.6.14}$$

where (x, y, z)mag are the associated magnetisations in the x, y and z-planes. It provides information on the vectorial components of magnetisation. The z-component of magnetisation gives access to the magnetic depth profile in the sample. More on polarised neutron reflectivity is given in [46, 47]

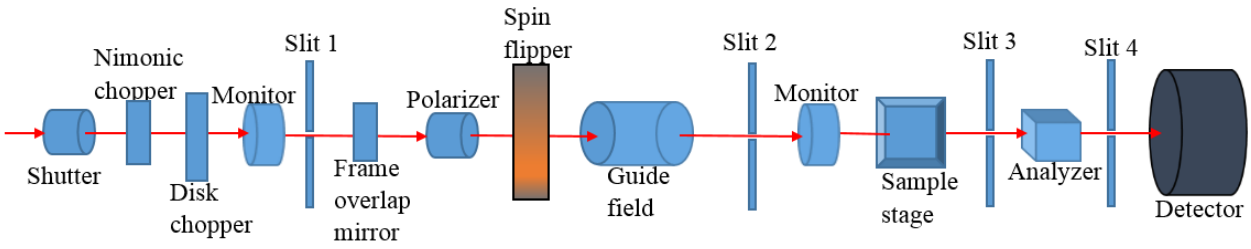

Figure 3.18: Schematic of Polref polarized neutron reflectivity setup.

3.6.5 POLREF polarised neutron reflectivity setup

Polarised neutron reflectivity measurements were conducted at the Polref beamline at Rutherford Appleton laboratory, STFC, UK. Polref is a time of flight reflectometer with an incident neutron beam with a wavelength range of 0.5 - 6.5 Å. The source frequency of the neutron beam is 50 Hz.

The setup is organised such that the neutron beam from the source is at an angle of 2.3° from the horizontal to reduce the fast neutrons and background γ-rays from the direct line-of-sight with the moderator. The distance between the source and the sample stage is about 23 m and from the sample environment to the detector is 3 m. The neutron beam incident on the sample passes through two synchronous disc choppers, which defines the wavelength band, a frame overlap mirror (to remove slow neutron from previous pulses), a polarising mirror, spin flipper, guide field and a beam monitor as shown in Figure 3.18. The flipper allows access to all the elements of the polarisation matrix discussed in section 3.6.4. The guide magnetic field is produced by permanent magnets that are designed to minimised effect of stray fields thereby sustaining the neutron polarisation. The detected beam is normalised to a monitor located just before the sample.

The sample environment is customised to the room temperature regime which uses a magnetic yoke whose field matches the controlled incident polarisation, allowing access to the elements of the polarisation matrix. In the cases of low temperature measurements, an electromagnet is used with a cryostat to keep the temperature within the required temperature range. The neutron beam hits the sample and the reflected beam from the sample goes through slits to the detector. Both the perpendicular Q_z and parallel Q_x components of the neutron wave vector to

the surface of the sample can be obtained in each measurement [45, 48]. In this thesis, we only used the Q_z component.

3.7 X-ray scattering II: Synchrotron x-rays

X-ray resonant magnetic reflectivity (XRMR) technique is discussed in this section. X-ray magnetic reflectivity was first observed by Gibbs in 1988 [49]. XRMR is a non-destructive technique for magnetic depth profiling that involves the combination of XRR and the x-ray magnetic circular dichroism (XMCD) effect. Here, the magnetic dichroism property of elements is exploited, providing a precise magnetic spatial distribution specific to the element and symmetry of a material. A circularly polarised x-ray beam tuned to the resonance energy of the element of interest is employed in the investigation. A synchrotron light source is used because it provides x-rays of tunable energies with well defined polarisation. The x-ray energy is matched to the energy of an electronic transition of the specific element (platinum in this thesis).

In this section, a brief description of the synchrotron radiation technique is covered as well as the theory of XRMR, which includes XMCD effect and resonant scattering. Finally, the XRMR setup used for measurements discussed in chapter 6, 5 and 7 is described.

3.7.1 Synchrotron radiation

Acceleration of charge particles leads to the emission of electromagnetic radiation. Synchrotron radiation is generated by the acceleration of electrons in a circular relativistic motion to emit radiation within the x-ray band. Electrons are redirected in a circular propagation path within a storage ring which consists of straight sections with curves of bending magnets. A uniform magnetic field is applied perpendicular to the orbit plane of a curved segment and a magnetic quadrupole field to the straight segments to help focus the beam. The magnetic field deflects the propagation path due to the Lorentz force. The RF cavity provides an electrostatic boost to the electrons by way of voltage pulses to compensate for the energy lost during propagation. A detailed theory of synchrotron radiation techniques is given by Nielsen and McMorrow [8].

X-ray intensity can be boosted with an insertion device, such as wigglers and undulators,

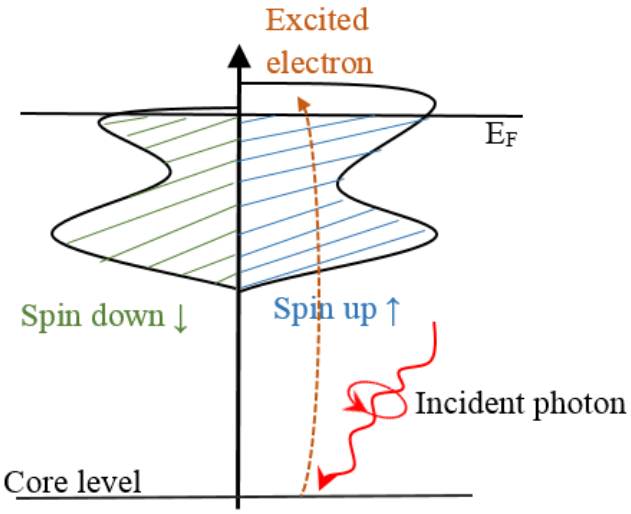

Figure 3.19: Illustration of resonance circular dichroism effect. A circularly polarised photon is absorbed by spin polarising an electron which gets excited into an unoccupied spin polarised valance band

which enhance the horizontal oscillations of the electrons. These devices are made of magnets of alternating vertical polarity placed within the straight segments of the storage ring. The undulator device provides radiation of higher intensity because of constructive interference of additional radiation generated from the insertion device. Although the beam intensity had been improved by undulators, the emitted x-ray beam is passed through a monochromator, which is use to tune the beam energy to a particular energy before the beam reaches the sample [50].

3.7.2 The x-ray resonance magnetic circular dichroism effect

The x-ray magnetic circular dichroism effect was discovered by Gisela and Schütz in 1987 [51]. Similar to the Faraday effect explained earlier, when an electromagnetic wave is scattered from a magnetic surface, the angle of polarisation changes with respect to the magnetisation in the material. Also, there is a significant change in the atomic scattered intensity of a circularly polarised beam at the absorption energy of the element of interest that provides spatial magnetic information in a stacked structure.

A circularly polarised photon incident on a material as shown in figure 3.19, excites a spin-polarised electron from the core state depending on the helicity of the incident beam. The spin-polarised electron gets excited into an unoccupied valence state obeying the Pauli exclusion

principle. The transition state depends entirely on the number of available states with the spin aligned parallel to the helicity of incident beam. In a magnetic material the density of states (DOS) of spin-up electrons is different from spin-down electrons and that of the unoccupied states is the reverse. Therefore as a result of the angular momentum provided by the circularly polarised photon, the spin polarised density of states (DOS) for the left circularly polarised (LCP) beam is different from the right circularly polarised (RCP) beam. Meaning the probability of excited spin-up electrons is different from spin-down electrons for each polarisation state. The resonance excitation occurs at energies close to the binding energy of the core electron and the amplitude of the electron transition depends on the helicity of the photon or direction of magnetisation. Hence, the excitation is characterised by a change in the absorption intensity of the polarised beam that is represented by the absorption coefficient, ϖ represented as:

$$\varpi = \varpi_0 + \varpi_c P_c \cos\phi \tag{3.7.1}$$

where ϖ_0 and ϖ_c are the polarisation independent and spin dependent absorption coefficients respectively and ϕ is the angle between the magnetisation and beam direction. The spin-dependent absorption coefficient is responsible for the XMCD effect and scales relative to the degree of circular polarisation P_c. The magnetic signal is extracted as the difference in the absorption coefficient for both helicities. Experimentally, differences in intensities associated with absorption for both helicities or for magnetisation parallel and antiparallel to beam helicity are measures of the spin asymmetry ratio, given in equation 3.6.12. It is important to note that the magnetic signal is the same for flipping helicity or magnetisation direction as long as the applied field saturates the magnetisation of the sample [52].

In this work the XRMR measurements were made at the Pt L_3 absorption edge. Therefore, the p-core state of Pt is considered to be energetically split into $p_{1/2}$ and $p_{3/2}$ level which on absorption of the circularly polarised beam excites the electrons into the d-band [53]. Excitation of $p_{1/2}$ or $p_{3/2}$ to unoccupied d-band states are known as the Pt L_2 and Pt L_3 absorption edges respectively. The Pt L_3 absorption edge was used because of its higher absorption intensity. The transition of $p_{3/2}$ to d-band is a dipole transition and contributes greatly to magnetic scattering.

3.7.3 Atomic magnetic scattering

As discussed earlier, all x-ray scattering cross sections are related to the change in the refractive indices as the beam propagates through the sample. In equation 3.3.8, the refractive index is shown to be associated with the atomic scattering factor. For magnetic x-ray scattering, the scattering factor is a combination of the charge scattering factor, F_c, as in equation 3.3.8, and the magnetic, F_m, structure factor written as a sum over all atoms or resonance magnetic atoms respectively. The charge structure factor is:

$$F_c = \sum \Big(f_0 + f_c'(E) + i f_c''(E) \Big) e^{iQ.r} \tag{3.7.2}$$

while the magnetic structure factor is

$$F_m = \sum \hat{z} \Big(f_m'(E) + i f_m''(E) \Big) e^{iQ.r} \tag{3.7.3}$$

where $f_m'(E)$ and $f_m''(E)$ are the real and imaginary parts of the resonant magnetic scattering factor, which are associated with dispersive and absorptive scattering respectively. $\hat{z}$ is the unit vector along the quantisation axis parallel to the local magnetic moment that is aligned in the plane of the sample in our case. The scattering factors depend on the momentum transfer, Q, the energy of the beam, E, and the polarisation of the beam. Therefore, the modified refractive index is given as

$$n^{\pm} = 1 - \delta^{\pm} + i\beta^{\pm} \tag{3.7.4}$$

where

$$\delta^{\pm} = \left(\frac{2\pi n_0 r_e}{k^2} \right) \big(f_0 + f_c'(E) \mp f_m'(E) \cos\alpha_i \cos\phi \big), \tag{3.7.5}$$

$$\beta^{\pm} = \left(\frac{2\pi n_0 r_e}{k^2} \right) \big(f_c''(E) \mp f_m''(E) \cos\alpha_i \cos\phi \big), \tag{3.7.6}$$

n_0 is the number of atoms, + is associated to the right circular polarisation or positive magnetic field and − is for the left circular polarisation or negative field [54].

3.7.4 Resonant x-ray experimental setup

All resonance x-ray experiments were conducted at the XMaS beamline (BM28) at the ESRF in Grenoble which is situated on a bending magnet section of the synchrotron facility. A detailed description of the beamline optics and experimental capabilities are reported by S. Brown *et. al* [55]. Although the scattering geometry is similar to XRR described earlier in section 3.3, the optics and the experimental environment are designed for the study of x-ray magnetic scattering at optimised photon energies. The incident x-ray beam from the monochromator is polarised by a diamond (111) quarter-wave phase plate to a circularly polarised x-ray beam before being incident on the sample. The beam propagation path is under vacuum in order to preserve as much flux before and after scattering.

The sample environment consists of a cryogenic sample holder (known as Zebedee) mounted vertically on a horizontal section placed along the beam path, all under vacuum. The sample is placed on a copper stub attached to the sample holder. The horizontal section of the sample environment is made of a magnet assembly with water cooled pole pieces that can generate a field of up to 0.4 T. The pole pieces are arranged to provide a field aligned parallel to the scattering plane. The magnet is affixed on an eleven axis Huber diffractometer. The intensity of the scattered beam is measured by an avalanche photodiode detector mounted on the 2θ arm and collected data were fit with GenX software. Measurements were made at the Pt L_3 absorption edge at a photon energy of 11.5 keV.

3.8 Electrical measurements

Electrical transport measurements were performed at room temperature controlled with a cryostat, using a conventional four probe technique, which is discussed in detail in the next section. Magnetoresistance measurements were made in the longitudinal mode where the current and the voltage probes where in the sample plane. Measurements were made in three different geometries: xy, xz and yz geometries as shown in figure 3.20. As explained in section 2.7.2 and 2.7.5 changes in resistivity $\Delta\rho$ are minimum/maximum when the applied field direction is perpendicular/parallel to the charge current/ spin polarisation direction. Hence, angular sweeps

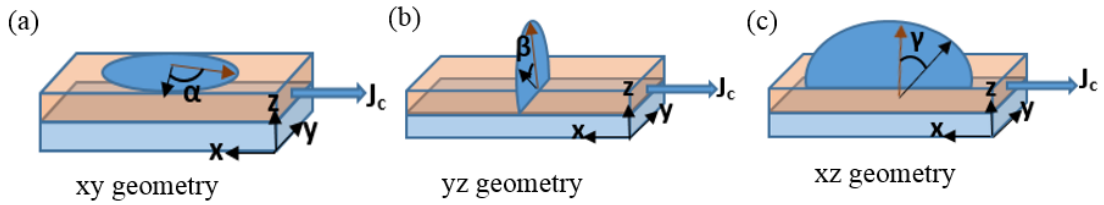

Figure 3.20: Magnetoresistance measurement geometries with current in the plane of the sample with magnetisation rotated (a) Inplane on the xy plane (b) out of plane on the yz plane (c) out of plane on the xz plane.

at a constant field of 2 T were performed for direct current (DC) and alternating current (AC) applications. Details of the four probe technique, the general MR setup, DC measurement and AC measurement are discussed below.

3.8.1 Four probe resistance measurement

Two contact resistance measurement includes the resistance of the contact in series with the resistance of the measured material. This makes the resistance measurement incorrect and may in a case of a very delicate material damage the sample. These limitations make the four probe measurement more appropriate. The four probe measurement involves passing a current through a sample and measuring the voltage drop across the voltage probes as shown in figure 3.21. The current applied to the sample may be DC or AC. A lock-in amplifier is employed in the case of AC measurement.

An ideal voltmeter has an infinite impedance which makes it impossible for current to flow through the voltage probes, meaning that the voltage drop measured is just that due to current flowing in the sample and not due to current flowing in the contacts, in this case constant resistance at voltage probes is irrelevant.

3.8.2 Experimental setup for magnetoresistance measurement

The experimental setup for the transport measurements that form the bulk of the work in chapter 6 is presented below. These measurements were conducted in Nanotechnology lab,

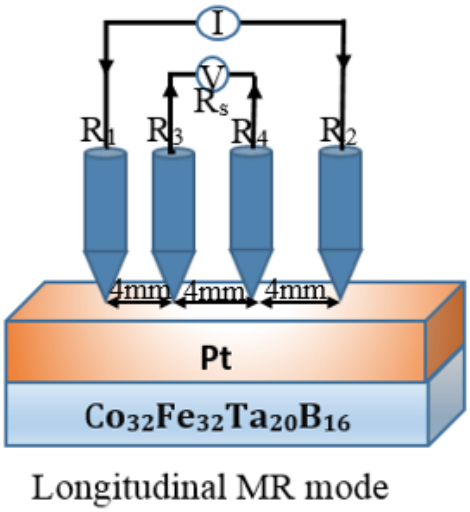

Figure 3.21: Schematic diagram of the four probe longitudinal resistance measurement showing the voltage and current contacts

Durham University, and Prof Brian Hickey's lab at the University of Leeds by Kathryn Moran. A schematic of the AC magnetoresistance setup at Durham University is shown in figure 3.22. The MR measurement setup performed at the University of Leeds consists of a Keithley 2400 current source, oscilloscope, electromagnet (field up to 3 Tesla) in a cryostat, Kepco BOP 50 -5M power supply, Stanford lock-in amplifier, nano-voltmeter and the Labview software in the computer used to control the signal generation and data acquisition. The setup is similar to the schematic on figure 3.22 where the blue section is embedded in a cryostat, the four-probe contacts are provided using wire bonding and the green section was substituted with a Keithley 2400 current source which provided a DC supply. In addition, a temperature controller connected to the sample stage is used to keep the temperature of the sample constant during measurement.

The sample was mounted on a sample holder as shown in figure 3.24a. The sample holder has a stage with 12 contacts (shown in figure 3.24b). Connections between the sample holder and sample was achieved by micro-wires with the help of wire bonding. The sample was connected to 4 of the 12 contacts making the four contacts for the applied current and measured voltage. Measurement of the voltage contact separation was done by taking a photo of the sample with the bonding and analysing the image with ImageJ. The sample holder was then affixed on a motorised sample stick and placed in the cryostat such that the sample sits within the electromagnet. The sample stick allows for in-plane and out-of-plane rotation of the sample

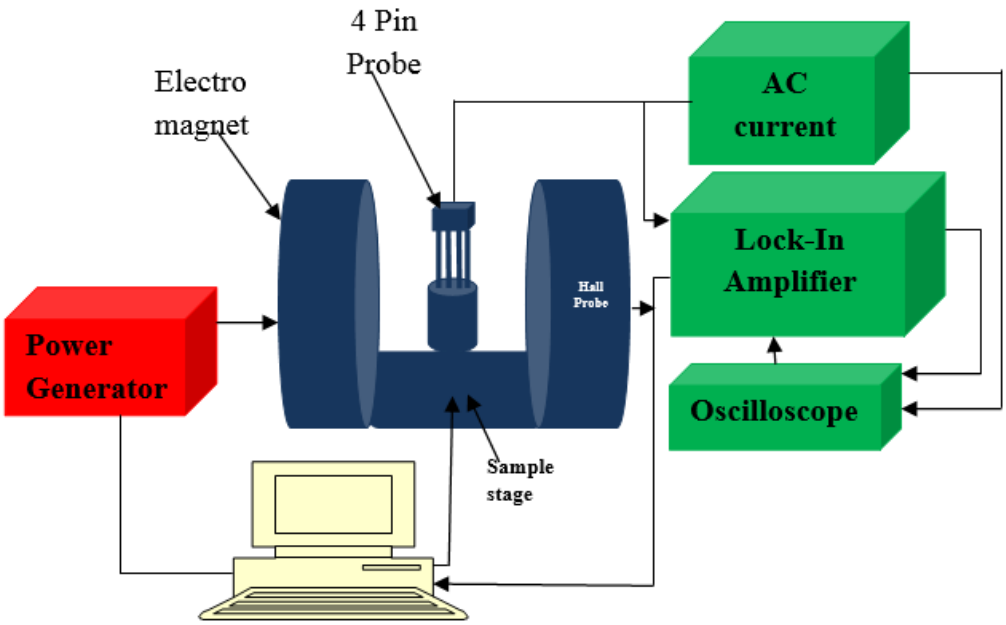

Figure 3.22: Schematic diagram of the magnetoresistance measurement setup at Durham University

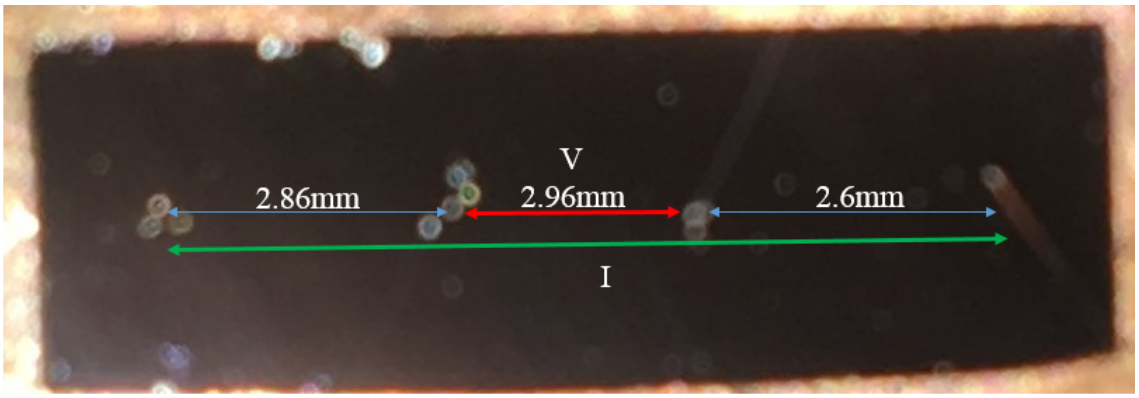

Figure 3.23: The sample probe separations with contacts made using nanowire bonding

at a fixed magnetic field of 2 T with a precision of 0.02°. The electromagnet controlled by the Kepco power supply provided the magnetic field and is calibrated with a Hall probe. Both DC and AC current of 0.7 mA was applied in three geometries (xy, xz and yz). The DC and AC setup is discussed in section 3.8.3 and 3.8.4 respectively. Labview software was used to control the instrument, collect and record the measured data.

The AC measurements were made using a fixed four probe contact with separations as labeled in figure 3.21 while the DC measurements were performed using a nanowire bonding as shown in figure 3.23 where the separations varied slightly in each sample and the resistivity was

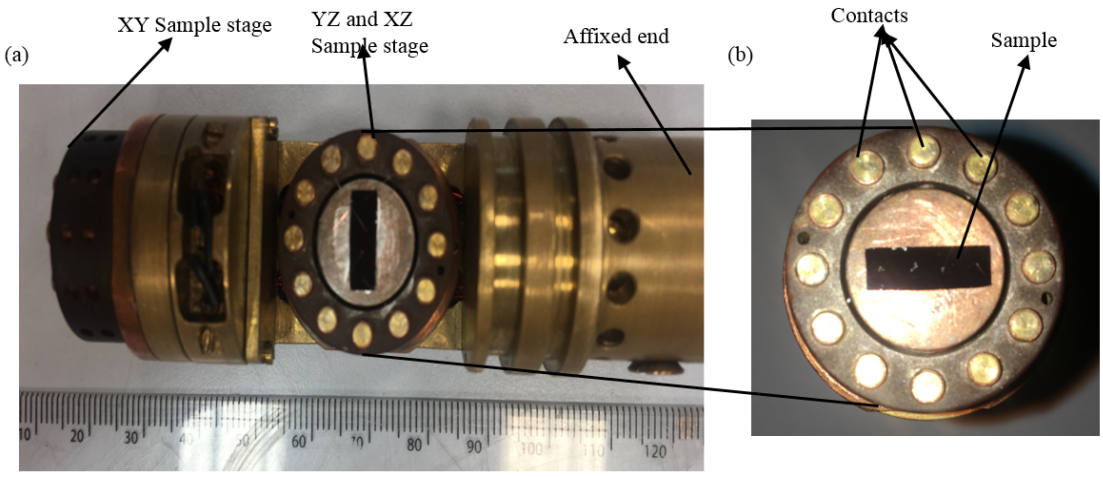

Figure 3.24: (a) Sample holder showing the sample stages (b) sample holder contacts

calculated using each individual probe separation.

3.8.3 Direct current measurement

A direct current of fixed amplitude was applied along the thin film slab and the longitudinal voltage averaged over four positive (+) and negative (-) current directions was measured. The acquired voltage measurements were converted to resistance and recorded as change in resistance at different angles. Similar measurements were made with single positive and negative current direction. A sensitive voltmeter was used to measure the voltage drop.

3.8.4 Alternating current measurement

AC measurement were made with similar applied current and magnetic field to the DC measurement. An oscillatory current of the form $I_0\cos(2\pi ft)$ of frequency (f=188 Hz) was applied through the thin film slab. A frequency of 188 Hz was chosen in order to avoid interfering noise signals. An alternating voltage drop across the sample was measured with phase sensitive detection with the help of a lock-in amplifier. The voltage drop consists of first, second and higher harmonics,which is a consequence of effects such as spin torque, thermal and magnetoresistance effects. In our case, only the first harmonic measurement was made by setting the software and lock-in amplifier to extract the resistance measurement as a function of changing angle.

Also, to test for continuity in a deposited thin film, the AC setup above is used. The current source used has an indicator that indicate the continuity of the thin film or proper contact of the four probes producing a reasonable resistance measurement. This indicator blinks when the film is discontinuous as it produces a high resistance reading ($>$10 kΩ).

3.9 Summary

This chapter began with a description of the sample preparation and fabrication techniques using sputter deposition. It progressed into x-ray structural characterisation techniques of XRR and XRD. Magnetic measurements with MOKE was covered along with the related optical phenomenon due to reflection, transmission and scattering of light beam from magnetic material. Other magnetic measurement techniques of SQUID magnetometry, PNR and XRMR were also discussed with their associated theories. A brief description of the experimental setup specific to the systems used in taking measurements here was provided to aid in understanding of the results shown in the later chapters.

References

[1] A. T. Hindmarch, *Spin Transport in Rare-earth Magnetic Heterostructures*. PhD thesis, University of Leeds, 2003.

[2] S. Swann, "Magnetron sputtering," *Physics in Technology*, vol. 19, no. 2, p. 67, 1988.

[3] D. Magnfält, *Fundamental Processes in Thin Film Growth: The Origin of Compressive Stress and the Dynamics of the Early Growth Stages*. PhD thesis, Linköping University Electronic Press, 2014.

[4] F. M. Penning, "Die Glimmentladung bei niedrigem Druck zwischen koaxialen Zylindern in einem axialen Magnetfeld," *Physica*, vol. 3, no. 9, pp. 873–894, 1936.

[5] M. D. Ltd, "Mantis product specifications for the Qprep500 sputtering system." `http://www.mantisdeposition.com/systems/view/product/info/qprep-series.html`, accessed: 2017-08-03.

[6] N. Chowdhury and S. Bedanta, "Controlling the anisotropy and domain structure with oblique deposition and substrate rotation," *AIP Advances*, vol. 4, no. 2, p. 027104, 2014.

[7] W. C. Röntgen, "On a new kind of rays," *Science*, pp. 227–231, 1896.

[8] J. Als-Nielsen and D. McMorrow, *Elements of Modern X-ray Physics*. John Wiley & Sons, 2011.

[9] L. Bogart, *An Investigation of the Structure, Pinning and Magnetoresistance of Domain Walls in $Ni_{81}Fe_{19}$ Planar Nanowires*. PhD thesis, Durham University, 2010.

[10] M. Yasaka, "X-ray thin-film measurement techniques," *The Rigaku Journal*, vol. 26, no. 2, 2010.

[11] D. Eastwood, *Grazing Incidence X-ray Scattering from Magnetic Thin Films and Nanostructures*. PhD thesis, Durham University, 2009.

[12] J. Nielsen and D. McMorrow, *Elements of Modern X-ray Physics*. New York: John Wiley & Sons Ltd, 2nd ed., 2011.

[13] L. G. Parratt, "Surface studies of solids by total reflection of X-rays," *Physical Review*, vol. 95, no. 2, p. 359, 1954.

[14] H. Kiessig, "Untersuchungen zur totalreflexion von röntgenstrahlen," *Annalen der Physik*, vol. 402, no. 6, pp. 715–768, 1931.

[15] D. Ellison, "D1 system: Installation, operation and maintenance manual," Bede x-ray metrology, 2004.

[16] T. Lafford, M. Wormington, K. Matney, D. Jacques, R. Bytheway, Q. Bo, F. Hofmann, and R. Truseell, "Bede x-ray application manual," Bede x-ray metrology, 2008.

[17] S. Cockerton and B. Tanner, "A new high dynamic range x-ray detector," *Advances in X-ray Analysis*, vol. 38, pp. 371–376, 1995.

[18] M. Björck and G. Andersson, "GenX: an extensible X-ray reflectivity refinement program utilizing differential evolution," *Journal of Applied Crystallography*, vol. 40, no. 6, pp. 1174–1178, 2007.

[19] W. L. Bragg, "The structure of some crystals as indicated by their diffraction of x-rays," *Proceedings of the Royal Society of London A: Mathematical, Physical and Engineering Sciences*, vol. 89, no. 610, pp. 248–277, 1913.

[20] M. Laue, "Eine quantitative Prüfung der Theorie für die Interferenzerscheinungen bei Röntgenstrahlen," *Annalen der Physik*, vol. 346, no. 10, pp. 989–1002, 1913.

[21] R. Coperation, "SmartLab Guidance reference manual," `http://static.mcpc.sustc.edu.cn/upload/files/20161114/ce35deb4b440b9e853abbcfd12dc1126.pdf`, accessed 2018-03-14.

[22] M. Faraday, "On the Magnetization of Light and the Illumination of Magnetic Lines of Force," *Philosophical Transactions of the Royal Society of London*, vol. 136, pp. 1–20, 1846.

[23] J. Kerr, "XLIII. On rotation of the plane of polarization by reflection from the pole of a magnet," *The London, Edinburgh, and Dublin Philosophical Magazine and Journal of Science*, vol. 3, no. 19, pp. 321–343, 1877.

[24] J. Bland, M. Padgett, R. Butcher, and N. Bett, "An intensity-stabilised He-Ne laser for measuring small magneto-optic Kerr rotations from thin ferromagnetic films," *Journal of Physics E: Scientific Instruments*, vol. 22, no. 5, p. 308, 1989.

[25] M. Ali, *Growth and Study of Magnetostrictive FeSiBC Thin Films for Device Applications*. PhD thesis, Sheffield University, 1999.

[26] J. Zak, E. Moog, C. Liu, and S. Bader, "Fundamental magneto-optics," *Journal of Applied Physics*, vol. 68, no. 8, pp. 4203–4207, 1990.

[27] G. Daalderop, F. Mueller, R. Albers, and A. Boring, "Theory of the magneto-optic kerr-effect in NiUSn," *Journal of Magnetism and Magnetic Materials*, vol. 74, no. 2, pp. 211–218, 1988.

[28] P. N. Argyres, "Theory of the Faraday and Kerr effects in ferromagnetics," *Physical Review*, vol. 97, no. 2, p. 334, 1955.

[29] H. Ebert, "Magneto-optical effects in transition metal systems," *Reports on Progress in Physics*, vol. 59, no. 12, p. 1665, 1996.

[30] M. N. Deeter and D. Sarid, "Magnetooptical characterization of multilayers by incident-angle analysis," *IEEE Transactions on Magnetics*, vol. 24, no. 6, pp. 2470–2472, 1988.

[31] B. D. Josephson, "Possible new effects in superconductive tunnelling," *Physics Letters*, vol. 1, no. 7, pp. 251–253, 1962.

[32] P. W. Anderson and J. Rowell, "Probable observation of the Josephson superconducting tunneling effect," *Physical Review Letters*, vol. 10, no. 6, p. 230, 1963.

[33] G. Aviv, "SQUIDs - Superconducting Quantum Interference Devices," in *Experimental Physics Course Report, Department of Physics, Ben-Gurion University of the Negev, Israel*, 2008.

[34] M. McElfresh, "Fundamentals of magnetism and magnetic measurements featuring quantum designs magnetic property measurement system," *Quantum Design*, vol. 11578, p. 132, 1994.

[35] "Magnetic property measurement system hardware reference manual." `http://mmrc.caltech.edu/MPMS/Manuals/QD%20HWD%20Ref.pdf`. Accessed: 2017-07-13.

[36] M. Tokaç, *Investigation of Interfacial Effects in Ferromagnetic Thin Films*. PhD thesis, Durham University, 2016.

[37] R. C. Black and F. C. Wellstood, "Measurements of magnetism and magnetic properties of matter," in *The SQUID Handbook: Applications of SQUIDs and SQUID Systems, Volume II*, ch. 12, pp. 391–440, Wiley-Blackwell, 2006.

[38] J. Chadwick, "Possible existence of a neutron," *Nature*, vol. 129, no. 3252, p. 312, 1932.

[39] B. N. Brockhouse and C. G. Shull, "The Nobel Prize in Physics in 1994," *Solid State Communications*, vol. 93, no. 6, p. 471, 1995.

[40] R. Nathans, C. Shull, G. Shirane, and A. Andresen, "The use of polarized neutrons in determining the magnetic scattering by iron and nickel," *Journal of Physics and Chemistry of Solids*, vol. 10, no. 2-3, pp. 138–146, 1959.

[41] S. Bennington, A. Hannon, S. Rogers, R. Smith, C. Wilson, S. Parker, C. Frost, C. Kinane, W. Skoda, and S. Langridge, "Introduction to Reflectivity," in *ISIS Neutron Training Course* (C, C. Kinane, W. Skoda, and S. Langridge, eds.), Springer New York, 2015.

[42] J. Penfold and R. Thomas, "The application of the specular reflection of neutrons to the study of surfaces and interfaces," *Journal of Physics: Condensed Matter*, vol. 2, no. 6, p. 1369, 1990.

[43] G. L. Squires, *Introduction to the Theory of Thermal Neutron Scattering*. Cambridge University Press, 3rd ed., 2012.

[44] S. Blundell and J. Bland, "Polarized neutron reflection as a probe of magnetic films and multilayers," *Physical Review B*, vol. 46, no. 6, p. 3391, 1992.

[45] C. J. Kinane, *The Interplay of Magnetism and Structure in Patterned Multilayer Thin Films*. PhD thesis, University of Leeds, 2008.

[46] M. Fitzsimmons and C. Majkrzak, "Application of polarized neutron reflectometry to studies of artificially structured magnetic materials," in *Modern Techniques for Characterizing Magnetic Materials*, pp. 107–155, Springer US: Boston, MA, 2005.

[47] C. Majkrzak, "Polarized neutron reflectometry," *Physica B: Condensed Matter*, vol. 173, no. 1-2, pp. 75–88, 1991.

[48] J. Goff, J. Bland, S. Langridge, and R. Dalgliesh, "Polref science case," `https://www.isis.stfc.ac.uk/Pages/polref-science-case.pdf`, ISISTGT2/SAC/02/P4_1, accessed: 2018-03-24.

[49] D. Gibbs, D. Harshman, E. Isaacs, D. McWhan, D. Mills, and C. Vettier, "Polarization and resonance properties of magnetic x-ray scattering in holmium," *Physical Review Letters*, vol. 61, no. 10, p. 1241, 1988.

[50] R. A. Ewings, *Neutron and X-ray Scattering Studies of Strongly Correlated Electron Systems*. PhD thesis, University of Oxford, 2008.

[51] G. Schütz, W. Wagner, W. Wilhelm, P. Kienle, R. Zeller, R. Frahm, and G. Materlik, "Absorption of circularly polarized x rays in iron," *Physical Review Letters*, vol. 58, no. 7, p. 737, 1987.

[52] S. Macke and E. Goering, "Magnetic reflectometry of heterostructures," *Journal of Physics: Condensed Matter*, vol. 26, no. 36, p. 363201, 2014.

[53] T. I. Hyde, P. W. Ash, D. A. Boyd, G. Randlshofer, K. Rothenbacher, and G. Sankar, "X-Ray Absorption SpectroscopicStudies of Platinum Speciation in Fresh and Road Aged Light-Duty Diesel Vehicle Emission Control Catalysts," *Platinum Metals Review*, vol. 55, no. 4, pp. 233–245, 2011.

[54] S. Brown, L. Bouchenoire, P. Thompson, R. Springell, A. Mirone, W. Stirling, A. Beesley, M. Thomas, R. Ward, M. Wells, *et al.*, "Profile of the U 5f magnetization in U/Fe multilayers," *Physical Review B*, vol. 77, no. 1, p. 014427, 2008.

[55] S. Brown, L. Bouchenoire, D. Bowyer, J. Kervin, D. Laundy, M. Longfield, D. Mannix, D. Paul, A. Stunault, P. Thompson, *et al.*, "The XMaS beamline at ESRF: instrumental developments and high-resolution diffraction studies," *Journal of Synchrotron Radiation*, vol. 8, no. 6, pp. 1172–1181, 2001.

Chapter 4

Data fitting procedure for PNR and XRMR scatttering in thin films

4.1 Introduction

GenX simulation software is designed with a differential evolution algorithm and is used in the analysis of experimental data from scattering techniques. Knowledge of information from sample parameters, such as thickness, roughness, density and relative amplitude of magnetic moment in a sample can be extracted from the best fitting simulations of the experimental data. GenX has been noted as flexible and extendable software which allows simulation of arbitrary number of datasets simultaneously and permits a fast implementation of new ideas. The software is free for users to download [1].

Although GenX has been used in the refinement of data from several scattering techniques, here specific focus is given to polarised neutron reflectivity (PNR) and x-ray resonant magnetic reflectivity (XRMR) data refinement. The refinement process involves optimising a model to fit it to the experimental data. The optimisation of the model to the data is not trivial because of the large number of local mimima [2]. Since data simulation uses a Gaussian function to describe the finite resolution of the instrument, beam footprint correction and over-illumination at small angle [3, 4], the most recommended measure of the goodness of the fits (figure of merit) is the χ^2 function, which was not the case in this work. Therefore a figure of merit was employed in this

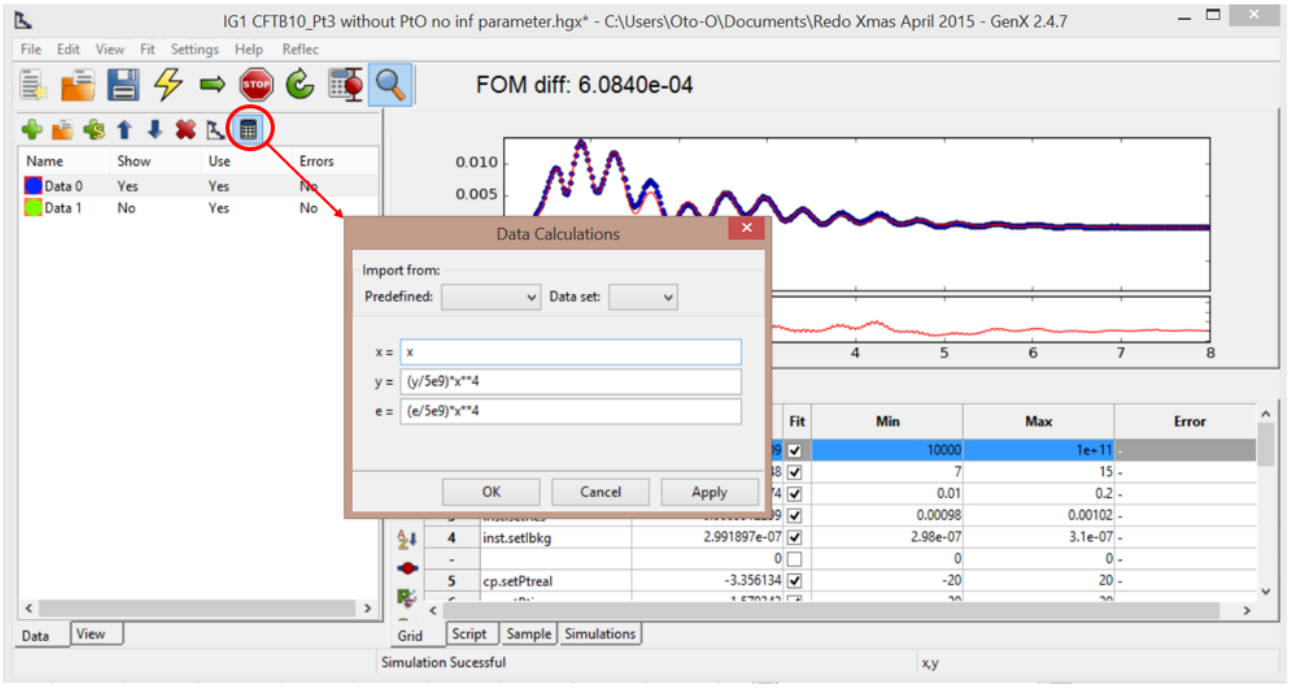

Figure 4.1: The data calculations menu in GenX software used in rescaling reflectivity data.

work. Steps for proper definition of simulation parameters, model, and possible procedures for tuning these parameters are discussed. Furthermore, a description of the procedure undertaken to ensure the suitability of model, determining the right number of fitting parameters to use and magnetic moment calculations for PNR simulation are also highlighted.

4.2 Scaling of experimental data for the fitting and statistical analysis

The refinement process begins with a choice of simulation model which depends on the experimental technique and the complexity of the problem to be solved. The recommended model for PNR is the `spec_nx` while that of XRMR is `mag_refl` [5]. The next step is the importation of experimental data. Since the magnitudes of the experimental data are unequal with some negative values, it is necessary to scale the reflectivity and spin asymmetry (SA) data to an order of 1 throughout the entire Q-range before simulations. Appropriate scaling of the data also influences the choice of which goodness of fit function (discussed later) to apply. The scaled

reflectivity data (Y) is defined by the equation

$$Y = y \times x^4 \times \mathrm{D} \tag{4.2.1}$$

where y is the intensity of the reflectivity data obtained from experiment, x is the scattering vector and D the scaling factor. The scattering vector is raised to the fourth power reflecting the Q^{-4} decay of the reflectivity profile. D is an arbitrary number which is typically very large for PNR and small for XRMR depending on their reflectivity intensity. This scaling can either be done externally before importing the dataset or by using the data calculation menu on the GenX software (see figure 4.1). On the data calculation menu, equation 4.2.1 for Y and an appropriate error calculation e are inserted. Therefore, for proper scaling reflectivity data (Y), Y is imported into the software or y imported if the calculation menu is used. The same procedure was done for both PNR and XRMR.

The spin asymmetry data, which includes some negative values can also be scaled if the figure of merit (FOM) function employed cannot accept negative values. In the PNR simulation, the SA data was scaled by adding 2 to the experimental value in order to ensure that all values are positive while that of the XRMR was not scaled at all.

4.3 Determination of the goodness of fit

The deviation of the simulated data to the experimental data is measured through a fitness criterion called the figure of merit (FOM). Ihringer *et al.* define a FOM as the quantitative measure of the conformity of the data and their weights to the simulation independent of the number of degrees of freedom [6]. In some FOM, the errors in the data are considered in the quantification of the goodness of fit giving a weighted fit. A simulation step with a lower FOM from the previous one indicates an improvement in the simulation. Comparison of the value of FOM for the different models employed in the simulation helps in the choice of the best model that captures the features of the data and best describes the sample investigated. More on the best fit model will be discussed later in the chapter but first different FOM used in the PNR

and XRMR simulations are discussed in subsequent sections.

4.3.1 Polarised neutron reflectivity

In all PNR simulations, both `logR1` and `chi2bar` (χ^2) functions were employed as FOM functions for analysis and comparison of fits. Given that all experimental data were collected up to higher scattering vector than most reported work on PNR, the `logR1` function was used in the simulation due to the wide variation in the count rate and the size of the error-bars. This was because it allows the proper simulation of data at higher scattering vector (low intensity, large error bars) providing equal weighting of the reflectivity intensity at higher and lower scattering vectors. This gives the dataset equal weighting when plotted on a log-scale. The `logR1` function is described by

$$\mathrm{FOM}_{\mathrm{logR1}} = \frac{\sum_i \left(\left| \log_{10}\sqrt{Y_i} - \log_{10}\sqrt{S_i} \right| \right)}{\sum_{\mathrm{i}} \log_{10}\sqrt{Y_i}} \tag{4.3.1}$$

where Y_i and S_i represents the experimental and simulated dataset respectively and i indicates individual elements of the dataset. After the best fit is obtained, the simulation optimisation is changed to χ^2 to extract the χ^2 optimisation value which is used to compare simulations (see figure 4.2). The χ^2 optimisation function is represented by

$$\mathrm{FOM}_{\mathrm{chi2bar}} = \frac{1}{\mathrm{N} - p} \times \sum_{\mathrm{i}} \left(\frac{Y_i - S_i}{E_i} \right)^2 \tag{4.3.2}$$

where N is the total number of data, p is the number of fitting parameters and E is the uncertainty in the experimental data. Although the χ^2 function is recommended as the most appropriate optimisation function, as it considers the uncertainty in the data, this was not the case here as measurements were taken up to a high Q-value of ~ 0.25 Å^{-1}. The χ^2 function is limited as it provides a good simulation only at low angles Q < 0.005 Å^{-1}, neglecting the higher angle data where the error-bars are large. Therefore, `logR1` was used in the simulation and the corresponding χ^2 value was used for comparison of fits. The χ^2 values from the fits were comparable and low (< 12) for room temperature PNR simulation and (< 1.2) for low temperature simulations discussed in chapter 5 and 7 respectively. Here, it was only possible to

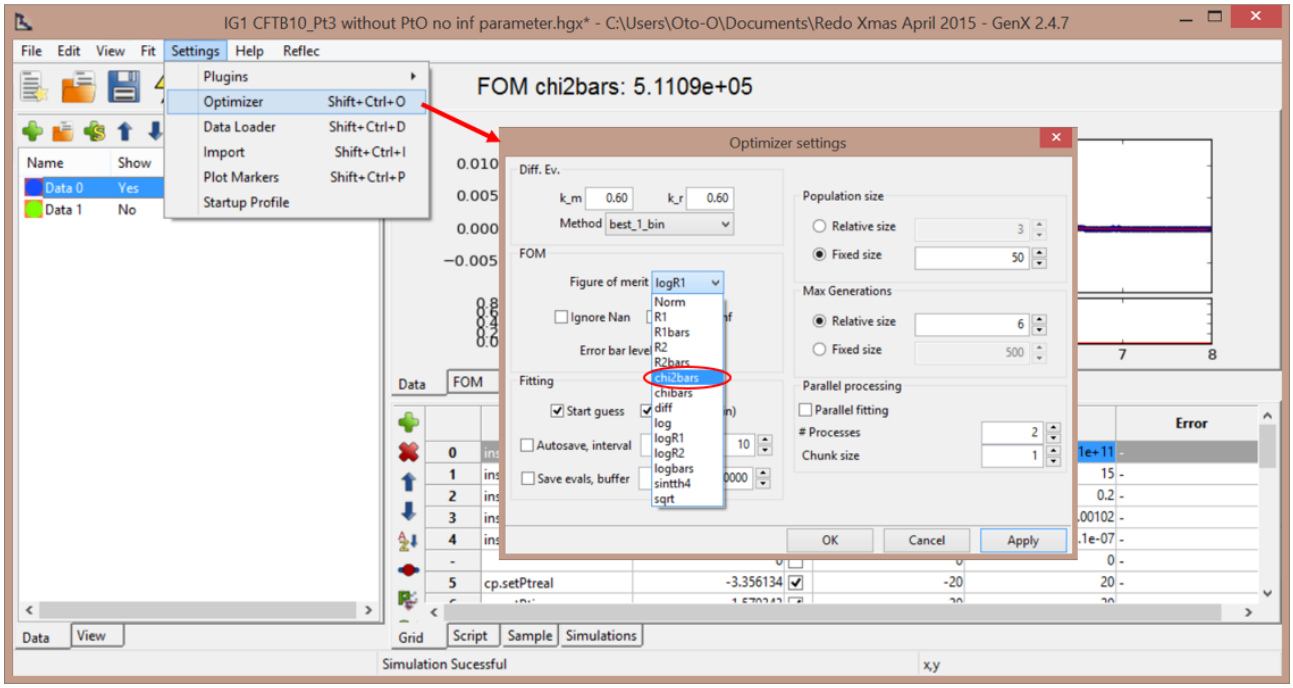

Figure 4.2: A screen shot of the optimisation FOM functions in GenX software.

use these FOM because the data values were all positive numbers after scaling.

4.3.2 X-ray resonance magnetic reflectivity

The XRMR simulation made use of the `diff` function described by

$$\mathrm{FOM}_{\mathrm{diff}} = \frac{1}{\mathrm{N} - p} \times \sum_{i} |\, Y_i - S_i|. \tag{4.3.3}$$

The $\mathrm{FOM}_{\mathrm{diff}}$ was used because it allows simulation of data even when some of the data values are negative numbers. It represents the average of the absolute difference between the simulated, S and experimental, Y, data. This function was chosen as it is robust enough to capture the variations and nature of data. It does not include error-bars.

4.4 Building the sample structure

The sample structure is built using the sample tab (labeled (d) on figure 4.3) on GenX software where the layers and the stacks of the sample are defined. The layers are expected to be in a stack. The stack is added by pressing the plus button labeled (c) on figure 4.3. Similarly the

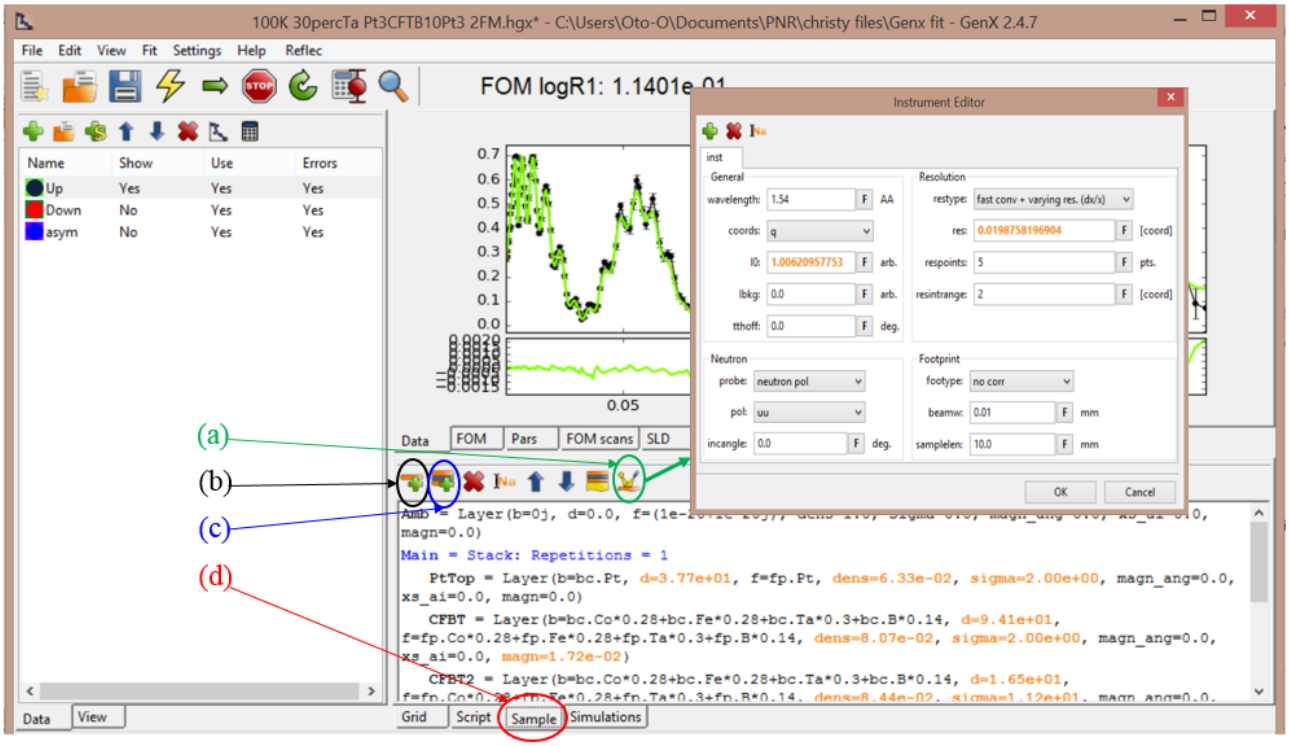

Figure 4.3: A screen shot of the sample tab and instrument editor in GenX software showing how to create sample layers that best describes the sample structure as labelled (a) instrument editor, (b) sample layer addition tab (c) sample stack addition tab and (d) sample tab.

layers are added by pressing the plus button (b) on figure 4.3. The name of each layer is unique and can be renamed. Each of the sample layer characteristics is defined by double clicking on the added layer which opens up a layer editor dialog where the layer thickness, roughness, number density and magnetic moment is defined. The number density can be calculated following the instruction on the GenX on-line tutorials [7] (http://genx.sourceforge.net/doc/faq.html) by the expression:

$$\mathrm{Dens(units/\AA^3)} = \frac{\mathrm{Dens(kg/m^3)}}{1.66 \times 10^3 \times \mathrm{u_{scatt}}} \tag{4.4.1}$$

where Dens are the densities in specified units and $\mathrm{u_{scatt}}$ is the molecular weight of the layer. The stack with different layers or a combination of many stacks with different layers makes up the sample model. The layer editor for the PNR and XRMR simulation is display in figure 4.4 as different parameters that defines the instrument and sample are required.

In neutron scattering refinement, the layer editor is divided into the standard and the neutron column. The layer elements composition (f), density ($dens$), thickness (d) and roughness ($sigma$)

on the standard column while the magnetic moment (*magn*) is defined on the neutron column as shown in figure 4.4a. The scattering length density (SLD) factor on the standard column is defined as *fp.(element component)* while that on the neutron column is defined as *bc.(element component)*. Here, the SLD is defined by element composition as GenX has a database of all scattering length density factors.

In the magnetic x-ray scattering layer editor, more parameters are defined, as shown in figure 4.4b. The layer editor is divided into four sections: scattering length (*Scatt. len.*), miscellaneous (*Misc.*), magnetism (*Magnetism*) and interfacial magnetic moment (*Interf. Mag. Mom.*). The scattering length section defines the structural SLD factor defined by the element composition of the layer (f), which describes the non-resonant x-ray scattering length, the resonant scattering length of the resonant species of atom, which in this case is Pt (fr), the magnetic scattering length related to circular dichoric effect (*fm1*) and magnetic scattering length related to linear dichroic effect (*fm2*). These scattering factors describes the refractive index of the medium the x-ray travels through as discussed in chapter 3. More on the definition of the scattering length factors in the simulation tab is discussed in section 4.5.

The *Misc.* section defines the layer roughness (*sigma_c*), density (*dens*), relative density of the resonant species (*resdens=1*) and thickness (d) of the layer while the *Magnetism* section defines the bulk magnetic moment in the layer.

The interfacial magnetic moment section is used to define the magnetism at the interface described as an exponential decay with Gaussian roughness around the interface with amplitude (*dmag*), exponential decay length (dd) and magnetic roughness (*sigma_m*). The upper interface is represented as *_u* while the lower interface as *_l*. In order for the Pt moment to be at the same interface point, the interfacial magnetic roughness and the width are set at zero for the temperature dependent XRMR simulation discussed in chapter 7.

The total magnetic moment is calculated as $mag * (1 + dmag\_u)$ where *mag* is the magnetic moment per formula unit. Therefore, in order to extract the actual *dmag* value in the simulation, the *mag* must be made to be significantly small while *dmag* is made to be large. This help reduce the possibility of introducing magnetic artefacts into the fitting algorithm.

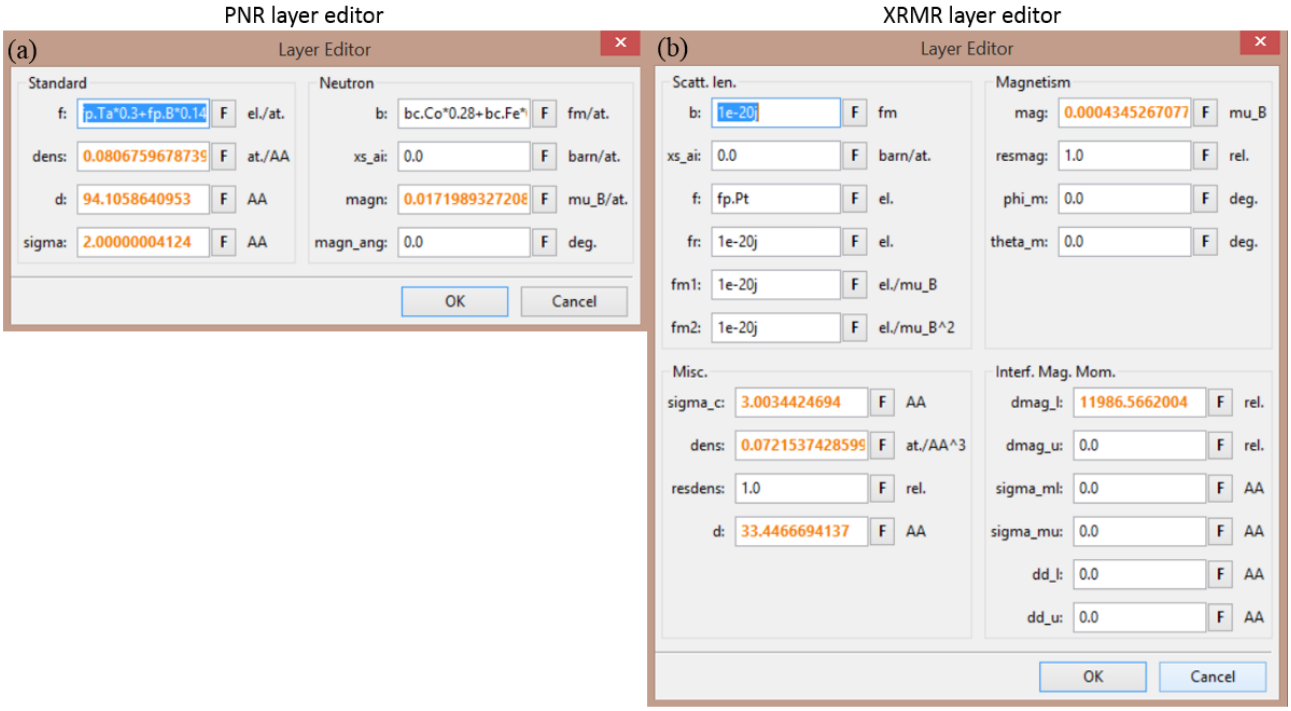

Figure 4.4: A screen shot of the layer editor in GenX software where the layer parameters are set-up. (a) The polarized neutron reflectivity layer editor (b) The x-ray resonance magnetic reflectivity layer editor.

4.4.1 Definition of instrument object

Within the sample tab is the instrument editor (labeled (a) in figure 4.3) where the instrument objects such as wavelength, incident intensity (*IO*), resolution (*res*), beam-width, sample length, probing ray, polarisation and unit of coordinate are defined. The resolution used for the PNR fit is the "*full convolution, varying resolution*" which allows each data point to have a different resolution during the fit while "*fast convolution*" is used in XRMR. The number of simulations (points to include in the resolution calculations) for each individual point is defined using "*respoint*".

4.5 Definition of simulation parameters in the simulation editor

In order to setup the simulator, commands to be conducted before the simulated data are calculated are set in the simulation tab. Different commands that describe the simulated data

are defined by adding the object and parameters which describe the characteristic nature of the data. Commands which define whether it is a specular reflectivity or spin asymmetry data and their polarisation are also added. These commands are added by pressing the green plus sign (red circled in figure 4.5) which brings-up a dialog box (parameter editor). In the parameter editor the object and parameter are chosen from a drop-down menu while the "expression" column is typed sandwiched by an inverted comma ('). Note, the chosen object, parameter and expression can only be updated when the yellow simulation button (blue circle in figure 4.5) is pressed. The definition of the simulation parameters in XRMR is slightly tricky as it involves the description of parameters that fully captures the interfacial polarisation of Pt atoms around the interface. The specifics in the creation of the simulation functions for the PNR and XRMR are presented in the sections below.

4.5.1 Polarised neutron reflectivity

In the PNR simulations three datasets are loaded which are the spin-up and spin-down reflectivity and spin asymmetry (SA) data. Therefore three datasets are seen on the simulation tab (indicated by the red arrows in figure 4.5). The simulation parameters for each of these datasets are added by clicking on the + sign on the simulation editor. When clicked, the parameter editor pops up where the instrument polarisation (setpol) is set to *'uu'* for spin-up reflectivity, *'dd'* for spin-down reflectivity and *'ass'* for SA data.

The simulation tab dynamically generates a script which can be manually edited in the script tab. Therefore, the simulated data set is scaled in the script tab by manually editing the python code that describes the data. This is done in a similar way to the experimental data by applying equation 4.2.1 to the reflectivity data. This is expressed by the python code I[−1]∗ = (data[0].$\boldsymbol{x}$ ∗ ∗4) ∗ (1e8/4) where `data[0]` represents the simulated data points y and D = 10^8/4. The SA is expressed as I[−1]+ = 2, meaning that the value 2 is added to simulated data values in order to ensure that the all SA data values are above zero. This allows the use of `logR1` or χ^2 FOM function in the simulation. Here, the only parameter defined in the simulations editor is the incident neutron polarisation of each data set, which is not the case in

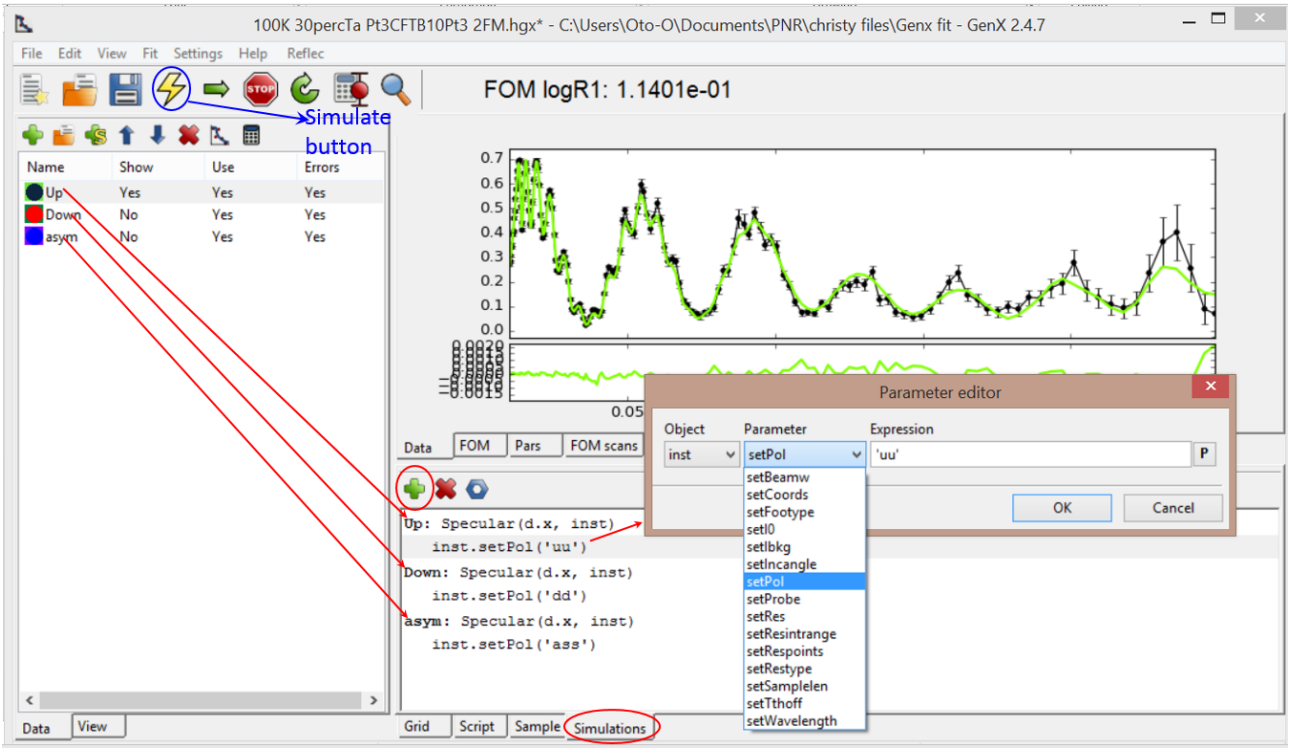

Figure 4.5: A screen shot of the simulation tab in GenX showing the configuration of the parameter editor to define the instrument polarisation for each datasets.

the XRMR discussed in the next section.

4.5.2 X-ray resonant magnetic reflectivity

Here two datasets (*Data 0* and *Data 1*) are loaded and so two datasets are seen on the simulation tab which represent the reflectivity and the SA data respectively. The instrument and sample description of each dataset is configured with the simulation tab. Similar to the PNR, the x-ray beam polarisation (*Xpol)* for both datasets is added first. The polarisation for *Data 0* is set as *'tot'* since it is specular x-ray reflectivity data while *Data 1* is set as *'ass'* as it is the SA data.

Next, is the definition of the custom variables using the blue nut shaped button (circled in the figure 4.6) where the initial values of real and imaginary magnetic and structural scattering factors of the resonance species (Pt) are defined. When clicked the *custom parameter editor* dialog box pops up. The parameter defined are "*Ptreal, 0*", "*Ptimag, 0*", "*Ptmagreal, 0*", "*Ptmagimag, 0*", "*PtTop_Phi, 0*" and "*PtBuf_phi, 0*" which represent the real and imaginary contribution of the charge scattering length factor of Pt, real and imaginary magnetic scattering

factor of Pt and the in-plane angle of the magnetic moment relative to the direction of incident x-ray for top Pt and buffer Pt respectively. These are used to define the respective resonant and non-resonant scattering factors of each dataset.

Recall from chapter 3, the refractive index for resonant magnetic scattering is expressed by [8]

$$\mathrm{n}^{\pm} = 1 - \delta^{\pm} + \mathrm{i}\beta^{\pm} \tag{4.5.1}$$

where

$$\delta^{\pm} = \left(\frac{2\pi \mathrm{n_0 r_e}}{\mathrm{k}^2}\right)\left(\mathrm{f_0} + \mathrm{f_c'(E)} \mp \mathrm{f_m'(E)}\cos\theta\cos\phi\right) \tag{4.5.2}$$

and

$$\beta^{\pm} = \left(\frac{2\pi \mathrm{n_0 r_e}}{\mathrm{k}^2}\right)\left(\mathrm{f_c''(E)} \mp \mathrm{f_m''(E)}\cos\theta\cos\phi\right). \tag{4.5.3}$$

The dispersion term $\delta^{\pm}((\mathrm{f_0} + \mathrm{f_c'}), \mathrm{f_m'})$ represents the real-part contributions from Thomson charge scattering factor $\mathrm{f_0}$, resonant charge scattering factor $\mathrm{f_c'}$ and resonant magnetic scattering factor $\mathrm{f_m'}$ that are represented as (f), (Fr) and (Fm) respectively in the simulation tab. Also, the absorption term $\beta^{\pm}(\mathrm{f_c''}, \mathrm{f_m''})$ represents the imaginary-part contributions from resonant charge scattering factor $\mathrm{f_c''}$ and resonant magnetic scattering factor $\mathrm{f_m''}$, represented as (Fr) and (Fm) in the simulation tab. The $+$ and $-$ represent the right and left circular polarisation or positive and negative magnetic field respectively [9]. Since *Data 0* is the specular reflectivity dataset, there is no magnetism. Therefore, the real and imaginary component of *Fm1* for the top and buffer Pt layer is defined to be zero while *Frreal* and *Frimag* are configured to extract their values from the custom parameter *Ptreal* and *Ptimag* respectively. This describes the structural profile of the Pt layer. It is important to note that the same scattering factors are used for the top and buffer Pt because the same Pt species is at both layers, as here the technique is only sensitive to Pt. The SA data, *Data 1*, is configure by setting the magnetic resonant scattering length factor *Fm* to be extracted from *Ptmagreal* and *Ptmagimag* and is defined for both the top and buffer Pt layer. Also, the top and buffer Pt magnetic moments are set to be distinctively estimated using the "*getmag*" command for the top and buffer Pt layer. The in-plane angle of magnetic moment relative to the incident x-ray beam is also defined. This angle maybe different

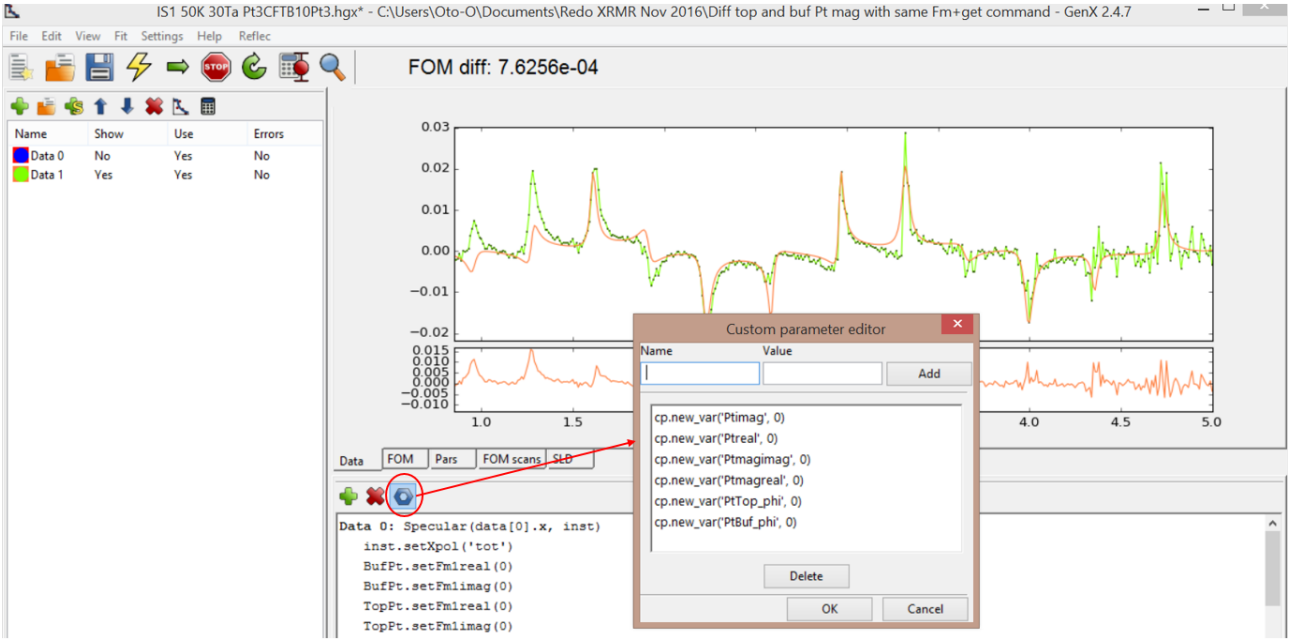

Figure 4.6: A screen shot of the custom parameter in the simulation tab where the scattering factors of the resonant species are defined.

for the top and buffer Pt layer in a trilayered Pt/CoFeTaB/Pt sample. Therefore it is uniquely defined for each layer. An example for the buffer Pt layer is configured by setting the *object* as '*BufPt*', *parameter* as '*SetPhi_m*' and the *expression* as '*180 if cp.getPtBuf_Phi()<=0 else 0* which specifies that the Pt moment is either parallel or antiparallel to the beam direction.

After the *simulation tab* is set, the parameters are automatically upload into the script. The simulation dataset are now scaled by manually editing *Data 0* using equation 4.2.1 by the code `I[-1]*=(data[0].x**4)/5e9` where $D = 1/(5 * 10^9)$. The SA data was not scaled as FOM_{diff} was used as the FOM and it allows simulation of negative values without error.

Finally, the instrument and layer parameters such as thickness, roughness, density and magnetic moment are uploaded on the *grid tab* as instructed on the GenX online tutorial [7]. The upper and lower limit (priors) of each parameter are adjusted before pressing the simulation button. The fitting parameter convergence is monitored from the FOM tab and the fit is judged to be physically realistic and good. If the fit is not good enough, the parameters are tuned by manually adjusting the priors on the *grid tab*. A better fit than the previous will have a lower FOM value.

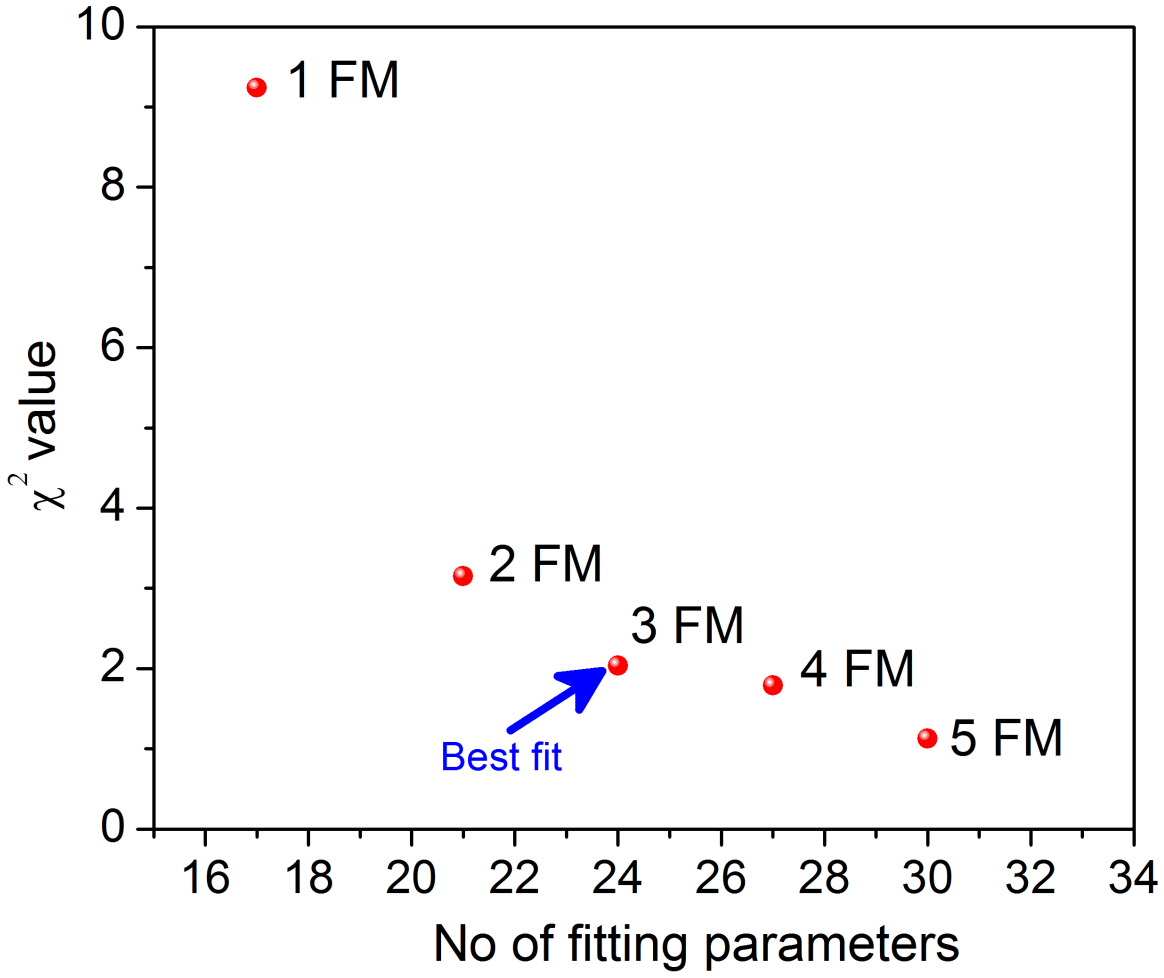

Figure 4.7: A plot of the reduced χ^2 FOM value against the number of fitting parameters for a Pt(3nm)/CFTB(10nm)/Pt(3nm) sample showing an initial significant improvement in fit with increased number of parameters which becomes insignificant after the number of parameters is 24. FM represents the CFTB layer.

4.6 Indicators to the best fitting parameter and model

A best fit in GenX is considered as the model that best fits the experimental data with the least number of parameters. In order to monitor the progress of the fit after the parameters are converged, comparison of the FOM values for different models are evaluated. An increase in the number of parameters has been reported to make the refinement algorithm aggressive and robust thereby improving the fit [2]. However, a plot of the FOM value against the number of parameters (see figure 4.7) indicates an initial improvement which stops at a certain number of parameters. At this point there is no significant improvement on the fit even when more parameters are added. Increased number of parameters was achieved in this instance by subdividing the FM layer into sub-layers for the PNR measurements.

The next indicator is the consideration of whether the model is physically realistic. According to the plot in figure 4.7, the model with three FM layer and 24 fitting parameters was obtained as the best and structurally realistic fit for a trilayered Pt/CFTB/Pt sample. This model is realistic because it can capture possible differences in the interfacial magnetic effect which might be different from the bulk (center) of the FM layer as discussed in chapter 7.

4.7 Extraction of magnetic moment from the scattering length profile for PNR fits

GenX software works out the structural and magnetic scattering length density profile. This is represented graphically in the *SLD tab*. The real and the imaginary part of the SLD profile relative to the depth of the sample is represented. These profiles can be exported using the *Export SLD...* : a drop-down menu in *Reflec tab*. In PNR, the exported SLD is in $Å^{-2}$ units, therefore the magnetic moment of the sample needs to be calculated in more conventional units. The neutron magnetic scattering length is expressed by the equation [10]

$$\rho_m = \sum_i^J N_i p_i = C \sum_i^J N_i \mu_i = C' M_v = -\frac{m_n}{2\pi\hbar^2}\mu_n \sum_i^J m_i \tag{4.7.1}$$

where J is the number of distinct isotopes, N_i the number density for the ith species and p_i is the scattering length of the ith species, $C = 2.645 \times 10^{-5}$Åμ_B for the magnetic moment per formula unit, μ_i, expressed in units of μ_B, $C' = 2.9109 \times 10^{-5}/4\pi$Å^{-2}T^{-1} when the volume magnetization density, M_v = magnetic moment/volume, is in Tesla or $C' = 2.853 \times 10^{-9}$Å^{-2}cm^3/emu when in emu/cm^3, m_n is the mass of neutron, μ_n is the magnetic moment of the neutron and m_i is the intensity of magnetisation in emu. With equation 4.7.1, the magnetisation of the sample can be estimated from the exported SLD values from GenX. The exported simulated and experimental datasets are rescaled back to original experimental dataset format using equation 4.2.1.

References

[1] "Instructions for GenX download." `https://sites.google.com/site/genxprog/downloads`. Accessed: 2018-03-08.

[2] M. Björck, "Fitting with differential evolution: an introduction and evaluation," *Journal of Applied Crystallography*, vol. 44, no. 6, pp. 1198–1204, 2011.

[3] M. Björck and G. Andersson, "GenX: an extensible X-ray reflectivity refinement program utilizing differential evolution," *Journal of Applied Crystallography*, vol. 40, no. 6, pp. 1174–1178, 2007.

[4] A. Gibaud, G. Vignaud, and S. Sinha, "The correction of geometrical factors in the analysis of x-ray reflectivity," *Acta Crystallographica Section A: Foundations of Crystallography*, vol. 49, no. 4, pp. 642–648, 1993.

[5] M. Björck, *A Structural Viewpoint of Magnetism in Fe and Co Based Superlattices*. PhD thesis, Acta Universitatis Upsaliensis, 2007.

[6] J. Ihringer, "A quantitative measure for the goodness of fit in profile refinements with more than 20 degrees of freedom," *Journal of Applied Crystallography*, vol. 28, no. 5, pp. 618–619, 1995.

[7] "GenX online tutorial." `http://genx.sourceforge.net/doc/tutorials/xrr_fitting.html`. Accessed: 2018-03-06.

[8] R. Springell, S. Langridge, A. Wildes, S. B. Wilkins, C. Sanchez-Hanke, K. T. Moore, M. T. Butterfield, J. Chivall, R. C. C. Ward, M. R. Wells, and G. H. Lander, "Chemical and magnetic structure of uranium/gadolinium multilayers studied by transmission electron microscopy, neutron scattering, and x-ray reflectivity," *Phys. Rev. B*, vol. 81, p. 134434, Apr 2010.

[9] S. Brown, L. Bouchenoire, P. Thompson, R. Springell, A. Mirone, W. Stirling, A. Beesley,

M. Thomas, R. Ward, M. Wells, *et al.*, "Profile of the U 5f magnetization in U/Fe multilayers," *Physical Review B*, vol. 77, no. 1, p. 014427, 2008.

[10] M. Fitzsimmons and C. Majkrzak, "Application of polarized neutron reflectometry to studies of artificially structured magnetic materials," in *Modern Techniques for Characterizing Magnetic Materials*, pp. 107–155, Springer US: Boston, MA, 2005.

Chapter 5

Investigation of asymmetry and magnetic proximity effect at Pt−CoFeTaB interfaces

5.1 Introduction

Spin-orbit coupling gives rise to several spin related phenomena and interactions that have contributed immensely to spintronic and spin caloritronic effect, and provide an effective mechanism for the manipulation of magnetisation. Most recently, spin-orbit coupling has been linked to effects related to spin current generation and detection at FM/NM interfaces such as spin pumping [1–3], SHE [4–6], SMR [7–10], longitudinal spin Seebeck effect (LSSE), interfacial Rashba effect [11] and interfacial DMI [12, 13]. These interfacial effects are significantly modified depending on the structural and magnetic properties of the FM and NM on an atomic scale at the interface making experimental interpretation challenging. In these experiments, nonmagnetic materials, particularly metals with large spin-orbit coupling such as Pt [14], Pd [15], Au [16], $\beta-$phase Ta [17] and W[18] are used. Of particular interest here is Pt which is the material investigated in this thesis for proximity induced magnetisation (PIM). The NM material because of its proximity with the FM material may exhibit PIM where there is a magnetisation and spin polarisation induced in the normally NM material by the adjacent FM. In spin current generation

experiments, PIM is considered to be the cause of contamination of pure spin current generated at the FM/NM interface, leading to an argument that SMR is associated with PIM in Pt [19] rather than being directly related to the SHE [20] close to the interface. A significant reduction in SHE signal in the presence of PIM has been observed [21]. In order to fully understand the spin dynamics at the interface, a detailed investigation of PIM in FM/NM interface is necessary.

PIM has been predicted to be associated with an increase in lattice constant which narrows the energy band thereby increasing the DOS near the Fermi level [22, 23]. PIM has been observed in both metal-metal [24–27] and metal-insulator interfaces [28, 29]. Most investigations have been made using the x-ray magnetic circular dichroism (XMCD) technique, which is element sensitive. XMCD measurements show a strong dependence on film thickness in that it is surface sensitive and averages over the photoelectron escape depth from the sample rather than providing a true depth sensitivity. Also, the sum rule used to extract data may lead to large uncertainties in that the region of polarisation is small relative to the entire thickness of the sample [30]. XMCD provides an average NM proximity induced magnetic moment in the material, hence a depth sensitive technique which can provide detailed depth-resolved information close to the interface is required. XRMR is employed for that reason.

This chapter begins with a brief description of the samples studied and the structural characterisation of these samples. The chapter progresses into magnetic investigations with MOKE and PNR. Finally, PIM investigations with XRMR technique at FM/NM and NM/FM interfaces conducted at the Pt L_3 absorption energy edge are reported in order to understand non-equivalent spin transport properties experienced at these interfaces. Studies have shown that spin-orbit interaction and DMI do not cancel out in symmetric NM/FM/NM system indicating a possible difference in the structural or magnetic properties at the interface which can affect spintronic device engineering [25, 31]. Results of the inequivalent spin transport properties in this chapter will be used in discussion of transport properties in chapter 7.

5.2 Structural sample description and analysis

The materials used for the investigation are Pt as the NM material and CoFeTaB (CFTB) alloy as the FM, structured as bilayer and trilayered samples. Sputter deposited samples of Pt(3nm)/CFTB(t_{CFTB}), CFTB(t_{CFTB})/Pt(3nm) and Pt(3nm)/CFTB(t_{CFTB})/Pt(3nm) on Si/SiO_2 substrates of size 10 mm × 10 mm were used for the XRR and XRD measurements. Various CFTB thicknesses (t_{CFTB}) of 3, 6 and 10 nm were made to check for the thickness dependence of the structural and magnetic properties of the samples. CFTB was deposited by DC magnetron sputtering, while the Pt layer was deposited with RF magnetron sputtering from a base pressure of 10^{-8} Torr. Pt deposition procedure is discussed in chapter 6.

Similar samples of size 30 mm×30 mm were simultaneously deposited for magnetic characterisation with PNR and XRMR techniques. These samples were used first for PNR measurements where the large surface area is needed to increase the quality of the signal as well as the signal to noise ratio. These samples were later cut to 10 mm×10 mm for XRMR. This was to ensure that the same sample was used for both measurements so that the results would be directly comparable.

This section begins with a description of the relevance of each compositional element in the alloyed CFTB, which is the ferromagnetic material under investigation in this thesis. Structural analysis of sputter deposited bilayer and trilayer Pt-CFTB samples using XRR and XRD technique is also presented.

5.2.1 CoFeTaB

CoFe alloy is observed to exhibit a BCC crystal structure with a cubic magnetocrystalline anisotropy, but when alloyed with B of composition greater than 10 % it produces an amorphous metallic glass with a reduced critical temperature, T_C, and reduced magnetisation [32, 33]. An Fe-based alloy when doped with a transition metal such as Ta (in our case) reduces the T_C and the magnetic moment per Fe atom as long as the Fe-based alloy is amorphous [34–36] otherwise it phase-separates into different crystalline regions with higher T_C. This explains why the B is used to keep the alloy amorphous. Therefore, the alloy CFTB of the composition

$Co_{32}Fe_{32}Ta_{20}B_{16}$ is an amorphous ferromagnetic material which is magnetic at room temperature. The CFTB used in this chapter is a room temperature ferromagnet CFTB with T_C slightly above room temperature which was proven by the evidence of magnetic signal with MOKE at room temperature. The T_C of alloyed CFTB is tunable depending on the percentage of Ta. A different CFTB of composition $Co_{28}Fe_{28}Ta_{30}B_{14}$ was used in the temperature dependent measurements presented in chapter 7, where a reduced T_C below room temperature was required.

5.2.2 Analysis by x-ray reflectivity

Grazing incidence XRR was performed with the Bede D1 reflectometer as described in chapter 3 on three series of samples made up of Pt deposited as buffer and capping layer of an amorphous CFTB of variable thickness, t, grown on Si/SiO_2 substrate. The sample series were Pt(3nm)/CFTB(tnm), CFTB(tnm)/Pt(3nm) and Pt(3nm)/CFTB(tnm)/Pt(3nm) which enables characterisation of the physical structure of each interface.

Reflectivity simulations were made with the GenX software, which uses the Parratt recursive formalism and approach as described in chapters 3 and 4. The simulation model consists of the individual deposited layers, SiO_2 isolation layer and the Si substrate. Each layer thickness was initialised to a nominal thickness value estimated from the quartz crystal monitor used during sputter deposition of each layer. The sample parameters were allowed to vary within a range of 10 % of the nominal values. The limit of the ranges of each parameter are later adjusted depending on the closeness of the optimum value to the limits. Structural information such as the layer thickness, t, and roughness at the interface, σ, were extracted from the best fit simulations of the shape and distribution of the Kiessig fringes as shown in figure 5.1. The Kiessig fringes are representations of the scattered x-rays from interference between the refracted waves at the interfaces. Individual film thickness can be roughly estimated from:

$$t = \frac{2\pi}{\Delta Q} \tag{5.2.1}$$

as indicated in figure 5.1a and c. The Pt thickness cannot be visually estimated in figure 5.1b because scattering process is more complex as there is scattering from two Pt layers which may

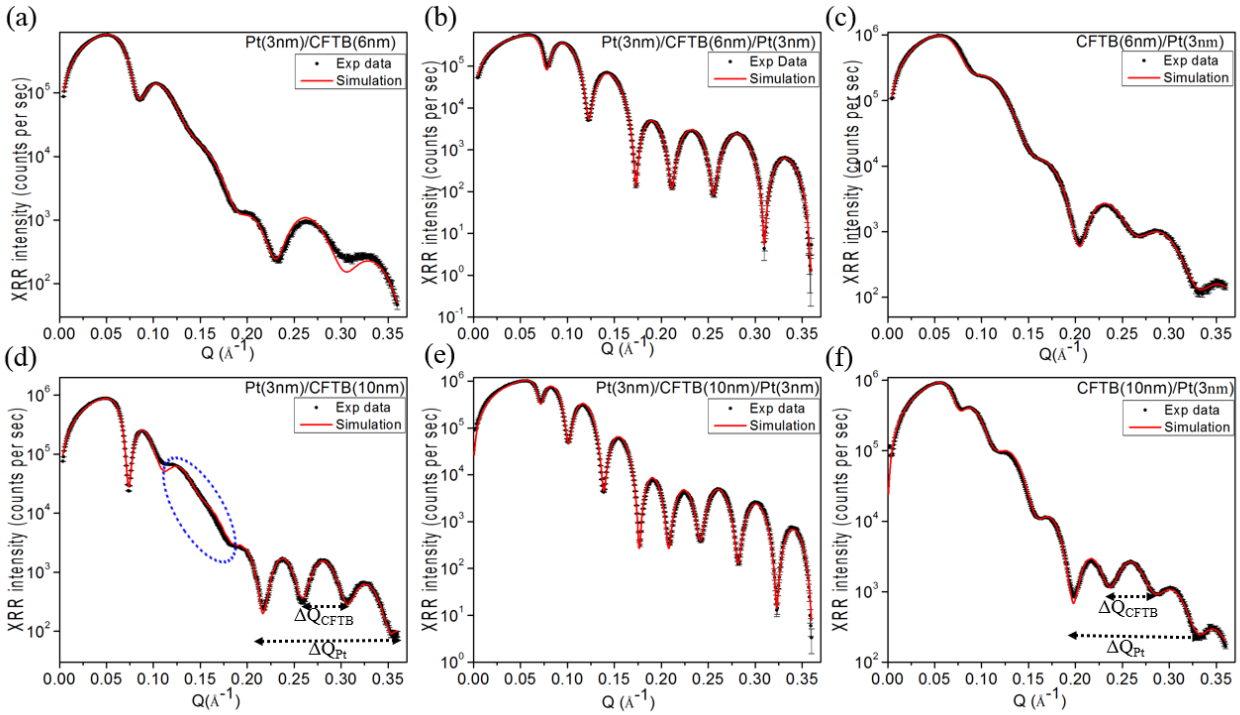

Figure 5.1: Best fit simulation of XRR measurement for Pt and CFTB bilayered and trilayered samples (as labeled) grown on Si/SiO_2 substrate using GenX simulation [37]. The numbers in brackets are the nominal thicknesses of the samples and the blue circle region indicate area where the simulated fit is poor.

also interfere in a more complex way making the identification of this layers more difficult. The periodicity of the each fringe is approximately equal to the CFTB layer thickness. Looking at figure 5.1a, c, d and f, the oscillations due to CFTB layer thickness are superimposed on weaker oscillations of larger periodicity caused by the thin Pt layer thickness. The ratio of CFTB to Pt layer thickness can be estimated using this simple approach to be 1:2 for the CFTB(6nm) series and 1:3 for the CFTB(10nm) series in good agreement with the nominal layer thicknesses.

Although the nominal layer thickness parameter is used through out this thesis to label the samples, the actual structural parameters are captured in this case in table 5.1. For a good fit to be obtained with the bilayered samples, an oxide layer was included in the model at the top of the sample stack to simulate the surface oxidation and any oxidation induced roughness. The effect of the oxide layer was significant in the bilayers but did not affect the trilayer sample simulations. Consequently, the trilayered series were fit without the native oxide layer. The native oxide layer for Pt/CFTB series was CoFeTaO with equal percentages of components as

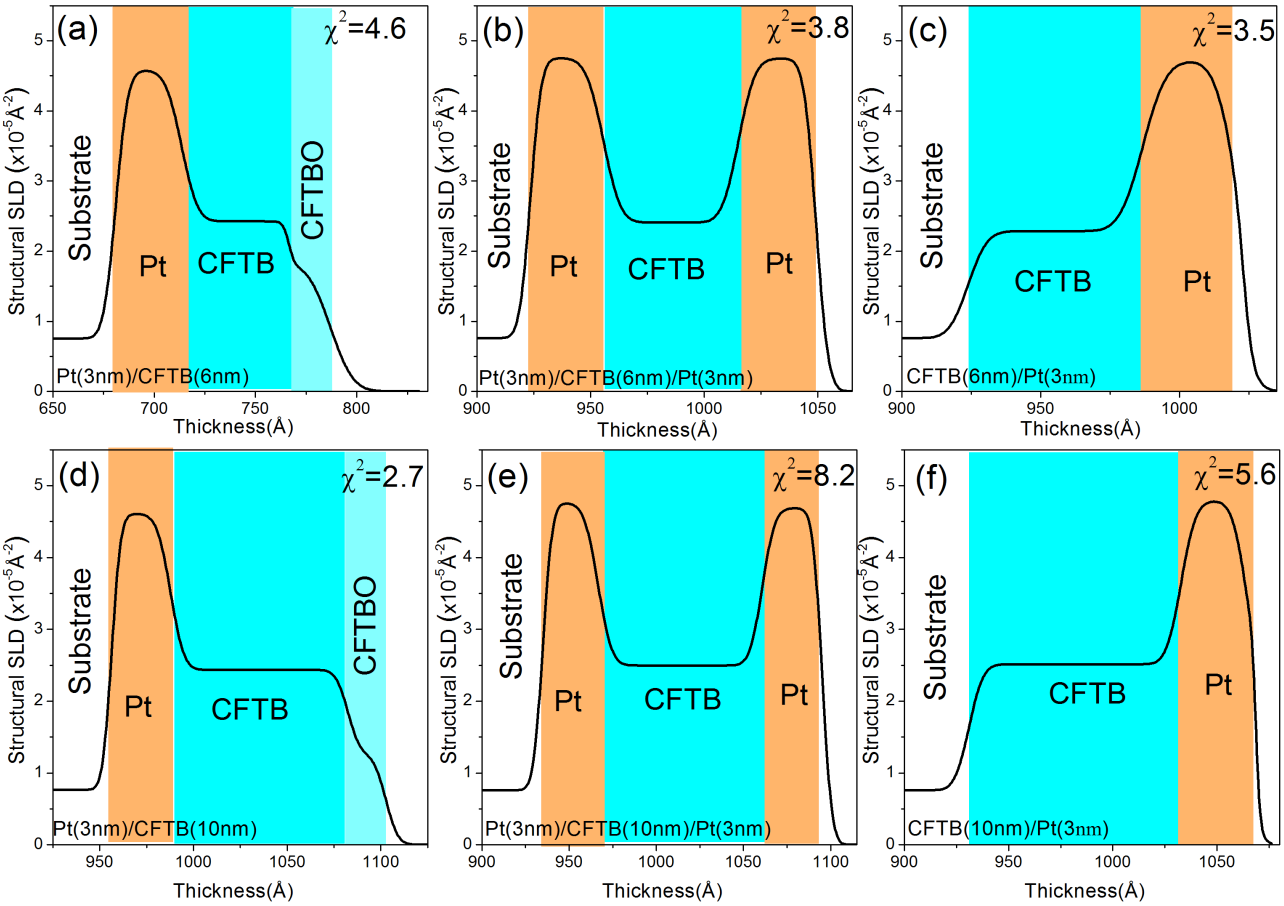

Figure 5.2: Extracted structural scattering length profile from the beat fit simulation of XRR measurement for Pt and CFTB bilayered and trilayered samples (as labeled) grown on Si/SiO_2 substrate using GenX simulation. The numbers in brackets are the nominal thicknesses of the samples.

Table 5.1: Sample parameters from the best fit XRR with the reduce χ^2 values indicated on the scattering length profile shown in figure 5.2.

Sample	Layer	Thickness (nm)	Roughness (nm)	Number Density(atoms $Å^{-3}$)
Pt(3nm)/CFTB(6nm)	Oxide layer	2.1 ± 0.3	0.9 ± 0.4	0.014 ± 0.006
	CFTB	5.3 ± 0.4	0.2 ± 0.1	0.081 ± 0.003
	Pt	3.2 ± 0.2	0.6 ± 0.1	0.062 ± 0.002
Pt(3nm)/CFTB(10nm)	Oxide layer	2.0 ± 0.5	0.5 ± 0.6	0.011 ± 0.002
	CFTB	9.5 ± 0.5	0.5 ± 0.6	0.081 ± 0.003
	Pt	3.1 ± 0.4	0.6 ± 0.3	0.063 ± 0.005
CFTB(6nm)/Pt(3nm)	Oxide layer	0.4 ± 0.3	0.2 ± 0.1	0.020 ± 0.006
	Pt	3.3 ± 0.3	0.6 ± 0.3	0.064 ± 0.001
	CFTB	6.3 ± 0.8	0.5 ± 0.3	0.082 ± 0.003
CFTB(10nm)/Pt(3nm)	Oxide layer	0.5 ± 0.3	0.2 ± 0.1	0.028 ± 0.008
	Pt	3.1 ± 0.2	0.5 ± 0.6	0.065 ± 0.001
	CFTB	10.2 ± 0.4	0.6 ± 0.2	0.084 ± 0.003
Pt(3nm)/CFTB(6nm)/Pt(3nm)	Top Pt	3.4 ± 0.2	0.4 ± 0.2	0.065 ± 0.001
	CFTB	6.0 ± 0.2	0.6 ± 0.3	0.080 ± 0.003
	Buffer Pt	3.2 ± 0.2	0.6 ± 0.3	0.065 ± 0.003
Pt(3nm)/CFTB(10nm)/Pt(3nm)	Top Pt	3.4 ± 0.4	0.4 ± 0.3	0.064 ± 0.002
	CFTB	9.4 ± 0.3	0.6 ± 0.4	0.083 ± 0.006
	Buffer Pt	3.2 ± 0.6	0.6 ± 0.5	0.065 ± 0.004

other oxide compositions such as CoO, FeO, Fe_3O_4, Ta_2O_5 and TaO_2 resulted in a significantly worse fit. Even including this simple oxide layer it is not possible to perfectly simulate the data as highlighted in the dotted region in figure 5.1d. The data may be better described by a more complex model, for example of the surface oxide, but we have no strong justification for including such additional complications. The thickness of the native oxide layer was about 2 nm for all CFTB thicknesses which corresponds to a typical native oxide thickness for oxidised Fe, Co or Ta layers (see figure 5.2a and d). The interface roughness of this oxide layer is about 1 nm. In the CFTB/Pt series, the oxide layer that provides the best fit with the least χ^2 value was PtO_2 with thickness less than 0.5nm in all samples in the series. The oxide layer was within the error limits with roughness within the least possible value. This implies that the surface oxide blends in with the roughness within the error limit. This may well be just an interfacial contamination rather than a true chemical oxidation of Pt.

The density of the oxide layer is significantly less than the density of the bulk of the capped material. In addition, the assumption of an alloyed layer between the Pt and CFTB did not improve the fitting accuracy of the reflectivity profile. Generally, the interface roughness is approximately less than $0.5 - 0.6$ nm in all sample series, which is due to the consistent growth that gives good quality interface formation between CFTB and Pt by sputtering and a constant roughness of the substrate.

The structural SLD profiles on figure 5.2 showed significant consistency between the upper and buffer Pt in both trilayered and bilayered samples which indicates that the interfaces are symmetric. Evidence of intermixing is inconclusive as the x-ray scattering length in XRR varies monotonically and the difference between roughness and intermixing are indistinguishable in specular reflectivity. Evidence of magnetic asymmetry in the Co/Pt and Co/Pd interfaces has been observed [25, 31] with little measurable difference in the interfacial roughness. Therefore, more investigations are required. Further structural investigation using XRD is discussed in the next section.

5.2.3 Analysis by x-ray diffraction

Looking at the SLD profiles of the XRR parameters in the previous section, there is no significant asymmetry between CFTB/Pt and Pt/CFTB interfaces. The densities and interface width from table 5.1 are symmetric. The XRR fits are not sufficient to give atomic scale structure information of the samples, but rather provides an average property. To investigate whether the structures are symmetric on an atomic scale XRD is employed.

X-ray diffraction profiles were obtained with a Rigaku x-ray kit using Cu Kα radiator. The diffraction pattern identifies the films as an amorphous CFTB with a crystalline faced centered cubic (FCC) Pt texture (see figure 5.3). Pt has successfully grown with FCC crystal structure on CFTB which is conspicuous in the XRD profile of Pt capped sample including the trilayered samples but not on SiO_2. Looking at figure 5.3, it is noticeable that it takes a few nm to gain this FCC texture. This is because the (111) crystallographic plane of a FCC unit cell of Pt film has the lowest surface energy. During deposition, the adatoms on arrival to the substrate are able to migrate longer to find the lowest energy surface because the vacuum conditions during deposition was good. The FCC metal deposited on amorphous substrate tend to form secondary grain growth that leads to the development of strong (111) fiber texture which explains the strong Pt (111) texture in the Pt capped and trilayered samples [38]. This suggests that the preferred orientation of Pt film was determined by the seed layer.

The (111) texture was easily formed on the amorphous CFTB, but difficult on the Si/SiO_2 (see figure 5.4) due to higher lattice mismatch with SiO_2 in comparison to CFTB. Although both seed layers are amorphous and the expected texture of an FCC metal on amorphous substrate is usually a strong (111) texture but it is different in Pt/CFTB series [38]. The difference in these substrates is that SiO_2 is an amorphous oxide while CFTB is an amorphous metal. It has also been reported that the oxygen fraction during deposition of Pt on SiO_2 can lead to a random orientation of Pt texture as the Pt layer is susceptible to amorphisation [39, 40]. Therefore it might be that the poor texture observed in Pt/CFTB series might be related to the oxide fraction in the substrate.

In addition, the XRD plots show asymmetry in the diffraction peaks for Pt/CFTB and

CFTB/Pt samples. It is important to note that all the sharp peaks corresponds to diffraction peak of the Si/SiO_2 substrate (see Fig 5.3 inset). Also, no trace of alloying of composite materials was detected in the diffraction peaks in that most obvious effect of alloying is represented with peak overlap or peak broadening with a change of lattice parameter. In this case, the peak overlap and broadening at 38.4 ° and 39.7 ° are the Si (111) and the Pt (111) peaks. There is no significant shift in the lattice parameter as shown in figure 5.3 in all the samples. Hence the conclusion that there is no alloy present. The lattice parameter estimated from the XRD Pt(111) peak gives a value of 0.392 Å, similar to the value of 0.391 Å obtained for bulk materials. There is a possible element of strain of 0.3% evidence in the sample by comparing the variation of the lattice parameter of the Pt layer in comparison to bulk material.

Pt (111) and (222) peaks were the dominant peaks with line broadening at 39.7 ° and 85.7 ° respectively which increases in intensity with CFTB thickness for the Pt capped and trilayered samples as shown in figure 5.4 b and c but with no significant thickness dependence for the Pt buffer samples (see figure 5.4a). When the CFTB thickness increases, the crystal quality of Pt grown on top of it improves. The Pt capped samples showed a decrease in full width at half maximum (FWHM) of the Pt (111) peak with increasing CFTB thickness, indicating an increase in crystallite size with CFTB thickness, but it is constant and significantly smaller for Pt/CFTB series. Consequently the crystal grain sizes for the Pt/CFTB series were not estimated. The trilayered peaks reveals that the broadening of Pt (111) peak is the sum of Pt/CFTB and CFTB/Pt broadening which shows thickness dependent probably due to the thickness dependence of the CFTB/Pt interface. Line broadening can be attributed to strain or crystallite grain size. In this case the impact of strain or disorder is not considered on the line broadening but rather assumed that the line broadening is due to grain size. This is due to the fact that the Scherrer equation is applied in the estimation of the crystalline grain size which ignores the strain contribution in the broadening. In order to estimate the strain effect along with the crystallite grain size, the Williamson-Hall Plot can be use [41]. The Scherrer equation [42] used here is described by

$$\mathrm{D} = \frac{\mathrm{K}\lambda}{\beta \cos\theta} \tag{5.2.2}$$

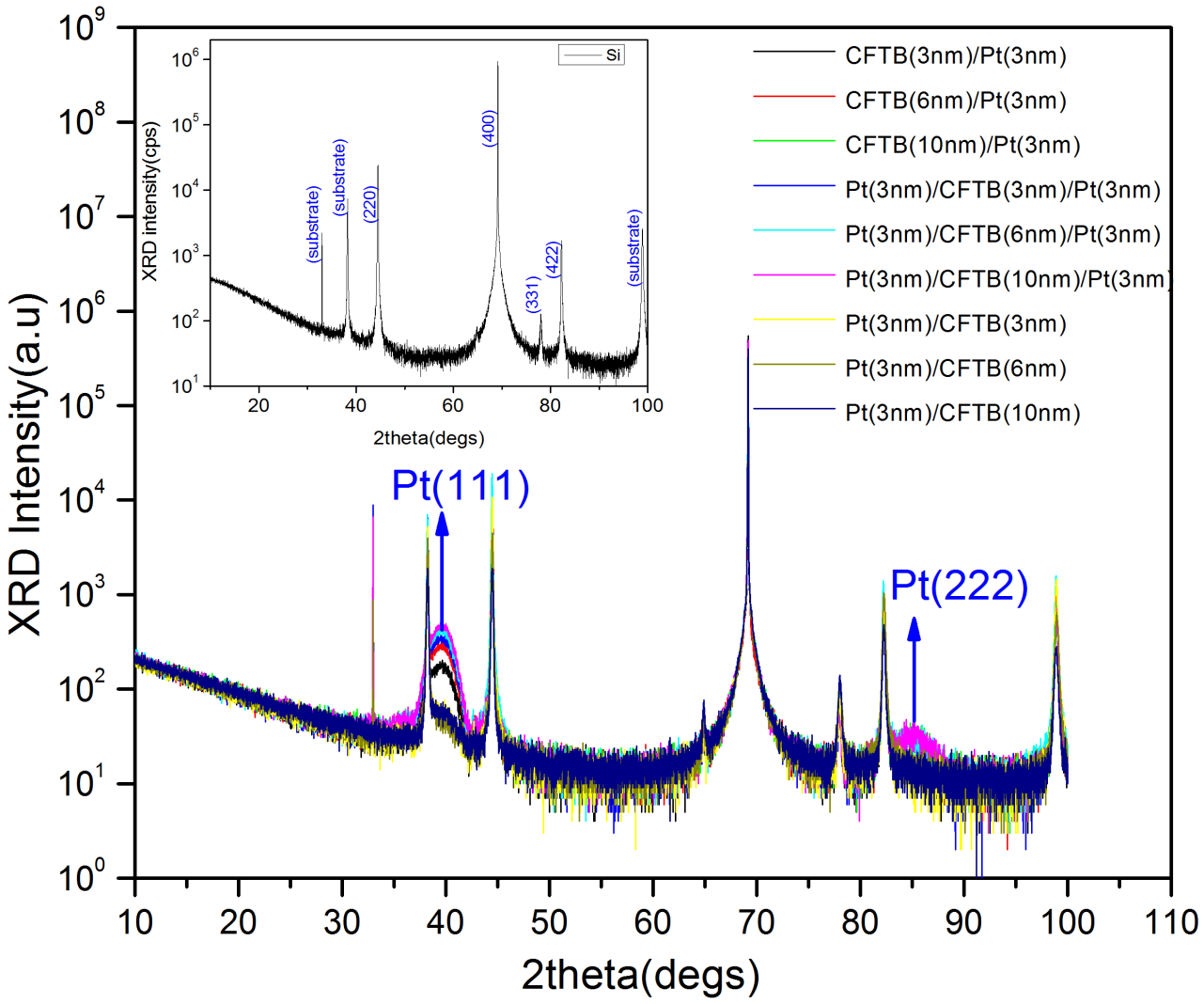

Figure 5.3: X-ray diffraction plots of Pt/CFTB, Pt/CFTB/Pt, CFTB/Pt samples and Si/SiO_2 (inset) substrate showing the Pt (111), (222) and Si/SiO_2 diffraction peaks.

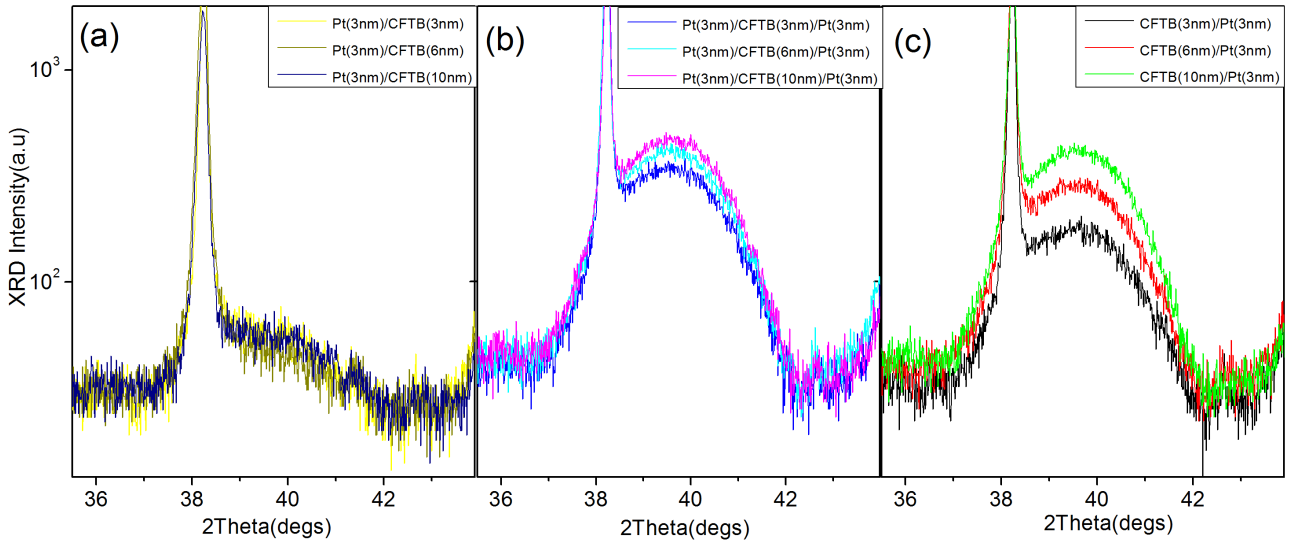

Figure 5.4: Zoomed XRD peaks between 35.5- 43.9 ° showing the overlapped Si(111) and Pt (111) peaks and line broadening for (a) Pt/CFTB (b) Pt/CFTB/Pt (c) CFTB/Pt sample series with no significant shift in lattice parameter.

Table 5.2: XRD crystal grain size estimated from the Pt (111) peak with the actual range of Pt XRR thickness for the CFTB/Pt and Pt/CFTB/Pt samples.

Crystalline grain size					
CFTB (nominal) thickness(nm)	CFTB/Pt series		Pt/CFTB/Pt series		
	Grain size(nm)	Pt thickness(nm)	Grain size(nm)	Pt cap thickness(nm)	Pt buffer thickness(nm)
3	2.8 ± 0.10	3.1 ± 0.2	2.89 ± 0.08	3.5 ± 0.2	3.2 ± 0.4
6	2.87 ± 0.08	3.3 ± 0.3	2.90 ± 0.07	3.4 ± 0.2	3.2 ± 0.2
10	3.10 ± 0.05	3.1 ± 0.2	3.06 ± 0.05	3.4 ± 0.4	3.2 ± 0.6

where D is the crystallite size, K is the crystallite shape factor which is approximately 0.9, λ is the wavelength of the radiation, β is the full width at half maximum (FWHM) of x-ray diffraction peak (in radians) and θ, the Bragg angle. The constant K describes the crystal geometry and is approximated as 0.9 for a spherical crystal [42]. The FWHM was extracted by deconvolution of the overlapped Si (111) peak and Pt(111) peak diffraction peaks. An estimate of the crystallite size using Equation 5.2.2 above is summarized in table 5.2.

According to table 5.2, a lower grain size was estimated for CFTB (3nm) sample which slightly increases with CFTB thickness. The observed lower grain size at lower thickness might be due to a strong interaction between the CFTB and Pt atoms which constrains mobility of the adatom around the interface that weakens as CFTB thickness increases.

The result reveals that the Pt texture improves with increasing CFTB thickness for all Pt capped samples including the trilayer. The crystal grain size is approximately equal to the overall Pt thickness which varies between 3.1 - 3.5 nm, meaning that the increase of CFTB thickness provides a smoother surface for better Pt growth in the CFTB/Pt and Pt/CFTB/Pt sample series. Also Pt as a heavier element deposited on CFTB may alter the layer texture, crystal orientation, stress or roughness at the interface. This increase in crystallite size due to grain growth would possibly influence the structural and magnetic scattering length density of the sample. This shows that there is a significant but subtle structural asymmetry. The Pt capping layers are fully FCC (111) textured, whereas the seed layer may possibly be amorphous at the start and perhaps only begins to become FCC (111) very close to the interface with CFTB.

5.3 Magnetic characterisation and analysis

The magnetic characterisation of the Pt/CFTB, Pt/CFTB/Pt and CFTB/Pt sample series is investigated in this section. The samples used in the structural investigations were simultaneously deposited with the PNR sample and the MOKE samples, but the MOKE samples were deposited on a separate piece. Two methods of investigation are reported in this section which both probe the total magnetisation in the material. Longitudinal MOKE was used to understand the in-plane anisotropy and the magnetisation reversal of these samples. In addition, PNR was used along with the known structural properties of the sample to provide magnetic depth profile of the ferromagnetic layers within the samples.

5.3.1 Magneto-optical analysis by longitudinal MOKE

Longitudinal MOKE magnetometry measurement were conducted with a laser beam of wavelength 658 nm and spot size of 7 μm at the sample. The samples for the measurement were grown with a 5 mm $\times$ 5 mm mask. MOKE hysteresis measurements at successive angles to the in-plane magnetic field of 45° from the starting point reveals isotropic magnetic behaviour within the film for all samples in the series including the plain CFTB sample. This is expected for an

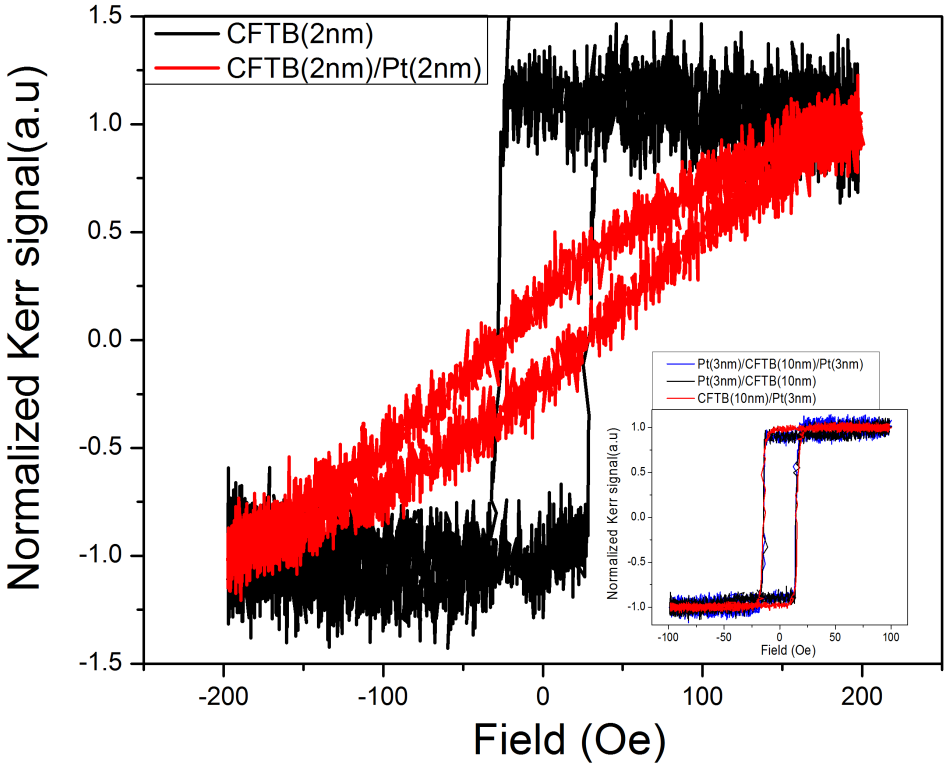

Figure 5.5: Normalised longitudinal MOKE hysteresis loop showing that Pt deposition on CFTB modifies the magnetic reversal of the sample. The inset shows equal coercive field for all sample series and the offset is due to an instrumental effect.

amorphous film because there is no crystalline directionality imposed. When Pt is deposited on CFTB, there is an abrupt switch in magnetisation compared to plain CFTB deposited on Si/SiO_2 substrate as shown in figure 5.5. This difference may likely be due to domain wall (DW) formation where the rapid reversal in the CFTB/Pt may be single nucleation and rapid wall propagation. Once the DW is nucleated, it immediately propagate through the sample. The gradual reversal in the plain CFTB sample indicates that DW is pinned and can only move slowly between the pinning site. This reduction in surface DW pinning may be from the Pt. The coercive field, H_c, obtained from the same sweep-rate for all sample series are equal and is independent of CFTB thickness. In general, the average H_c in all films is < 30 Oe, as shown in the inset of figure 5.5 and the observed offsets are artifact from the instrument.

Based on the observed H_c for all sample series, the in-plane magnetic field applied during the PNR and XRMR measurement was > 50 Oe to properly saturate the magnetisation in the samples. The PNR and the XRMR analysis are discussed in subsequent sections.

5.3.2 Interfacial studies by polarised neutron reflectivity

Several studies have demonstrated the depth dependent changes in the in-plane sample magnetisation with the polarised neutron reflectivity (PNR) technique. Interfacial magnetic investigation of an exchange bias system showed a changed in the magnetisation at the Fe_3O_4/NiO (FM/antiferromagnet) interface [43]. Other investigations in FM/semiconductor [44] and FM/NM [45] structures have observed changes in the magnetic depth profile at the interface giving an indication of the feasibility of PNR for the study of proximity magnetisation effect at the interface. Therefore, initial investigations into PIM and the magnetic asymmetry at different interfaces began with the PNR technique.

The PNR measurements were performed on the Polref beamline at the ISIS neutron source at Rutherford Appleton Laboratory, where a collimated beam of polarised neutrons at grazing incidence is employed in the magnetic depth characterisation. Measurements were performed on the three sample series defined earlier. Polarised neutron reflected intensity was measured as a function of the incident neutron wave vector Q normal to the sample surface as described in section 3.6. A large in-plane magnetic field of about 150 Oe was applied with a magnetic yoke in order to magnetically saturate the sample during measurement. The corresponding reflectivity of the neutrons from the change of refractive index for spin-up R^+ (spin polarised parallel to direction of sample magnetisation) and spin down R^- (spin polarisation anti-parallel to sample magnetisation) were collected. PNR measurements were conducted over a large Q range in order to capture features such as intermixing and alloying at the interfaces in the films. This is not common in most PNR measurements as it requires a large sample area to enhance the signal to noise at high Q, which explains why a sample of 30 mm×30 mm was used for the measurement.

The reflectivity data for both spin states were simultaneously fitted with the GenX code. In the simulation, the FM layer of the sample was divided into N slabs of constant scattering length density b_{tot}. Using Parratt's recursion algorithm, the thickness, density, interface roughness and magnetic moment varies to minimised χ^2. A minimum value of N that gives a good fit with the least χ^2 value (in our case N = 2 for bilayer and N=3 for trilayer) was chosen. At N > 2 there

is no significant reduction in χ^2 value proving that this model with N=2 captures the overall features in the system including the SLD variations around the interface. The SLD is a function of the depth z normal to the sample surface and is a sum of the nuclear b_{nuc} and magnetic b_{mag} contributions. Therefore, both structural and magnetic depth profiles for the entire system were extracted from the best fit simulation. This provides the cross-sectional depth profiles of the entire system as shown in figure 5.6.

The χ^2 minimisation values which measure the goodness of the fit are shown on the reflectivity plots (top plots) in figure 5.6. Having a χ^2 close to 10 indicates a good PNR fit. The theoretical model assumed an idealised model of the interface with the form of an error function, which may not be true. This explains why some data points of the spin asymmetry (center plots in figure 5.6) in the Pt/CFTB/Pt do not fall within the error bar limits. At higher angles there could be some artifacts because of low signal level. In addition, the spin asymmetry is not fitted to the data, but rather derived from the fitted reflectivity. Therefore, having a spin asymmetry line close to the data point is a good fit. Also at higher angles, there may be some instrument artifacts that have not previously been seen, as very few people do measurements at such high θ. It is also possible that the model used may stop providing good description of the sample at such high Q range.

PNR SLD results revealed an asymmetry in the magnetic scattering length density profile between the top and bottom interfaces with an average peak magnitude of 10^{-6} Å^{-2} (300 emu/cm^3) close to the substrate in all cases. In all sample series, magnetic moments close to the substrate are larger than the surface with a compositional grading throughout the FM layer. In the Pt buffer films, the mechanism of the grading may possibly be explained as Pt at the bottom pushing Ta up and oxygen from the top pulling it up by chemical means. Similarly in the Pt capped films, the Pt deposition may cause the Ta to float up leading to low magnetisation at the surface as shown on the magnetic SLD profile. It may be possible that these two mechanism both operate in the trilayered films, pushing the peak magnetisation upward into the CFTB layer. Therefore, Pt/CFTB samples shows higher interfacial magnetic moment compare to CFTB/Pt interface. This could be as a result of Ta diffusion, thereby creating a compositional and magnetic grading which reduces the magnetisation closer to the surface [46]. Note that the

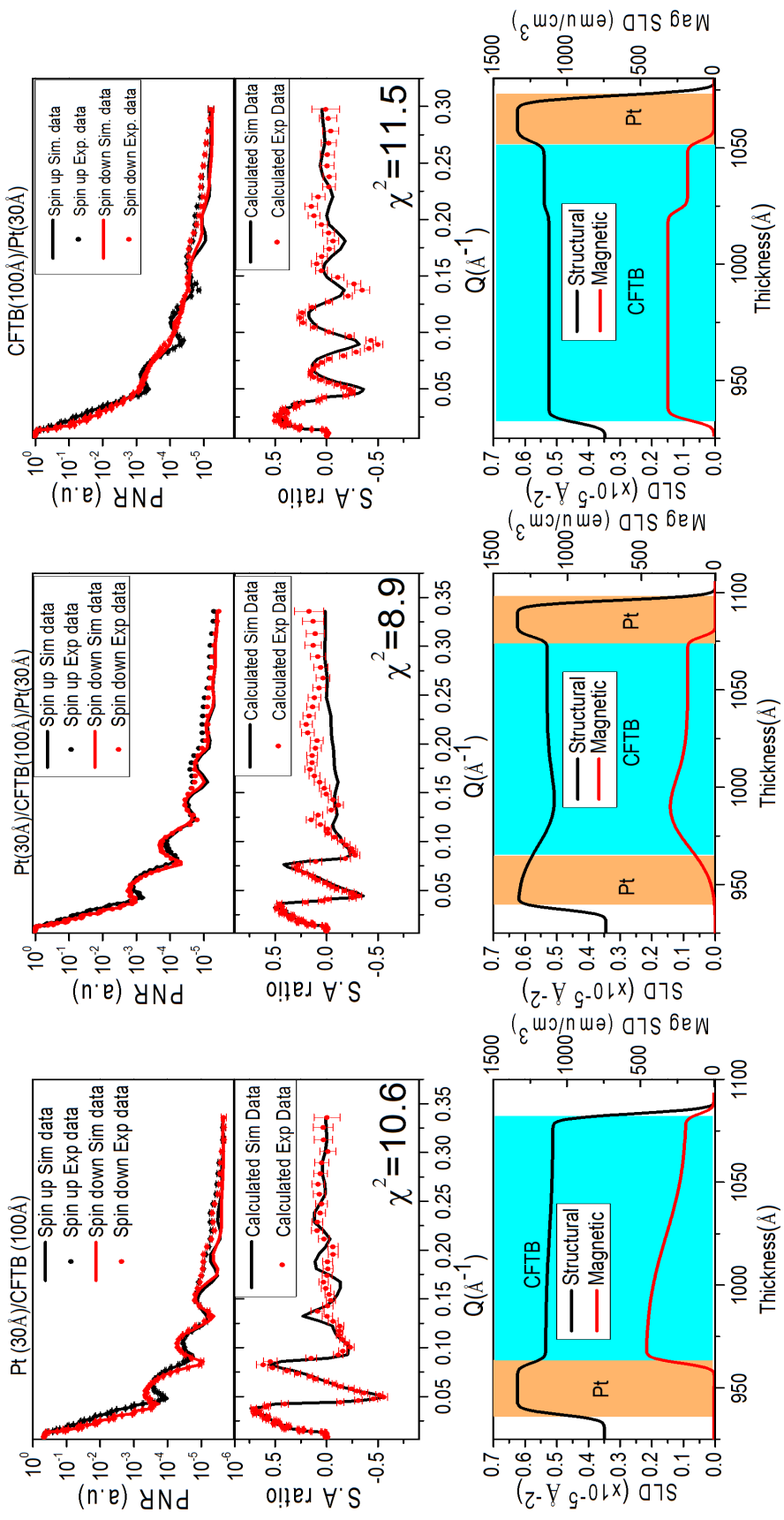

Figure 5.6: The polarised neutron reflectivity fits (upper panel), spin asymmetry calculated from the reflectivity plots (middle panel) and SLD profile extracted from the best fit simulations of the reflectivity data (lower panel). The χ^2 value is provided as the inset on the reflectivity plots.

amorphous structure is already inhomogeneous, therefore should have little effect other than in the magnetism.

The CFTB moment reduces over a layer of about 10 Å at the interface for bilayers and the top interface of the trilayers, but the Pt/CFTB interfacial moment for the trilayers reduces over 30 Å about the interface, suggesting interdiffusion and alloying at this interface. Also, the capped Pt layer may force more interdiffusion in the lower interface because of the impact energy and momentum impacted on the sample structure during deposition because Pt atoms are of a heavier atomic size. This effect was also observed by Singh *et al* [47] and Tokaç *et al* [48] in Fe/Ge and CFTB/Ta systems respectively. The chemically induced diffusion (Fe-O) bonding in a tunneling junction have been reported in [49]. The imaginary SLD profile for all sample series which describes the neutron absorption by boron atoms revealed an even distribution of boron in the FM layer (not shown).

The observed reduction in the CFTB/Pt interface indicates no PIM in Pt or possible proximity polarisation of Pt atom overwhelmed by the magnetic moment in the CFTB layer. As the induced magnetic moment due to Pt polarisation is too small, PNR cannot see the Pt polarisation but does see the CFTB magnetisation at both interfaces with observed asymmetry in both composition and magnetisation. Consequently, PNR is not a suitable technique for PIM investigation in FM-NM systems because it gives the total magnetic moment of the entire system and possibly the magnetic moment of the NM layer maybe overshadowed by that of the FM layer. Therefore further investigation for PIM is required and is discussed in the next section.

5.4 Magnetic proximity effect in Pt using X-ray resonance magnetic reflectivity

In thin films, boundary effects becomes significant thereby leading to an extended magnetic interaction between nearest neighbouring atoms at the interface. This can lead to proximity polarisation of NM atoms around the interface through indirect exchange coupling between the

NM and FM atoms around the interface in a NM-FM heterostructure. PIM investigation in Pt is mainly done using XMCD. Valvidared et. al. reported a Pt polarisation of < 0.001 μ_B/Pt atom in $CoFe_2O_4$/Pt implying no PIM at the interface because the XMCD signal obtained was within the noise level. Similarly, a significant PIM has been observed in Pt/Co [50–52], Pt/Fe [53] and Ni/Pt [24] systems. An overview of these XMCD investigations as a function of Pt thickness have been put together by Klewe *et al* (see figure 5.7). The Pt moments labeled [24], [51] and [54] were recorded at 10 K, which is likely to decrease for room temperature measurements as indicated by the red and green arrows (shaded area). The rest of the measurements were obtained at room temperature. This plot indicates a strong dependence with thickness because total film volume contributes to the absorption measured by the XMCD technique. Hence it would be difficult to identify some interfacial contributions in thicker samples with small interface to volume ratio because the XMCD obtained moment is effectively averaged over the full film thickness. Also, PIM investigations in Pt/YIG systems has proven to be controversial where Lu *et al.* report an observed Pt polarisation of 0.054 μ_B/Pt atom at 300 K and 0.076 μ_B/Pt atom at 20 K in a YIG/Pt sample supporting the idea that spin Hall magnetoresistance may be attributed to PIM. On the contrary, Geprägs *et al* investigated a Pt/YIG sample and observed no evidence of Pt polarisation, supporting the contrasting idea that SMR is directly due to spin current generation. Therefore, it is evident that another technique is required for PIM investigation. XRMR is a technique for PIM investigation that is not averaged over the sample thickness providing detailed information on the depth distribution of the magnetic moment across the interface.

Several investigations have been performed with XRMR on FM/Pt samples where some of these had been reported in Pt/Fe [27, 56, 57], Pt/ Ni [56], Pt/ NiFe [56], Pt/$NiFe_2O_4$ (NFO) [27, 56, 57] and Pt/Co [58] samples. Pt/Fe samples exhibit the largest Pt spin polarisation of 0.43 - 0.6 μ_B/ Pt atom, followed by Pt/Co with a moment of 0.21 μ_B/ Pt atom, $Ni_{33}Fe_{67}$ with 0.44 μ_B/ Pt atom, $Ni_{81}Fe_{19}$ with 0.22 μ_B/ Pt atom, Pt/Ni with 0.08 and 0.04 μ_B/ Pt atom for Pt/NFO. Although there are some comparable results for the estimated moment of Pt polarisation between XRMR and XMCD techniques in Pt/Fe samples, there is great disparity in other sample structures.

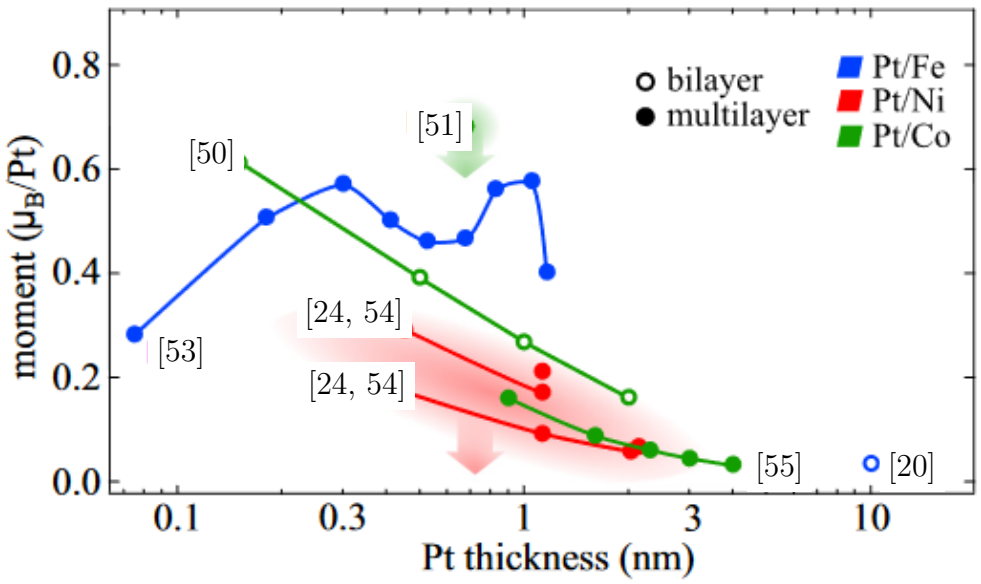

Figure 5.7: Overview of the XMCD investigation of MPE in Pt/FM bilayer (open dots) and multilayer (solid dots) from [56] where the magnetic moments observed in [24, 51, 54] were obtained at 10K while the rest were at room temperature. The downward arrow (green and red) indicates the expected reduction in magnetic moment at room temperature.

In this section, magnetic polarisation of Pt atoms in proximity to CFTB is investigated with XRMR. The measurements were conducted at the XMaS beamline at the ESRF, France using synchrotron x-ray radiation. Details of the experimental technique have been discussed in chapter 3. The measurements are taken at gazing incidence using a circularly polarised x-ray beam tuned to the energy of the Pt L_3 absorption edge. The degree of circular polarisation of the x-ray beam deduced from a model that describes the phase plate performance was 88% [59]. The XRMR technique allows the exploitation of both the reflectivity and dichroic properties to determination the element specific magnetisation profiles through the sample. Both structural and magnetic profiles specific to the Pt L_3 edge were obtained for each sample series at room temperature.

XRMR data were collected at a fixed Pt L_3 resonance energy of 11.569 keV in order to exclude contributions from materials in the sample other than Pt to the asymmetric dichroic effect. The reflectivity scans were performed using left circularly polarised x-ray beam, switching the magnetisation between parallel and antiparallel directions to the incident beam. Magnetic switching was accomplished with an electromagnet that applies a field of ± 130 Oe in the sample

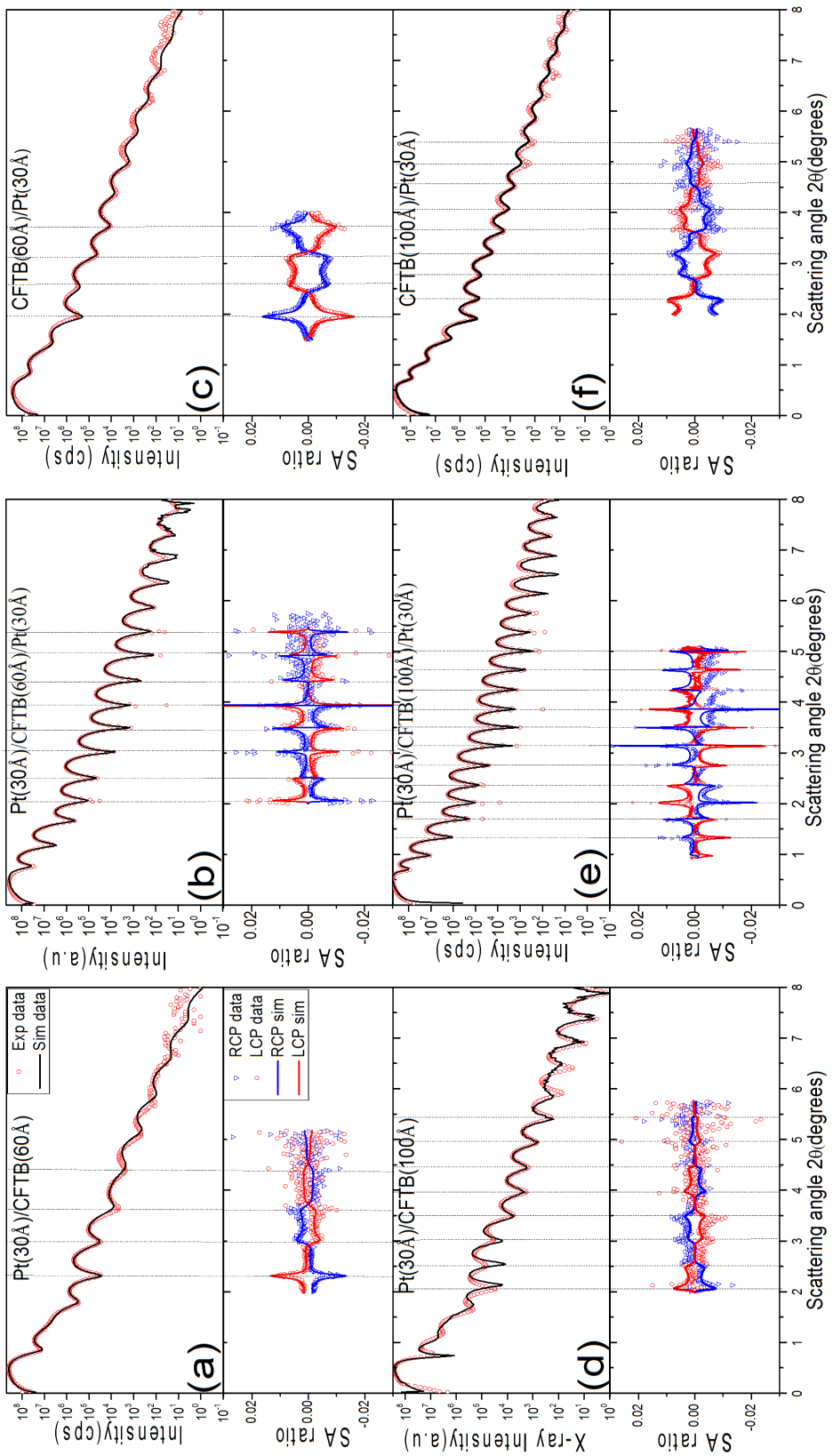

Figure 5.8: Specular resonance x-ray reflectivity (upper panel) and spin asymmetry (lower panel) for the Pt/CFTB (a and d), Pt/CFTB/Pt (b and e) and CFTB/Pt (c and f) samples performed at Pt L_3 absorption edge at 11.569 keV. The solid lines represent the best fit calculations from the described model in this section. Note that the scales for the reflectivity plots are the same but those of Spin asymmetry differs.

Table 5.3: Structural parameters from the best fitting GenX simulations of the XRMR data using the `diff` FOM where the roughness represents the roughness of the top interface of the layer.

Sample	Layer	Thickness (nm)	Roughness (nm)	Density(atoms Å^{-3})
Pt(3nm)/CFTB(6nm)	Oxide layer	2.2 ± 0.1	0.6 ± 0.1	0.011 ± 0.003
	CFTB	5.3 ± 0.1	0.4 ± 0.1	0.080 ± 0.004
	Pt	3.1 ± 0.1	0.6 ± 0.1	0.061 ± 0.002
Pt(3nm)/CFTB(10nm)	Oxide layer	2.2 ± 0.1	0.5 ± 0.1	0.012 ± 0.002
	CFTB	9.5 ± 0.1	0.3 ± 0.1	0.085 ± 0.005
	Pt	3.0 ± 0.1	0.5 ± 0.1	0.065 ± 0.003
CFTB(6nm)/Pt(3nm)	Pt	3.5 ± 0.1	0.3 ± 0.1	0.056 ± 0.004
	CFTB	6.4 ± 0.1	0.6 ± 0.1	0.087 ± 0.002
CFTB(10nm)/Pt(3nm)	Pt	3.3 ± 0.1	0.3 ± 0.1	0.066 ± 0.004
	CFTB	10.2 ± 0.1	0.6 ± 0.1	0.080 ± 0.003
Pt(3nm)/CFTB(6nm)/Pt(3nm)	Top Pt	3.5 ± 0.1	0.4 ± 0.1	0.063 ± 0.002
	CFTB	5.9 ± 0.1	0.6 ± 0.1	0.082 ± 0.002
	Buffer Pt	3.3 ± 0.1	0.6 ± 0.1	0.058 ± 0.004
Pt(3nm)/CFTB(10nm)/Pt(3nm)	Top Pt	3.4 ± 0.1	0.4 ± 0.1	0.060 ± 0.003
	CFTB	9.3 ± 0.1	0.6 ± 0.1	0.084 ± 0.001
	Buffer Pt	3.4 ± 0.1	0.6 ± 0.1	0.055 ± 0.004

plane. Measurements were taken after confirming a change in sign of XRMR asymmetric ratio between RCP and LCP beam. The spin asymmetry (SA) ratio was also obtained from the resonance reflectivity scan by switching sample magnetisation repeatedly at every point along the specular reflectivity curve.

$$\mathrm{SA} = \frac{\mathrm{I}^{+} - \mathrm{I}^{-}}{\mathrm{I}^{+} + \mathrm{I}^{-}} \tag{5.4.1}$$

The SA measurements were taken as a function of scattering angle 2θ.

GenX simulations of the reflectivity and SA scan were simultaneously fitted to obtain the best fit of structural and magnetic scattering length density (SLD) depth profiles of the samples. Here, a modified Parratt algorithm was used to consider the resonance induced changes of the scattering factor. The interface was modeled using the Nevot-Croce approximation [60], which describes the interface as a Gaussian shaped profile. The simulation model included a sample stack divided into single slabs for each sample layer. The samples thickness, interface roughness, density and resonance scattering factor were allowed to vary.

5.4.1 XRMR investigation of Pt-CFTB interface for magnetic proximity effect

The specular reflectivity and spin asymmetric (SA) ratios are shown in figure 5.8. Excellent agreement is found between simulated and experimental data, with a slight deviation only at higher angles attributed to the influence of the low signal to noise level. The reflectivity fits shown in the upper panel of each pairs of plots in figure 5.8 are used to derive the structural parameters in table 5.3. The SA fits, which are shown in the lower panel of each pair of plot in figure 5.8, show about 3% and 1% Pt magnetic signal in the trilayered and bilayered structure respectively. The SA changes sign as the magnetisation or helicity was switched, confirming the presence of a magnetic effect. The SA slightly increases with CFTB thickness for both interfaces. It can be observed that the SA peak doubles in the trilayer in comparison with the bilayer due to an increase in the number of reflective interfaces and the total sample thickness and hence more complicated interferences terms.

The extracted structural parameters from the XRMR best fits are as shown on table 5.3. The thicknesses and roughnesses of the different layers are comparable with the XRR values in table 5.1, while the density of the Pt layer is generally smaller especially for the Pt buffer layer. The Pt buffer layer is largely amorphous which may be attributed to the decrease in density. Crystalline packing should have a higher density in comparison to the amorphous counterpart, which would probably require a higher sensitivity of resonance scattering to observe this. Also, the interface width, which captures the effect of topological roughness and intermixing at the interface, is slightly larger at the Pt/CFTB compared to the CFTB/Pt interface. This could be a consequence of intermixing at the interface as the amorphous/amorphous interface width is larger than the amorphous/crystalline interface width.

The depth resolved structural and magnetic scattering length density profiles are shown in figure 5.9. The structural SLD profile (black lines) represents the chemical characteristic of the sample, which is a function of the charge structure factor F_c. Similarly, the magnetic SLD (red lines) depicts the magnetic distribution of Pt polarisation within the vicinity of the interface with the FM layer and is a function of the magnetic structure factor F_m. The magnitude of F_m

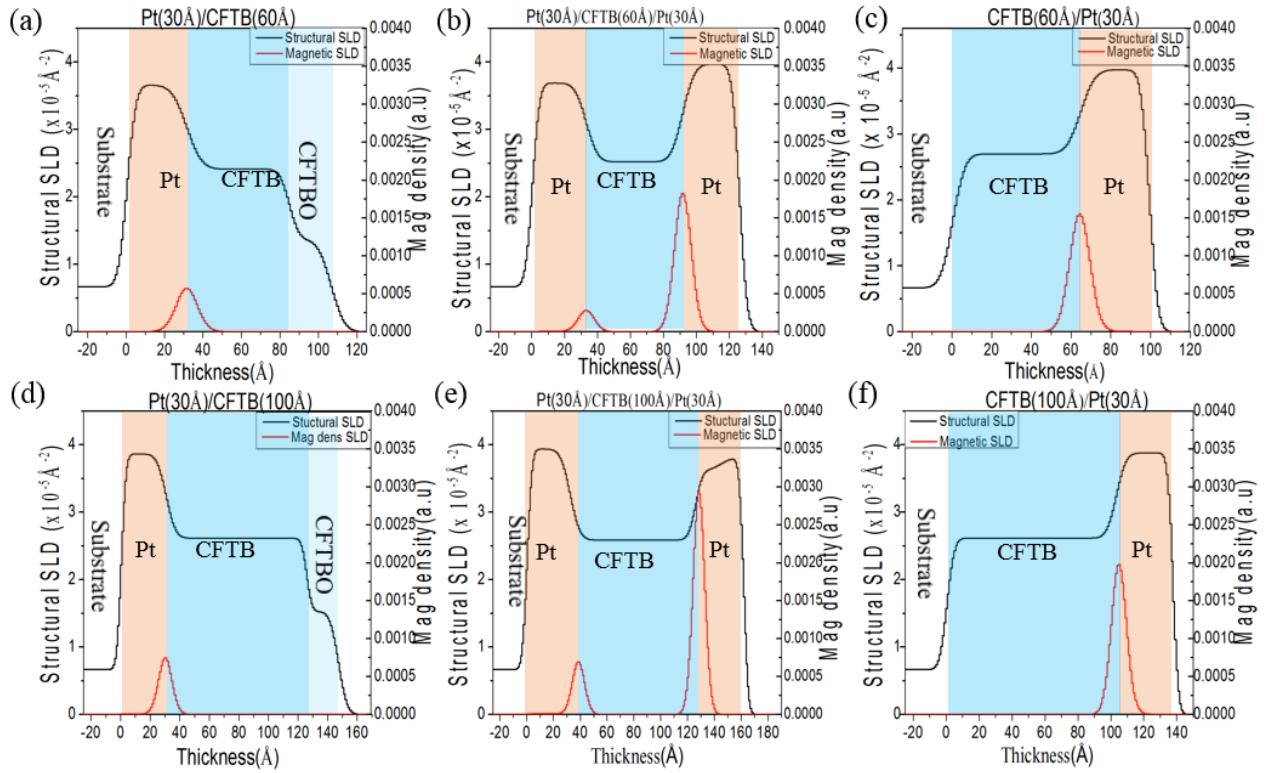

Figure 5.9: The extracted profile of the structural (black) and magnetic (red) SLD profile of (a) Pt(30Å)/CFTB(60Å) (b) Pt(30Å)/CFTB(60Å)/Pt(30Å) (c) CFTB(60Å)/Pt(30Å) (d) Pt(30Å)/CFTB(100Å) (e) Pt(30Å)/CFTB(100Å)/Pt(30Å) (f) CFTB(100Å)/Pt(30Å).

is proportional to the Pt moment per atom and is treated as an arbitrary fitting parameter in the GenX simulator. Hence it is only possible to obtain the relative change in the Pt magnetic moment, not the absolute values of Pt magnetic moment. Looking at figure 5.9, the magnetic SLD profiles confirm the presence of PIM in Pt. The PIM effect decreases exponentially with a characteristic decay length of 15 Å from the interface (FWHM $\sim$ 11 Å) which is comparable to $\sim$ 18 Å in Pt/Co [61], $\sim$ 10 Å (FWHM) in Pt/Co [58], Pt/$NiFe_2O_4$ [57] and Pt/Fe [27]. It is observed that the PIM in the Pt/CFTB interface is much smaller than that of the CFTB/Pt interface in both bilayered and trilayered samples with values that are consistent between sets of samples. Grissler *et al* [58] pointed out a strong dependence of Pt magnetisation on the chemical density specific to the sample, which can explain the reasons for low PIM in the lower density Pt of the buffer layer. This could also be linked to the interfacial morphology at the interface as discussed in the XRD analysis.

The estimated Pt magnetic moment obtained from the peak-height of the Pt magnetisation

concentration in the sample is plotted on figure 5.10b. Also a plot of the estimated value of crystalline grain size to CFTB thickness shows a similar increasing trend as the estimated magnetic SLD dependence on CFTB thickness (see figure 5.10). This supports the observation that PIM strongly depends on the crystalline morphology at the interface which can be attributed to interfacial mixing that leads to the formation of poor Pt crystal texture at the Pt/CFTB interface in comparison to the CFTB/Pt interface. Also, Pt texture on thermally oxidised Si substrate is reported to be a (111) texture [62], but can be changed to a random orientation depending on the fraction of oxygen at the interface [39], which explains the possible asymmetry observed in the Pt/CFTB and CFTB/Pt interfaces.

In addition, the induced Pt magnetisation scales with the magnetic moment of the CFTB layer suggesting that the strength of magnetic coupling between Pt and CFTB layer depends on the magnitude of the magnetic moment in the CFTB layer. This coupling may be a consequence of band hybridisation and exchange interaction at the interface which defines the electrochemical potential relative to the individual layer of the interface. This can modify the spin transport properties of the system. The difference in orbital and Fermi energy is minimised or tuned by the morphology of the interface. The 3d electrons from CFTB and the 4s electrons from the Pt interact modifying the DOS near the Fermi level, leading to spin polarisation of Pt atom.

Furthermore, aside from the presence of PIM there is an asymmetry in the magnetic profiles at the two interfaces. Therefore, it is inappropriate to assume symmetry in tunneling junctions or similar sample structures across such interfaces. This observed asymmetry can significantly influence spin transport in FM/NM systems affecting the potential application in spin devices.

5.4.2 XRMR of Pt-YIG interface

Due to the closeness of Pt to the Stoner criterion, the interpretation of the observed Spin Hall magnetoresistance for spin current generation in a ferrimagnetic insulator(FMI)/ nonmagnetic (NM) material structure such as yttrium iron garnet ($Y_3Fe_5O_{12}$, YIG)/Pt has been controversial. This is due to the opinion that in the presence of PIM the generated pure spin current is contaminated by charge current. Geprägs *et al* [20, 63] observed no spin polarisation of Pt atom

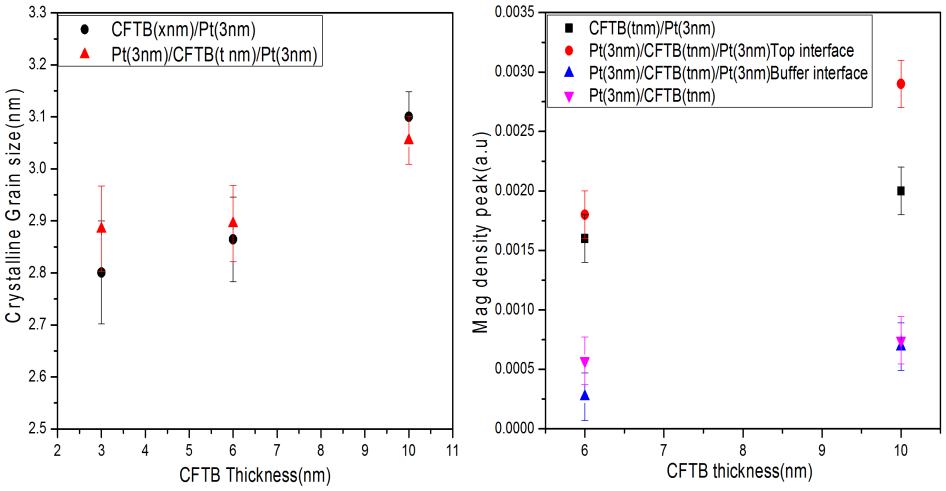

Figure 5.10: A plot of (a) estimated crystalline grain size from Pt(111) peak for CFTB/Pt (black) and Pt/CFTB/Pt (red) samples (b) peak magnetic moment at Pt/CFTB (blue and purple) and CFTB/Pt (black and red) interfaces for bilayered (black and purple) and trilayered (red and blue) samples as a function of CFTB thickness. This shows a slight increase with increasing CFTB thickness.

in a YIG(62nm)/Pt(3nm, 7nm, 10nm) using XMCD at room temperature. Conversely, Lu *et al* [64] reported evidence of Pt polarisation moment of 0.054 μ_B at 300 K and 0.076 μ_B at 20 K for YIG/Pt(1.5nm) contradicting the report by Geprägs *et al*. XRMR being a depth sensitive magnetic probing technique is used in this section to clarify the possible evidence of PIM in YIG/Pt structure.

Here a sample of 8 mm × 8 mm YIG(38nm)/Pt(3nm) sample fabricated by Amy Westerman from Prof Bryan Hickey's group at the University of Leeds was used for XRD and XRMR measurements at room temperature. The sample was grown on a gadolinium gallium garnet (GGG) substrate. The YIG layer was grown by RF magnetron sputtering under a deposition pressure of 2.4 mTorr with 5 % oxygen and 95 % argon gas. The sample was later annealed in air for two hours at a temperature of 850°C. The M_s and the coercive field H_c measured with a VSM are 124 ± 2 emu/cc and 0.3 ± 0.1 Oe respectively. A 3 nm layer of Pt was later deposited on the annealed YIG under an argon gas pressure of 2.4 mTorr using DC magnetron sputtering.

The result of XRD and XRMR analyses are shown in figure 5.11. The XRD measurements reveals poor Pt growth on the YIG layer. The anticipated location of the Pt(111) peak is indicated by the red arrow in figure 5.11a. The resonance x-ray reflectivity confirms the layer

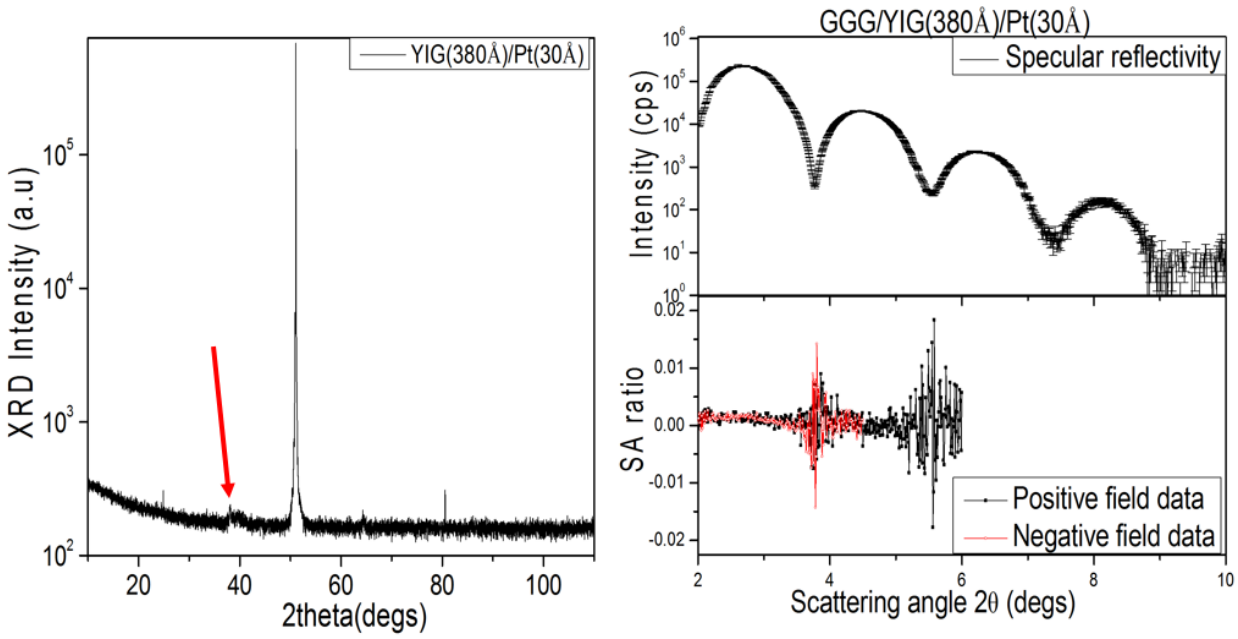

Figure 5.11: (a) XRD diffraction pattern for YIG/Pt on GGG substrate showing the anticipated angle (red arrow) of the Pt(111) peak (b) XRMR specular reflectivity(upper panel) and spin asymmetry ratio (lower panel) of YIG(380Å)/Pt(30Å) on a GGG substrate which indicates no Pt polarisation in the sample.

structure of the sample while the spin asymmetry shows no evidence of polarisation of Pt atoms because there is no significant split between the positive and negative field data. These results support the report by Geprägs *et al.* of negligible PIM in YIG/Pt, buttressing the fact that spin current generation in this system is due to spin Hall effect. Magnetoresistance investigation of spin current generation will be discussed in detail in chapter 6.

5.5 Summary

In this chapter, Pt interfacial spin polarisation in CFTB-Pt interface was investigated. XRR and XRD have been used to study the structural properties of the CFTB-Pt samples categorised into three sample series which are Pt/CFTB, CFTB/Pt and Pt/CFTB/Pt samples. For each sample series, samples with different CFTB thickness of 30 Å, 60 Å and 100 Å were prepared by magnetron sputtering deposition on Si/SiO_2 substrates. The film structural quantities such as thickness and interface roughness have been quantified by a best fit simulation of the XRR specular reflectivity measurement. Among the Pt/CFTB series, an oxide layer of approximately

20 ± 3 Å was obtained, while on the other sample series this was negligible. Direct interpretation of the XRD peaks has shown that the microstructure of all films is characterised as an amorphous CFTB with varying Pt(111) texture. Calculations of the crystallite grain size in Pt indicates a small increase with increasing CFTB thickness. The effect of this microstructure on the magnetic behaviour of the samples was investigated with PNR and XRMR.

The magnetic anisotropy of the samples has been studied with the longitudinal MOKE giving a idea of the minimum field required to saturate and reverse the in-plane magnetisation for PNR and XRMR measurements. The coercive fields obtained were about 25 Oe for all sample series.

PNR fits of both spin state experimental data have shown the depth resolved structural and magnetic profiles of the samples. The highest magnetic moment close to the buffer interface obtained was $\sim 10^{-6}$ Å^{-2} (300 emu/cm^3), distributed over the FM layer in the material. The magnetic profile shows a reduced moment close to the sample surface and higher moment closer to the substrate in all sample series. The imaginary SLD profile from the PNR measurements shows an even distribution of B atoms within the FM layer.

Simultaneous GenX simulations of the specular reflectivity and spin asymmetry from XRMR measurements taken at the Pt L_3 absorption edge energy reveals proximity magnetic polarisation of Pt for all CFTB sample series. The Pt polarisation is found to extend 15 ± 3 Å from each side of the interface which increases with increasing CFTB thickness for the top Pt interface. The PIM at the buffer Pt interface is significantly smaller with slight increase with increase CFTB thickness. This indicates that the PIM is strongly dependent on the interface growth of the Pt layer. PIM effect can greatly influence the magnetoresistance measurements. Therefore the effect of PIM on magnetoresistance measurements is discussed in chapter 6.

Also, XRMR investigation on YIG (38nm)/Pt(3nm) shows no PIM in Pt, confirming that the generated spin current by spin Hall effect observed by spin Hall magnetoresistance in YIG/Pt is pure.

References

[1] Y. Tserkovnyak, A. Brataas, and G. E. Bauer, "Enhanced Gilbert damping in thin ferromagnetic films," *Physical Review Letters*, vol. 88, no. 11, p. 117601, 2002.

[2] O. Mosendz, V. Vlaminck, J. Pearson, F. Fradin, G. Bauer, S. Bader, and A. Hoffmann, "Detection and quantification of inverse spin Hall effect from spin pumping in permalloy/normal metal bilayers," *Physical Review B*, vol. 82, no. 21, p. 214403, 2010.

[3] F. Czeschka, L. Dreher, M. Brandt, M. Weiler, M. Althammer, I.-M. Imort, G. Reiss, A. Thomas, W. Schoch, W. Limmer, *et al.*, "Scaling behavior of the spin pumping effect in ferromagnet-platinum bilayers," *Physical Review Letters*, vol. 107, no. 4, p. 046601, 2011.

[4] M. I. Dyakonov and A. Khaetskii, "Spin Hall effect," in *Spin physics in semiconductors*, pp. 211–243, Springer, 2008.

[5] J. Hirsch, "Spin Hall Effect," *Physical Review Letters*, vol. 83, no. 9, p. 1834, 1999.

[6] A. Hoffmann, "Spin Hall effects in metals," *IEEE Transactions on Magnetics*, vol. 49, no. 10, pp. 5172–5193, 2013.

[7] Y.-T. Chen, S. Takahashi, H. Nakayama, M. Althammer, S. T. Goennenwein, E. Saitoh, and G. E. Bauer, "Theory of spin Hall magnetoresistance (SMR) and related phenomena," *Journal of Physics: Condensed Matter*, vol. 28, no. 10, p. 103004, 2016.

[8] H. Nakayama, M. Althammer, Y.-T. Chen, K. Uchida, Y. Kajiwara, D. Kikuchi, T. Ohtani, S. Geprägs, M. Opel, S. Takahashi, *et al.*, "Spin Hall magnetoresistance induced by a nonequilibrium proximity effect," *Physical Review Letters*, vol. 110, no. 20, p. 206601, 2013.

[9] M. Althammer, S. Meyer, H. Nakayama, M. Schreier, S. Altmannshofer, M. Weiler, H. Huebl, S. Geprägs, M. Opel, R. Gross, *et al.*, "Quantitative study of the spin Hall magnetoresistance in ferromagnetic insulator/normal metal hybrids," *Physical Review B*, vol. 87, no. 22, p. 224401, 2013.

[10] C. Hahn, G. De Loubens, O. Klein, M. Viret, V. V. Naletov, and J. B. Youssef, "Comparative measurements of inverse spin Hall effects and magnetoresistance in YIG/Pt and YIG/Ta," *Physical Review B*, vol. 87, no. 17, p. 174417, 2013.

[11] I. M. Miron, K. Garello, G. Gaudin, P.-J. Zermatten, M. V. Costache, S. Auffret, S. Bandiera, B. Rodmacq, A. Schuhl, and P. Gambardella, "Perpendicular switching of a single ferromagnetic layer induced by in-plane current injection," *Nature*, vol. 476, no. 7359, p. 189, 2011.

[12] T. Moriya, "Anisotropic superexchange interaction and weak ferromagnetism," *Physical Review*, vol. 120, no. 1, p. 91, 1960.

[13] I. Dzyaloshinsky, "A thermodynamic theory of weak ferromagnetism of antiferromagnetics," *Journal of Physics and Chemistry of Solids*, vol. 4, no. 4, pp. 241–255, 1958.

[14] L. Liu, T. Moriyama, D. Ralph, and R. Buhrman, "Spin-torque ferromagnetic resonance induced by the spin Hall effect," *Physical Review Letters*, vol. 106, no. 3, p. 036601, 2011.

[15] Z. Tang, Y. Kitamura, E. Shikoh, Y. Ando, T. Shinjo, and M. Shiraishi, "Temperature dependence of spin Hall angle of palladium," *Applied Physics Express*, vol. 6, no. 8, p. 083001, 2013.

[16] T. Seki, Y. Hasegawa, S. Mitani, S. Takahashi, H. Imamura, S. Maekawa, J. Nitta, and K. Takanashi, "Giant spin Hall effect in perpendicularly spin-polarized FePt/Au devices," *Nature Materials*, vol. 7, no. 2, p. 125, 2008.

[17] L. Liu, C.-F. Pai, Y. Li, H. Tseng, D. Ralph, and R. Buhrman, "Spin-torque switching with the giant spin Hall effect of tantalum," *Science*, vol. 336, no. 6081, pp. 555–558, 2012.

[18] C.-F. Pai, L. Liu, Y. Li, H. Tseng, D. Ralph, and R. Buhrman, "Spin transfer torque devices utilizing the giant spin Hall effect of tungsten," *Applied Physics Letters*, vol. 101, no. 12, p. 122404, 2012.

[19] Y. Lu, J. Cai, S. Huang, D. Qu, B. Miao, and C. Chien, "Hybrid magnetoresistance in the proximity of a ferromagnet," *Physical Review B*, vol. 87, no. 22, p. 220409, 2013.

[20] S. Geprägs, S. Meyer, S. Altmannshofer, M. Opel, F. Wilhelm, A. Rogalev, R. Gross, and S. T. Goennenwein, "Investigation of induced Pt magnetic polarization in $Pt/Y_3Fe_5O_{12}$ bilayers," *Applied Physics Letters*, vol. 101, no. 26, p. 262407, 2012.

[21] W. Zhang, M. B. Jungfleisch, W. Jiang, Y. Liu, J. E. Pearson, S. G. te Velthuis, A. Hoffmann, F. Freimuth, and Y. Mokrousov, "Reduced spin-Hall effects from magnetic proximity," *Physical Review B*, vol. 91, no. 11, p. 115316, 2015.

[22] V. L. Moruzzi and P. M. Marcus, "Magnetism in fcc rhodium and palladium," *Physical Review B*, vol. 39, pp. 471–474, Jan 1989.

[23] H. Chen, N. E. Brener, and J. Callaway, "Electronic structure, optical and magnetic properties of fcc palladium," *Physical Review B*.

[24] F. Wilhelm, P. Poulopoulos, G. Ceballos, H. Wende, K. Baberschke, P. Srivastava, D. Benea, H. Ebert, M. Angelakeris, N. Flevaris, *et al.*, "Layer-resolved magnetic moments in Ni/Pt multilayers," *Physical Review Letters*, vol. 85, no. 2, p. 413, 2000.

[25] D.-O. Kim, K. M. Song, Y. Choi, B.-C. Min, J.-S. Kim, J. W. Choi, and D. R. Lee, "Asymmetric magnetic proximity effect in a Pd/Co/Pd trilayer system," *Scientific Reports*, vol. 6, 2016.

[26] T. P. Hase, M. S. Brewer, U. B. Arnalds, M. Ahlberg, V. Kapaklis, M. Björck, L. Bouchenoire, P. Thompson, D. Haskel, Y. Choi, *et al.*, "Proximity effects on dimensionality and magnetic ordering in Pd/Fe/Pd trialyers," *Physical Review B*, vol. 90, no. 10, p. 104403, 2014.

[27] T. Kuschel, C. Klewe, J.-M. Schmalhorst, F. Bertram, O. Kuschel, T. Schemme, J. Wollschläger, S. Francoual, J. Strempfer, A. Gupta, *et al.*, "Static magnetic proximity effect in $Pt/NiFe_2O_4$ and Pt/Fe bilayers investigated by x-ray resonant magnetic reflectivity," *Physical Review Letters*, vol. 115, no. 9, p. 097401, 2015.

[28] A. Hoffmann, J. W. Seo, M. R. Fitzsimmons, H. Siegwart, J. Fompeyrine, J.-P. Locquet, J. Dura, and C. Majkrzak, "Induced magnetic moments at a ferromagnet-antiferromagnet interface," *Physical Review B*, vol. 66, no. 22, p. 220406, 2002.

[29] M. Valvidares, N. Dix, M. Isasa, K. Ollefs, F. Wilhelm, A. Rogalev, F. Sánchez, E. Pellegrin, A. Bedoya-Pinto, P. Gargiani, *et al.*, "Absence of magnetic proximity effects in magnetoresistive Pt/$CoFe_2O_4$ hybrid interfaces," *Physical Review B*, vol. 93, no. 21, p. 214415, 2016.

[30] C. Ederer, M. Komelj, M. Fähnle, and G. Schütz, "Theory of induced magnetic moments and x-ray magnetic circular dichroism in Co/Pt multilayers," *Physical Review B*, vol. 66, no. 9, p. 094413, 2002.

[31] S. Bandiera, R. Sousa, B. Rodmacq, and B. Dieny, "Asymmetric interfacial perpendicular magnetic anisotropy in Pt/Co/Pt trilayers," *IEEE Magnetics Letters*, vol. 2, pp. 3000504–3000504, 2011.

[32] A. Hindmarch, C. Kinane, M. MacKenzie, J. Chapman, M. Henini, D. Taylor, D. Arena, J. Dvorak, B. Hickey, and C. Marrows, "Interface induced uniaxial magnetic anisotropy in amorphous CoFeB films on AlGaAs (001)," *Physical Review Letters*, vol. 100, no. 11, p. 117201, 2008.

[33] S. Horry, "Critical Phenomena in Hybrid Magnetic Nanostructure," Master's thesis, Durham University, United Kingdom, 2012.

[34] J. Hafner, M. Tegze, and C. Becker, "Amorphous magnetism in Fe-B alloys: First-principles spin-polarized electronic-structure calculations," *Physical Review B*, vol. 49, no. 1, p. 285, 1994.

[35] Y. Luo, M. Esseling, A. Käufler, K. Samwer, T. Dimopoulos, G. Gieres, M. Vieth, M. Rührig, J. Wecker, C. Rudolf, *et al.*, "Co-rich magnetic amorphous films and their application in magnetoelectronics," *Physical Review B*, vol. 72, no. 1, p. 014426, 2005.

[36] K. Fukamichi and R. Gambino, "The Curie temperature and magnetization of Fe-base amorphous binary alloys containing transition metal," *IEEE Transactions on Magnetics*, vol. 17, no. 6, pp. 3059–3061, 1981.

[37] M. Björck and G. Andersson, "GenX: an extensible X-ray reflectivity refinement program utilizing differential evolution," *Journal of Applied Crystallography*, vol. 40, no. 6, pp. 1174–1178, 2007.

[38] C. V. Thompson, "Grain Growth in Thin Films," *Annual Review of Materials Science*, vol. 20, no. 1, pp. 245–268, 1990.

[39] D.-S. Lee, D.-Y. Park, H.-J. Woo, S.-H. Kim, J. Ha, and E. Yoon, "Preferred orientation controlled giant grain growth of platinum thin films on SiO_2/Si substrates," *Japanese Journal of Applied Physics*, vol. 40, no. 1A, p. L1, 2001.

[40] M. H. Kim, T.-S. Park, D.-S. Lee, E. Yoon, D.-Y. Park, H.-J. Woo, D.-I. Chun, and J. Ha, "Highly (200)-oriented Pt films on SiO_2/Si substrates by seed selection through amorphization and controlled grain growth," *Journal of Materials Research*, vol. 14, no. 3, pp. 634–637, 1999.

[41] G. Williamson and W. Hall, "X-ray line broadening from filed aluminium and wolfram," *Acta Metallurgica*, vol. 1, no. 1, pp. 22–31, 1953.

[42] J. I. Langford and A. Wilson, "Scherrer after sixty years: a survey and some new results in the determination of crystallite size," *Journal of Applied Crystallography*, vol. 11, no. 2, pp. 102–113, 1978.

[43] A. Ball, A. Leenaers, P. Van Der Zaag, K. Shaw, B. Singer, D. Lind, H. Fredrikze, and M. T. Rekveldt, "Polarized neutron reflectometry study of an exchange biased Fe_3O_4/NiO multilayer," *Applied Physics Letters*, vol. 69, no. 10, pp. 1489–1491, 1996.

[44] S. Singh, S. Basu, D. Bhattacharya, and A. Poswal, "Physical and magnetic roughness at metal-semiconductor interface using x-ray and neutron reflectometry," *Journal of Applied Physics*, vol. 107, no. 12, p. 123903, 2010.

[45] T. Zhu, Y. Yang, R. Yu, H. Ambaye, V. Lauter, and J. Xiao, "The study of perpendicular magnetic anisotropy in CoFeB sandwiched by MgO and tantalum layers using polarized neutron reflectometry," *Applied Physics Letters*, vol. 100, no. 20, p. 202406, 2012.

[46] M. Kowalewski, W. Butler, N. Moghadam, G. Stocks, T. Schulthess, K. Song, J. Thompson, A. Arrott, T. Zhu, J. Drewes, *et al.*, "The effect of Ta on the magnetic thickness of permalloy ($Ni_{81}Fe_{19}$) films," *Journal of Applied Physics*, vol. 87, no. 9, pp. 5732–5734, 2000.

[47] S. Singh, S. Basu, M. Gupta, M. Vedpathakz, and R. Kodama, "Investigation of interface magnetic moment of Fe/ Ge multilayer: A neutron reflectivity study," *Journal of Applied Physics*, vol. 101, no. 3, p. 033913, 2007.

[48] M. Tokaç, C. Kinane, D. Atkinson, and A. Hindmarch, "Temperature dependence of magnetically dead layers in ferromagnetic thin-films," *AIP Advances*, vol. 7, no. 11, p. 115022, 2017.

[49] A. T. Hindmarch, V. Harnchana, A. S. Walton, A. P. Brown, R. M. Brydson, and C. H. Marrows, "Zirconium as a boron sink in crystalline CoFeB/MgO/CoFeB magnetic tunnel junctions," *Applied Physics Express*, vol. 4, no. 1, p. 013002, 2010.

[50] M. Suzuki, H. Muraoka, Y. Inaba, H. Miyagawa, N. Kawamura, T. Shimatsu, H. Maruyama, N. Ishimatsu, Y. Isohama, and Y. Sonobe, "Depth profile of spin and orbital magnetic moments in a subnanometer Pt film on Co," *Physical Review B*, vol. 72, no. 5, p. 054430, 2005.

[51] F. Wilhelm, P. Poulopoulos, A. Scherz, H. Wende, K. Baberschke, M. Angelakeris, N. Flevaris, J. Goulon, and A. Rogalev, "Interface magnetism in 3d/5d multilayers probed by X-ray magnetic circular dichroism," *Physica Status Solidi (A)*, vol. 196, no. 1, pp. 33–36, 2003.

[52] G. Schütz, R. Wienke, W. Wilhelm, W. Zeper, H. Ebert, and K. Spörl, "Spin-dependent x-ray absorption in Co/Pt multilayers and $Co_{50}Pt_{50}$ alloy," *Journal of Applied Physics*, vol. 67, no. 9, pp. 4456–4458, 1990.

[53] W. Antel Jr, M. Schwickert, T. Lin, W. OBrien, and G. Harp, "Induced ferromagnetism and anisotropy of Pt layers in Fe/Pt (001) multilayers," *Physical Review B*, vol. 60, no. 18, p. 12933, 1999.

[54] P. Poulopoulos, F. Wilhelm, H. Wende, G. Ceballos, K. Baberschke, D. Benea, H. Ebert, M. Angelakeris, N. Flevaris, A. Rogalev, *et al.*, "X-ray magnetic circular dichroic magnetometry on Ni/Pt multilayers," *Journal of Applied Physics*, vol. 89, no. 7, pp. 3874–3879, 2001.

[55] S. Rüegg, G. Schütz, P. Fischer, R. Wienke, W. Zeper, and H. Ebert, "Spin-dependent x-ray absorption in Co/Pt multilayers," *Journal of Applied Physics*, vol. 69, no. 8, pp. 5655–5657, 1991.

[56] C. Klewe, T. Kuschel, J.-M. Schmalhorst, F. Bertram, O. Kuschel, J. Wollschläger, J. Strempfer, M. Meinert, and G. Reiss, "Static magnetic proximity effect in Pt/$Ni_{1-x}Fe_x$ bilayers investigated by x-ray resonant magnetic reflectivity," *Physical Review B*, vol. 93, no. 21, p. 214440, 2016.

[57] T. Kuschel, C. Klewe, P. Bougiatioti, O. Kuschel, J. Wollschläger, L. Bouchenoire, S. D. Brown, J.-M. Schmalhorst, D. Meier, and G. Reiss, "Static Magnetic Proximity Effect in Pt Layers on Sputter-Deposited $NiFe_2O_4$ and on Fe of Various Thicknesses Investigated by XRMR," *IEEE Transactions on Magnetics*, vol. 52, no. 7, pp. 1–4, 2016.

[58] J. Geissler, E. Goering, M. Justen, F. Weigand, G. Schütz, J. Langer, D. Schmitz, H. Maletta, and R. Mattheis, "Pt magnetization profile in a Pt/Co bilayer studied by resonant magnetic x-ray reflectometry," *Physical Review B*, vol. 65, no. 2, p. 020405, 2001.

[59] L. Bouchenoire, S. Brown, P. Thompson, J. Duffy, J. Taylor, and M. Cooper, "Performance of phase plates on the XMaS beamline at the ESRF," *Journal of Synchrotron Radiation*, vol. 10, no. 2, pp. 172–176, 2003.

[60] Nvot, L. and Croce, P., "Caractrisation des surfaces par rflexion rasante de rayons X. Application l'tude du polissage de quelques verres silicates," *Rev. Phys. Appl. (Paris)*, vol. 15, no. 3, pp. 761–779, 1980.

[61] J.-M. Tonnerre, N. Jaouen, E. Bontempi, D. Carbone, D. Babonneau, M. De Santis, H. Tolentino, S. Grenier, S. Garaudée, and U. Staub, "Soft x-ray resonant magnetic

reflectivity studies for in-and out-of-plane magnetization profile in ultra thin films," in *Journal of Physics: Conference Series*, vol. 211, p. 012015, IOP Publishing, 2010.

[62] P. Chowdhury, P. Kulkarni, M. Krishnan, H. C. Barshilia, A. Sagdeo, S. Rai, G. Lodha, and D. Sridhara Rao, "Effect of coherent to incoherent structural transition on magnetic anisotropy in Co/Pt multilayers," *Journal of Applied Physics*, vol. 112, no. 2, p. 023912, 2012.

[63] S. T. Goennenwein, M. Schneider, F. Wilhelm, K. Ollefs, A. Rogalev, M. Opel, R. Gross, *et al.*, "Comment on " Pt magnetic polarization on $Y_3Fe_5O_{12}$ and magnetotransport characteristics"," *arXiv preprint arXiv:1307.4869*, 2013.

[64] Y. Lu, Y. Choi, C. Ortega, X. Cheng, J. Cai, S. Huang, L. Sun, and C. Chien, "Pt magnetic polarization on $Y_3Fe_5O_{12}$ and magnetotransport characteristics," *Physical Review Letters*, vol. 110, no. 14, p. 147207, 2013.

Chapter 6

Magnetoresistance in CoFeTaB/Pt bilayers

6.1 Introduction

Here, a new magnetoresistance in a simple FM/NM bilayer, where the nonmagnetic (NM) material is characterised by a large spin-orbit coupling, is reported. Several reports on the effect of magnetisation on electrical conductivity have helped to better understand the phenomena associated with spin transport in materials. These have wide applications in sensors and memory devices. The magnetoresistance measurement is an investigative technique that has proven to be an easy and a very enlightening technique. Detailed information on the change in electrical resistivity with magnetisation due to charge transport and spin-dependent scattering as a result of spin-orbit coupling has been widely reported in the literature [1–4]. Spin-dependent scattering resulting from the spin Hall effect (SHE) in a NM material, observed as a spin accumulation at an interface generating spin current transverse to the current propagation has also been reported [5–7]. The spin current generation process is reversible via inverse spin Hall effect(ISHE), but there remains some controversial issues on the origin and other contributory effects such as magnetic proximity effect and the Rashba effect, which challenge its application [8]. This has lead to great interest and research in the field.

As these magnetoresistance measurements are very sensitive to sample texture, it is imperative

to devise a means of sample deposition that will help to enhance the expected results and which will be presented in this chapter. The procedure for Pt deposition employed to obtain a continuous film growth on SiO_2 at reduced film thickness is discussed in detail. This is important as spin propagation is affected by discontinuities and inhomogeneities within the sample and at the interface. The following sections contain only a brief description of the structure of the sample as more detailed information has been provided in chapter 5. In order to know the magnetic field required to switch the magnetisation of the sample both in-plane and out-of-plane, magneto-optical Kerr effect (MOKE) measurements are also presented. Finally, a detailed discussion of the analysis of the results of a new form of magnetoresistance observed in CFTB/Pt and Pt/CFTB bilayers is presented.

6.2 Deposition conditions for Pt continuous film growth

Thin films are useful for device fabrication in spintonics application. Often, thin film properties are modified by the deposition technique, substrate material and substrate temperature hence a requirement for continuous film deposition procedure is needed in order to achieve the desired properties. Sample thicknesses and interface morphology are also very critical in such applications [9]. Spin dependent phenomena such as spin pumping [10–12], magnetoresistance [3, 13–19] and the Rashba effect [20, 21] depend on the interface structure between the spin generator and spin sink. Pt films with a FM layer have been observed to exhibit a new pure spin current phenomenon where the spin transport dynamics depended on the spin mixing conductance at the interface between FM and Pt [16, 17]. Increased growth temperature, grain size and roughness lead to an increase of electrical resistivity [22]. In addition, size effects due to reduced dimensionality of the material relative to the mean free path of the electrons increases the resistivity. An increase in resistivity can be attributed to electron scattering at the interface [23], surface of the conducting film [24] and from grain boundaries [25]. Therefore to improve the electrical conductivity a uniform interface or surface is critical.

Studies have shown that sputtering conditions define the minimum thickness, d_{min}, below which a film becomes discontinuous [26]. The growth of a thin film typically begins with

initial island growth. These islands gradually grow and coalesce into an island that comes into equilibrium shape developing a continuous film. Although thinner Pt layer growth has been achieved on other substrates, such as gadolinium gallium garnet (GGG) [27], the minimum continuous Pt film growth on Si/SiO_2 substrate to be achieved is 3nm [22]. Therefore, here we report the conditions for continuous film growth of 2nm by tuning the deposition conditions of thin film thereby improving the quality on Si/SiO_2 substrate using sputtering deposition. The advantage of sputtering over other deposition techniques is that it provides a large deposition source which implies larger deposition area in comparison to other techniques with smaller sources such as thermal or electron beam evaporation.

A continuous Pt film deposition was achieved by varying the sputtering conditions and checking for continuity by measuring the resistance of the grown sample. Details of system description and the findings are discussed below.

6.2.1 System description

The experimental setup is similar to that discussed in chapter 3. Film purity was enhanced by conducting depositions from a base vacuum pressure of 10^{-8} Torr. The sample stage was allowed to rotate to give more uniform coverage as the source is off at the side of the vacuum chamber. This helped to enhanced continuity of film growth during deposition as the sputtered atom flux needs to arrive at the substrate with an optimum energy so as to be able to find the best location to settle. This requires that it loses a certain amount of energy by collision with the working gas in the chamber. Therefore an optimum position was obtained by changing the pressure and all measurements were taken at the same position and pressure for a proper comparison. A 99.99 % Pt target of diameter 2 inches was used and the deposited substrate was thermally oxidised SiO_2 of 27 mm$\times$5 mm dimension. A shadow mask was used to confine the growth to a 25 mm$\times$3 mm area. This helped to keep the dimensions constant for easy calculation of the sample resistivity. The thickness of the film was confirmed by XRR technique.

Electrical measurements for continuity of the film used a four probe resistance measurement method with an ac setup as discussed in section 3.8.4, where the current source used has an

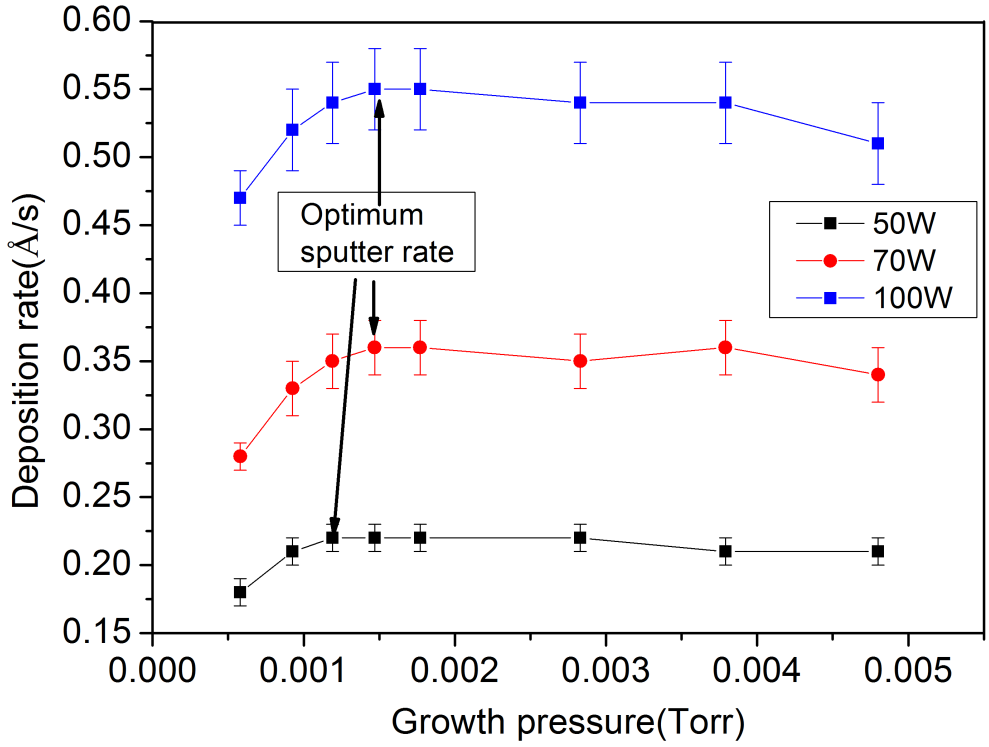

Figure 6.1: A plot of deposition rate of platinum against growth pressure showing the optimum sputter rate for continuous film growth of Pt layer as defined in reference [28].

indicator which confirms the continuity of the film.

6.2.2 Sputtering conditions affecting the continuous film growth

Several condition such as base pressure, growth pressure, sputter power, target and substrate temperature influence the deposition process. Here, the sputtering conditions varied were the sputtering power and the deposition pressure that controls the deposition rate, which depends on the surface binding energy of the materials ejected from the target. The deposition pressure was varied between 0.5 - 5 mTorr by varying the Ar gas flow rate in the chamber. An increase in argon flow leads to an increase in the growth pressure, as the pumping speed is constant. The deposition rate at varying pressures was determined for three power values (50 W, 70 W and 100 W). The substrate temperature was $\sim 20 \pm 1$ °C across all measurements.

As the power is increased the sputtered atoms become more energetic. As the pressure is increased there will be an increased bombardment of the target by Ar ions leading to a higher deposition rate, as shown in figure 6.1. Also a change in the growth pressure leads to an initial

increase in deposition rate with growth pressure, which plateaus at the point where the ion density increase is balanced by more collisions with Ar atoms that causes back diffusion. At the onset of back diffusion increasing the growth pressure results in a decrease in the deposition rate. The point before back diffusion is referred to as the optimum point for film growth which defines the highest achievable deposition rate [28]. The optimum growth pressure obtained here is 1.22 mTorr for 50 W power and 1.48 mTorr for 70 and 100 W. The equality in the growth pressure for a power of 70 W and 100 W suggests an optimum power of 70 W because beyond 70 W, the optimum sputter rate does not improve with pressure. Below 0.5 mTorr, the plasma could not be sustained because the mean free path between the ionising electron-atom collisions was large and the ionisation efficiency was low. A d_{min} of 2 nm was obtained for Pt films grown with a sputter power of 70 W at deposition rate of 0.36 Å/s and a growth pressure of 1.48 mTorr. This was confirmed with a resistivity value of 14.6 $\mu\Omega$cm measured using the four probe electrical measurement technique. Subsequent growth of Pt(2nm) with CFTB exhibited a smooth Pt/CFTB interface with a roughness of $\sim$ 6 Å from XRR measurements. Therefore, a smooth continuous Pt film of 2 nm was achievable. More discussion of the magnetoresistance measurements, which uses the obtained Pt thickness, is discussed later in section 6.5.

6.3 Structural properties of Pt thin film samples

Layer thickness, interface width and density were confirmed with XRR technique. It showed similar properties as the bilayered samples discussed in chapter 5. The nominal thickness quoted for all structural parameters were within an error limit of $\pm$ 6 Å for all samples. The interface roughness is about 0.5 - 0.6 nm, confirming a smooth interface achieved by the Pt deposition method discussed above. The XRD peaks show that the sample is made up of amorphous CFTB with a Pt (111) texture which is stronger for the CFTB/Pt series and weaker in Pt/CFTB sample series. Pt growth on SiO_2 is poor in comparison to CFTB which explains the necessity of the growth deposition procedure. Details on the crystalline properties of the samples have been provided in chapter 5.

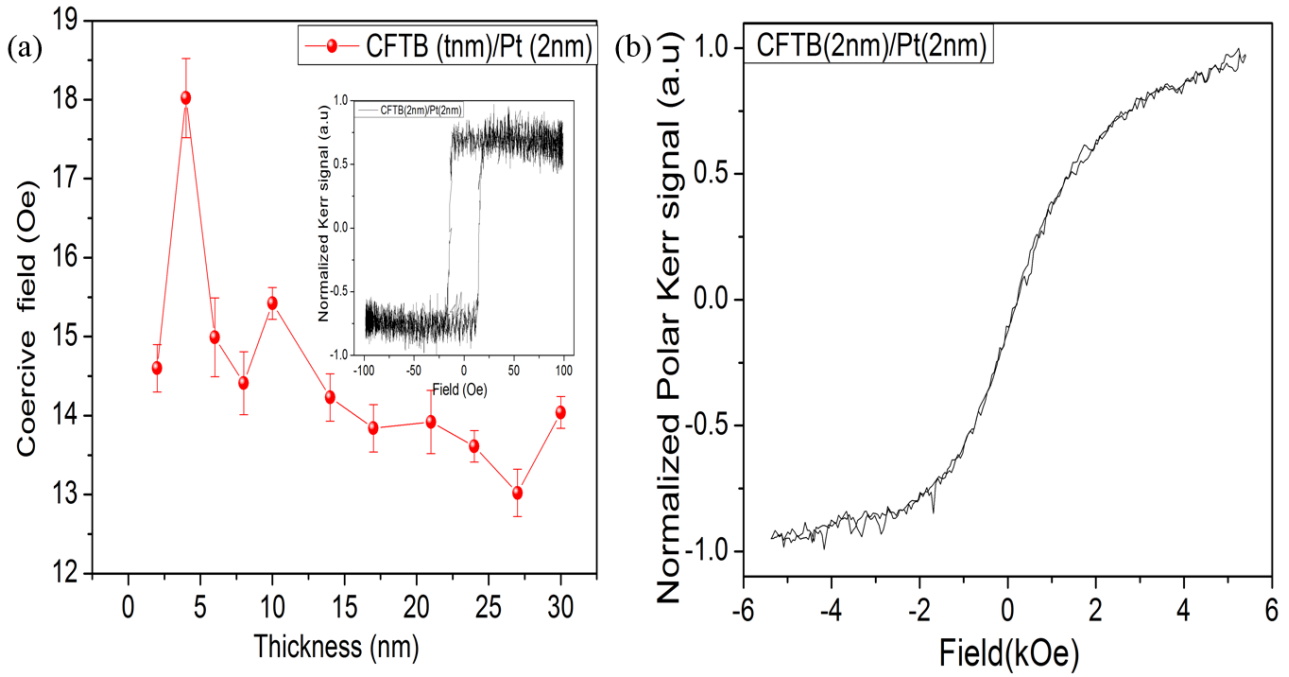

Figure 6.2: (a) A plot of coercive field against CFTB thickness from longitudinal MOKE measurements of the CFTB (t nm)/Pt (2 nm) sample series showing no significant change in coercive field with CFTB thickness. Inset shows the normalised hysteresis loop of a CFTB (2 nm)/ Pt(2 nm) sample used for the bulk of the magnetoresistance discussions showing small in-plane magnetic saturation field.(b) Polar magneto-optical Kerr effect hysteresis loop for CFTB (2nm)/Pt (2nm) showing an out plane hard-axis.

6.4 Longitudinal Magneto-optical analysis

MOKE hysteresis loops were measured as representations of the magnetisation in a film which is justified as the Kerr signal is proportional to the magnetic signal from the sample, as discussed in section 3.4. The magnetic anisotropy within the films may be due to magnetocrystalline, shape or stress anisotropies. According to XRD measurements the FM material is amorphous hence the magnetocrystalline contribution is ruled out. The shape anisotropy contribution is excluded as the samples show similar hysteresis loops independent of shape. It has been reported that factors such as substrate condition, deposition parameter and sample geometry may affect the shape and stress anisotropy [29]. This also explains the reason for the Pt layer deposition procedure discussed earlier in the section 6.2.

Longitudinal MOKE hysteresis loop measurements were conducted by rotating the sample at 45 ° interval and the polar MOKE geometry to investigate the in-plane and out of plane anisotropy effect within the film. The sample size for all measurements was 5 mm×5 mm. The

results of the longitudinal MOKE measurements are shown in the inset of figure 6.2a which presents a distinct magnetic reversal that was similar for all angles of sample rotation. This indicates an isotropic magnetisation behaviour within the samples, suggesting that the samples have an easy plane which is in the plane of the sample. The hysteresis loop measurements exhibits a coercive field of ~ 18 Oe which indicates that the average in-plane magnetic anisotropy is small. A CFTB thickness dependence of coercive field for CFTB (tnm)/ Pt (2nm) series showed a slight dependence on CFTB thickness (see figure 6.2a).

The polar MOKE measurement was conducted at the University of Leeds by Kathryn Moran with a large field of about 6 kOe. The experimental setup for the polar MOKE is similar to that presented in section 3.4.4. The polar MOKE result is presented on figure 6.2b. It can be seen that the out-of-plane magnetisation can be saturated with a magnetic field of about 5 kOe and the samples hard axis of magnetisation is confirmed to be out-of-plane.

These MOKE results are crucial for the magnetoresistance (MR) measurements as they define the magnitude of external magnetic field required to saturate the magnetisation during MR measurements. Resistivity and magnetoresistance measurements obtained and analyses are discussed in the next section.

6.5 Magnetoresistance measurement

Several MR effects described as a change in the resistance of a sample with magnetic field or magnetisation direction have been studied. Some of these effects are giant magnetoresistance (GMR) [30, 31], for which Fert and Grünberg won the 2007 Nobel prize, tunneling magnetoresistance (TMR) [32, 33], colossal MR (CMR) [34, 35], anisotropic magnetoresistance, AMR, [1, 36] and the most recently discovered spin-Hall magnetoresistance, SMR, [3, 16, 17, 27]. These have found application in electronic sensors, data storage devices and microelectromechanical systems [37, 38]. The GMR generates a large MR effect of about 80 % and is designed with alternate layers of FM and NM, such that an alignment of the magnetisation of the FM layers parallel or antiparallel varies the resistance of the sample. The TMR exhibits a similar resistance change as the GMR but designed with an insulating spacer. In the CMR, the resistance change in the

presence of an applied magnetic field is associated with a ferromagnetic to paramagnetic phase transition in manganese-based perovskite oxides. The AMR effect exhibits a resistance change depending on the angle between the direction of the charge current and the magnetisation. Similarly, in SMR the resistance change depends on the angle between the spin-polarisation and the magnetisation, which leads to the generation of a transverse pure spin current. For further details on the theory of SMR, readers are directed to a review paper by Chen *et al.* [7]. SMR had led to other MR effects such as Hanle MR, observed in Pt/ $Y_3Fe_5O_{12}$ (YIG) where the SMR effect changed with applied magnetic field magnitude due to Hanle's effect [39]. Also a nonlinear contribution of higher harmonics was observed in association with AMR and SMR in Ta/Co and Pt/Co by Avci *et al.* and was termed a unidirectional SMR [40]. More focused discussions of AMR and SMR are presented later in this section.

The AMR effect is described as being due to a change in the atomic orbital distribution that is distorted due to the influence spin-orbit coupling. This leads to an asymmetry in spin-dependent scattering. The asymmetry in the spin angular momentum leads to an asymmetric rotation of spins in applied field. When a charge current is applied in the plane of the sample, the direction of the current distorts the orbitals leading to a difference in the scattering cross-section for charge carriers, which results in a change of the resistivity relative to the magnetisation direction. There are certain cases where the AMR may be attributed to the presence of a static PIM or non-equilibrium spin polarisation from the NM layer[15, 16, 27]. The static PIM occurs due to coupling across a FM/NM interface that occurs spontaneously as discussed in chapters 5 and 7. It depends on band hybridisation and the occupancy of the spin-up and spin-down sub-bands around the Fermi level at the interface [41]. The non-equilibrium PIM is induced by external perturbation, such as current flow across the interface which modifies the occupancy of the interfacial spin state. This effect adjusts the chemical potentials of the spin-up and spin-down electrons relative to each other, creating a spin imbalance and polarisation. It is important to note that in the case of a FMI, where there are no states around the Fermi level, there should be no AMR effect. If AMR is present it can be due to the presence of large impurity density, imperfections and roughness which may induce spin states around the Fermi level [41].

Similarly, when a current is applied to a NM material with strong spin-orbit interaction, there

is spin-dependent scattering with accumulated spins of different state at the lateral boundaries as a result of the SHE. The spin scattering leads to a gradient in the chemical potential that results in a change in the longitudinal resistivity known as SMR [42]. The accumulated spins are absorbed as a spin torque in an adjacent FM or FMI layer in a FM/NM stack, or reflected at the FM/NM interface, with the generation of a spin current [3, 7, 16, 17, 27]. The reflected spin current may also be converted to charge current by the inverse spin Hall effect (ISHE) and contributes to the total resistivity of the sample. When the spin polarisation is perpendicular to the direction of magnetisation, the generated transverse spin current is absorbed (high resistivity) and reflected back into the NM layer when the spin polarisation is parallel to the magnetisation direction (low resistivity).

Depending on the mechanism for the spin torque generated, the torque can be categorised as a damping-like (due to SHE) or field-like (due to Rashba effect), as described in section 2.7. Other sources of field-like torque include spin swapping [43, 44], where spin polarised electrons in the FM layer scatters into the NM layer inducing a field-like torque. The spin current transmission across the interface is governed by the spin mixing conductance, $G_{\uparrow\downarrow}$, at the interface, which is described by a complex term, discussed in section 2.7.5. According to Chen *et al.* the effect of $G_{\uparrow\downarrow}$ describes the scattering dynamics that includes the spin current generation in the NM layer, spin current transport across the interface and the spin relaxation dynamics across the interface [3]. The characteristic interfacial structure which decides $G_{\uparrow\downarrow}$ determines the dynamic magnetisation behaviour of the sample [19]. Theoretical investigations by K. Xia *et al.* reveal that the $G_{\uparrow\downarrow}$ can remain very large even in the present of a small conductance and suggested that interfacial disorder may increase both the real and imaginary components of $G_{\uparrow\downarrow}$ [45]. The real part of $G_{\uparrow\downarrow}$ (G_r) is related to direct transmission of spin current through the interface while the imaginary component (G_i) is related to the spin-current precession about the local magnetisation, which could be the magnetisation or NM polarisation across the interface [45]. The imaginary part of $G_{\uparrow\downarrow}$ may be seen as the influence of an exchange field on the spin accumulation, which may result in asymmetric rotation of the spins relative to the magnetic field resulting in a change in resistivity [3]. This is also considered as a field-like torque mechanism. In most SMR investigations this G_i is assumed to vanish because it is negligible and it has been

believed that the different G_i contributions cancel out because it can take both positive and negative values [45]. It is important to note that the spin torque depends on $G_{\uparrow\downarrow}$, but the charge current as in the case of the AMR depends on the conductivity contributed by the individual spin state (i.e $G_{\uparrow}$ and $G_{\downarrow}$). Also, there is no experimental evidence of a detectable influence of the imaginary component in spin mixing dynamics in MR measurements yet reported, which was one of the motivations of this work.

Both AMR and SMR exhibit an angular dependence of the resistivity on direction of magnetisation, but in a case with more complex spin-dependent scattering involving spin flip mechanism, the MR effect deviates from the conventional MR effect observed. Therefore in this section, resistivity change with NM and FM layer thickness in a CFTB/Pt and Pt/CFTB sample stack were investigated. Further discussion on the unconventional MR effect observed in these samples noted above and methods used to decouple the individual MR effects measured are discussed.

6.5.1 Experimental measurement configuration

The samples investigated in this section were sputter deposited under the Pt deposition conditions at ambient temperature as described in section 6.2. Two sample series of Pt/CFTB and CFTB/Pt deposited on SiO_2 substrate with varying CFTB thickness with Pt(2nm) and varying Pt thickness with CFTB(2nm) were fabricated for the studies.

Electrical measurements were conducted using a four probe technique with both an AC setup, as discussed in section 3.8.4, and a DC setup, discussed in section 3.8.3. All measurements were carried out with the current in the plane CIP (longitudinal) geometry along the x axis, as shown on the inset in figure 6.3d, with an applied current of 0.7 mA. The current of 0.7 mA was used in order to improve the signal to noise ratio with less Joule heating in the sample during measurement. Here, Joule heating is a major limitation because when the current is passing through the material, the charge particles are accelerated by the electric field giving up kinetic energy in form of heat which increased proportional to the square current (I^2). Therefore, it is important to apply a current within a controlable limit of Joule heating. The AC measurements

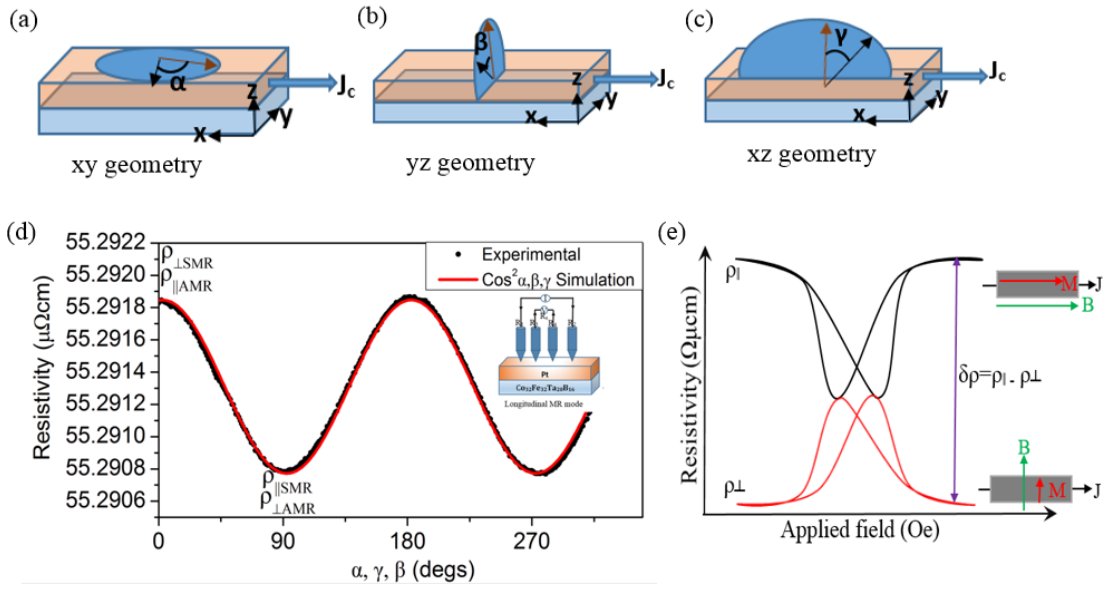

Figure 6.3: Angular-dependent magnetoresistance measurement geometry in (a) xy plane (b) xz plane (c) yz plane (d) Angular dependence magnetoreistance measurement of CoFeTaB(2nm)/Pt(2nm) identifying the relative resistivity as the magnetisation is parallel or perpendicular to the charge current(AMR) or spin polarisation (SMR) for both in-plane and out of plane measurements performed with AC current. The inset shows the longitudinal magnetoresistance measurement mode (e) Schematic of field sweep magnetoresistance showing the resistivity when magnetization is parallel and perpendicular to charge current.

conducted in Durham University were longitudinal in-plane (ip) resistivity measurements carried out at a frequency of 188 Hz with varying NM and FM layer thicknesses. DC measurements on CFTB(2nm)/Pt(2nm) and Pt(2nm)/ CFTB(2nm) were performed by Kathryn Moran in Prof Bryan Hickey's group at the University of Leeds. The DC measurements were performed with the sample rotated with magnetisation in the xy, xz and yz plane, as shown in figure 6.3a, b and c. These three geometries were used to distinguish between AMR, SMR and other contributions embedded in the in-plane AC measurements.

The maximum applied field for all AC measurements was 500 Oe, while that of DC measurement was 20 kOe, which was chosen in order to ensure complete saturation of the magnetisation for the out of plane measurements. Longitudinal resistivity measurements were conducted at room temperature using AC and DC current. The DC measurements where conducted in a cryostat where the temperature was controlled to be $\sim$ 295 K in order to reduce Joule heating during measurement.

Following the AMR and SMR theory, the angular dependent resistivity measurement is

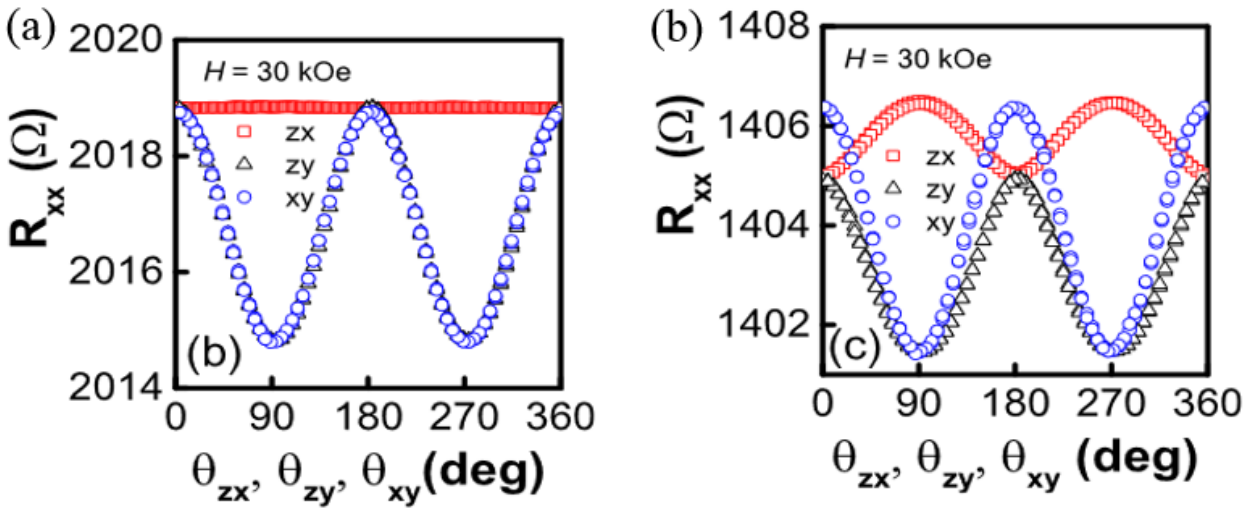

Figure 6.4: Angular-dependent magnetoresistance measurements for (a) FeMn(30Å)/Pt(30Å) bilayer; (b) NiFe(30Å)/Pt(30Å) bilayer from [46] showing the resistance change for xy plane (blue dot), xz plane (red square) and yz plane (black triangle)

shown in figure 6.3d. This is observed as the sample is rotated on a sample stage/stick in an externally applied magnetic field. The in-plane measurement of the xy plane (figure 6.3a) shows an angular dependence consistent with AMR, where the maximum resistivity (0 and 180 deg) represents magnetisation oriented parallel to the charge current density J_c ($\rho_{\parallel}$) and a minimum resistivity (90 and 270 degs) where the magnetisation was oriented perpendicular to J_c ($\rho_{\perp}$). The corresponding MR dependent on magnetic field is illustrated in figure 6.3e where resistivity is maximum/minimum when magnetisation is parallel/perpendicular to charge current. The in-plane resistance is from both AMR, SMR and other MR contributions from the sample. These contributions can be separated by taking out of plane (oop) measurements in the xz (figure 6.3b) and yz (figure 6.3c) geometry. The xz geometry is expected to show a similar profile, but with reduced magnitude, as the in-plane geometry describing the AMR contribution from the sample as shown in figure 6.4 b[47, 48]. It is negligible when there is no AMR in the sample, but SMR as in the case of Pt/YIG [16, 27], Pt/$CoFe_2O_4$ [17] and FeMn/Pt [46] as shown in figure 6.4a. In such cases the MR effect is dominated by the conventional SMR contribution and can be detected by measurements in the yz plane (see figure 6.3c). The conventional SMR contributions exhibits a high resistance (0 and 180 deg) when the spin polarisation on the y axis is perpendicular to the magnetisation and low resistance (90 and 270 degs) in the parallel

orientation as in figure 6.3d and 6.4a.

6.5.2 Dependence of in-plane resistivity on CFTB thickness

The resistivity is calculated from the equation

$$\rho = \frac{\mathrm{RA}}{\mathrm{l}} \tag{6.5.1}$$

where R is the measured resistance, A the area of the sample represented by the product of thickness to sample width and l is the distance between the voltage probes. The change in resistivity is a good representation of the equation

$$\rho(\theta) = \Delta\rho \cos^2(\theta) + \rho_\perp \tag{6.5.2}$$

where $\Delta\rho = \rho_\parallel - \rho_\perp$ as θ represents the angle α between charge current and samples magnetisation on the xy plane. The experimental data collected under an applied magnetic field of 0.5 kOe from an ip rotation is consistent with the expected $\cos^2\alpha$ signature. It shows the characteristics of AMR and SMR, which cannot be distinguished in this geometry.

A plot of $\rho_\perp$ extracted from a best fit of the experimental data with equation 6.5.2 for CFTB(tnm)/Pt(2nm) samples is presented in figure 6.5. The resistivity calculations as a function of CFTB thickness (red dots in figure 6.5a) show a gradually increase with increasing CFTB thickness. This assumes that all of the current passes through the CFTB layer only. The change with thickness suggests that some of the current flows through the Pt layer and there is an interfacial effect.

On the contrary, $\rho_\perp$ calculated as a function of Pt thickness decreases with increase CFTB thickness (black dots in figure 6.5a). This assumes that all current flows through the Pt layer. Here the Pt thicknesses are the same, hence the resistivity should be constant, but that is not the case because some of the current is flowing through the CFTB layer. The resistivity gradually decreases until it flattens out at about 9 $\mu\Omega$cm, close to the reported value for the bulk resistivity of Pt at room temperature ($\sim$ 10 $\mu\Omega$cm [22, 49]).

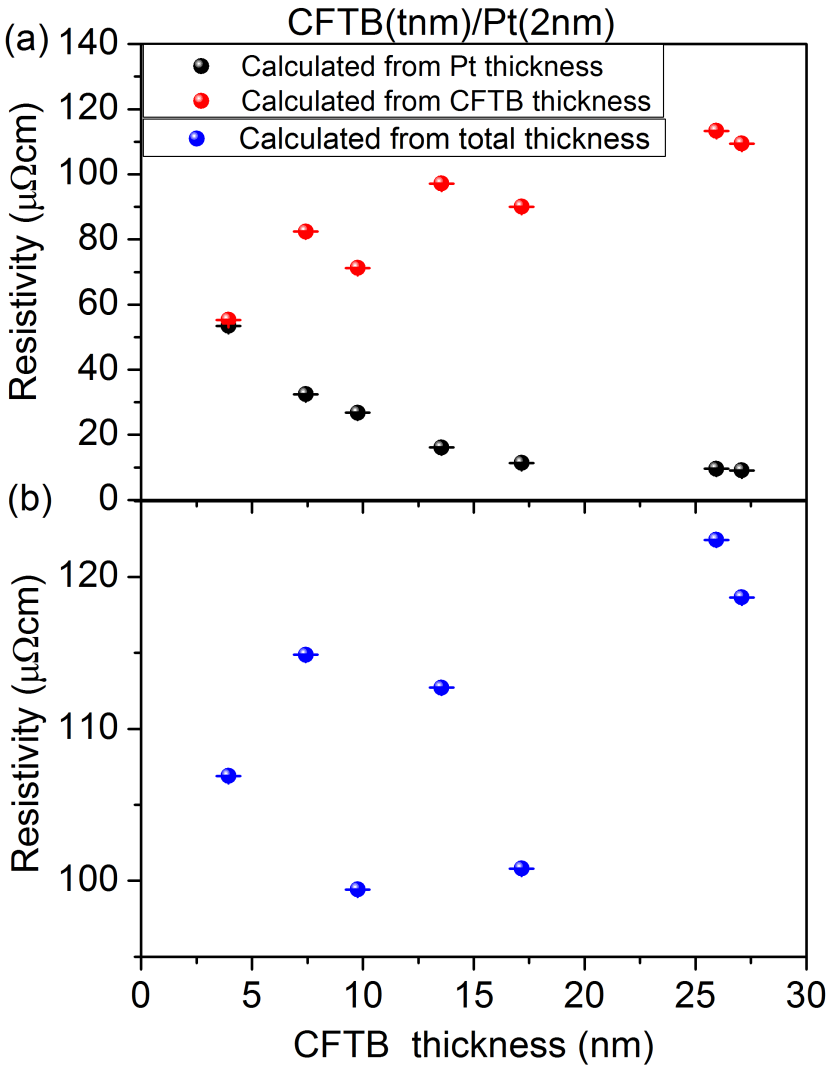

Figure 6.5: The change in resistivity of the sample estimated from (a) Pt thickness (black dots) and CFTB thickness (red dots) (b) total thickness (blue dots) as a function of total thickness where the resistivity values are for $\rho_{\perp}$.

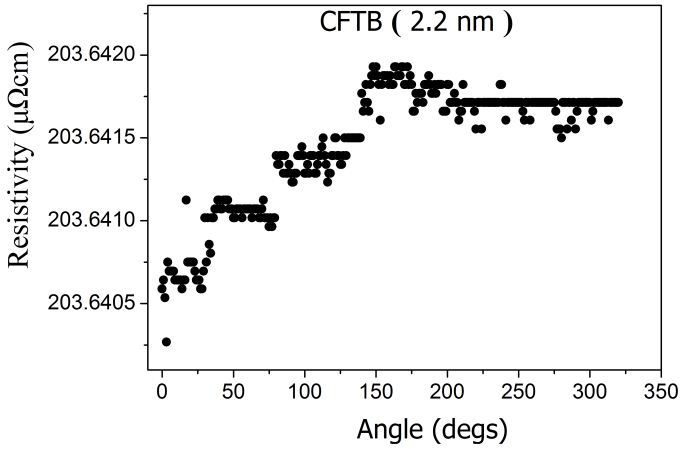

Figure 6.6: Angular dependence magnetoresistance measurement of CFTB (2nm) sample showing that the sample is highly resistive in comparison to a thin Pt layer measured with AC current setup.

Assuming that the current flows evenly through the entire sample, the $\rho_\perp$ shows no significant dependence on thickness as shown in figure 6.5b. The noisy signal in comparison to the Pt thickness plot suggests that the CFTB does not have a uniform resistivity as the thickness changes, possibly due to Ta diffusion within the sample. Ta had been reported to alter the magnetic properties of material creating a dead layer or regions of lower magnetic moment[50]. This explains why thinner CFTB was chosen for the SMR measurements as this leads to maximum current flow through the Pt as the CFTB is about an order of magnitude larger than the multilayer resistivity and shows no angular dependence, as shown in figure 6.6. More on the SMR measurements are discussed later in section 6.5.4. In general, the resistivity obtained in figure 6.5 is lower than that for the CFTB only measurement shown on figure 6.6, which confirms that most of the current flows through the Pt.

The MR is displayed in terms of the ratio defined as

$$\frac{\Delta\rho}{\rho} = \frac{\rho_\parallel - \rho_\perp}{\rho_\perp} \tag{6.5.3}$$

where ρ represents the lowest resistance saturation state, which is different from definition from literatures such as [1] based on the shape of the samples used. The thickness dependence of MR ratio is presented in figure 6.7. It is observed that the MR ratio is larger for thinner CFTB layer thickness as less current flows through the CFTB layer, suggesting that the origin is from the

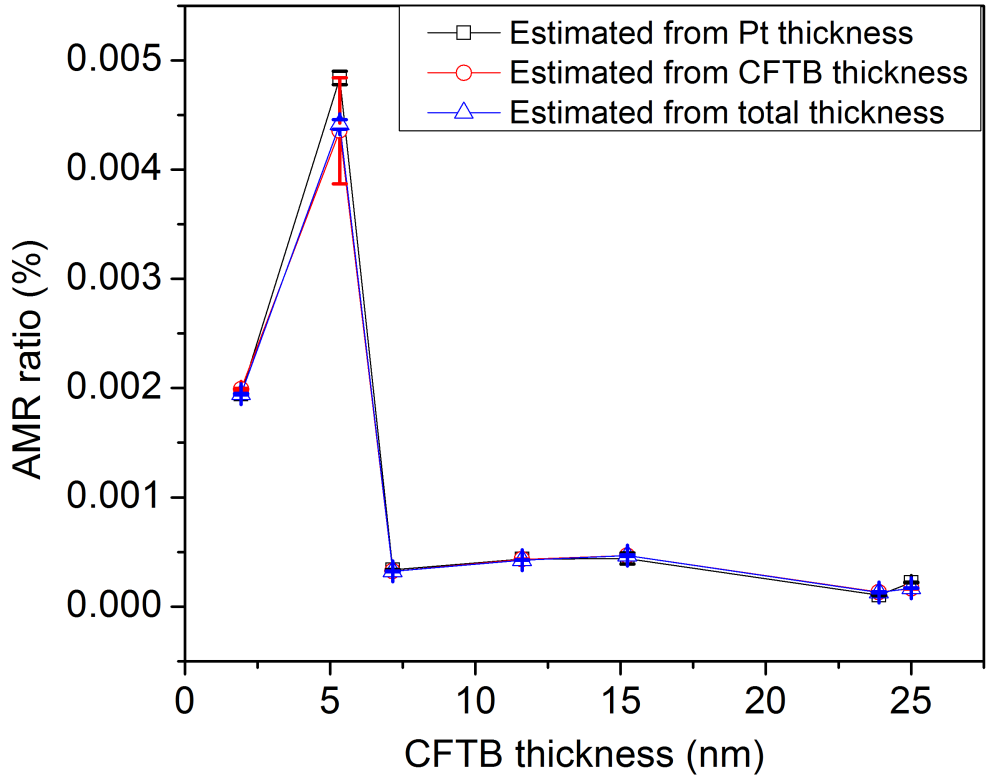

Figure 6.7: Thickness dependence of AMR ratio for CFTB(tnm)/Pt(2nm) measured at room temperature. The solid lines are guided lines for the eyes.

Pt interface. This can also be attributed to the high impact of the increase spin accumulation effect, which decreases as the current shunt through the CFTB layer at increase thickness. This confirms that at thinner CFTB layer thickness, the CFTB is very resistive as the MR ratio is dominated by scattering due to spin accumulation at the interface induced by SHE in the Pt. Therefore thinner CFTB is suitable for SMR investigations. The MR ratio observed is of a similar order of magnitude to the SMR, suggesting a possible contribution due to SHE [16, 17]. Based on this result, further investigations as a function of Pt thickness were conducted on a thin CFTB of 2 nm and discussions are presented in the next section.

6.5.3 Thickness dependent of in-plane resistivity with Pt thickness

The resistivity measurements made on CFTB(2nm)/Pt(tnm) and Pt(tnm)/CFTB(2nm) are presented in figure 6.8a. Here the resistivity calculations assume that all the current flows through the Pt layer as the CFTB layer is highly resistive. The $\rho_{\perp}$ as a function of Pt thickness decays asymptotically with increasing thickness. It is clear that there is a strong correlation

between the film resistivity and Pt thickness. This may be due to in-plane surface confinement which additionally limits the mean free path λ of the conduction electrons. The result also is consistent with spin accumulation at the Pt/CFTB interfaces, as the NM layer becomes larger than the spin diffusion length, which is $\sim$ 1.5 nm in Pt [4, 40, 51]. This reflects the impact of size effect as Pt thickness increases. As the Pt thickness is comparable to λ, there is more scattering leading to increased resistivity. In thin films with thickness $<$ 20 nm, the resistivity contribution is largely attributed to be from scattering from grain boundaries, interface and surface roughness. At the interface, the interfacial electrons from Pt may penetrate the CFTB and are affected by the strong exchange interaction in the CFTB layer. As a result, there may be a change in density of states at the Fermi level in the Pt interface leading to the observed thickness dependence as pointed out by Lu *et al.* [52]. Also, as the in-plane MR effect has contributions from AMR and SMR, it is important to note that the observed high resistivity at thin Pt layer may possibly be due to spin current generation via SHE.

Looking into the difference in resistivity between CFTB(2nm)/Pt(tnm) and Pt(tnm)/CFTB(2nm) samples series, the CFTB(2nm)/Pt(tnm) series exhibit a slightly higher $\rho_{\perp}$ which may possibly be due to different interface structure or Pt structure and grain size. The XRD measurements presented in section 5.2.3, CFTB/Pt samples exhibit a strong Pt (111) texture while Pt/CFTB samples exhibits a weak Pt (111) texture. Meaning, the CFTB/Pt is characterised by larger Pt crystalline grains in comparison to the Pt/CFTB counterpart. Contrary to reports of reduced resistivity for strongly textured or larger gain size sample [53], the results here exhibit a larger resistivity for the CFTB/Pt sample series. This suggests that the difference may be due to scattering from the interface with less contribution from the grain boundaries.

As discussed in section 2.6.1, Fuchs and Sondheimer formulated equations that describes diffuse scattering of conduction electrons in a sample [24, 54]. According to these equations, the resistivity equation that describes the scattering for sample thicknesses larger than the λ is expressed as

$$\rho_{\text{ave}} = \rho_0 \left(1 + \frac{3\lambda}{8\text{t}}\right) \tag{6.5.4}$$

where ρ_0 is the bulk resistivity and t is the thickness.

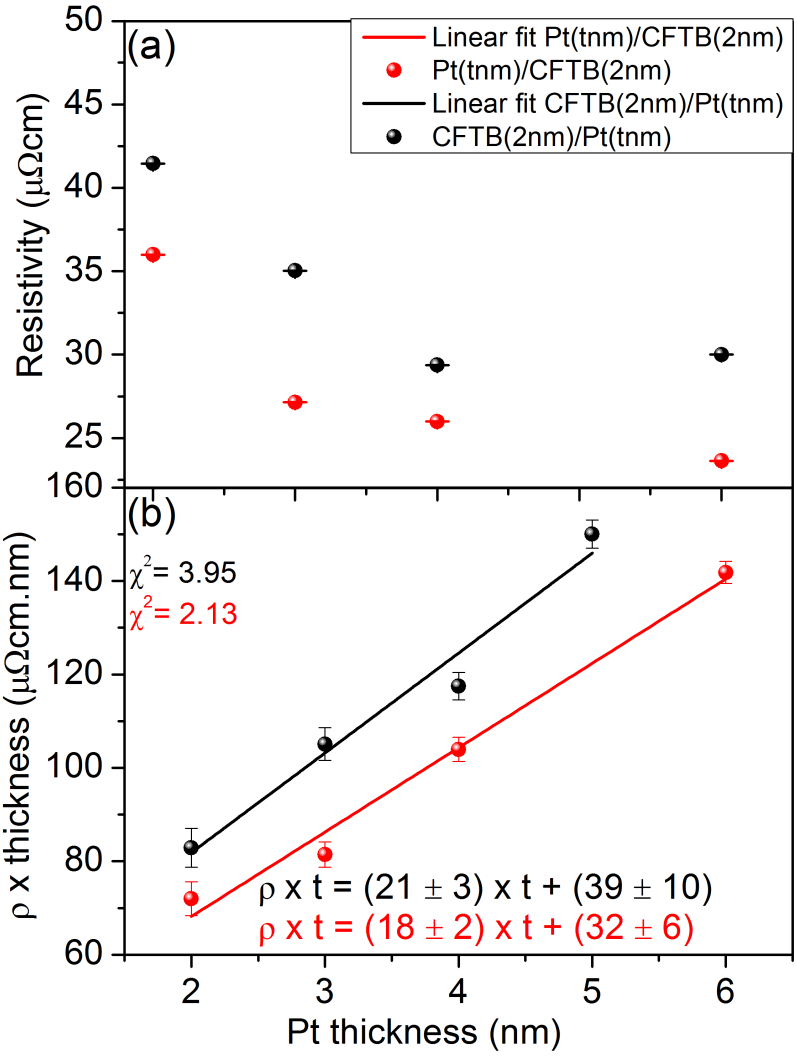

Figure 6.8: (a) Dependence of the transverse resistivity $\rho_{\perp}$ on Pt film thickness in Pt (t nm)/CFTB (2 nm) (red dots) and CFTB (2 nm)/Pt(t nm)(black dots) structures (b) A plot of $\rho_{\text{ave}} * \text{t}$ as a function of Pt layer thickness, t. The linear fit through all data points using the Fuchs-Sondheimer expression exhibits a strong linear dependence. The linear fit equation where the value of the bulk resistivity and mean free path are extracted are shown on the inset.

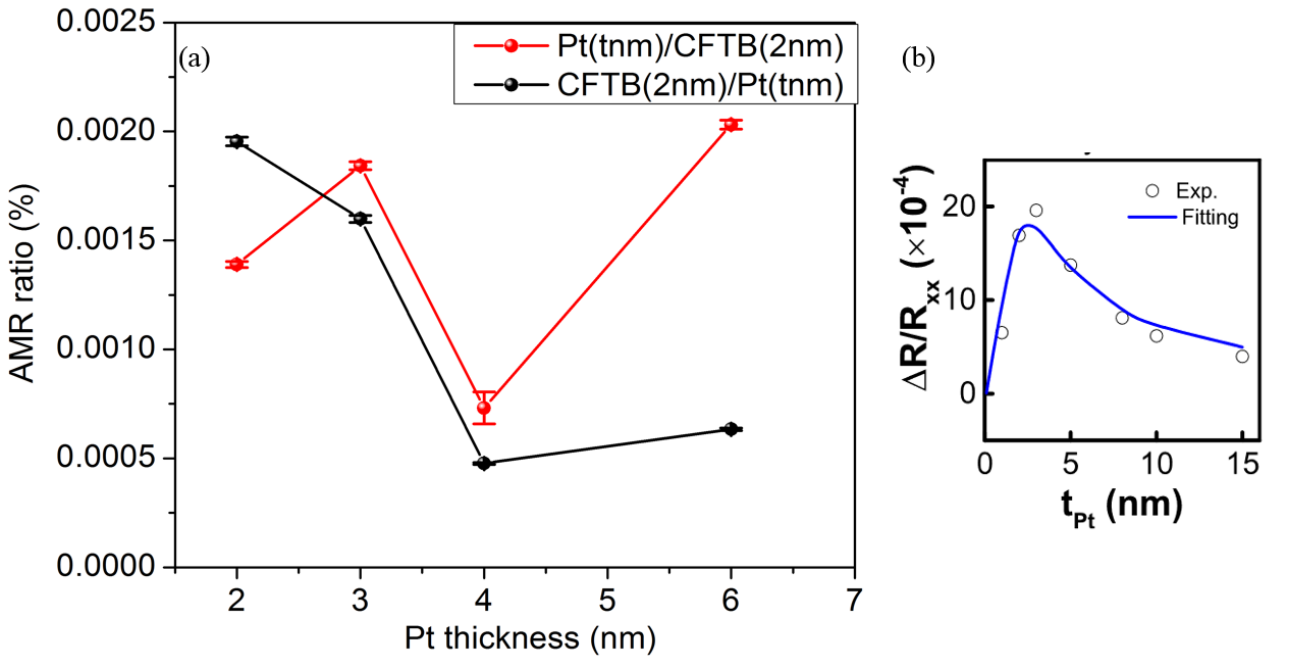

Figure 6.9: A plot of MR ratio value estimated from equation 6.5.3 as a function of Pt thickness for Pt (t nm)/CFTB (2 nm) (red dots) and CFTB(2 nm)/Pt(t nm) (black dots) (b) A typical plot of Pt thickness dependent expected from SMR from [46].

The value of the bulk resistivity and mean free path can be extracted from a linear fit to a plot of $\rho_{ave} \times$ t as a function of Pt thickness using equation 6.5.4. This plot shows a strong linear trend with Pt thickness as presented in figure 6.8b. The values extracted for the CFTB(2nm)/Pt(tnm) samples represented with the black dots in figure 6.8b are $\rho_0 = 21 \pm 3$ $\mu\Omega$cm and $\lambda = 4.9 \pm 1.4$ nm while that of the Pt(tnm)/CFTB(2nm) represented by the red dots are $\rho_0 = 18 \pm 2$ $\mu\Omega$cm and $\lambda = 4.7 \pm 1.8$ nm. The bulk resistivity values extracted are slightly higher than the ~ 10 $\mu\Omega$cm resistivity documented in literature for the bulk resistivity of Pt at room temperature [22, 49]. This is typical of a sputtered film. Also, the mean free path values are significantly larger than the value of 1.2 nm quoted in the literature for Pt [55]. The λ values are similar for both sample series strongly suggesting that the resistance change are of the same origin. For thicknesses less than the mean free path, the Fuchs and Sondheimer formulated equation is expressed as [1]

$$\rho = \rho_0 \frac{4\lambda}{3} \frac{1}{\left(\ln(\frac{\lambda}{t}) + 0.423\right)}. \tag{6.5.5}$$

This model does not fit the above data set, hence the resistivity and mean free path can not be extracted for comparison.

A plot of MR ratio estimated from equation 6.5.3 is presented in figure 6.9a. The MR ratio of CFTB/Pt series slightly increases with decreasing thickness confirming that the magnetic contributions are from the interface as in most metals. It does not show the conventional Pt thickness dependent profile with a peak as shown in figure 6.9b because there are other underlying contributory effects in these samples. The MR ratio is ~ 0.002 % which is comparable with MR ratio observed in SMR experiments [27]. Also thinner samples exhibits a slightly higher MR ratio hence CFTB(2nm)/Pt(2nm) and Pt(2nm)/CFTB(2nm) are chosen for further investigations which will help in the separation of the individual MR contributions. Out-of-plane MR measurements were used to distinguish between the individual MR contributions and are discussed in the next section.

6.5.4 Identifying MR contributions with different origins

It is not possible to distinguish between the AMR and SMR effects with the in-plane measurement geometry. Also since the samples hard axis is out of the sample plane, a higher external magnetic field is required to reverse magnetisation in the oop geometry. Therefore, the measurements presented in this section were conducted at the University of Leeds with a 2 T applied magnetic field, which is larger than the out-of-plane saturation field of the samples. The field was high enough to eliminate domains which can lead to domain decay in remanence hence the system can be considered as a macrospin. Here, three measurement geometries were employed. The xy geometry represents the in-plane sample rotation, the xz geometry is for sample rotation on the xz plane making an angle γ between the charge current and magnetisation and yz geometry represents rotation on the yz plane making an angle β between the spin polarisation σ and magnetisation m. According to the conventional SMR (cSMR) theory, the resistivity is expected to depend on the magnetisation direction on the yz plane and the xz plane for the AMR (see figure 6.10).

For ease of comparison, angular dependent MR analysis was conducted on CFTB(2nm)/Pt(2nm)

and Pt(2nm)/CFTB(2nm) samples to help evaluate the individual MR contributions as well as study the impact of structural inversion on these MR effects. The experimental results and the corresponding sample geometry are shown in figure 6.10. From the experiment with in-plane magnetic field rotation, an angular dependence with a period of 180° is observed. The result follows a $\cos^2\alpha$ dependence according to equation 6.5.2, similar to the thickness dependence results presented earlier in this chapter. Here, the longitudinal resistivity is maximum for charge current J_c direction parallel (90°) and antiparallel (270°) to sample magnetisation and minimum when J_c is perpendicular to direction of magnetisation (0° and 180°). The resistivities were calculated using the total nominal field thickness and the individual voltage probe spacing according to equation 6.5.1. The difference between the obtained value of resistivity in figures 6.10 and 6.3 is because the resistivity in figure 6.3 is calculated using the Pt thickness only while that of figure 6.10 uses the total thickness of the material.

At this point it is important to define the field direction relative to the sample for the out of plane measurement. This will help in better understanding of the MR profile. The 0° point is when the magnetic field is perpendicular to J_c or σ with the magnetic field pointing towards the substrate (front) and the 180° is when the magnetic field is perpendicular to J_c or σ with magnetic field pointing away from the substrate (back). The results of the out-of-plane (oop) measurements performed with the field rotating along xz and yz plane deviates from the $\cos^2\theta$ dependence. The oop MR profile can be represented with a longitudinal resistivity expressed as

$$\rho(\theta) = a\cos^2\theta + b\cos\theta + \rho_\perp \tag{6.5.6}$$

where θ is the angle between J_c and the magnetisation in the case of AMR and angle between spin polarisation σ and magnetisation for SMR. The factors a and b are constants relating to the individual $\cos^2\theta$ and $\cos\theta$ contributions respectively. It is obvious that the observed profile represents a superposition of a $\cos^2\theta$ and $\cos\theta$ dependence for both oop measurements. Equation 6.5.6 captures the MR angular dependence observed for the oop measurements. The $\cos^2\theta$ dependence represents the cMR profile while the $\cos\theta$ dependence the unconventional MR (uMR) contributions. The uMR effect acts as a force pulling the generated spin current in

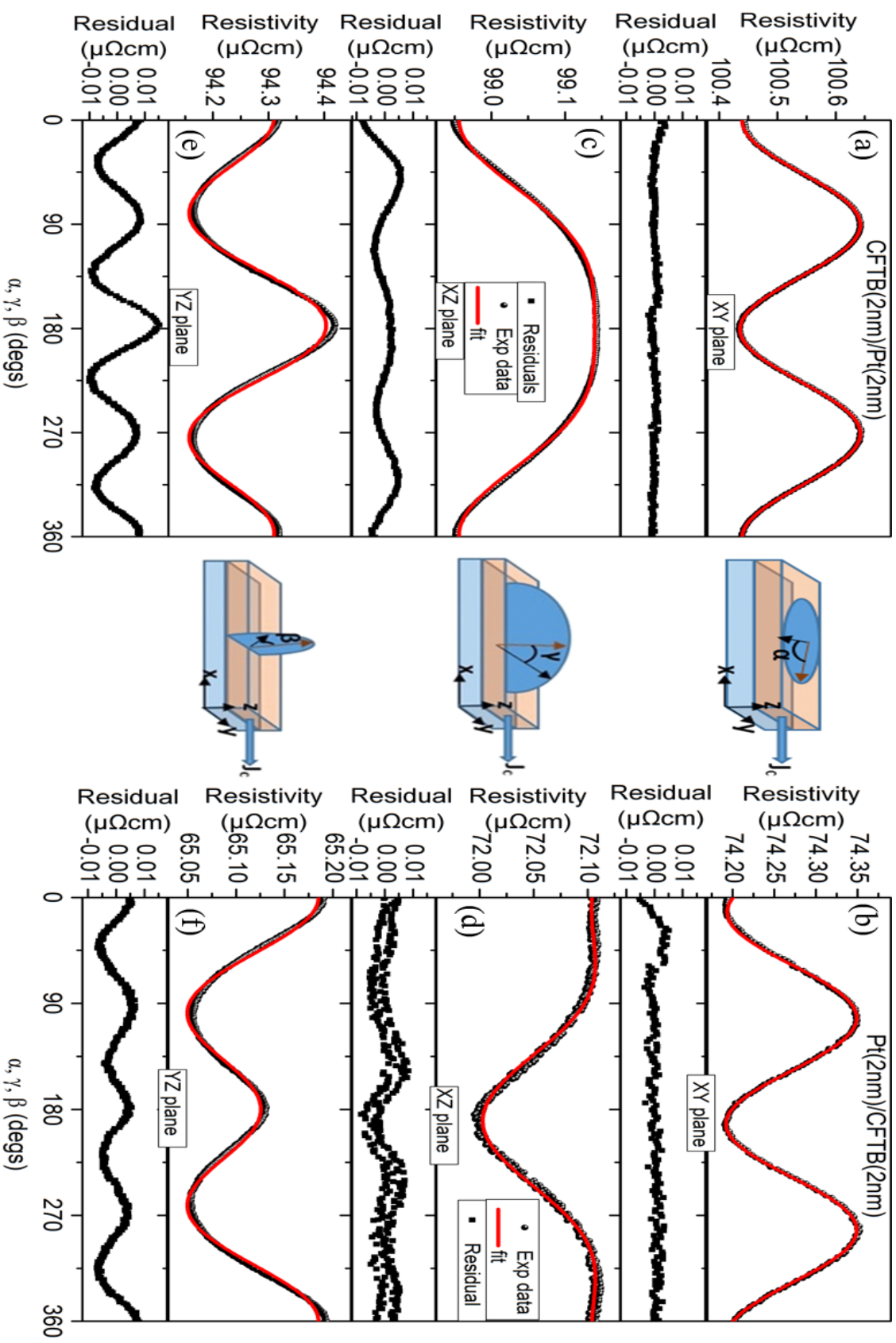

Figure 6.10: Angular-dependence magnetoresistance measurements for CFTB(2nm)/Pt(2nm) and Pt(2nm)/CFTB(2nm) sample where (a) and (b) are with rotating magnetic field in the xy plane, (c) and (d) are rotating in the xz plane and (e) and (f) are in the yz plane. The red lines are the best fit simulation of equation 6.5.6. The central panel sketches indicate the rotation of magnetic field defined by angles α, γ and β.

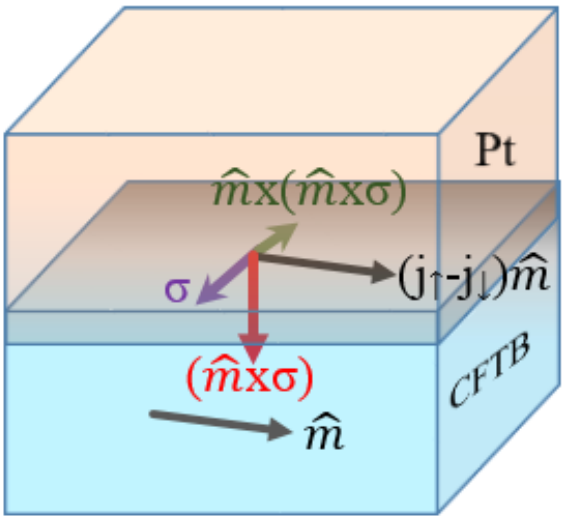

Figure 6.11: Spin-current relaxation mechanism at the interface showing the direction of electric current $(J_\uparrow - J_\downarrow) \times \hat{m}$, spin polarisation σ, damping-like torque $\hat{m} \times (\hat{m} \times \sigma)$ (described by G_r) and field-like torque $(\hat{m} \times \sigma)$(described by G_i).

the plane of the sample thereby causing precession, which has been theoretically modeled as a crystal field by Cahaya *et al.* [11]. This effect is significantly small in the ip plane but larger in the oop measurements.

As earlier stated, the change in magnetisation observed is governed by the spin mixing conductance $G_{\uparrow\downarrow}$ which is a sum of the G_r and G_i [56]. The observed change in resistivity depends on the relative orientation of the magnetisation and the torques experienced by the electron spin as pointed out by Zhang *et al.* [14]. When an electric current is applied to a FM/NM structure, a damping-like torque due to SHE expressed as $\hat{m} \times (\hat{m} \times \sigma)$ and field-like torque due to Rashba effect expressed as $\hat{m} \times \sigma$ have been reported where the $\hat{m}$ is the magnetisation vector. The origin of these effects are from G_r, as it results in direct transmission of the spin current through the interface. In SMR theory, G_i is usually assumed to be negligible and hence ignored in all calculations as it had been observed to be negligibly small in YIG/NM [57, 58]. Here, the uMR is attributed to a contribution due to the G_i, which is significantly large in these samples. The influence of G_i is characterised by the precession of the spin current generated, yielding a field-like torque $\hat{m} \times \sigma$ that can be absorbed or reflected at the interface as shown in figure

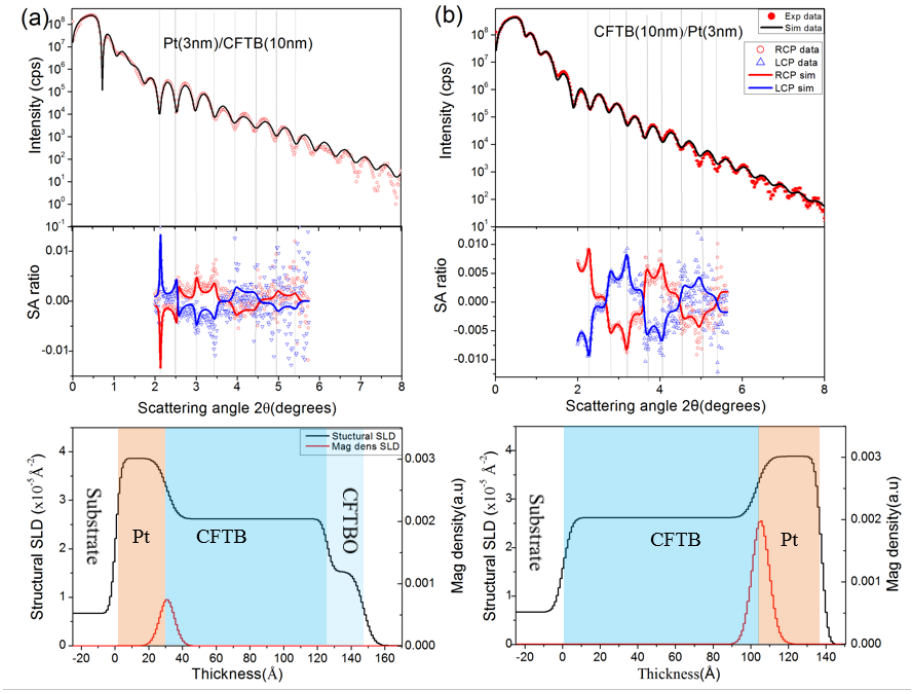

Figure 6.12: XRMR reflectivity (top panel), spin asymmetry ratio(middle panel) and scattering density profile of (a) Pt(3nm)/CFTB(10nm) (b) CFTB(10nm)/Pt(3nm) showing the variation in magnitude of Pt polarisation. Simulations were performed using `diff` FOM

6.11. The transmission of this torque leads to the observed change in resistivity that exhibits a $\cos\theta$ dependence. A model of G_i as an interface effective field by Cahaya *et al.* suggested the effect to be controlled by the local moment and would likely affect the spin torque efficiency [11]. This is exactly what is observed in figure 6.10 as the spin torque mechanism deviates from the conventional $\cos^2\theta$ dependence. Also, Pt polarisation has been observed in these samples (discussed in chapter 5), which can act as a local moment enhancing the precession of the generated spin current. The magnitude of the observed Pt polarisation is larger in the CFTB/Pt in comparison to Pt/CFTB as shown in figure 6.12. This explains the origin of the uMR observed in the xz plane.

According to equation 6.5.6, the conventional MR ratio is represented by the ratio $a/\rho_\perp$ while $b/\rho_\perp$ represents the unconventional MR contribution. The extracted MR values from a fit of equation 6.5.6 to the experimental data, represented by the red lines in figure 6.10, are summarised in table 6.1. The ratio of the change in resistance due to cMR to uMR in the plane of the sample is 104 ± 5 for CFTB(2nm)/Pt(2nm) and 222 ± 6 in Pt(2nm)/CFTB(2nm). This indicates that the uMR contribution is negligibly small in the in-plane measurement.

In the xz plane MR measurement (figure 6.10c and d), the resistivity change due to $\cos\theta$ is much larger than the $\cos^2\theta$ contribution. The $\cos^2\theta$ contribution is attributed to spin polarisation of Pt which leads to the generation of a spin polarised current, which contaminates the pure spin current generation [17]. This effect is here defined as the conventional AMR (cAMR) contribution. This effect has been reported to be significantly large in Pt/Co and Ta/Co because some of the current is shunted through the FM layer [48]. The unconventional spin Hall magnetoresistance uSMR is attributed to the imaginary component of the spin mixing conductance as explained above. In chapter 5, Pt polarisation was confirmed to be present in these samples which validates these arguments on the presence of a local magnetic moment. The ratio of the change in resistivity in cAMR to the uSMR for CFTB(2nm)/Pt(2nm) and Pt(2nm)/CFTB(2nm) are $\sim 0.5 \pm 0.01$ and $\sim 0.7 \pm 0.01$ respectively, suggesting that the uSMR signal is large. The cSMR is a response due to spin current generation which is transmitted or reflected at the interface as a result of the action, or inaction of the damping-like torque in enabling absorption, of the spin current. This is described by the G_r, but the uSMR contribution is characterised by G_i, mediated by the precession of the spin current at the interface, creating a field-like torque which is absorbed changing the resistivity.

Similarly, measurements done with sample rotation along yz plane exhibits both the cSMR and uSMR with a larger conventional SMR (cSMR) compared to the unconventional SMR (uSMR) contribution. This observed result also shows the change in resistivity due the precession of the spin current at the interface. The ratio of cSMR to uSMR is 4.17 ± 0.05 and 3.47 ± 0.04 for CFTB(2nm)/Pt(2nm) and Pt(2nm)/CFTB(2nm) respectively. According to table 6.1, the cMR ratio is dominated with cSMR of $\sim 0.2\%$ which is larger than values observed in most SMR experiment with an $\sim 0.05\%$ uSMR contributions for both sample structure studies. The cSMR in CFTB(2nm)/Pt(2nm) is slightly higher than that of the Pt(2nm)/CFTB(2nm). This difference may be attributed to differences in the interface texture, as had been discussed in chapter 5. The XRD measurements (not shown) indicate a structural difference due to the crystalline structure of the Pt in CFTB(2nm)/Pt(2nm) and Pt(2nm)/CFTB(2nm), where the Pt texture in Pt(2nm)/CFTB(2nm) is weak. This can significantly modify the spin mixing conductance at the interface. Also, the XRMR results reveal an asymmetry in the Pt polarised moment for the

Table 6.1: Magnetoresistance parameters extracted from the best fit of equation 6.5.6 showing the percentage composition of the conventional(cMR) and unconventional MR (uMR) contributions for fields on xy, yz and yz geometry.

Sample	Rotation plane	$\rho_\perp$ ($\mu\Omega$cm)	a ($\mu\Omega$cm)	b ($\mu\Omega$cm)	a/b	$a/\rho_\perp$(%)	$b/\rho_\perp$ (%)
CFTB(2nm)/Pt(2nm)	xy	100.6424 ± 0.0001	0.2047 ± 0.0001	0.0019 ± 0.0001	104 ± 5	0.2079 ± 0.0001	0.0019 ±0.0001
	xz	99.0923 ± 0.0004	0.0444 ± 0.0006	0.0923 ± 0.0003	0.45 ± 0.01	0.0499 ± 0.0006	0.0897 ± 0.0003
	yz	94.1555 ± 0.0006	0.1968 ± 0.0011	0.0467 ± 0.0002	4.17 ± 0.05	0.198 ± 0.001	0.0495 ± 0.0005
Pt(2nm)/CFTB(2nm)	xy	74.3488 ± 0.0002	0.1556 ± 0.0003	0.0007 ± 0.0002	222 ± 6	0.2093 ± 0.0004	0.0009 ± 0.0003
	xz	72.0862 ± 0.0003	0.0364 ± 0.0004	0.0504 ± 0.0002	0.72 ± 0.01	0.0472 ± 0.0006	0.0681 ± 0.0003
	yz	65.0516 ± 0.0004	0.1037 ± 0.0006	0.0298 ± 0.0003	3.47 ± 0.04	0.157 ± 0.001	0.0459 ± 0.0005

Table 6.2: Magnetoresistance parameters extracted from the best fit of equation 6.5.6 obtained from figure 6.13 confirming that there is no Rashda effect.

Sample	Rotation plane	$R_\perp$ ($\mu\Omega$cm)	a ($\mu\Omega$cm)	b ($\mu\Omega$cm)	a/b	$a/R_\perp$(%)	$b/R_\perp$ (%)
CFTB(2nm)/Pt(2nm)/CFTB(2nm)	xy	155.6429 ± 0.0003	0.5245 ± 0.0004	0.0008 ± 0.0002	656 ± 164	0.3369 ± 0.0003	0.0005 ± 0.0001
	xz	144.9163 ± 0.0003	0.0151 ± 0.0004	0.0452 ± 0.0003	0.33 ± 0.01	0.0104 ± 0.0003	0.0312 ± 0.0002
	yz	185.6516 ± 0.003	0.613 ± 0.002	0.0494 ± 0.0001	12.41 ± 0.25	0.3302 ± 0.001	0.0266 ± 0.0005

samples, which may possibly explain the observed results. The uMR is significantly smaller for the in-plane geometry and is different from the unidirectional SMR(USMR) effect reported in [47]. For all out of plane measurements the uMR is $\sim 0.1\%$, which again strongly suggests that the $\cos\theta$ contribution in both xz and yz geometry are of the same origin.

In order to confirm the origin of observed MR, an MR measurement with changing current direction was conducted. Results show a consistent profile for both positive and negative applied current which confirms that the observed MR effect does not depend on current polarity as observed in a NM/FM system in [47, 59]. The current dependent profile is shown in appendix A. A change in the magnetic field direction yields a reversal in the MR profile, indicating a strong coupling of the effect to the samples magnetisation.

As an additional check to validate the argument above, MR measurement was conducted on a CFTB(2nm)/Pt(2nm)/CFTB(2nm) sample. The MR effect is similar to those of the bilayered samples confirming that the effect is not of Rashba effect origin. Results are shown in figure 6.13 and the extracted parameter is as sated on table 6.2. It is reported that Rashba effect is due to symmetry breakage at the interface and therefore as such the effect should cancel out in a symmetric sample which is not the case in this sample. Also, the residuals plots show the presence of a higher harmonic contribution that is significant only in the yz plane. On the xz plane, no higher harmonics MR contributions was observed in the bilayered sample. At this instant the reasons for this cancellation effect is unclear.

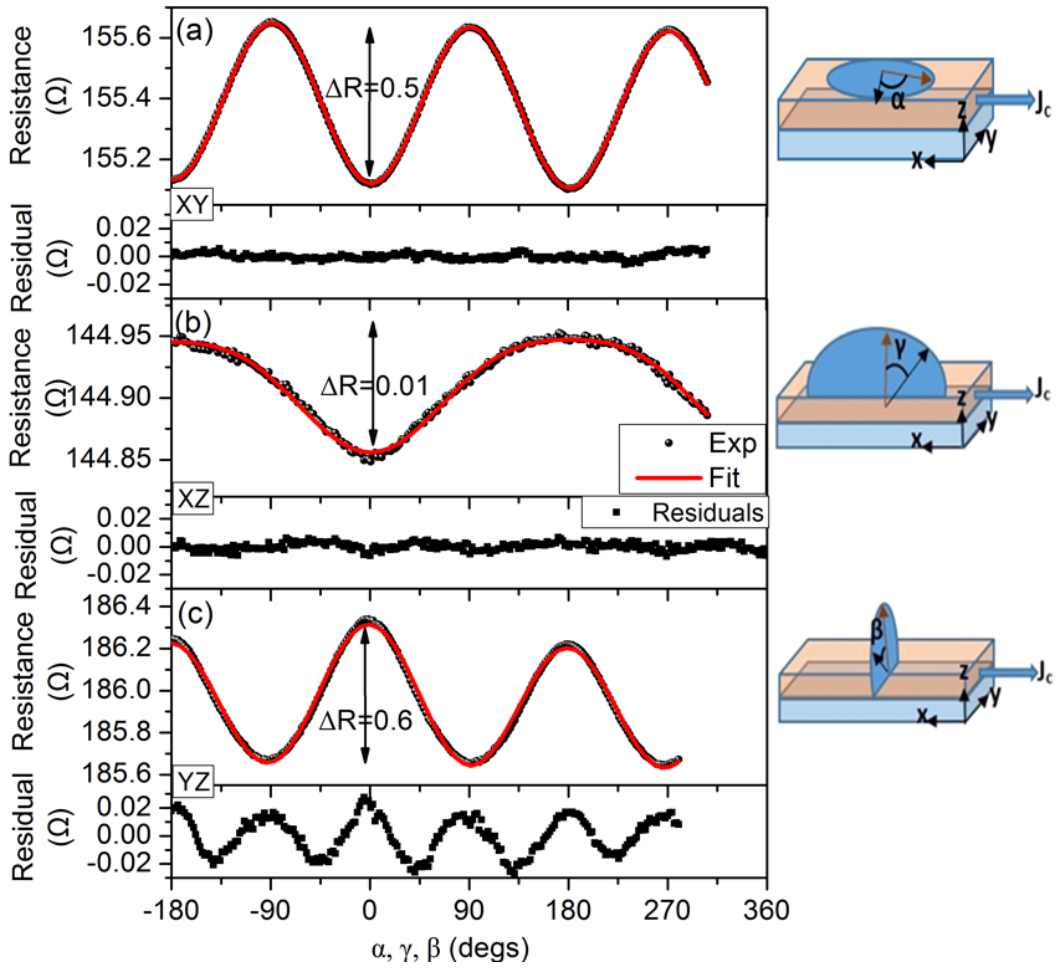

Figure 6.13: Magnetisation rotation measurement of longitudinal resistance signal for CFTB(2nm)/Pt(2nm)/CFTB(2nm) with magnetic field rotated in (a) xy plane (b) xz plane and (c) yz plane demonstrating that the observed MR effect is not of Rashba origin. The red lines is a fit of equation 6.5.6.

6.6 Possible anomalous Hall effect contribution

According to Isasa *et al.*, the angular dependence of the longitudinal, ρ_{L} and transverse ρ_{T} resistivity is described by equation [60]

$$\rho_{\mathrm{L}} = \rho_{\perp} + \Delta\rho_1(1 - \mathrm{m}_{\mathrm{y}}^2) \tag{6.6.1}$$

and

$$\rho_{\mathrm{T}} = \Delta\rho_1 \mathrm{m}_{\mathrm{x}}\mathrm{m}_{\mathrm{y}} + \Delta\rho_2 \mathrm{m}_{\mathrm{z}} \tag{6.6.2}$$

where equation 6.6.1 is the same as equation 6.5.2 shown earlier, $\Delta\rho_2$ accounts for the anomalous Hall-like component with a cosine dependence of magnetisation and $\mathrm{m}_{\mathrm{x,y,z}}$ is magnetisation in (x,y,z) direction. Since the contacts for the DC measurements were done using nano-wire bonding, if there is a misalignment whereby the contacts are not on a straight line, there may be a pick-up of some transverse resistivity component along with the longitudinal resistivity measurement. From equation 6.6.2, the transverse component of $\Delta\rho_2$ in z-direction may lead to the additional cosine signal obtained in the xz and yz plane. Here, the cosine signal is significant only in the xz and yz plane and they are of similar magnitude. Therefore the obtained cosine signal may be due to anomalous Hall effect caused by misalignment of the probes. This experimental artefact may be ruled out only if the samples are fabricated as Hall bars and the wire bonding is done to the labeled terminals as shown on appendix B.1 and not to the sample slab. This will enable the measurement of the anomalous Hall effect contributions by measuring the transverse resistivity and comparing the obtained value to the uMR reported in this thesis.

6.7 Other contributions

Residual plots of SMR measurements have not been commented on in the literature, but this could be very insightful as it can show possible MR contributions from different sources. Therefore, a plot of the residuals from the MR signals in figure 6.10 was performed and indicates the presence of contributions of higher harmonics. The observed contribution is negligible in

the in-plane measurements but of a higher and approximately the same magnitude for both out-of-plane measurements. The residual plots are presented as the lower frame to each labeled magnetoresistance measurements in figure 6.10. This effect may be of a similar origin as the uMR observed earlier in section 6.5.4. Avci *et al.* has reported the presence of a second harmonic contribution in Co/Pt and Co/Ta bilayers, which was attributed to other non-equilibrium spin accumulation effects [47, 48]. This strongly agrees with our findings, as the precession of the spin current defined by G_i is one of such non-equilibrium spin accumulation effects. Avci *et al.* observed that USMR is nonlinear in current direction, but in this case the higher order angular term due to uSMR is observed to shows an angular dependence with magnetization. In addition, van Gorkom *et al.* have also reported the presence of second and fourth order MR angular dependence, which does not follow the usual $\cos^2\theta$ profile and dependents on the crystal symmetry that leads to more defect dominated scattering than phonon dominated scattering [61]. Therefore, it is possible that the fourth harmonic observed in the residual plots may be from the crystal symmetry of the textured Pt layer reported earlier as they are slightly different. As earlier mentioned, this has not been considered in most SMR measurement which indicates that there may possibly be some other contributions in the observed SMR results reported in the literature.

AMR effect has also been reported to be dependent on the crystallographic orientation of materials [1, 62, 63]. Although the crystalline texture of Pt in CFTB/Pt and Pt/CFTB differs following the XRD measurement in chapter 5, which suggests that the scattering mechanism at the interfaces may likely be different but the observed uMR magnitude are approximately the same for both samples in the out of plane geometries. Therefore, the influence of Pt texture is excluded as one of the contributions here.

6.8 Summary

In summary, an unconventional magnetoresistance response has been observed in CFTB(2nm)/ Pt(2nm), Pt(2nm)/CFTB(2nm) and the trilayer samples which exhibits the conventional AMR and SMR reported in literatures with an additional contribution. The Pt structural properties

are similar to those discussed in chapter 5. The Pt/CFTB exhibits a weak FCC (111) texture while the CFTB/Pt samples have a strong (111) texture with the CFTB layer amorphous.

Magnetic characterisation with longitudinal MOKE show a coercive field of 20 Oe and for a polar MOKE shows a hard axis with saturation field of 5 kOe. Therefore the applied in-plane magnetic field for longitudinal resistivity measurement conducted on CFTB(tnm)/Pt(2nm), CFTB(2nm)/Pt(tnm) and Pt(tnm)/CFTB(2nm) was 500 Oe and that of the out of plane MR measurement was 20 kOe, which is much greater than the coercive field of the samples.

It was observed that in all in-plane measurement, the MR ratio is larger for samples with thinner CFTB and Pt layer. Therefore further MR measurements included out-of-plane measurements were conducted on CFTB(2nm)/Pt(2nm) and Pt(2nm)/CFTB(2nm) which exhibited a $\cos^2\theta$ and $\cos\theta$ dependence. The $\cos^2\theta$ dependence indicates that the in-plane MR response is dominated by MR response due to SHE, with a ratio of 0.2 %, which is larger than values reported in the literature. The additional $\cos\theta$ dependence is assumed to be due to the imaginary component of the $G_{\uparrow\downarrow}$, which is as a result of the precession of the spin current causing a slight canting of the angle between the spin polarisation and charge current with magnetisation. This causes a torque with a field-like symmetry, rather than a damping-like torque. Engineering of this field-like torque may be a route to improve efficiency in spin-orbit torque devices and could be used as a read out in a simplified magnetic memory device structure as the read and write head requires a simple bilayer structure contrary to the multiple layer stakes used in conventional read and write heads.

References

[1] T. McGuire and R. Potter, "Anisotropic magnetoresistance in ferromagnetic 3d alloys," *IEEE Transactions on Magnetics*, vol. 11, no. 4, pp. 1018–1038, 1975.

[2] I. A. Campbell, A. Fert, and O. Jaoul, "The spontaneous resistivity anisotropy in ni-based alloys," *Journal of Physics C: Solid State Physics*, vol. 3, no. 1S, p. S95, 1970.

[3] Y.-T. Chen, S. Takahashi, H. Nakayama, M. Althammer, S. T. Goennenwein, E. Saitoh, and G. E. Bauer, "Theory of spin Hall magnetoresistance," *Physical Review B*, vol. 87, no. 14, p. 144411, 2013.

[4] C. Hahn, G. De Loubens, O. Klein, M. Viret, V. V. Naletov, and J. B. Youssef, "Comparative measurements of inverse spin Hall effects and magnetoresistance in YIG/Pt and YIG/Ta," *Physical Review B*, vol. 87, no. 17, p. 174417, 2013.

[5] S.-Y. Huang, X. Fan, D. Qu, Y. Chen, W. Wang, J. Wu, T. Chen, J. Xiao, and C. Chien, "Transport magnetic proximity effects in platinum," *Physical Review Letters*, vol. 109, no. 10, p. 107204, 2012.

[6] Y. Kato, R. Myers, A. Gossard, and D. Awschalom, "Observation of the spin Hall effect in semiconductors," *Science*, vol. 306, no. 5703, pp. 1910–1913, 2004.

[7] Y.-T. Chen, S. Takahashi, H. Nakayama, M. Althammer, S. T. Goennenwein, E. Saitoh, and G. E. Bauer, "Theory of spin Hall magnetoresistance (SMR) and related phenomena," *Journal of Physics: Condensed Matter*, vol. 28, no. 10, p. 103004, 2016.

[8] T. Kimura, Y. Otani, T. Sato, S. Takahashi, and S. Maekawa, "Room-temperature reversible spin Hall effect," *Physical Review Letters*, vol. 98, no. 15, p. 156601, 2007.

[9] A. T. Hindmarch, "Interface magnetism in ferromagnetic metal–compound semiconductor hybrid structures," in *Spin*, vol. 1, pp. 45–69, World Scientific, 2011.

[10] J.-C. Rojas-Sánchez, N. Reyren, P. Laczkowski, W. Savero, J.-P. Attané, C. Deranlot, M. Jamet, J.-M. George, L. Vila, and H. Jaffrès, "Spin pumping and inverse spin Hall effect

in platinum: the essential role of spin-memory loss at metallic interfaces," *Physical Review Letters*, vol. 112, no. 10, p. 106602, 2014.

[11] A. B. Cahaya, A. O. Leon, and G. E. Bauer, "Crystal field effects on spin pumping," *Physical Review B*, vol. 96, no. 14, p. 144434, 2017.

[12] M. Weiler, M. Althammer, M. Schreier, J. Lotze, M. Pernpeintner, S. Meyer, H. Huebl, R. Gross, A. Kamra, J. Xiao, *et al.*, "Experimental test of the spin mixing interface conductivity concept," *Physical Review Letters*, vol. 111, no. 17, p. 176601, 2013.

[13] C. Chappert, A. Fert, and F. N. Van Dau, "The emergence of spin electronics in data storage," *Nature Materials*, vol. 6, no. 11, p. 813, 2007.

[14] S. S.-L. Zhang, G. Vignale, and S. Zhang, "Anisotropic magnetoresistance driven by surface spin-orbit scattering," *Physical Review B*, vol. 92, no. 2, p. 024412, 2015.

[15] N. Vlietstra, J. Shan, V. Castel, B. Van Wees, and J. B. Youssef, "Spin-Hall magnetoresistance in platinum on yttrium iron garnet: Dependence on platinum thickness and in-plane/out-of-plane magnetization," *Physical Review B*, vol. 87, no. 18, p. 184421, 2013.

[16] H. Nakayama, M. Althammer, Y.-T. Chen, K. Uchida, Y. Kajiwara, D. Kikuchi, T. Ohtani, S. Geprägs, M. Opel, S. Takahashi, *et al.*, "Spin Hall magnetoresistance induced by a nonequilibrium proximity effect," *Physical Review Letters*, vol. 110, no. 20, p. 206601, 2013.

[17] M. Isasa, A. Bedoya-Pinto, S. Vélez, F. Golmar, F. Sánchez, L. E. Hueso, J. Fontcuberta, and F. Casanova, "Spin Hall magnetoresistance at Pt/$CoFe_2O_4$ interfaces and texture effects," *Applied Physics Letters*, vol. 105, no. 14, p. 142402, 2014.

[18] A. Kobs and H. P. Oepen, "Disentangling interface and bulk contributions to the anisotropic magnetoresistance in Pt/Co/Pt sandwiches," *Physical Review B*, vol. 93, no. 1, p. 014426, 2016.

[19] M. Tokaç, S. Bunyaev, G. Kakazei, D. Schmool, D. Atkinson, and A. Hindmarch, "Interfacial structure dependent spin mixing conductance in cobalt thin films," *Physical Review Letters*, vol. 115, no. 5, p. 056601, 2015.

[20] X. Wang, J. Xiao, A. Manchon, S. Maekawa, *et al.*, "Spin-Hall conductivity and electric polarization in metallic thin films," *Physical Review B*, vol. 87, no. 8, p. 081407, 2013.

[21] L. X. Hayden, R. Raimondi, M. Flatté, and G. Vignale, "Intrinsic spin Hall effect at asymmetric oxide interfaces: Role of transverse wave functions," *Physical Review B*, vol. 88, no. 7, p. 075405, 2013.

[22] J. Agustsson, U. Arnalds, A. Ingason, K. B. Gylfason, K. Johnsen, S. Olafsson, and J. T. Gudmundsson, "Electrical resistivity and morphology of ultra thin Pt films grown by dc magnetron sputtering on SiO_2," in *Journal of Physics: Conference Series*, vol. 100, p. 082006, IOP Publishing, 2008.

[23] Y. Namba, "Resistivity and temperature coefficient of thin metal films with rough surface," *Japanese Journal of Applied Physics*, vol. 9, no. 11, p. 1326, 1970.

[24] E. H. Sondheimer, "The mean free path of electrons in metals," *Advances in Physics*, vol. 1, no. 1, pp. 1–42, 1952.

[25] A. Mayadas and M. Shatzkes, "Electrical-resistivity model for polycrystalline films: the case of arbitrary reflection at external surfaces," *Physical Review B*, vol. 1, no. 4, p. 1382, 1970.

[26] M. Kawamura, T. Mashima, Y. Abe, and K. Sasaki, "Formation of ultra-thin continuous Pt and Al films by RF sputtering," *Thin Solid Films*, vol. 377, pp. 537–542, 2000.

[27] M. Althammer, S. Meyer, H. Nakayama, M. Schreier, S. Altmannshofer, M. Weiler, H. Huebl, S. Geprägs, M. Opel, R. Gross, *et al.*, "Quantitative study of the spin Hall magnetoresistance in ferromagnetic insulator/normal metal hybrids," *Physical Review B*, vol. 87, no. 22, p. 224401, 2013.

[28] M. Farooq and Z. Lee, "Optimization of the sputtering process for depositing composite thin films," *Journal of the Korean Physical Society*, vol. 40, no. 3, pp. 511–515, 2002.

[29] B. Cullity and C. Graham, *Introduction to Magnetic Materials*. John Wiley & Sons, 2nd ed., 2009.

[30] G. Binasch, P. Grünberg, F. Saurenbach, and W. Zinn, "Enhanced magnetoresistance in layered magnetic structures with antiferromagnetic interlayer exchange," *Physical Review B*, vol. 39, no. 7, p. 4828, 1989.

[31] M. N. Baibich, J. M. Broto, A. Fert, F. N. Van Dau, F. Petroff, P. Etienne, G. Creuzet, A. Friederich, and J. Chazelas, "Giant magnetoresistance of (001) Fe/(001) Cr magnetic superlattices," *Physical Review Letters*, vol. 61, no. 21, p. 2472, 1988.

[32] T. Miyazaki and N. Tezuka, "Giant magnetic tunneling effect in $Fe/Al_2O_3/Fe$ junction," *Journal of Magnetism and Magnetic Materials*, vol. 139, no. 3, pp. L231–L234, 1995.

[33] J. S. Moodera, L. R. Kinder, T. M. Wong, and R. Meservey, "Large magnetoresistance at room temperature in ferromagnetic thin film tunnel junctions," *Physical Review Letters*, vol. 74, no. 16, p. 3273, 1995.

[34] G. Jonker and J. Van Santen, "Ferromagnetic compounds of manganese with perovskite structure," *Physica*, vol. 16, no. 3, pp. 337–349, 1950.

[35] E. Nagaev, "Lanthanum manganites and other giant-magnetoresistance magnetic conductors," *Physics-Uspekhi*, vol. 39, no. 8, pp. 781–805, 1996.

[36] W. Thomson, "XIX. On the electro-dynamic qualities of metals: Effects of magnetization on the electric conductivity of nickel and of iron," *Proceedings of the Royal Society of London*, vol. 8, pp. 546–550, 1857.

[37] I. Žutić, J. Fabian, and S. D. Sarma, "Spintronics: Fundamentals and applications," *Reviews of Modern Physics*, vol. 76, no. 2, p. 323, 2004.

[38] S. Wolf, D. Awschalom, R. Buhrman, J. Daughton, S. Von Molnar, M. Roukes, A. Y. Chtchelkanova, and D. Treger, "Spintronics: a spin-based electronics vision for the future," *Science*, vol. 294, no. 5546, pp. 1488–1495, 2001.

[39] S. Vélez, V. N. Golovach, A. Bedoya-Pinto, M. Isasa, E. Sagasta, M. Abadia, C. Rogero, L. E. Hueso, F. S. Bergeret, and F. Casanova, "Hanle magnetoresistance in thin metal films with strong spin-orbit coupling," *Physical Review Letters*, vol. 116, no. 1, p. 016603, 2016.

[40] C. O. Avci, *Current-induced Effects in Ferromagnetic Heterostructures due to Spin-orbit Coupling*. PhD thesis, ETH ZURICH, 2015.

[41] C. Klewe, T. Kuschel, J.-M. Schmalhorst, F. Bertram, O. Kuschel, J. Wollschläger, J. Strempfer, M. Meinert, and G. Reiss, "Static magnetic proximity effect in $Pt/Ni_{1-x}Fe_x$ bilayers investigated by x-ray resonant magnetic reflectivity," *Physical Review B*, vol. 93, no. 21, p. 214440, 2016.

[42] A. Brataas, G. E. Bauer, and P. J. Kelly, "Non-collinear magnetoelectronics," *Physics Reports*, vol. 427, no. 4, pp. 157–255, 2006.

[43] M. B. Lifshits and M. I. Dyakonov, "Swapping spin currents: Interchanging spin and flow directions," *Physical Review Letters*, vol. 103, no. 18, p. 186601, 2009.

[44] H. B. M. Saidaoui and A. Manchon, "Spin-Swapping Transport and Torques in Ultrathin Magnetic Bilayers," *Physical Review Letters*, vol. 117, no. 3, p. 036601, 2016.

[45] K. Xia, P. J. Kelly, G. Bauer, A. Brataas, and I. Turek, "Spin torques in ferromagnetic/normal-metal structures," *Physical Review B*, vol. 65, no. 22, p. 220401, 2002.

[46] Y. Yang, Y. Xu, K. Yao, and Y. Wu, "Thickness dependence of spin Hall magnetoresistance in FeMn/Pt bilayers," *AIP Advances*, vol. 6, no. 6, p. 065203, 2016.

[47] C. O. Avci, K. Garello, A. Ghosh, M. Gabureac, S. F. Alvarado, and P. Gambardella, "Unidirectional spin Hall magnetoresistance in ferromagnet/normal metal bilayers," *Nature Physics*, vol. 11, no. 7, pp. 570–575, 2015.

[48] C. O. Avci, K. Garello, J. Mendil, A. Ghosh, N. Blasakis, M. Gabureac, M. Trassin, M. Fiebig, and P. Gambardella, "Magnetoresistance of heavy and light metal/ferromagnet bilayers," *Applied Physics Letters*, vol. 107, no. 19, p. 192405, 2015.

[49] C. Corti, "Thermophysical data on platinum: resistivity and conductivity values recommended," *Platin Metal Rev.*, vol. 28, pp. 164–165, 1984.

[50] M. Kowalewski, W. Butler, N. Moghadam, G. Stocks, T. Schulthess, K. Song, J. Thompson, A. Arrott, T. Zhu, J. Drewes, *et al.*, "The effect of Ta on the magnetic thickness of permalloy ($Ni_{81}Fe_{19}$) films," *Journal of Applied Physics*, vol. 87, no. 9, pp. 5732–5734, 2000.

[51] W. Zhang, V. Vlaminck, J. E. Pearson, R. Divan, S. D. Bader, and A. Hoffmann, "Determination of the Pt spin diffusion length by spin-pumping and spin Hall effect," *Applied Physics Letters*, vol. 103, no. 24, p. 242414, 2013.

[52] Y. Lu, Y. Choi, C. Ortega, X. Cheng, J. Cai, S. Huang, L. Sun, and C. Chien, "Pt magnetic polarization on $Y_3Fe_5O_{12}$ and magnetotransport characteristics," *Physical Review Letters*, vol. 110, no. 14, p. 147207, 2013.

[53] T. G. Rijks, S. Lenczowski, R. Coehoorn, and W. De Jonge, "In-plane and out-of-plane anisotropic magnetoresistance in $Ni_{80}Fe_{20}$ thin films," *Physical Review B*, vol. 56, no. 1, p. 362, 1997.

[54] K. Fuchs, "The conductivity of thin metallic films according to the electron theory of metals," in *Mathematical Proceedings of the Cambridge Philosophical Society*, vol. 34, pp. 100–108, Cambridge Univ Press, 1938.

[55] S. Tanuma, C. J. Powell, and D. R. Penn, "Calculations of electron inelastic mean free paths. V. Data for 14 organic compounds over the 50–2000 eV range," *Surface and Interface Analysis*, vol. 21, no. 3, pp. 165–176, 1994.

[56] Y. Tserkovnyak, A. Brataas, and G. E. Bauer, "Spin pumping and magnetization dynamics in metallic multilayers," *Physical Review B*, vol. 66, no. 22, p. 224403, 2002.

[57] X. Jia, K. Liu, K. Xia, and G. E. Bauer, "Spin transfer torque on magnetic insulators," *EPL (Europhysics Letters)*, vol. 96, no. 1, p. 17005, 2011.

[58] A. Kapelrud and A. Brataas, "Spin pumping and enhanced Gilbert damping in thin magnetic insulator films," *Physical Review Letters*, vol. 111, no. 9, p. 097602, 2013.

[59] K. Olejník, V. Novák, J. Wunderlich, and T. Jungwirth, "Electrical detection of magnetization reversal without auxiliary magnets," *Physical Review B*, vol. 91, no. 18, p. 180402, 2015.

[60] M. Isasa, S. Vélez, E. Sagasta, A. Bedoya-Pinto, N. Dix, F. Sánchez, L. E. Hueso, J. Fontcuberta, and F. Casanova, "Spin Hall Magnetoresistance as a Probe for Surface Magnetization in Pt/$CoFe_2O_4$ Bilayers," *Phys. Rev. Applied*, vol. 6, p. 034007, Sep 2016.

[61] R. P. van Gorkom, J. Caro, T. M. Klapwijk, and S. Radelaar, "Temperature and angular dependence of the anisotropic magnetoresistance in epitaxial Fe films," *Phys. Rev. B*, vol. 63, p. 134432, Mar 2001.

[62] W. Limmer, M. Glunk, J. Daeubler, T. Hummel, W. Schoch, R. Sauer, C. Bihler, H. Huebl, M. Brandt, and S. Goennenwein, "Angle-dependent magnetotransport in cubic and tetragonal ferromagnets: Application to (001)-and (113) A-oriented (Ga, Mn) As," *Physical Review B*, vol. 74, no. 20, p. 205205, 2006.

[63] P. Muduli, K.-J. Friedland, J. Herfort, H.-P. Schönherr, and K. Ploog, "Antisymmetric contribution to the planar Hall effect of Fe_3Si films grown on GaAs (113) substrates," *Physical Review B*, vol. 72, no. 10, p. 104430, 2005.

Chapter 7

Temperature dependence of the magnetic proximity effect in the Pt/CoFeTaB/Pt system

7.1 Introduction

In this chapter, the results of the change in magnetic moment with temperature in a Pt/CFTB/Pt trilayered structure are presented with the major aim of understanding the evolution of proximity induced magnetic moment (PIM) as a function of temperature. Many studies have shown that spintronic applications are influenced by the magnetic characteristics at the interface that is as a result of the coupling across the interface between the ferromagnetic atoms and the nonmagnetic atoms, some of which may result in an induced magnetic moment (PIM) [1–3] or a reduced magnetic moment (magnetic dead layer) at the interface [4–7]. These changes result from variation in the anisotropy of the material and in the thermal activation energies leading to thermal instability. Although much work has been done on the influence of magnetic dead layers, little has been done in PIM. Therefore it is helpful to understand the relationship of the local magnetisation of the FM layer, here CoFeTaB (CFTB), and the non-magnetic layer, here Pt, at the interface to understand the underlying PIM mechanism.

In tunneling barrier and spin valve structures the asymmetry in the interfacial magnetic

moment can greatly influence the spin transport mechanism within the system. Also a study by Hase *et al.* on Pd/Fe/Pd revealed a significant difference in magnetic moment with temperature in Fe and Pd sublattice due to PIM [8]. This variation was attributed to the change in the Pd susceptibility with temperature. Thermal instability in a device can also affect the performance of the device and limits its applications. Hence it is very important to investigate the temperature dependence of the interfacial magnetic moment at the FM/NM interfaces.

In the following, details of the structural properties, which include a compositional description of the sample and the structural parameters of the sample, such as thickness and interface roughness extracted from best fitting GenX simulations of XRR data are discussed. A magnetic investigation with SQUID magnetometry was performed to extract the Curie temperatures, T_C, and the total magnetic moment of the material. SQUID measurements were conducted on the three sample series, which are CFTB(100Å)/Pt(30Å), Pt(3Å)/CFTB(100Å) and Pt(30Å)/CFTB(100Å)/Pt(30Å) that are similar to those discussed in chapter 5. Based on the results of the SQUID magnetometry, a detailed investigation of the magnetisation reversal within the sample was preformed with longitudinal MOKE measurements. Also, PNR was used to determine the depth distribution of the magnetic moments through the sample over a temperature range of 50 - 300 K. Finally, a detailed study of the change of proximity induced magnetic effect in Pt, performed with XRMR technique, is discussed.

7.2 Sample description and structural characterisation

In this chapter the ferromagnetic material used was amorphous CFTB of composition $Co_{28}Fe_{28}Ta_{30}B_{14}$, where the numbers in superscript are the atomic percentages. Increasing the Ta concentration to 30% is expected to reduce T_C to around 85 K [9] meaning it is nonmagnetic at room temperature. The CFTB has a 3D Bloch-like low temperature magnon excitation consistent with conventional 3D Heisenberg ferromagnetism. The choice of FM material allows magnetic measurements of the magnetic phase transition from ferromagnetism to paramagnetism below room temperature. Magnetic measurements below room temperature allow the avoidance of the effect of induced interfacial diffusion due to high temperatures. The NM material used is Pt: a heavy metal which

Table 7.1: Sample parameters of the 30 % Ta concentration Pt(30 Å)/CFTB(100 Å)/Pt(30 Å) sample from the best fit XRR data using GenX code with `LogR1` FOM where the reduced χ^2 value after simulation is 82.3.

Sample	Layer	Thickness (Å)	Interface roughness (Å)	Density($Å^{-3}$)
Pt(30 Å)/CFTB(100 Å)/Pt(30 Å)	Top Pt	33 ± 2	4 ± 2	0.064 ± 0.003
	CFTB	97 ± 3	6 ± 2	0.078 ± 0.002
	Buffer Pt	34 ± 8	4 ± 4	0.059 ± 0.010

has attracted much interest in spin current generation techniques. Here, the major interest is to understand polarisation at low temperature by proximity to CFTB and possibly how the polarisation turns on and off with temperature at each interface.

A single sample was used to perform all measurements in this chapter. A sputter deposited thin film sample of Pt(30 Å)/CFTB(100 Å)/Pt(30 Å) was prepared on a 30 mm×30 mm Si/SiO_2 substrate for the PNR measurements. Each layer was deposited *in-situ*, one after the other without breaking vacuum. The sample was later cut to a 5 mm×5 mm piece for SQUID and transverse MOKE magnetometry measurements and a 10 mm×10 mm piece, for x-ray reflectivity measurements, after polarised neutron reflectivity measurements were obtained.

Figure 7.1 presents the structural characterisation of the film. The x-ray reflectivity measurement was carried out using the D1 Bede reflectometer with a Cu K_α radiation source as described in section 3.3.4. The reflectivity data were fitted with the GenX code [10] with a model that included a layer for the thermally oxidised SiO_2 substrate. No native oxide layer was included in the model because the inclusion of one showed no change to the goodness of fit of the simulation of the film. XRR experimental data and the best fitting simulation are shown in figure 7.1a and the corresponding depth-resolved scattering profile in figure 7.1b. The structural parameters obtained from the simulations are summarised in table 7.1. Although the XRR structural scattering length density profile represents the two interfaces as symmetric, the extracted density in table 7.1 for the buffer Pt is 8 % less but similar to the density of the top Pt within error limits. This is indicative of the presence of chemical intermixing at the buffer (NM/FM) interface. Interfacial roughness can significantly alter the properties at the interface because the reduced symmetry at the interface alters the atomic layer bonding of the elements comprising the interface [11, 12]. This can lead to alterations in the spin mixing conductivity,

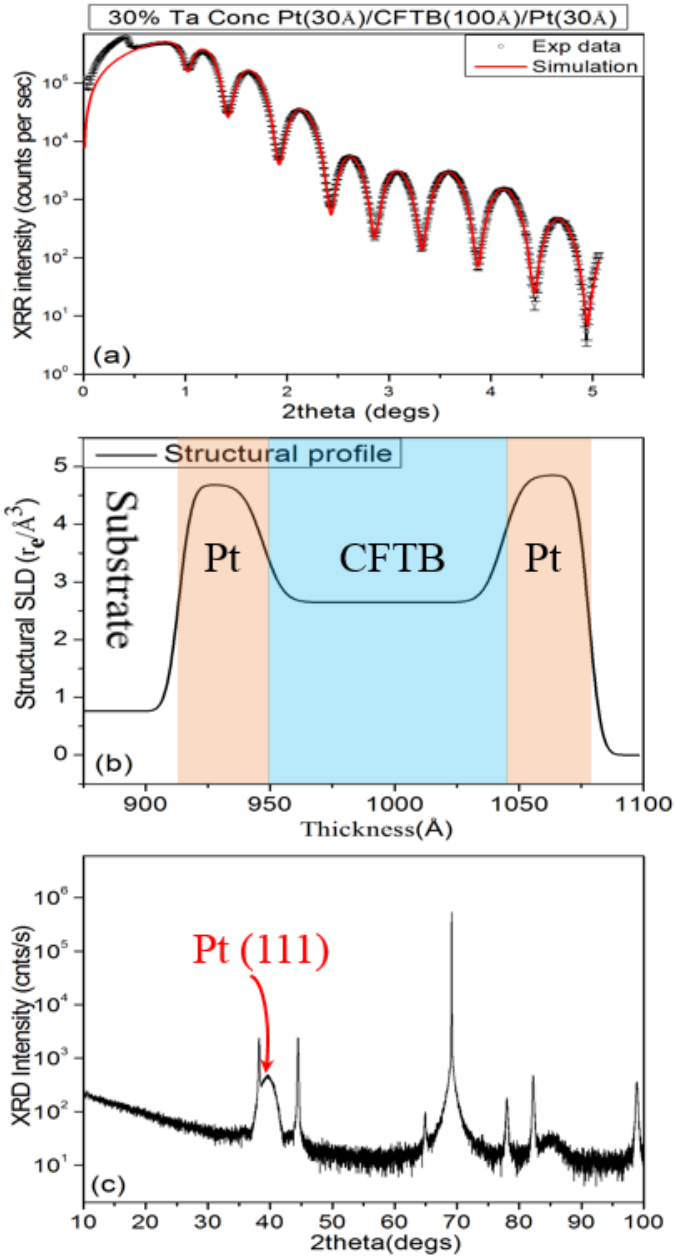

Figure 7.1: Structural characteristic: (a) X-ray reflectivity showing the experimental data (black open circles) and simulated data (red line) (b) The structural scattering depth profile showing the distribution of the FM and NM material across the sample (c) X-ray diffraction peaks confirming the growth condition of the film.

which affects the magnetoresistance and spin-current transfer properties of the sample. The interface roughness in each layer is below 10 Å, indicating that the film is continuous in the direction normal to the scattering plane. In addition, the interfacial roughness of the buffer interface (6 Å) is slightly higher that the top interface (4 Å) which confirms the asymmetry of the two interface studied.

The x-ray diffraction measurement was performed with the Rigaku SmartLab diffractometer with 9 kW Cu-K_α x-ray source monochromated to produce x-ray of wavelength 1.54 Å as outlined in section 3.3.6. XRD over a range of 2θ between 10° to 100° was conducted. The results are represented in figure 7.1c. Similar to the room temperature CFTB measurements discussed in chapters 5 and 6, the scan confirms the sample to be made up of an amorphous FM layer with the Pt having a weak FCC (111) texture. The broad peaks at 40° and 86° are the diffraction of x-rays from Pt and correspond to the face centered cubic (FCC) (111) and (222) diffraction peak respectively. The broadening describes the crystalline texture of Pt on SiO_2 and CFTB which cannot be distinguished. Since it shows a similar profile as the room temperature CFTB sample in chapter 5, therefore a peak asymmetry is assumed where the crystalline texture of Pt on SiO_2 is much weaker texture, smaller vertical coherence length than Pt on CFTB. From the Scherrer equation [13] described in section 5.2.3, the estimated crystallite grain size of about ∼30 Å is obtained for the top interface and negligible at the buffer interface as presented in section 5.2.3. The rest of the sharp diffraction peaks are from the Si/SiO_2 substrate with the XRD scan shown as an inset on figure 5.3.

Studies have shown that crystallite size depends on the sample preparation technique, substrate material, the presence of a seed layer or the annealing procedure [14, 15]. The crystallite formation depends on the initial growth texture that is characterised by the bonding at the interface. This can influence the magnetic properties of the material that varies with temperature at the interface. Hence a different PIM may be expected at the two interfaces due to the asymmetry in the crystal structure of Pt. In the next section, the variation in the total magnetic moment as a function of temperature is investigated using SQUID magnetometer.

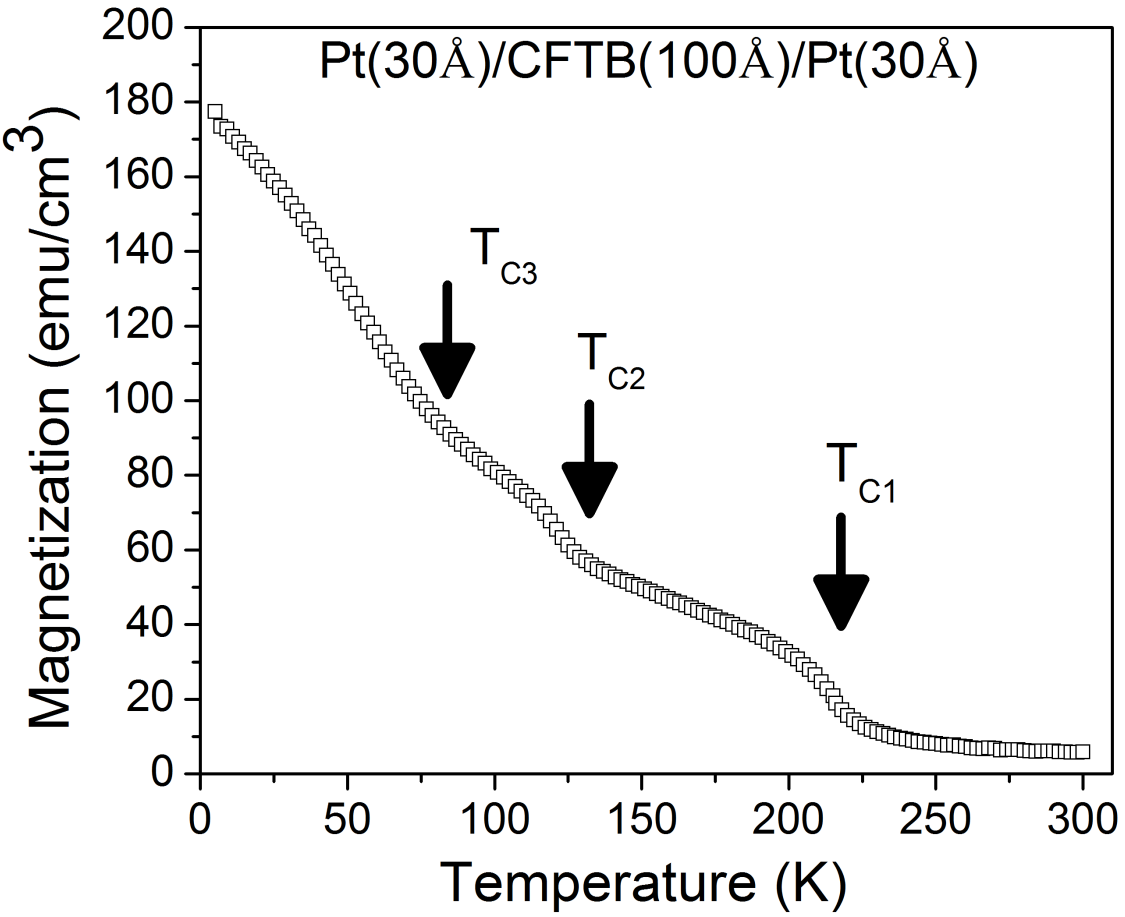

Figure 7.2: Magnetisation as a function of temperature from SQUID magnetometry for the Pt(30Å)/CoFeTaB (100Å)/Pt (30Å) trilayer performed under an applied field of 50 Oe.

7.3 SQUID magnetometry

The intrinsic magnetic structure of a magnetically ordered materials depends on temperature and transitions into a disordered state at the Curie temperature T_C, at which point the magnetic behaviour is dominated by long-range spin fluctuations that results in the gradual transition from ordered ferromagnetic to disordered paramagnetic regime above T_C. To better understand the physics of PIM at the Pt/CFTB interface, a Quantum Design MPMS system was used to determine the magnetic response as a function of temperature in the range 5 K to 300 K. The sample was field cooled at 500 Oe to 5 K as described in section 3.5.2 to ensure that the magnetisation was at saturation. Temperature dependence magnetisation data was recorded at 2 K intervals with the sample making three complete passes through the SQUID coils for each data point, recorded with an applied field of 50 Oe.

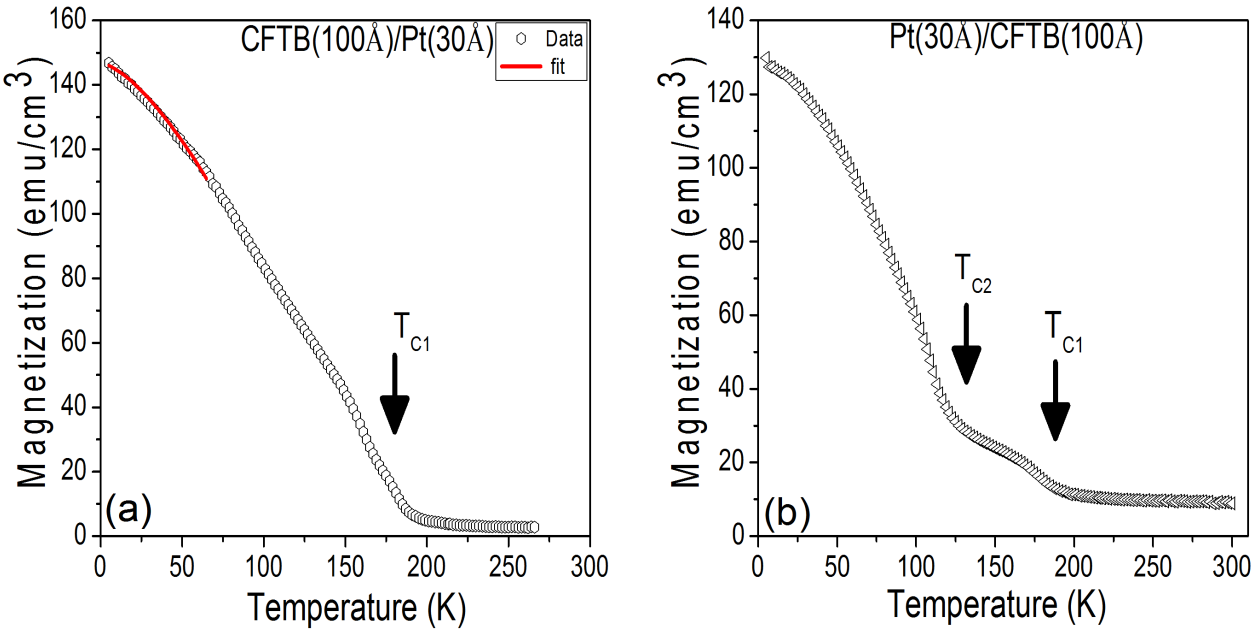

Figure 7.3: Magnetisation as a function of temperature from SQUID magnetometry for (a) the CoFeTaB (100Å)/Pt (30Å) bilayer where the solid red line is the fit of the Bloch equation and (b) the Pt (30 AA)/CoFeTaB (100Å) bilayer performed under an applied field of 50 Oe.

The magnetic response of three samples of structures Pt (30Å)/CFTB (100Å)/Pt (30Å), CFTB (100Å)/Pt (30Å) and Pt (30 Å)/CFTB (100Å) grown on Si/SiO_2 substrate were measured in order to identify and decouple the individual transition point labels T_C in the trilayered sample. Measurement of saturation magnetisation M_S as a function of temperature is characterised by a fall in M_S as the temperature increases and reduces to zero at the Curie temperature T_C. Excluding the influence of quantum fluctuations, at $T \geq 0$ K the film becomes perfectly ordered but the ordering is weakened by excitations as temperature increases. In FM systems like those considered here, these excitations are called spin waves which are quantised and called magnons. The transition from the ferromagnetic to the paramagnetic regime can be characterised by the power law which describes the critical behaviour. The behaviour at low temperature within the spin wave regime ($< T_C/3$) can be described by the Bloch $T^{\frac{3}{2}}$ power law equation given as

$$M(T) = M(0)\left(1 - \left(\frac{T}{T_c}\right)^{\frac{3}{2}}\right) \tag{7.3.1}$$

where M(0) is the spontaneous magnetisation at zero temperature. In a FM, the region close to, but below T_C, is usually characterised with critical fluctuations and the phase transition at

T_C. The phase transition is identified as a point of abrupt change in magnetic behaviour [16]. Looking at the response in figure 7.2 for Pt(30 Å)/CFTB(100 Å)/Pt(30 Å), there is evidence of more than one transition point notated as $T_{C(1-3)}$ in the magnetic response. These identified phase transitions may be attributed to compositional variations across the sample which have been observed in the room temperature PNR measurement discussed in chapter 5 suggesting non-uniformity in the magnetisation across the sample. This inhomogeneity is related to the tantalum distribution, as it varies the T_C. This maybe as a result of the asymmetry in magnetic properties at the interface which probably reflects the contribution of the different moments at the interface and within the sample. Also, at the interfaces there may be some form of rigidity due to this inhomogeneity or bondings between the FM and NM atoms where the system have some strong energetic magnetic preference making the FM region to show signs of strong permanent magnetism at certain temperatures. Apart from T_{C1} which is the point of transition from ordered ferromagnetism to dis-ordered paramagnetism, there is also T_{C2} and T_{C3} which happen at regions dominated with critical fluctuations and excitations where the energy of the system is gradually increasing towards the disordered state. This makes it slightly difficult to extract values T_C using equation 7.3.1 from this magnetisation profile.

In order to resolve the origin of the different T_C observed in the trilayered sample, a SQUID measurement of bilayered CFTB (100Å)/Pt (30Å) and Pt (30 Å)/CFTB (100Å) was conducted. The temperature dependence magnetisation plots are shown in figure 7.3. A fit of equation 7.3.1 to experimental data for CFTB (100Å)/Pt (30Å) shown on figure 7.3a (red line) resulted in a T_{C1} of $\sim$ 170 K which is in fairly good agreement with the measured T_C for this sample. The Pt (30 Å)/CFTB (100Å) shows evidence of two transition points T_{C2} and T_{C1} at $\sim$ 110 K and $\sim$ 170 K respectively (see figure 7.3 b) and the three transition points T_{C3}, T_{C2} and T_{C1} in Pt(30 Å)/CFTB(100 Å)/Pt(30 Å) at $\sim$ 80 K, $\sim$ 120 K and $\sim$ 215 K respectively. The T_{Cs} for Pt(30 Å)/CFTB(100 Å) and Pt(30 Å)/CFTB(100 Å)/Pt(30 Å) were derived by checking the point of abrupt change in magnetisation. It is also noted that there is a difference in M(0) in CFTB(100 Å)/Pt(30 Å) and Pt(30 Å)/CFTB(100 Å) even though they are of the same composition. Although the source of this asymmetry is not clear but may be due to the Pt polarisation. The magnetization of the samples were calculated considering the volume of the

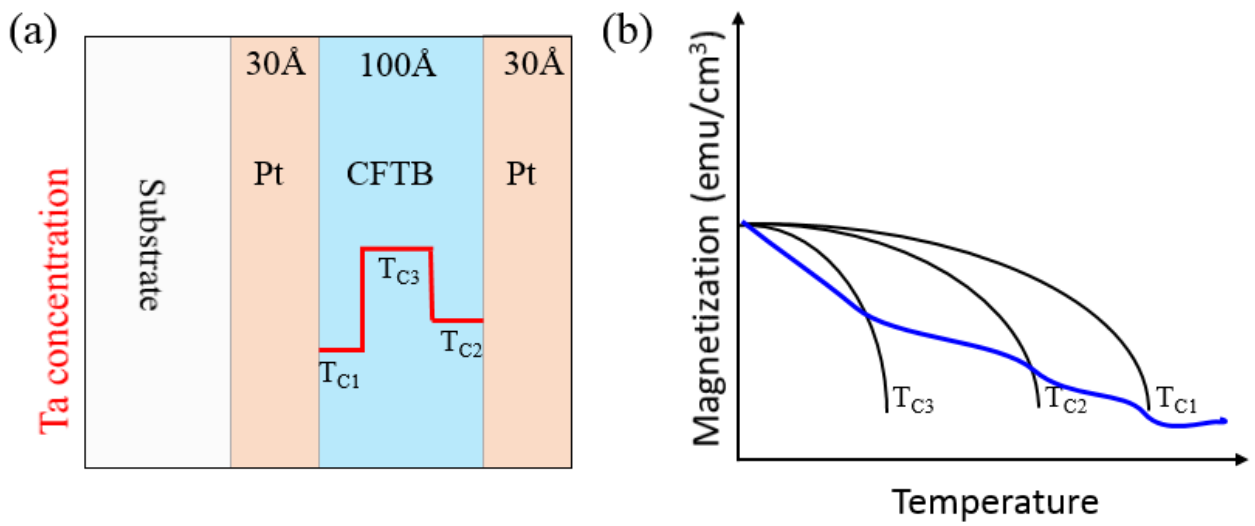

Figure 7.4: Schematic diagram showing (a) Ta diffusion in CFTB where the Ta concentration is proportional to the magnetisation (red line) (b) T_C associated to each region in relation to the SQUID measurement and Ta concentration (black lines) and possible magnetisation profile across each T_{Cs} (blue line).

FM layer only. Also, the diamagnetic contribution from the Si/SiO_2 was not subtracted from the calculation of the magnetisation. In the trilayered structure, the T_{C1} is enhanced with an excess of 45 K which suggest possible presence of proximity polarisation of Pt or other magnetic coupling within the sample.

Significant diffusion of Ta within CFTB layers has been observed to vary the magnetisation and T_C through the sample [9, 17]. Diffusion of Fe atoms towards oxides such as SiO_2 during film deposition has also been reported [18]. Therefore, the observed transition points can be attributed to compositional variation due to element diffusion within the film during growth. This can be explained in terms of Ta diffusion which modifies the magnetisation and local T_C of the film depending on its concentration in the region. Figure 7.4a depicts three possible regions of Ta concentration within the FM layer (indicated by the red line) which can affect the temperature dependence total magnetisation of the film as shown in figure 7.4b. The CFTB region close to the buffer Pt/CFTB interface is T_{C1}, while the region adjacent to the top CFTB/Pt interface is T_{C2}. Sandwiched between these two regions is the third region labeled T_{C3}. The region labeled T_{C3} characterises the bulk CFTB magnetic behaviour with the maximum Ta concentration, the least magnetic moment and the lowest T_C, while T_{C2} and T_{C1} characterise the magnetic moment of regions adjacent to the top and buffer interface respectively (see figure

7.4b). At $\sim$ 80 K the magnetisation within the T_{C3} region switches off leaving those within the T_{C2} and T_{C1} regions and at about 120 K, the T_{C2} region loses its spontaneous magnetisation. Consideration of the sum of the three T_C is likely to result in the blue sketch line in figure 7.4b which looks similar to the temperature magnetisation response of the trilayered sample shown in figure 7.3. Assuming region T_{C2} and T_{C1} are still magnetic between 80K and 120K while that of T_{C3} has vanished, there should be some form of decoupling between these two layers. A transverse MOKE investigation within this temperature range can provide more information on such coupling. This investigation is discussed in the next section.

7.4 Magnetisation coupling within the CoFeTaB layer using MOKE magnetometry

Magnetisation switching is important in the design and realisation of magneto-electronic applications. Therefore to further understand the SQUID measurement, a low temperature transverse MOKE measurement was performed by Ben Nicholson (a colleague in Durham University) on the same sample. The experimental set up is similar to the description in section 3.4.4 but with a cryostat setup in the sample space. The cryostat can cool to around 80 K as liquid nitrogen was used in cooling the sample environment. Hysteresis loops were obtained by the Kerr effect with the Kerr signal normalised to the maximum (low temperature) value. The MOKE signal is proportional to the films magnetisation with a penetration depth of $\sim$ 15 nm.

The MOKE hysteresis loop exhibits a distinct saturation field with a coercivity of $\sim$ 12 Oe. A plot of the MOKE remanent Kerr signal as a function of temperature shows a similar trend to the SQUID data. A deeper investigation around the T_{C2} shows a double switching field for 100 K to 118 K (indicated with the red arrow on figure 7.6) which vanishes at $\sim$ 120 K, where the magnetisation in region T_{C2} switches off. The two switching fields of 10 Oe and 12 Oe reveals a two-jump reversal from the magnetisation in region T_{C1} and T_{C2}. As temperature increases the signal amplitude from region with coercieve field of 10 Oe decreases, vanishing at 120 K. In detail, the magnetisation around the two interfaces switches at distinctively different

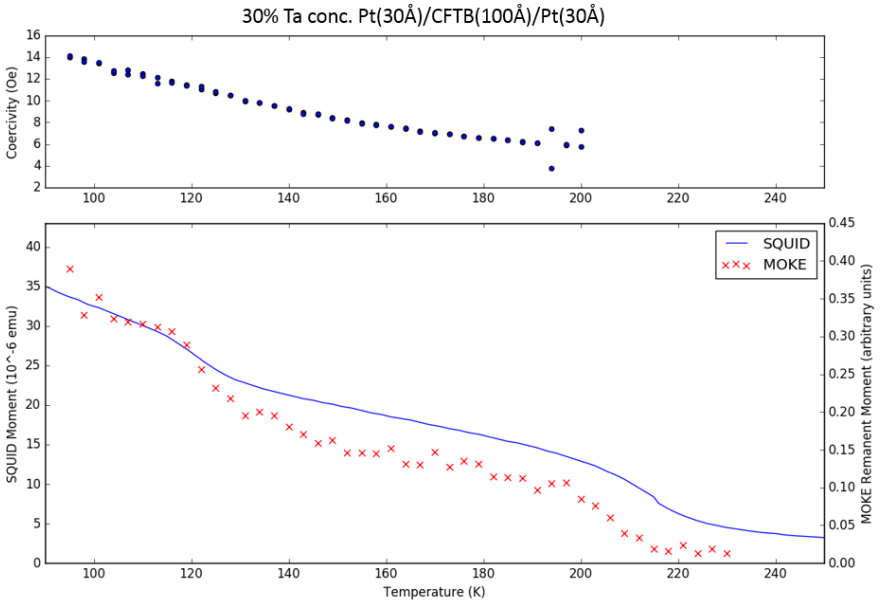

Figure 7.5: A plot of the MOKE coercivity (upper panel) and remanent magnetic moment (lower panel) as a function of temperature for the Pt(30Å)/CoFeTaB (100Å)/Pt (30Å) film showing a similar trend as the SQUID measurement (solid line)

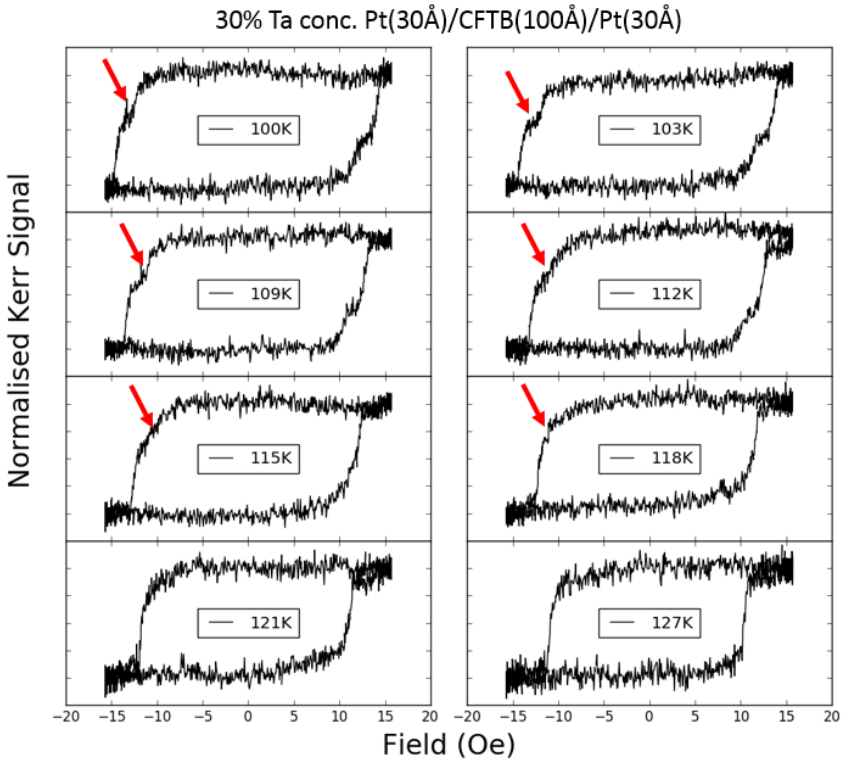

Figure 7.6: Low temperature MOKE measurements of (30Å)/CoFeTaB (100Å)/Pt (30Å) showing a double switching magnetisation (indicated with red arrows) representing the decoupling between the magnetisation of the CFTB layers around the top and buffer interfaces.

fields. This suggests that this temperature range is above the local T_C in region T_{C3} as the magnetisation of region T_{C3} had vanished. The magnetisation of region T_{C1} and T_{C2} are not rigidly coupled by strong exchange coupling. These two switching fields may be thought as to be responsible for the observed gradual decrease of magnetisation around 110 K as temperature increases observed in the SQUID measurement in figure 7.2. The difference in the switching field for these regions is small suggesting that the magnetisation in region T_{C1} and T_{C2} only varies slightly. The observed effect is similar to the observed exchange coupling by proximity magnetic effect in a FM/NM/FM sample at temperature below the FM T_C reported by Magnus *et al.* [19]. Hence the temperature dependent MOKE measurements exhibits a good agreement with the SQUID results suggesting the need for a depth resolved investigation of magnetisation in the sample in order to distinguish the magnetism in the top and bottom regions. The SQUID measurements were done in applied field of 50 Oe, meaning the magnetization obtained is close enough to the remanent magnetic moment. To further understand the influence of this atomic diffusion on magnetic behaviour, a depth-resolved method of investigation was used to explore the magnetisation of the entire film (PNR) and the magnetic proximity effect associated with the interfaces in the film (XRMR). Detailed discussion of these follows in sections 7.5 and 7.6.

7.5 Polarised neutron reflectivity interfacial analysis

Low temperature CFTB has been identified as showing a magnetic transitional crossing from a three-dimensional to two-dimensional system for films within nm thickness range [20]. The distribution of compositional elements of the alloy is inhomogeneous making PNR an appropriate technique for temperature dependent investigations providing a structural and magnetic depth profile of the film. In this section, PNR measurements carried out on the Polref beamline at ISIS facility, Rutherford Appleton Laboratory, Didcot, as described in section 3.6.5, are presented. Details on the structural profile and magnetisation changes around the interface over a temperature range of 50 - 300 K are discussed.

7.5.1 Extraction of structural parameters and depth profile

A measurement at 300 K was initially carried out for the extraction of structural parameters and error estimation of the observed magnetic moment. The film was then field cooled to 50 K in an external magnetic field of 500 Oe before low-temperature measurements were taken under a field of 50 Oe, which is enough to saturate the magnetisation in the film plane, as observed in the low-temperature MOKE measurements discussed in section 7.4. An electromagnet was employed to generate the applied field. In order to increase the temperature for the next measurement, the film was heated to the next temperature and allowed to thermalise for about 2 minutes before the next data collection.

The structural scattering length density depth profile and parameters describing it were obtained by fitting the 300 K data with a model composed of one layer representing each physical layer of the sample stack using GenX simulation software. The model included two layers to represent the substrate where one is for the pure Si substrate and the other is for the SiO_2 layer because the thickness of the SiO_2 is responsible for the fast oscillations observed at the lower Q range. This suggests the thermally-grown oxide layer on the substrate to be of fused quartz SiO_2 which was confirmed by the value of the density obtained. The obtained profile is consistent with that obtained previously from XRR. The PNR and the XRR reflectivities exhibit well defined Kiessig fringes which are from the constructive/destructive interference of the reflections from the different interfaces of the film. The reduction in reflectivity intensity follows a Q^{-4} law. The 300 K data was chosen for structural analysis based on the understanding from the SQUID and MOKE measurements which confirms that the film is nonmagnetic at this temperature. Therefore the potentials are governed by nuclear scattering density only. The structural profile is shown in figure 7.8. The estimated thickness values were approximately the same for both techniques with any difference within the error limits. Slight variation in the roughness and density of the buffer Pt layer was observed as this might be due to the difference in sensitivity of the two techniques. The x-ray measurements have more flux and better resolution to small changes in the structural parameters while the neutron measurements have less flux with a 4 % resolution making it less sensitive to structural changes. In addition, the extracted density of

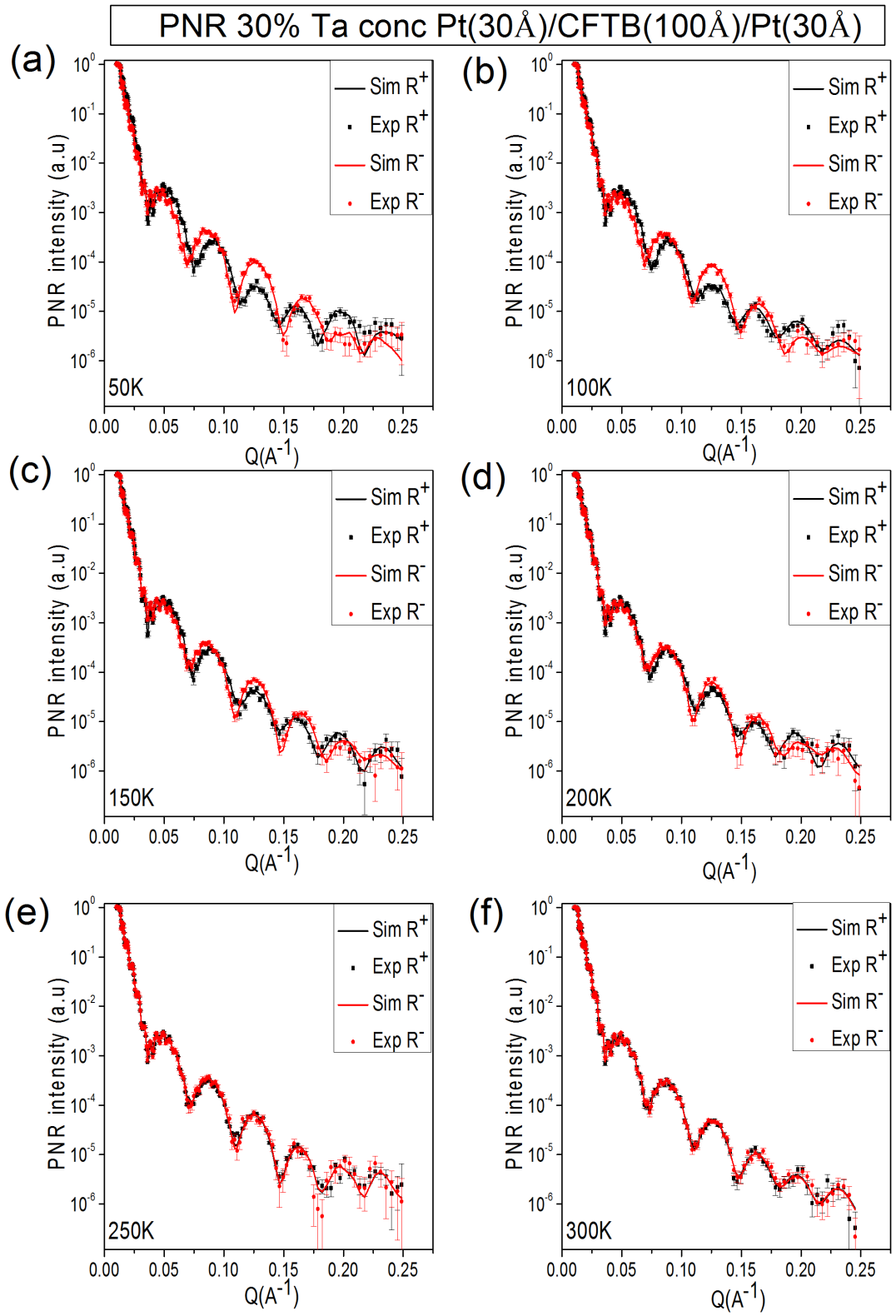

Figure 7.7: PNR spin-up (black dots) and spin-down (red dots) data with their corresponding best fitting simulations (lines) for the Pt(30Å)/CoFeTaB (100Å)/Pt (30Å) sample performed under an applied field of 50 Oe using the 3 CFTB layer model.

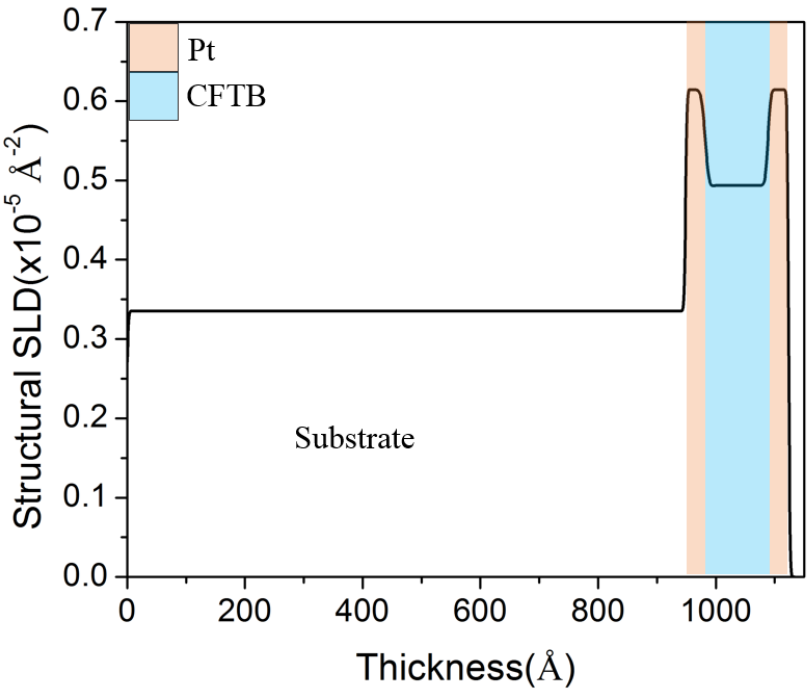

Figure 7.8: Structural scattering length density profile of Pt (30Å)/CoFeTaB (100Å)/Pt (30Å) extracted from a simulation of PNR experimental data with GenX software.

Table 7.2: Sample parameters of the 30 % Ta concentration Pt(30 Å)/CFTB(100 Å)/Pt(30 Å) sample from the best fit simulation of PNR data at 300 K using the one CFTB layer model.

Sample	Layer	Thickness (Å)	Roughness (Å)	Density(Å^{-3})
Pt(30 Å)/CFTB(100 Å)/Pt(30 Å)	Top Pt	34 ± 6	3 ± 2	0.065 ± 0.003
	CFTB	105 ± 4	8 ± 2	0.080 ± 0.004
	Buffer Pt	32 ± 6	4 ± 2	0.063 ± 0.010

the CFTB layer was slightly higher in PNR compared to the XRR measurement. The summary of the extracted structural parameters are shown in table 7.2

As there is no difference in the position and periodicity of the Kiessig fringes in the various frames of figure 7.7, it was assumed that the structural features do not vary with temperature. The thermal expansion of each composite element of the sample stack changes in the order of 10^{-5} per K. The coefficient of thermal expansion of Pt is 8.8×10^{-6} per K, Co is 13.0×10^{-6} per K at 25 K, Fe is 11.8×10^{-6} per K at 25 K and 293 K [21], Ta is 6.5×10^{-6} per K at 295 K and 2.8×10^{-6} per K at 50 K [22]. Hence, structural expansion across the temperature range is insignificant in comparison to the 4 % resolution of Q_z.

Below 250 K, the one FM layered model breaks down and is unable to capture the splitting

of the spin up and spin down reflectivity curves which characterise the magnetic properties of the sample. Hence another model was required in order to extract the magnetic properties. This new model is discussed in the next section.

7.5.2 Low temperature measurement and magnetic depth profile

In order to extract the magnetic scattering length density depth profile, a different model was employed which comprises two Pt layers for the top and buffer Pt and three CFTB layers with different composition, magnetism and T_C to capture the changes in magnetisation around both interfaces and the centre of the CFTB layer and two substrate layers as described in sections 7.3 and 7.4. The thickness, density, roughness and magnetic moments were allowed to vary as the fit converged to the local minimum after about 250000 iterations within the assigned range of physically reasonable values. For quantitative analysis, both the reflectivity and the spin asymmetry (SA) were simultaneously fitted to extract the magnetic scattering length density profile at each temperature. The quality of the reflectivity data remains high through all temperatures as the intensity of the reflectivity signal remained above the background noise for Q value up to 0.2 $Å^{-1}$

In this model, the scattering length density of the three CFTB layers varied. The density of the CFTB layer close to the Pt buffer layer was usually small and relatively close to the density of Pt for most of the temperature range investigated. This may be indicative of the presence of alloying or intermixing at this interface which might be due to growth process and was also observed in the room temperature CFTB. Although the Pt/CFTB interface is rougher than the CFTB/Pt interface, the overall roughness around the interfaces is below 10 Å showing evidence of high quality of interfaces. The middle layer CFTB roughness was generally higher but the influence of this was ignored as in reality it is part of the bulk CFTB layer. The sum total of the CFTB thickness agrees with the values for the single FM layered model quoted above but is slightly higher at lower temperature. In general, the buffer Pt thickness and density are slightly lower than the top layer through all temperatures with a difference in density of about ~ 3 % from the bulk. The estimated structural parameters of the three FM layer model are

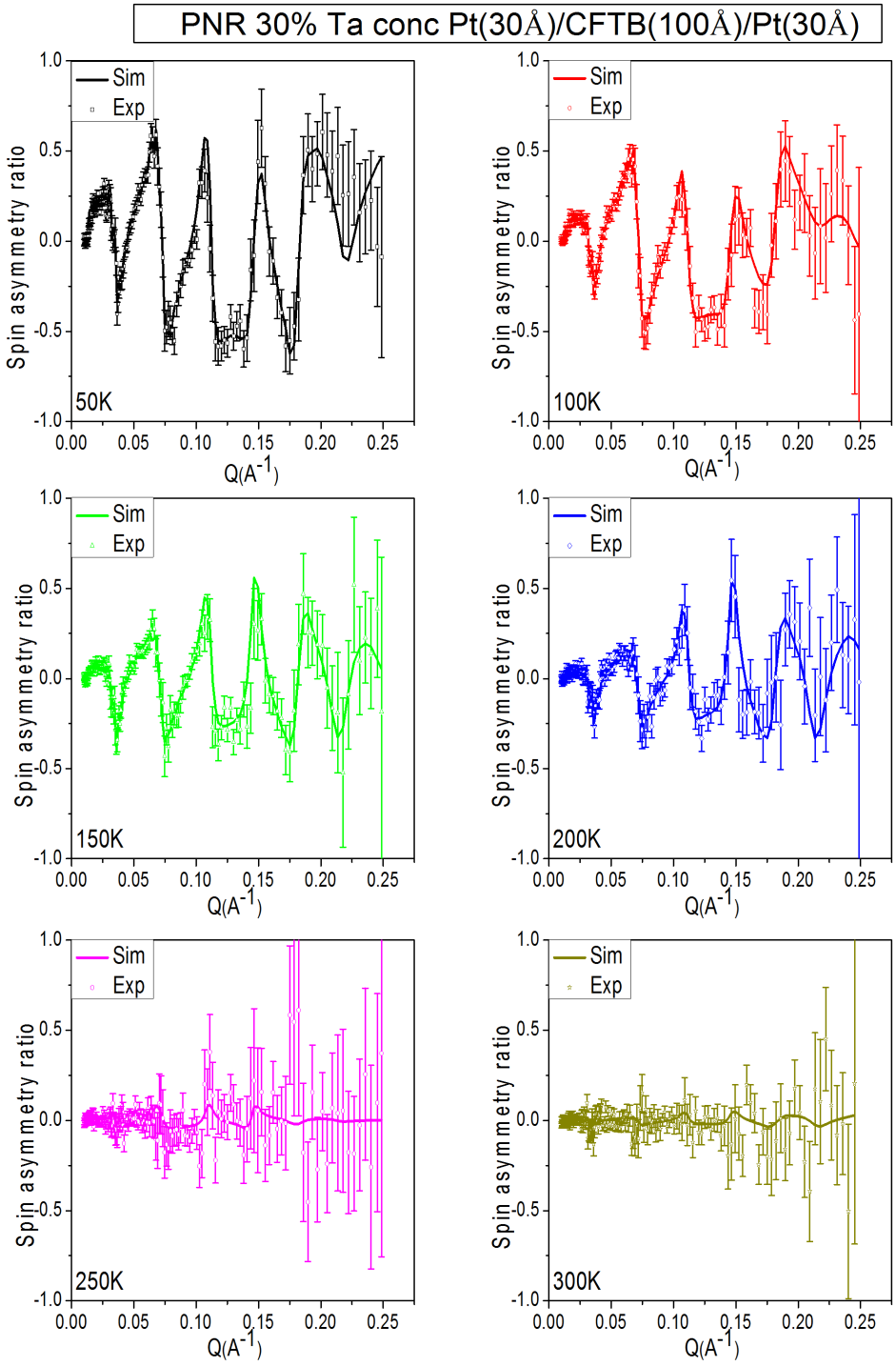

Figure 7.9: PNR spin asymmetry (SA) data (open circles) and best fitting simulation for Pt(30Å)/CoFeTaB(100Å)/Pt(30Å) performed under an applied field of 50 Oe, which characterises the magnetic depth profile of the sample at different temperatures. The reduced χ^2 values are quoted in table 7.4

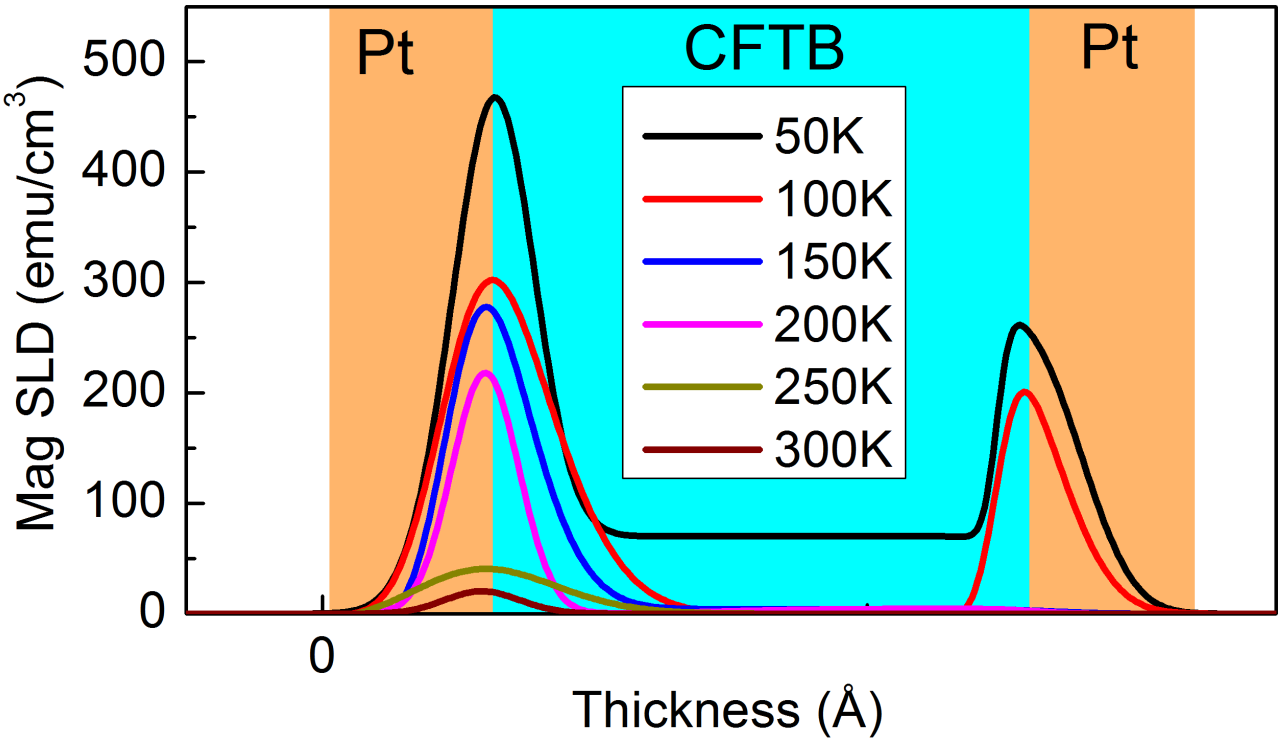

Figure 7.10: Extracted scattering length profile of (30Å)/CoFeTaB (100Å)/Pt (30Å) from GenX simulations of PNR, showing a reduction in magnetic moment of the sample with increase in temperature

summarised in table 7.3, and the corresponding χ^2 test values for each fit is below 1.4 as shown in table 7.4

At low temperature, the reflectivity response depends on the neutron spin orientation as it interacts with the electron spin within the sample. The difference in the scattering response due to the spin-up and spin-down electrons in the material represents the SA. The SA is given by equation 3.6.12 and describes the splitting between the spin up (R^+) and spin down (R^-) reflectivity in figure 7.7. This splitting gives information about the depth dependent magnetic properties of the film. The SA is automatically generated during measurement (shown on figure 7.9). Figures 7.7 and 7.9 show the low temperature measurements (marked) and the best fitting simulations (solid lines) to the reflectivity and the SA data at various temperatures. The remarkable agreement between simulation and experimental data support the suitability of the model. The SA ratio increases with decreasing temperature supporting the point of increased magnetisation at reduced temperature.

Figure 7.10 shows the low temperature PNR magnetic depth profile across the temperature

Table 7.3: Structural parameters from the GenX simulation of PNR data with the three CFTB layer model.

Temperature	Layer	Thickness (Å)	Roughness (Å)	Density(atoms Å^{-3})
50 K	Top Pt	33 ± 8	2 ± 1	0.067 ± 0.003
	CFTB 3	11 ± 1	2 ± 2	0.089 ± 0.002
	CFTB 2	87 ± 6	7 ± 4	0.080 ± 0.004
	CFTB 1	8 ± 1	6 ± 1	0.069 ± 0.006
	Buffer Pt	34 ± 4	5 ± 2	0.065 ± 0.004
100 K	Top Pt	35 ± 4	2 ± 1	0.066 ± 0.003
	CFTB 3	14 ± 2	3 ± 3	0.084 ± 0.004
	CFTB 2	87 ± 8	13 ± 5	0.081 ± 0.005
	CFTB 1	10 ± 4	7 ± 5	0.077 ± 0.003
	Buffer Pt	27 ± 5	5 ± 3	0.066 ± 0.007
150 K	Top Pt	35 ± 2	2 ± 3	0.067 ± 0.003
	CFTB 3	44 ± 4	7 ± 3	0.088 ± 0.002
	CFTB 2	57 ± 3	11 ± 8	0.081 ± 0.009
	CFTB 1	9 ± 8	2 ± 1	0.080 ± 0.002
	Buffer Pt	29 ± 4	5 ± 5	0.065 ± 0.001
200 K	Top Pt	36 ± 2	2 ± 2	0.063 ± 0.002
	CFTB 3	55 ± 3	5 ± 3	0.082 ± 0.003
	CFTB 2	43 ± 3	14 ± 7	0.079 ± 0.005
	CFTB 1	3 ± 2	6 ± 2	0.063 ± 0.002
	Buffer Pt	34 ± 1	4 ± 3	0.064 ± 0.004
250 K	Top Pt	37 ± 2	2 ± 2	0.067 ± 0.005
	CFTB 3	92 ± 5	2 ± 3	0.080 ± 0.003
	CFTB 2	5 ± 5	16 ± 3	0.051 ± 0.008
	CFTB 1	4 ± 1	6 ± 1	0.067 ± 0.001
	Buffer Pt	35 ± 4	2 ± 1	0.064 ± 0.003
300 K	Top Pt	36 ± 3	3 ± 1	0.065 ± 0.002
	CFTB 3	11 ± 3	6 ± 2	0.072 ± 0.007
	CFTB 2	90 ± 3	11 ± 5	0.081 ± 0.003
	CFTB 1	3 ± 1	7 ± 3	0.056 ± 0.007
	Buffer Pt	35 ± 2	6 ± 2	0.063 ± 0.002

Table 7.4: Minimised chi-squared per degree of freedom value from the PNR best fits shown in figures 7.7 and 7.9 quantifying the goodness of the fit.

Temperature (K)	χ^2 value
50	1.36
100	1.14
150	0.99
200	0.98
250	1.16
300	1.17

range of 50 K-300 K extracted from the simulations of the reflectivity and SA measurements shown in figure 7.7 and 7.9 fitted simultaneously. Although different models can lead to similar results this ambiguity can be overcome by extending measurements to higher Q range [23]. Therefore these analyses were made using the most realistic model as described earlier which takes into account the information on local T_C obtained from SQUID and MOKE magnetometry. The extracted magnetic SLD reveals a lower local symmetry in magnetic potential as compared to the nuclear (structural) as indicated by [24], meaning the magnitude of the structural SLD is much larger than the magnetic SLD. The changes in magnetisation profile with temperature exhibits an enhanced magnetisation around the interfaces suggesting a proximity magnetisation effect which can be attributed to Ta distribution across the sample. Regions with higher Ta concentration exhibits lower magnetisation [9]. As initially suggested in section 7.5.1 from material density variation, alloying of CFTB with Pt may possibly be a contribution to the magnetisation change. There is a general decrease of magnetisation with increase temperature. Also the changes in the profile across the temperature range indicate that the magnetisation in the CFTB may be divided into three regions similar to that identified in section 7.2. Region 1 is the region around the buffer interface, region 2 defines the center of the CFTB layer while region 3 is around the top interface. It is noticed that region 1 has the highest magnetisation which remains visible through to 200 K but the magnetisation of region 2 and 3 disappears above 50 K and 100 K respectively.

The nominal values of the magnetic SLD of the film were calculated for each temperature. A plot of the peak value of the magnetic moment against temperature for each interface shows

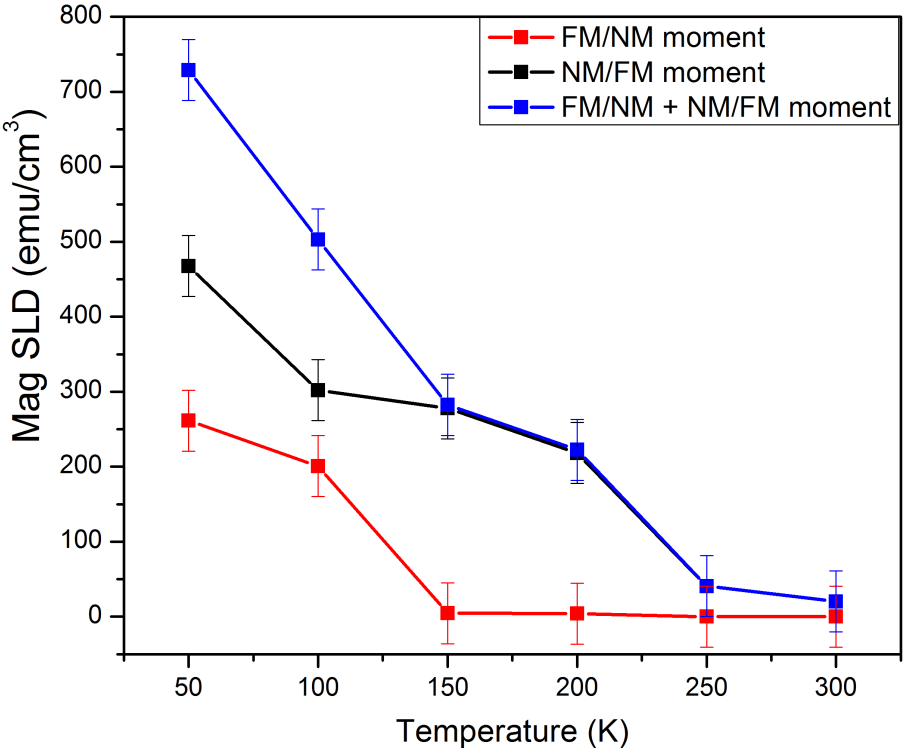

Figure 7.11: A plot the peak of the observed magnetic moment from figure 7.10 extracted from a best fit simulation of PNR and SA data for the Pt(30Å)/CoFeTaB (100Å)/Pt (30Å) sample showing a similar trend as the SQUID measurement

a decrease in magnetisation with temperature as shown in figure 7.11. Taking the sum of both moments shows a comparable magnetisation trend and magnetic moment for an equivalent size of SQUID sample represented in table 7.5. This validates the fits obtained and the suitability of the model. The error bars were estimated by turning off the magnetic moment for 250 K and 300 K simulation as this did not change the fit. This suggests that the magnetic moment seen at 250 K and 300K are artifacts from the simulation software because the film is non magnetic at these temperatures. The value of the moment at 250 K was used as an estimate of the error in magnetisation extracted from these analyses which seem a good approximation in the analyses. A magnetic moment of 0.066 μ_B/atom for Pt is estimated at 250 K which seem quite small and explains why PIM signals from Pt cannot to observed with the PNR technique.

Table 7.5: Magnetisation against temperature extracted from SQUID magnetometry and PNR measurement of an equivalent sample size

Temperature (K)	SQUID magnetisation (emu/cm^3)	PNR magnetic density (emu/cm^3)
50 K	129 ± 8	122 ± 7
100 K	81 ± 8	84 ± 7
150 K	50 ± 8	47 ± 7
200 K	32 ± 8	37 ± 7
250 K	8 ± 8	7 ± 7
300 K	6 ± 8	3 ± 7

7.6 X-ray resonance magnetic reflectivity interfacial analysis

Proximity induced magnetism (PIM) as an interfacial effect has been difficult to properly quantify because of the low volume at the interface. This can result in a significant difference in the magnetic properties around the interface and the bulk of the sample. The origin of PIM has been associated with exchange coupling and was first reported by Zuckermann in a FM/NM system [25]. Although very little had been reported in a FM/NM thin films, an enhancement of the magnetic ordering temperature by PIM had been observed in FM/antiferromagnet (AFM) system [26, 27]. An investigation of PIM with nanoparticles by capping the FM particles with NM material was found to exhibit enhanced magnetisation with enhanced T_C of the FM component. An enhanced T_C from 16 K to 180 K had been observed in Co nanoparticles capped with Pt of 0.53 nm [28]. Similar results with a 20 K enhancement was observed in Fe capped with Cu and it was argued to be associated to the Cu creating channels that mediates coupling between the Fe nanoparticles [29]. This enhancement in T_C has also been attributed to bonding of 3d electrons with the conduction band of NM capping materials [30, 31] and/or alloying at the interface [32]. Conventionally, PIM at the NM/FM interfaces reported can take the model [8, 33]

$$\mathrm{PIM} = \chi \mathrm{H_{ex}} = \chi_{\mathrm{P}} \mathrm{J} S \mathrm{M_{FM}} \tag{7.6.1}$$

where χ is the magnetic susceptibility, $\mathrm{H_{ex}}$ is the exchange field, S is Stoner enhancement factor, J is exchange coupling and $\mathrm{M_{FM}}$ is the magnetization of the FM layer whereby the phenomenon

is described to be due to band hybridisation. Most of these reported results have not investigated the change of PIM with temperature and several are conducted on systems of nanoparticles [34]. In all of these reports the method of investigation does not directly show the depth profile of PIM.

The strength of PIM is reported to decay exponentially as shown in chapter 5, but the relative range of this decay away from the interface is under debate [35, 36]. The fundamental understanding of the mechanism of PIM at FM/NM interfaces remains elusive and its critical technological issues unresolved due to the limitations of the available interface selective probing methods. There has been little work reported which investigates the influence of temperature on PIM. Hase *et al.* reported a significant change in magnetisation with temperature between Pd and Fe atoms for a Pd/Fe sample [8]. The magnetisation between Pd and Fe was observed to scale linearly with temperature being that the proximity to Fe induces a large moment in the Pd at the interface. XRMR has proven to provide a detailed depth dependent magnetisation profile at the interface. Therefore in this section, the evolution of the Pt polarisation with temperature using XRMR is presented, this will help in a better understanding of the observed temperature dependent spin pumping and inverse spin Hall effect (ISHE) by Zhang *et al.* which was attributed to temperature dependent proximity polarisation [37]. Discussions relating the XRMR measurements to the PNR measurements discussed earlier in this chapter are also presented.

7.6.1 Low temperature XRMR analysis

The XRMR measurements were performed at the XMaS beamline at ESRF, France using a circularly polarised x-ray beam tuned to the energy of the Pt L_3 absorption edge. This element specific technique is only sensitive to magnetism in Pt in contrast to the PNR measurements where the Pt magnetisation is too small to be resolved, meaning it is essentially invisible to PNR. The data were collected at a fixed energy of 11.566 keV as discussed in chapter 3. The sample was first field-cooled with a 500 Oe magnetic field to 50 K. Both the specular reflectivity and SA data were collected with an applied field of 50 Oe in the scattering plane. These data were

simultaneously simulated with GenX simulation software to extract the respective structural (sSLD) and magnetic scattering length density (mSLD) profiles. The model applied in the simulations contains the substrate, buffer Pt, CFTB and cap Pt layer. The presence of an oxide layer did not improve the simulation. Hence, no oxide layer was included in the simulation as pointed out in chapter 5.

Results of the specular reflectivity and best fits are shown in figure 7.12. A vertical offset was applied to all datasets in order to plot them on the same figure. This provides the structural details of the sample. Structural parameters obtained from the fits are within error bar limits and they are identical to those obtained from the lab x-ray measurements summarised in table 7.1. The Kiessig fringes for each temperature are indistinguishable, which indicates that there is no significant structural change across the measured temperature range. In the plots the deepest minima are observed on the 250 K data, which seems to be poorer than the rest of the simulation. This may be because the sample is non-magnetic at 250 K but is simulated with some magnetic parameters for better comparison with other results. Figure 7.13 represents the SA from the XRMR measurement for positive (red open dots) and negative (blue open dots) magnetisation with the solid black lines representing the simulations. The percentage magnitude of the SA ratio is $\sim 3\%$ at 50 K and gradually reduces to zero at 250 K. This confirms the presence of induced Pt polarisation that reduces with increasing temperature. The periodic peak position in SA is associated with the minima of the Kiessig fringes shown in figure 7.12. This is due to the fact that it contains the normalization to the total scattering intensity from the sample.

The extracted mSLD profiles are represented in figure 7.14. At both interfaces the Pt polarisation changes as a function of temperature. The induced moment on Pt extends ~ 2 nm from the interface. Reduced magnetisation with temperature may be associated to dimensionality crossover in materials as the Pt layer is very thin exhibiting the property of a 2D magnet and the interfacial magnetic layer thickness of the CFTB is small. As the temperature changes the boundary effect at the interface becomes significant, altering the magnitude of the interaction across the nearest neighbour separation. The evidence of PIM of Pt at the interface induces stronger moment at the interface with the interface acting as a 2D defect where below the 2D

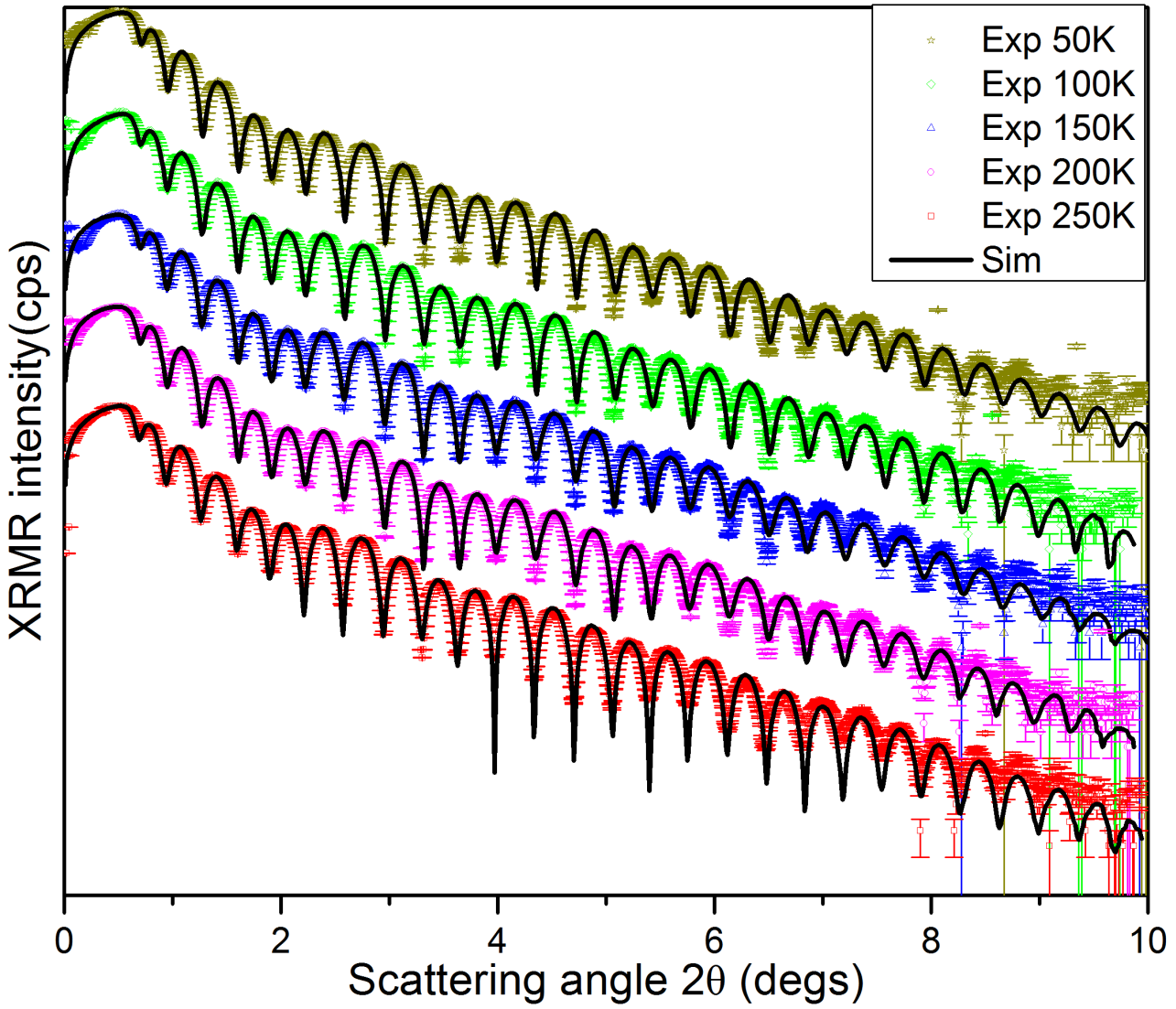

Figure 7.12: Low temperature specular x-ray reflectivity measured at the Pt-L3 edge for the Pt (30 Å)/CFTB (100Å)/Pt (30Å) sample with a vertical offset on the datasets to allow all data to be plotted on the same figure. The best fit simulations are represented with the black solid lines

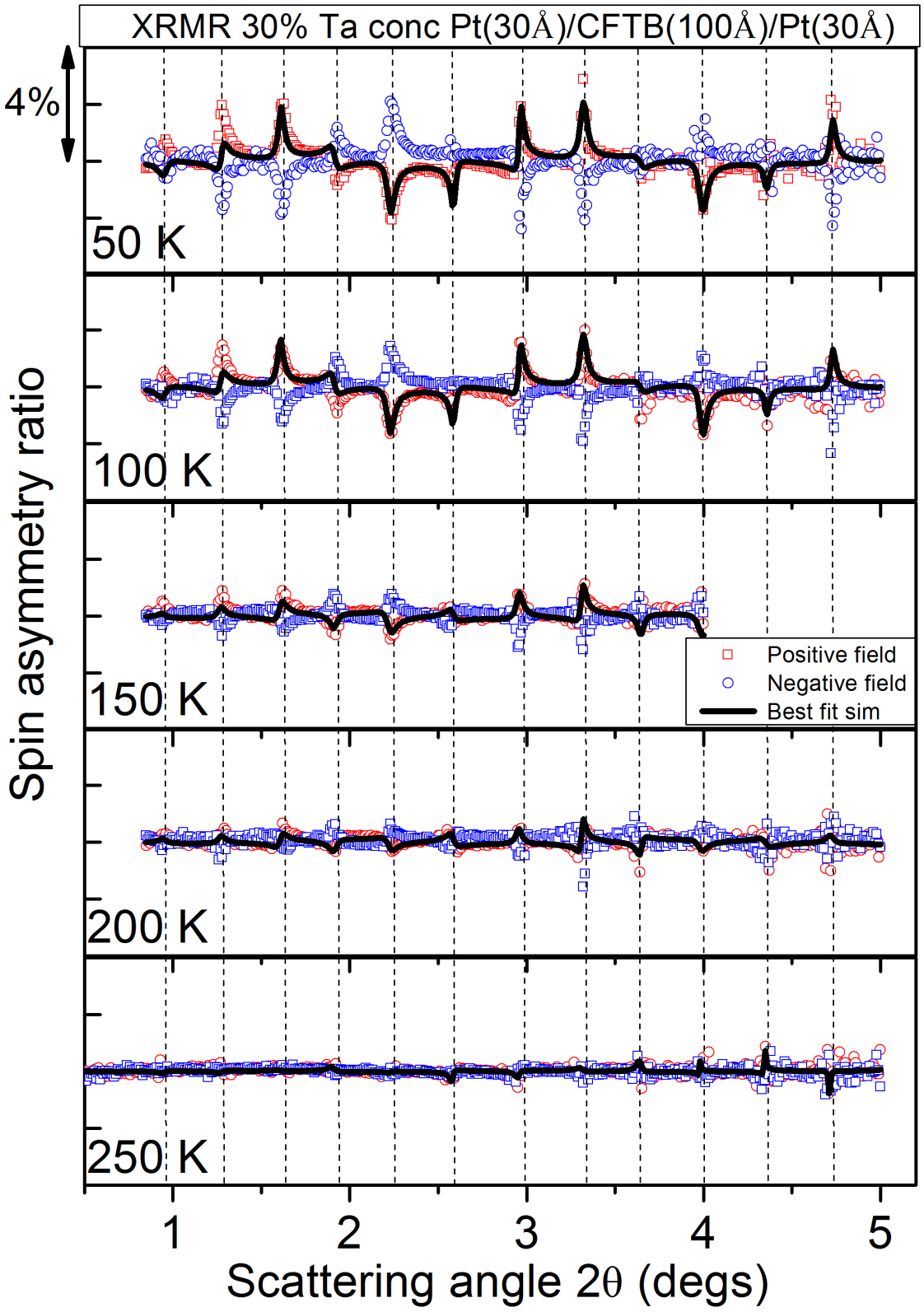

Figure 7.13: Spin asymmetry data for positive (red circles) and negative (blue circles) field directions and best fit (black lines) of Pt (30Å)/CoFeTaB (100Å)/Pt (30Å) showing decrease signal with increase temperature.

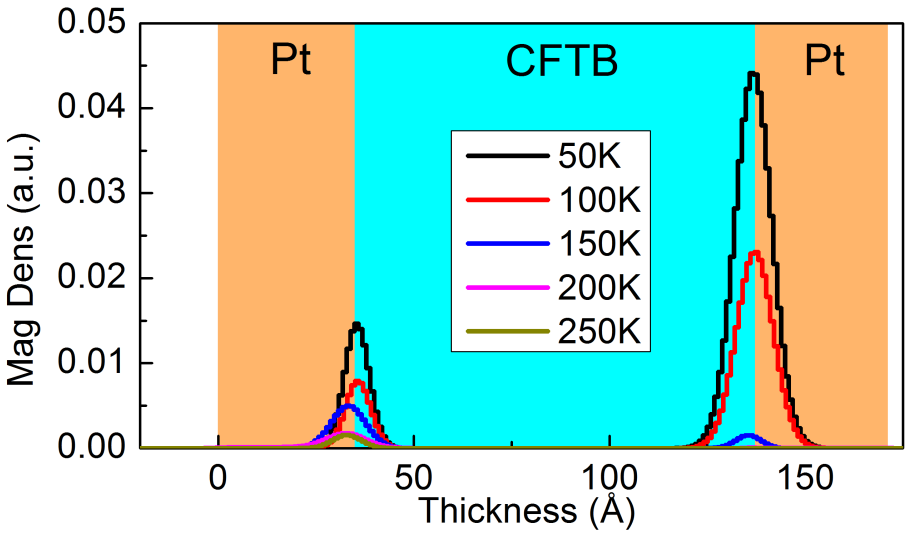

Figure 7.14: The extracted magnetic scattering length density profile of Pt (30Å)/CoFeTaB (100Å)/Pt (30Å) from simultaneous simulation of reflectivity and spin asymmetry XRMR data where the error is 0.0015.

region the Pt polarisation vanishes. The SQUID measurements confirms this as it shows more than one transition temperature.

The top interface shows the largest polarisation at 50 K that rapidly reduces between 100 K and 150 K before vanishing at above 150 K. Although the top CFTB magnetic moment vanishes at 150 K, there is still some Pt polarisation at the top interface which indicates that the polarisation can occur even in the vicinity of small FM moment or above the intrinsic ordering temperature of the FM layer as reported by Magnus *et al.* [19]. This could be due to atomic correlation within the amorphous layer. At the interface the NM material exhibits superparamagnetic properties where the Pt layer still assume magnetic property even when the CFTB magnetisation vanishes, which could be dependent on the composition. Structural disorder had been observed to result in enhanced magnetic polarisation above the ordering temperature in amorphous films [38, 39] suggesting that amorphous materials can exhibit more PIM than crystalline materials. Although we have not seen significant differences in the structural properties from the reflectivity plot, it may be possible that there is a slight enhanced coupling between the amorphous CFTB and Pt at the interface.

At the buffer interface, the Pt polarisation gradually reduces and vanishes at above 200K which agrees well with the PNR measurement because the magnetic moment at temperature

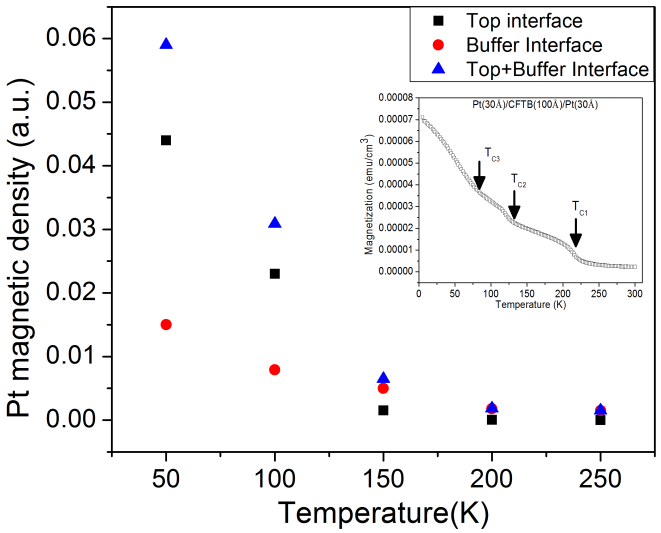

Figure 7.15: A plot of the peak magnitude of the mSLD profile in figure 7.14 for the top interface (squares), buffer interface (circles) and sum of both interfaces (triangles) showing an asymptotic decay of Pt polarisation with increasing temperature. Inset: the SQUID magnetometry measurement of Pt(30Å)/CFTB(100Å)/Pt(30Å).

above 200 K was observed to be an artifact from the software.

7.6.2 Temperature dependence of magnetic proximity effect

Taking the peak height as a representation of the magnitude of Pt magnetisation, a plot of the magnetic moment against temperature shows an asymptotic decay with temperature. This is represented in Figure 7.15. At low temperature, the magnetisation of Pt at the top interface decays similarly to the CFTB magnetisation as observed with SQUID and PNR technique and vanishes at high temperature. At the buffer interface, the magnetisation of Pt drops rapidly at low temperature to 150 K but that of PNR persisted through to 200K. At both interface the PIM are similar within the error bars for temperatures above 150 K but below 150 K the ratio of PIM in top to buffer interface is 2 : 1. This indicates that the magnetic susceptibility for Pt polarisation is temperature dependent, which is contrary to the known temperature independent magnetic susceptibility Pauli paramagnetism, as Pt assumes a superparamagnetic state. Looking at Figure 7.15, there is a significant difference in the magnetic moment at the upper and lower interface.

In order to investigate the ordering temperature due to CFTB and Pt, a plot of the ratio of XRMR polarised magnetic moment to CFTB magnetic moment was performed for both

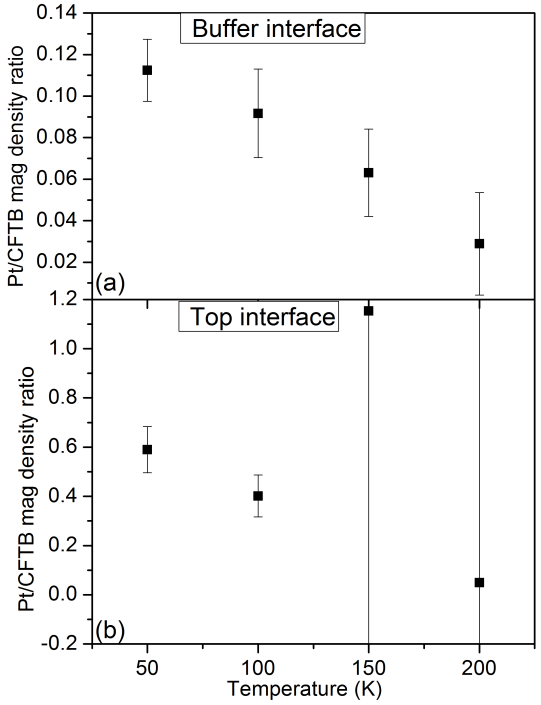

Figure 7.16: The temperature dependence of the ratio of Pt magnetic moment to CFTB magnetic moment using the units from the GenX simulator ($Å^{-2}$) for (a) buffer interface (b) top interface

interfaces (see figure 7.16). The results shows a linear response below the T_C of each interface, which indicates that the Pt magnetisation scales with the amount of magnetisation in CFTB as reported by [8]. The 250 K data points were removed from figure 7.16 because from the MOKE measurement there is no magnetic moment in the CFTB. The magnetic moment from SQUID measurement is significantly small at 250 K (see table 7.5). In addition, the errors at higher temperatures are very large as the observed moment is very small. This is due to an artificial limitation of the fitting algorithm.

Figure 7.17 represents a plot of the Pt polarised moment against the CFTB magnetisation. The top interface is comprise of two data point, which means that a conclusive inference cannot be derived from these points. Therefore, the assume linear trendline (gray dash line in figure 7.17) is only a guide to the eye. Figure 7.17 shows a linear dependence below the temperature where the magnetic moment vanishes in CFTB. When the CFTB is magnetic, there is Pt polarisation, which could be due to charge transfer or bonding between the Pt and the CFTB atoms around the interface. This effect switches off when the CFTB is nonmagnetic shown by

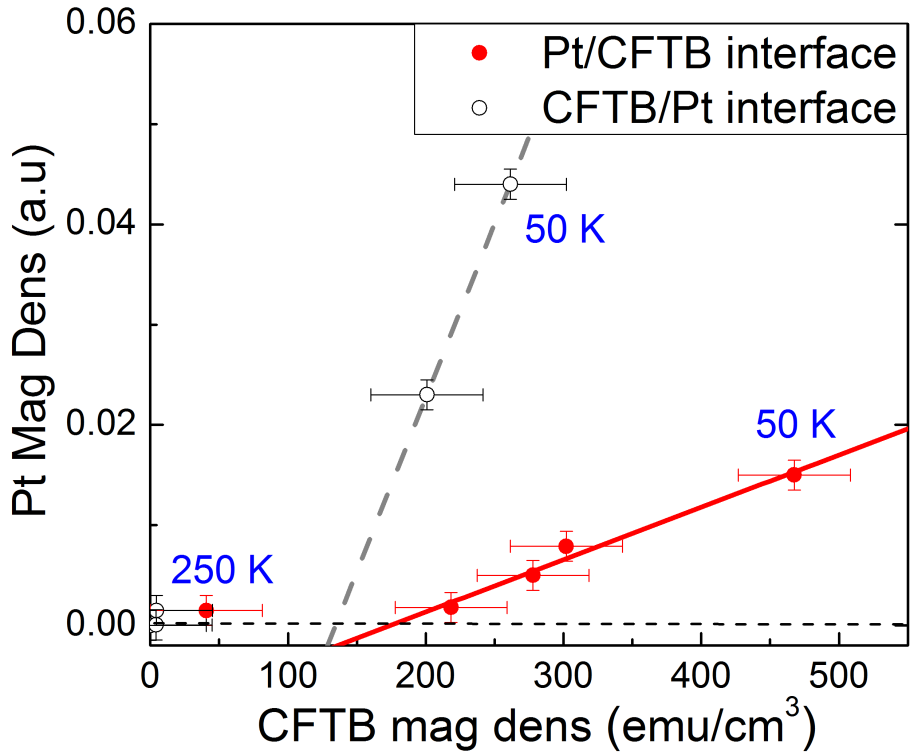

Figure 7.17: A plot of Pt magnetic moment against CFTB magnetic moment for the buffer interface (red) and the top interface (black) showing a linear response within the temperature range where CFTB is still magnetic where the gray linear line is a guide to the eye.

zero Pt moment on figure 7.16 for top and buffer interfaces.

A non-zero CFTB magnetisation is required for PIM to occur, indicating that this effect may not be due to interfacial charge-transfer. Also, equation 7.6.1 can not fully capture this behaviour but can be modified to

$$\mathrm{PIM} = \chi(\mathrm{H_{ex}} - \mathrm{H^0_{ex}}) = \chi \mathrm{J}(\mathrm{M_{FM}} - \mathrm{M^0_{FM}}) \tag{7.6.2}$$

where the interfacial magnetisation in CFTB required to initiate PIM corresponds to the contribution $\mathrm{H^0_{ex}} = \mathrm{JM^0_{FM}}$ to the effective exchange field, $\mathrm{H_{ex}} - \mathrm{H^0_{ex}}$).

The PIM in the top interface in larger but the CFTB magnetization is small while at the buffer interface, PIM is smaller with lager CFTB magnetisation. These suggest possible effect due to interfacial exchange coupling and/or difference in magnetic susceptibility between the Pt/CFTB and CFTB/Pt interfaces. The difference in the local structure at the interface may be as a result of interfacial roughness or intermixing but in this sample the roughness is below

10 Å and the reflectivity data showed no significant difference in the interfaces. This suggests that although the exchange coupling between the interface may not be different, the magnetic susceptibility may be modified by other means beyond interfacial mixing. The decrease in particle size in Pt and Pd nanoparticals have been reported to reduce susceptibility [40] and variation in lattice strain between interfaces may modify the density of states at these interfaces thereby modifying the magnetic susceptibility [41]. The mechanism to describe this asymmetry in the Pt magnetisation remains elusive and requires further investigation.

7.7 Summary

The temperature dependent magnetic response of low dimensional magnetism in Pt (30Å)/CoFeTaB (100Å)/Pt (30Å) with 30 % Ta concentration in the CFTB was investigated. The XRD measurements revealed that the samples crystalline texture is Pt (111) texture with amorphous CFTB similar to the room temperature CFTB samples discussed in chapter 5.

Magnetic investigations with SQUID and MOKE magnetometry, and PNR and XRMR techniques were performed. The SQUID measurement revealed an enhanced Curie temperature of 45 K in the trilayered sample in comparison to the bilayered sample which suggests a magnetic proximity effect. In the trilayered sample, three phase transitions were observed, which were associated with Ta diffusing inhomogeneously within the amorphous CFTB layer and the influence of the Pt adjacent layers.

A proper investigation of the phase transition at 110 K in the trilayered sample with longitudinal MOKE revealed a double switching which vanishes at 120 K. This double switching is associated to the decoupling of the magnetic moment at regions around both interfaces in the CFTB layer.

Further magnetic investigation with PNR provides a detailed depth dependent measurement of changes of magnetisation with temperature across the sample. The data obtained showed a good signal to background noise up to 0.2 $Å^{-1}$ at all temperature. From the results of the best fit simulation to the data measured over a large Q range, the structural and magnetic depth profiles were obtained. Reduced magnetisation was observed around the top interface

at low temperature that vanishes above 100 K while the magnetisation of the buffer interface persists to 200 K close to the T_C. Taking the peak magnitude of the PNR magnetisation as the representation of the magnetic moment at the interface allows a quantitative analysis of the observed magnetic moment. The sum of the magnetisation from the interfaces shows a similar trend to the SQUID data.

The PNR, SQUID and MOKE magnetisation measurements are dominated by the CFTB signal, therefore to explain the temperature enhancement observed in the SQUID data XRMR technique was used to provides the magnetisation of Pt alone. XRMR measurement shows the existence of a net magnetic moment from the modified Pt at the interfaces that changes with temperature. The Pt magnetisation decays into the CFTB layer with a width of 1.5 nm, which suggests intermixing at the interface. The comparable change in the magnetic density with temperature for PNR and XRMR gives strong evidence of temperature dependent magnetic susceptibility of Pt which scales with the CFTB magnetic moment as the ratio of the XRMR/ PNR magnetisation gave a linear response for each interface. Tuneability of magnetic moment through temperature can allow increased functionality in microwave devices, magnetic sensor devices and logic devices. Also, the confirmation of the different transition state above T_{Cs} associated to the each interface can be a remarkable step towards better understanding of the interactions between NM and FM at the interface in FM/NM systems.

References

[1] F. Wilhelm, P. Poulopoulos, G. Ceballos, H. Wende, K. Baberschke, P. Srivastava, D. Benea, H. Ebert, M. Angelakeris, N. Flevaris, *et al.*, "Layer-resolved magnetic moments in Ni/Pt multilayers," *Physical Review Letters*, vol. 85, no. 2, p. 413, 2000.

[2] C. Klewe, T. Kuschel, J.-M. Schmalhorst, F. Bertram, O. Kuschel, J. Wollschläger, J. Strempfer, M. Meinert, and G. Reiss, "Static magnetic proximity effect in $Pt/Ni_{1-x}Fe_x$ bilayers investigated by x-ray resonant magnetic reflectivity," *Physical Review B*, vol. 93, no. 21, p. 214440, 2016.

[3] E. Jal, J. B. Kortright, T. Chase, T. Liu, A. X. Gray, P. Shafer, E. Arenholz, P. Xu, J. Jeong, M. G. Samant, *et al.*, "Interface Fe magnetic moment enhancement in MgO/Fe/MgO trilayers," *Applied Physics Letters*, vol. 107, no. 9, p. 092404, 2015.

[4] L. Liebermann, J. Clinton, D. Edwards, and J. Mathon, "" Dead" Layers in Ferromagnetic Transition Metals," *Physical Review Letters*, vol. 25, no. 4, p. 232, 1970.

[5] S. Y. Jang, C.-Y. You, S. Lim, and S. Lee, "Annealing effects on the magnetic dead layer and saturation magnetization in unit structures relevant to a synthetic ferrimagnetic free structure," *Journal of Applied Physics*, vol. 109, no. 1, p. 013901, 2011.

[6] K. Oguz, P. Jivrajka, M. Venkatesan, G. Feng, and J. Coey, "Magnetic dead layers in sputtered $Co_{40}Fe_{40}B_{20}$ films," *Journal of Applied Physics*, vol. 103, no. 7, p. 07B526, 2008.

[7] T. Monchesky and J. Unguris, "Magnetic properties of Co/ GaAs (110)," *Physical Review B*, vol. 74, no. 24, p. 241301, 2006.

[8] T. P. Hase, M. S. Brewer, U. B. Arnalds, M. Ahlberg, V. Kapaklis, M. Björck, L. Bouchenoire, P. Thompson, D. Haskel, Y. Choi, *et al.*, "Proximity effects on dimensionality and magnetic ordering in Pd/Fe/Pd trialyers," *Physical Review B*, vol. 90, no. 10, p. 104403, 2014.

[9] M. Tokaç, C. Kinane, D. Atkinson, and A. Hindmarch, "Temperature dependence of

magnetically dead layers in ferromagnetic thin-films," *AIP Advances*, vol. 7, no. 11, p. 115022, 2017.

[10] M. Björck and G. Andersson, "GenX: an extensible X-ray reflectivity refinement program utilizing differential evolution," *Journal of Applied Crystallography*, vol. 40, no. 6, pp. 1174–1178, 2007.

[11] M. Hollingworth, M. Gibbs, and S. Murdoch, "Magnetostriction and surface roughness of ultrathin NiFe films deposited on SiO_2," *Journal of Applied Physics*, vol. 94, no. 11, pp. 7235–7239, 2003.

[12] Y. Kim and T. J. Silva, "Magnetostriction characteristics of ultrathin permalloy films," *Applied Physics Letters*, vol. 68, no. 20, pp. 2885–2886, 1996.

[13] J. I. Langford and A. Wilson, "Scherrer after sixty years: a survey and some new results in the determination of crystallite size," *Journal of Applied Crystallography*, vol. 11, no. 2, pp. 102–113, 1978.

[14] T. McGuire and R. Potter, "Anisotropic magnetoresistance in ferromagnetic 3d alloys," *IEEE Transactions on Magnetics*, vol. 11, no. 4, pp. 1018–1038, 1975.

[15] L. Bogart, *An Investigation of the Structure, Pinning and Magnetoresistance of Domain Walls in $Ni_{81}Fe_{19}$ Planar Nanowires*. PhD thesis, Durham University, 2010.

[16] S. Blundell, *Magnetism in Condensed Matter*. New York: Oxford University Press, 2001.

[17] M. Tokaç, *Investigation of Interfacial Effects in Ferromagnetic Thin Films*. PhD thesis, Durham University, 2016.

[18] A. Hindmarch, K. Dempsey, D. Ciudad, E. Negusse, D. Arena, and C. Marrows, "Fe diffusion, oxidation, and reduction at the CoFeB/MgO interface studied by soft x-ray absorption spectroscopy and magnetic circular dichroism," *Applied Physics Letters*, vol. 96, no. 9, p. 092501, 2010.

[19] F. Magnus, M. Brooks-Bartlett, R. Moubah, R. Procter, G. Andersson, T. Hase, S. Banks, and B. Hjörvarsson, "Long-range magnetic interactions and proximity effects in an amorphous exchange-spring magnet," *Nature Communications*, vol. 7, 2016.

[20] K. Fukamichi and R. Gambino, "The Curie temperature and magnetization of Fe-base amorphous binary alloys containing transition metal," *IEEE Transactions on Magnetics*, vol. 17, no. 6, pp. 3059–3061, 1981.

[21] E. R. Cohen, D. R. Lide, and G. L. Trigg, *AIP Physics Desk Reference*. 3rd ed.

[22] J. Jensen, R. G. Stewart, W. Tuttle, and H. Brechna, *Brookhaven National Laboratory Selected Cryogenic Data Notebook: Sections I-IX*, vol. 1. Brookhaven National Laboratory, 1980.

[23] M. A. Uribe Laverde, *Magnetic Proximity Effect in Oxide-based Superconductor/Ferromagnet Superlattices*. PhD thesis, Université de Fribourg, 2014.

[24] J. Stahn, J. Chakhalian, C. Niedermayer, J. Hoppler, T. Gutberlet, J. Voigt, F. Treubel, H. Habermeier, G. Cristiani, B. Keimer, *et al.*, "Magnetic proximity effect in perovskite superconductor/ferromagnet multilayers," *Physical Review B*, vol. 71, no. 14, p. 140509, 2005.

[25] M. Zuckermann, "The proximity effect for weak itinerant ferromagnets," *Solid State Communications*, vol. 12, no. 7, pp. 745 – 747, 1973.

[26] K. Lenz, S. Zander, and W. Kuch, "Magnetic proximity effects in antiferromagnet/ferromagnet bilayers: The impact on the Néel temperature," *Physical Review Letter*, vol. 98, p. 237201, Jun 2007.

[27] J. van Lierop, K.-W. Lin, J.-Y. Guo, H. Ouyang, and B. W. Southern, "Proximity effects in an exchange-biased $Ni_{80}Fe_{20}Co_3O_4$ thin film," *Physical Review B*, vol. 75, p. 134409, Apr 2007.

[28] A. Ebbing, O. Hellwig, L. Agudo, G. Eggeler, and O. Petracic, "Tuning the magnetic properties of Co nanoparticles by Pt capping," *Physical Review B*, vol. 84, p. 012405, Jul 2011.

[29] W.-C. Lin, P.-C. Huang, K.-J. Song, and M.-T. Lin, "Enhanced Curie temperatures in Fe and Co magnetic nanoparticle assembly on single-crystalline Al_2O_3NiAl(100) with normal metal capping layer," *Applied Physics Letters*, vol. 88, no. 15, p. 153117, 2006.

[30] F. Luis, F. Bartolomé, F. Petroff, J. Bartolomé, L. García, C. Deranlot, H. Jaffrès, M. Martínez, P. Bencok, F. Wilhelm, *et al.*, "Tuning the magnetic anisotropy of Co nanoparticles by metal capping," *EPL (Europhysics Letters)*, vol. 76, no. 1, p. 142, 2006.

[31] F. Luis, J. Bartolomé, F. Bartolomé, M. Martínez, L. García, F. Petroff, C. Deranlot, F. Wilhelm, and A. Rogalev, "Enhancement of the magnetic anisotropy of Co clusters by Au capping," *Journal of Applied Physics*, vol. 99, no. 8, p. 08G705, 2006.

[32] Y. Huttel, E. Navarro, N. D. Telling, G. van der Laan, F. Pigazo, F. J. Palomares, C. Quintana, E. Roman, G. Armelles, and A. Cebollada, "Interface alloying effects in the magnetic properties of Fe nanoislands capped with different materials," *Phys. Rev. B*, vol. 78, p. 104403, Sep 2008.

[33] W. L. Lim, N. Ebrahim-Zadeh, J. Owens, H. G. Hentschel, and S. Urazhdin, "Temperature-dependent proximity magnetism in Pt," *Applied Physics Letters*, vol. 102, no. 16, p. 162404, 2013.

[34] P. Manna and S. Yusuf, "Two interface effects: Exchange bias and magnetic proximity," *Physics Reports*, vol. 535, no. 2, pp. 61 – 99, 2014.

[35] H. Wende, A. Scherz, F. Wilhelm, and K. Baberschke, "Induced magnetism at thin-film interfaces probed by means of x-ray magnetic circular dichroism," *Journal of Physics: Condensed Matter*, vol. 15, no. 5, p. S547, 2003.

[36] P. Poulopoulos, A. Scherz, F. Wilhelm, H. Wende, and K. Baberschke, "Direct probe of

induced magnetic moments at interfaces via x-ray magnetic circular dichroism," *Physica Status Solidi (A)*, vol. 189, no. 2, pp. 293–300, 2002.

[37] W. Zhang, M. B. Jungfleisch, W. Jiang, Y. Liu, J. E. Pearson, S. G. te Velthuis, A. Hoffmann, F. Freimuth, and Y. Mokrousov, "Reduced spin-Hall effects from magnetic proximity," *Physical Review B*, vol. 91, no. 11, p. 115316, 2015.

[38] M. Ahlberg, G. Andersson, and B. Hjörvarsson, "Two-dimensional XY-like amorphous $Co_{68}Fe_{24}Zr_8/Al_{70}Zr_{30}$ multilayers," *Physical Review B*, vol. 83, no. 22, p. 224404, 2011.

[39] P. Korelis, P. E. Jönsson, A. Liebig, H.-E. Wannberg, P. Nordblad, and B. Hjörvarsson, "Finite-size effects in amorphous $Fe_{90}Zr_{10}/Al_{75}Zr_{25}$ multilayers," *Physical Review B*, vol. 85, no. 21, p. 214430, 2012.

[40] D. A. van Leeuwen, J. M. van Ruitenbeek, G. Schmid, and L. De Jongh, "Size-dependent magnetisation of Pd clusters and colloids," *Physics Letters A*, vol. 170, no. 4, pp. 325–333, 1992.

[41] S. C. Hong, J. I. Lee, and R. Wu, "Ferromagnetism in Pd thin films induced by quantum well states," *Physical Review B*, vol. 75, no. 17, p. 172402, 2007.

Chapter 8

Conclusion and further work

In this thesis, several experimental techniques were employed in the study of interfacial magnetic effects in amorphous CoFeTaB (CFTB) thin films with Pt deposited on Si/SiO_2 substrates by magnetron sputtering. Proximity induced magnetism (PIM) in the Pt layer adjacent to CFTB layer, its changes with temperature and its consequent influence on spin transport at the interface are explored. A characteristic spin-dependent phenomenon was studied by magnetoresistance measurements with a specific interest in the effect due to the interface and possible interfacial effects due to the influence of PIM.

8.1 Summary and conclusion

The general subject, its application and aims of studies were introduced in chapter 1. An overview of the underlying Physics and experimental techniques employed are given in chapter **??** and 3 respectively. Chapter 4 describes the details of data simulation for polarised neutron and resonance x-ray experimental data using the GenX software.

In chapter 5, interfacial spin polarisation in Pt/CFTB, Pt/CFTB/Pt and CFTB/Pt samples were investigated at room temperature using PNR and XRMR. The CFTB layer composition was made of 32 % Co, 32 % Fe, 20 % Ta and 16 % B, which makes the layer magnetic at room temperature. The films were structurally characterised using XRR and XRD. The XRR data establish the fact that the films are continuous at the interface with an overall roughness <1 nm.

It was found from the XRD measurements that the Pt crystalline texture for Pt/CFTB and CFTB/Pt interface are asymmetric where the CFTB/Pt sample showed a strong Pt(111) texture with a crystalline grain size of ~ 2.8 nm that is slightly dependent on the CFTB thickness. The Pt/CFTB samples showed a weak (111) texture with no significant thickness dependence while the CFTB layer was confirmed to be amorphous.

Magnetic characterisation of these samples with longitudinal MOKE suggested similar coercive field of $< 20 \pm 6$ Oe for all samples of the same CFTB layer thickness and isotropic magnetisation in the sample plane. Further investigation with PNR provided the depth resolved structural and magnetic scattering length density profiles with higher magnetic density at the buffer (Pt/CFTB) interface in comparison to the top (CFTB/Pt) interface showing magnetic asymmetry which was inferred to be due to the morphology of the interface following the observed Pt texture from XRD. Evidence of compositional grading across the CFTB layer was noticed, which can be due to Ta diffusion within the CFTB layer. The PNR results show total magnetic moment in the sample which may include PIM in Pt. The magnitude of PIM moment is too small to be seen with the PNR technique. Therefore, the PNR results is dominated by the CFTB magnetic moment. The PIM moment in Pt was investigated using XRMR; an element sensitive technique and the measurements showed evidence of PIM in all samples, which increases slightly with increase CFTB thickness. The PIM in Pt is higher at the top interface in comparison to the buffer interface, indicating a dependence on the crystalline grain size or texture at these interfaces. The interface width at the buffer interface is slightly higher indicating greater intermixing at this interface which should show higher moment due to PIM at this interface due to more contact between the Pt and Co or Fe atoms. On the contrary, the magnetic moment at this interface was smaller suggesting that intermixing does not play a dominant role. The Pt magnetic moment increases slightly with increase CFTB thickness just as the crystalline grain size increases slightly with CFTB thickness. Therefore, measurements confirm that PIM depends on the crystalline texture at the interface and the CFTB magnetic moment around the interface.

A PIM investigation was also conducted on a YIG(380Å)/Pt(30Å) sample in order to clarify an argument in the science community on the origin of spin current in YIG. Reports in literature

on PIM in YIG systems have used XMCD technique, which is limited as it does not provide a magnetic depth profile. XRMR measurements showed no PIM signal, supporting the argument that the spin current generated in YIG is sourced from SHE and not contaminated by PIM. This result supports the idea that the application of spin current generation may soon be a reality.

The magnetoresistance response in Pt/CFTB and CFTB/Pt and CFTB/Pt/CFTB samples was investigated in chapter 6. Structural sample optimisation was conducted to determine the optimal Pt thickness, which was 2 nm for continuous film growth on Si/SiO_2 substrate.

Magneto-optical Kerr effect measurements on transverse and polar geometry confirmed the magnetic easy axis of the samples to be in-plane and the hard axis out-of-plane of the samples, which confirms the isotropic behavior observed in the longitudinal MOKE measurement in chapter 5. The insignificant thickness dependence of the coercive field with CFTB thickness suggests that the films are continuous and ferromagnetic.

Following after were the magnetoresistance measurements in three geometries in a field larger than the coercive fields. These different geometries enables the isolation of the different contributory effects observed in the in-plane geometry. In-plane electrical resistivity measurements from CFTB(tnm)/Pt(2nm) gives evidence of increased resistivity with thickness when the resistivity calculations were made as a function to CFTB thickness. On the contrary when calculations are made as a function of Pt thickness, results shows an asymptotic decay with increase thickness. Either case, this suggest current shunting through the CFTB or Pt layer as the case may be. Investigation of 2 nm CFTB showned no angular dependence confirming the FM material to be highly resistive and possibly acting as an insulator. This indicates that Pt deposition on this highly resistive layer will help uncover the phenomenological spin transport mechanisms in these samples as the bulk of the current will be passing through the Pt layer.

Thickness dependent investigations on the Pt(tnm)/CFTB(2nm) and CFTB(2nm)/Pt(tnm) sample series follows the Fuchs-Sondheimer surface scattering model with a decrease in resistivity with increasing Pt thickness. An estimated bulk resistivity and mean free path of 21 ± 3 $\mu\Omega$cm and 4.9 ± 0.5 nm respectively for Pt(tnm)/CFTB(2nm) and 18 ± 2 $\mu\Omega$cm and 4.7 ± 0.5 nm respectively for CFTB(2nm)/Pt(tnm) series was obtained at room temperature which suggest

that the resistivity change is of the same origin. The MR ratio of ~ 0.002 %, comparable to those obtained in SMR measurements was observed which signals more measurements in the out-of-plane geometries are necessary as the out-of-plane measurement in the yz geometry gives the SMR signal and xz geometry provides the AMR signal.

The out of plane magnetoresistance measurements performed on CFTB(2nm)/Pt(2nm) and Pt(2nm)/CFTB(2nm) show evidence of conventional AMR (cAMR) and conventional SMR (cSMR) with an additional unconventional MR (uMR) contribution in both geometries. The uMR also occurs in the in-plane geometry, but is significantly smaller, its influence in the out-of-plane geometry is significantly stronger; approximately ~ 0.1 %. This has not been obtained or reported in the literature and it shows a $\cos\theta$ dependence. The proposed origin of this uMR is the imaginary component of the spin mixing conductance or a consequence of the Rashba effect at the interface due to a field-like torque at this interface. The Pt polarisation at the interface creates a local magnetisation which causes the precession of the generated spin current leading to a field-like torque. Also the obtained cSMR ratio is $\sim 0.2\%$, which is larger than values obtained from most SMR experiments.

A validation measurement on CFTB(2nnm)/Pt(2nm)/CFTB(2nm) gave evidence of a similar MR profile for all geometries, confirming the origin of the uMR as not of Rashba origin as the interface of the sample are symmetric.

Residual plots of all measurements indicate higher harmonic contributions that are dependent on the magnetisation direction and are stronger in the out-of-plane geometries. Residual plots in most MR experiments have not been given any consideration in the literature, therefore signals a possible higher harmonics contributions in MR results reported so far. These results may help improve device fabrication efficiency by providing a simpler structure for spintronics applications.

In chapter 7, the temperature dependent modification of interfacial magnetic properties of Pt(3nm)/CFTB(10nm)/Pt(2nm) was examined with a combinational technique of PNR and XRMR, which is uncommon. The CFTB composition was made up of 28 % Co, 28 % Fe, 30 % Ta and 14 % B in order to ensure that the sample is nonmagnetic at room temperature, allowing a proper investigation through to the paramagnetic phase of the sample. The structural

characterisation confirms the CFTB layer to be amorphous with a Pt (111) FCC texture.

The temperature magnetisation profile from SQUID magnetometry indicated the sample with three T_{Cs} suggesting inhomogeneity of the magnetic moment within the sample. This inhomogeneity was explained to be due to variable Ta diffusion in the sample as β-Ta has been reported to reduce the magnetisation of samples where the Ta crystalline phase is of the form of a tetragonal unit cell. Comparison of the trilayered sample to bilayered CFTB(10nm)/Pt(3nm) and Pt(3nm)/CFTB(10nm) showed an enhanced T_C on the trilayered sample suggesting PIM or some kind of coupling.

Investigation of the remanent magnetic moment of the sample, from MOKE measurements with temperature, exhibited a similar profile to the SQUID data. Hence, a thorough investigation around $T_C = 110$ K revealed two decoupled magnetic regions, one with a coercive field of $\sim$ 12 Oe and the other $\sim$ 10 Oe. These suggest that the CFTB layer is possibly divided into three regions where at 110 K, the magnetization of the centre region is lost, decoupling the magnetisation of the remaining two regions either side of this layer.

Further magnetic investigation with PNR on the sample provided structural and magnetic depth profiles extracted using GenX simulations of the experimental data. Results confirm compositional non-uniformity in the magnetic properties of the CFTB layer with an enhanced magnetic moment at the interfaces and a uniform moment at the center. This divides the CFTB layer into three regions confirming the interpretation of the SQUID and MOKE measurements. The change in magnetic SLD profile with temperature shows a uniform profile in the centre CFTB layer which becomes paramagnetic at 100 K. At 150 K the upper CFTB layer (close to top interface) turns paramagnetic. The magnetic moment decreases with increase temperature and the average sum of the magnetic moment in the system shows similar magnetisation profile as the SQUID magnetometry. The interfacial magnetic enhancement suggests the presence of PIM in the sample which was investigated with XRMR: an element sensitive technique.

The PIM in Pt was confirmed with XRMR and is found to be asymmetric at both interfaces and decreases with temperature. At 50 K, the PIM is greater at the top interface in comparison with the buffer interface. A quantitative investigation of the scaling of the CFTB magnetic moment to Pt polarisation for both interfaces indicated a linear scaling but the PIM vanishes

while the CFTB magnetic moment was still significant. This indicates that this asymmetry is due to an difference in the magnetic susceptibility of Pt. This may be due to intermixing, decrease in grain size or texture in the system thereby modifying the magnetic susceptibility of Pt. The asymmetry can also be due to strain, as it has been reported in literature.

8.2 Further work

This thesis has demonstrated a sequential investigation of PIM effect at room temperature and low temperatures and it consequent influence on spin transport. Further studies on PIM and its underlying influence on spin transport about the interface can be extended. Highlights of some of the possible routes to extend this work for better understanding and possible application in device fabrication are discussed.

The room temperature investigation of PIM can be extended to other amorphous Fe-base materials. It would be quite interesting to possibly quantify the amount of induced moment due to the PIM effect, which will require the distinct calibration of the XRMR system to extract the resonant scattering factors. Also, XRMR investigation at Pd absorption edge in CFTB/Pd interface is another direction of investigation as Pd is another paramagnetic material within the Stoner region.

As the MR ratio obtained due to the SHE is quite high, a thickness dependent MR investigation may be able to provide more information on the spin mixing conductance and the results obtained can be compared to the value extracted from a ferromagnetic resonance (FMR) experiment. By this, the imaginary contributions of the spin mixing conductance can be quantified as the FMR experiments provide the value of the real part of the spin mixing conductance.

Although, the work presented in chapter 7 looks as though it has reached a satisfactory conclusion where the temperature dependent PIM was presented to be dependent on susceptibility. The magnetic profile obtained for CFTB to support this result is justifiable. However, further investigations on the relation of PIM on the structural modifications due to temperature change is required for a better understanding of the factors that influences induced polarisation in Pt.

Factors such as crystalline grain size, texture, strain and amount of intermixing at the interface can be considered. In addition, transport measurement as a function of temperature is another way to extend the temperature dependent investigations. This will help in the understanding of influence of PIM on spin transport at low temperature and to investigate the regimes where PIM is not present.

Appendices

Appendix A

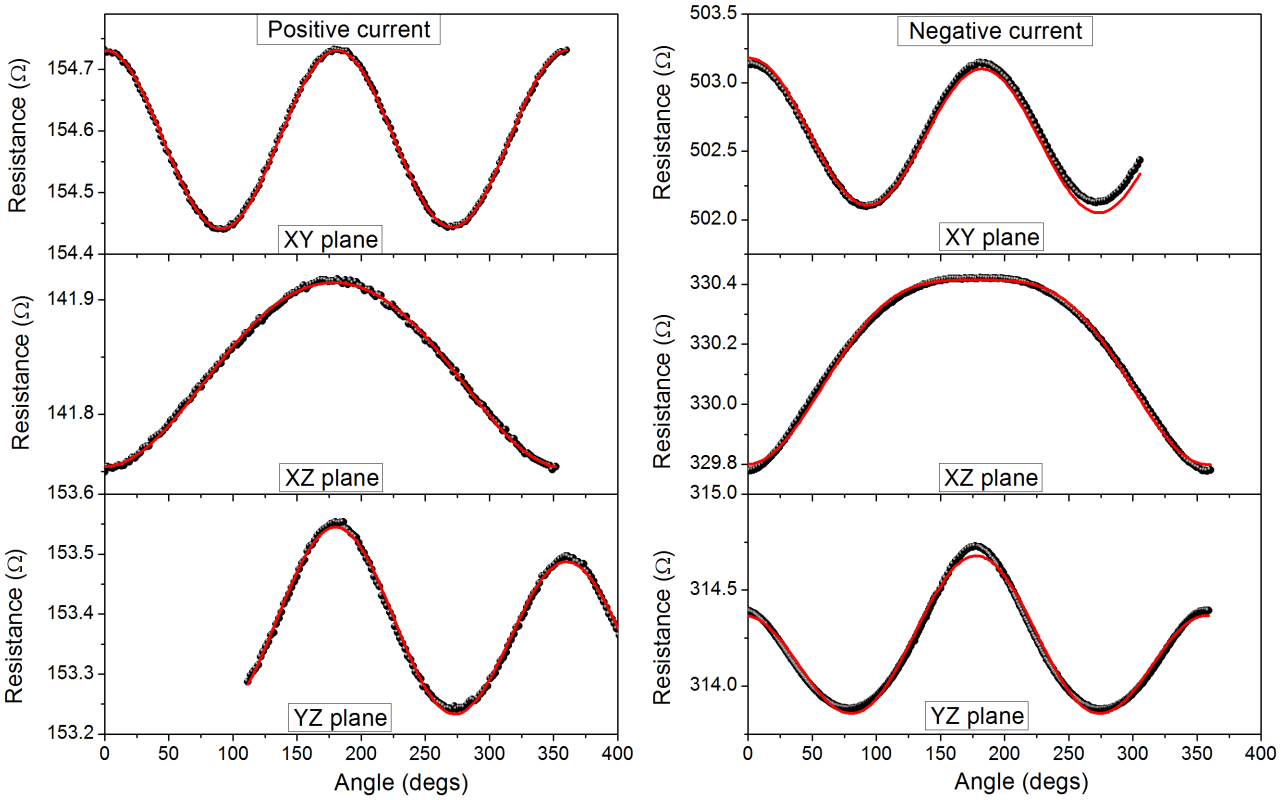

Figure A.1: Magnetoresistance measurement of CFTB(2nm)/Pt(2nm) sample for positive current and negative current as labeled showing similar trend for each individual geometry.

Appendix B

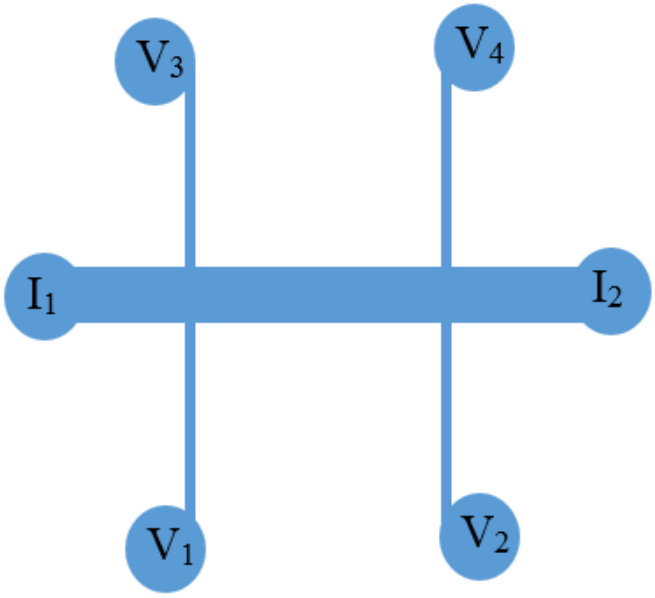

Figure B.1: The recommended Hall bar pattern for magnetoresistance measurement using wire bonding, which will enable the measurement of longitudinal and transverse resistivity.